Substrate Integrated Waveguide Antennas and the use of Graphene for Waveguide Calibration

Yasameen F. Azeez

A thesis presented for the degree of
Doctor of Philosophy

School of Engineering & Digital Arts
University of Kent
United Kingdom
August, 2019

Abstract

Recently, there has been an increased interest in high data rate (millimeter wave frequencies) systems, towards 5G network. Millimeter wave systems have an advantage of wide bandwidth, higher resolution, cost efficiency and smaller component sizes. Substrate integrated waveguide (SIW) is a good candidate for millimeter-wave systems, offering low loss, high quality factor and lower cost.

This thesis presents a brief introduction to the conventional waveguide, planar transmission lines, the main characteristics of the substrate integrated waveguide antenna (SIW) including losses, bandwidth and design rules for SIW.

The novelty of the slotted substrate integrated waveguide (SSIW), that allowed the integration of lumped elements along the slot, is presented in chapter 2. The slotted SIW supports half mode $\mathrm{TE}_{1/2,0}$. A novel antenna in SSIW is designed using CST (microwave studio) and fabricated. Additionally, the various parameters of the SSIW antenna have been studied, as well as their effect on resonant frequency and matching. To enhance gain, a 2×2 SSIW array has been simulated and shown to improve the gain by 6 dBi.

A novel tri-band antenna is presented in chapter 3. The final design is a tri-band substrate integrated waveguide antenna. This design could Possibly tune the resonant frequencies with additional slots to the antenna. The design has open-end terminations and acts as a dual waveguide region based on half mode $TE_{1/2,0}$ of each region. Different modes and their resonant frequencies were studied, as well as parameters' effects on tri-band SIW antenna. To increase gain and reduce side lobe level, a 2 × 2 array has been simulated and fabricated.

The possibility of tuning the response of SIW waveguides using graphene is studied in Chapter 4. This was done by applying an electric field to the graphene to modulate its conductivity. The difficulties associated with this are studied and some solutions are suggested to tuning the waveguide.

Chapter 4 also presents measurements of the conductivity of mono-, bi- and tri-layers of graphene at millimeter-wave frequencies and suggests a waveguide calibration scheme for the network analyzer measurements based on the layers of graphene.

Acknowledgements

Many thanks to my great supervisor Dr. Paul Young for his guidance and support throughout my PhD study. Many thanks for the financial support from my sponsor “The Higher Committee for Education Development in Iraq”. I would also like to thank my parents and my husband for their support and help.

Many thanks to the National Physical Laboratory for allowing me to do measurements. Last but not least, special thanks to Simon Jakes for his fabrication work and help during my PhD study.

List of Abbreviations

1 G	First generation of wireless cellular technology (mobile telecommunications.
5 G	Fifth generation wireless
AF	Array factor
CST	Computer simulation technique.
EM	Electromagnetic waves
FHMSIW	Folded half mode substrate integrated waveguide.
GSS	Graphene sandwich structure
HMSIW	Half mode Substrate integrated waveguide.
HPBW	Half power beamwidth
IEEE 802	Set of standards that define communication for wireless LANs. (wireless local area networks, or WLANs).
MIMO	Multiple input, multiple output.
PCB	Printed circuit board
PPWG	Parallel plate waveguide.
RWG	Rectangular waveguide.
SISW	Substrate integrated slab waveguide.
SIW	Substrate integrated waveguide.
SLL	Side lobe level
SOLT	Short Open Load and Through
SOS	System on substrate
SSIW	Slotted substrate integrated waveguide
TE	Transverse electric.
TEM	Transverse electro-magnetic
TM	Transverse magnetic.
TRL	Through-Reflect-Line.
VNA	Vector network analyzer
Wi-Fi	Wireless fidelity

List of Variables

V	Description	Units
A	Attenuation constant	Nepers/m
B	Phase constant	Radians/m
Γ	Propagation constant	
ε_{eff}	Effective permittivity	Fm^{-1}
Θ	Phase offset	rad
Λ	Wavelength	m
$\boldsymbol{\lambda_c}$	Cut-off wavelength	m
$\boldsymbol{\lambda_g}$	Guided wavelength	m
$\boldsymbol{\lambda_m}$	Wavelength in medium	m
$\boldsymbol{\sigma}$	Conductivity	sm^{-1}
$\boldsymbol{v_m}$	Velocity in a medium	$\mathrm{m\ s}^{-1}$
ω	Angular frequency	$\mathrm{rad\ s}^{-1}$
A	Waveguide width	m
a_{eff}	Effective waveguide width	m
E	Electric field intensity	V/m
F	Frequency	Hz
f_c	Cut-off frequency	Hz
K	Wavenumber	m^{-1}
k_c	Cut-off wavenumber	m^{-1}
L	Inductance	H
R	Resistance	Ω
Z	Impedance	Ω
Y	Admittance	S
A	Width of the waveguide	mm
B	Height of the waveguide	mm
m, ,n	Positive integer number that generate the $\mathrm{TE}_{\mathrm{mn}}$ and $\mathrm{TM}_{\mathrm{mn}}$ modes	

A^+, A^-	Amplitudes of the wave propagating forwad and backward	
α_c	Attenuation constant due to conduction losses.	dB/cm
α_d	Attenuation constant due to dielectric losses.	dB/cm
α_R	Attenuation constant due to radiation losses	dB/cm
P	Spacing between the vias	mm
d	Diameter of the vias	mm
L_3	Widest width from slot to the edge of waveguide	mm
W_s	Width of slot of SSIW	mm
L_2	Narrow width from slot to the edge of waveguide	mm
N	Number of elements	
a_i	Excitation amplitude	
$\emptyset_i$	Excitation phase	

List of Contents

Chapter One: Introduction

1.1 Introduction……………………………………………………………………....1

1.2 Millimeter wave communications……………………………………...…………1

1.3 Waveguides…………………...………………………………………………….2

1.4 Planer transmission line……………………………………………………….5

1.5 Substrate integrated waveguide antenna………..……………………………,….6

1.5.1 Size and bandwidth of SIW…………………..…………….……….…..... 7

1.5.2 Losses in SIW………..…………………………………………………..8

1.5.3 Design rule for SIW……………………………………......……………….10

1.6 Transitions……………………………………………………………...........11

1.7 Substrate integrated waveguide power dividers……………...…………….………..12

1.8 SIW filters and couplers……………………………….……......……………..14

1.9 Thesis organization……………………......…………………….....…………15

1.10 References………………………..……………………………….………..16

Chapter Two: Slotted substrate integrated waveguide antenna

2.1 Introduction……………………………………………………………………19

2.2 Literature review……………………………………………………………......20

2.3 SSIW theoretical analysis…………………………………………………………23

2.4 SSIW design (simulation and fabrication)………………………………………...26

2.4.1 Study the Parameters effect of SSIW……………………………………..28

2.4.2 Design procedure:………………………………………………………...33

2.4.3 Comparison results between simulation and measurements………………...35

2.5 One by two slotted SIW……………………………………………………………..39

2.6 Two by two slotted SIW array……………………………………………………44

2.7 Conclusion……………………………………………………………………...48

2.8 References:……………………………………………………………………...50

Chapter Three: Tri-band substrate integrated waveguide antenna

3.1 Introduction……………………………………………………………………….52

3.2 Literature review………………………...……………………………………..52

3.3 Some proposed SIW slot antenna designs…………………………………...…55

3.3.1 SIW single slot antenna design with L_1=20 mm…………………………...55

3.3.2 Increasing slot length to improve matching (L_2=40 mm)…………………..59

3.3.3 Adding sections of the slot to the two ends of the main slot in the direction of the wider section of SIW……………………………………………………68

3.3.4 Adding two sections of the slots at the two end of the main slot in opposite direction………………………………………………………………………73

3.4 Final design of tri-band SIW with addition slots for tuning the device……………..77

3.5 Parameters effect on resonant frequency……………………………………………79

3.6 Comparison the results between simulation and measurements……………………82

3.7 1 × 2 SIW array……………………………………………………………………..88

3.8 2 × 2 dual band SIW…………………………………………………………..…93

3.9 Comparison between simulation and measurements………………………………...94

3.10 Conclusion…………………………………………………………………….....99

3.11 References…………………………………………………………………….....100

Chapter Four: The use of graphene for waveguides and graphene

4.1 Introduction……………………………………………………………………101

4.2 Literature review ……………………………………………………………...102

4.3 Electromagnetic model of graphene…………………………………………...105

4.4 Tuneable substrate integrated waveguide using silicon dioxide graphene…………110

4.5 Calibration standards using graphene………………………………………………114

4.5.1 TRL Calibration……………………………………………….......…116

4.6 Establishing a new form of primary impedance standard…………………………118

4.6.1 Graphene on open aperture……………………………………………………119

4.6.2 Quartz sample only on the waveguide…………………………………...120

4.6.3 Quartz sample with metal on top……………………………………………121

4.6.4 Graphene sample on top……………………………………………………123

4.6.5 Graphene sample on bottom……………………………………………………..124
4.6.6 Graphene on bottom metal on top………………………………………..125
4.6.7 Graphene in waveguide aperture only with metal on top…………………...126
4.7 Comparison between simulation and measurements………………………………..127
4.8 De-embedding the effect of quartz from the graphene sample……………………..131
4.9 Conclusion…………………………………………………………………………..135
4.10 References…………………………………………………………………………..136

Chapter Five: Conclusion and Future work

5.1 Conclusion…………………………………………………………………………..…139
5.2 Future work……………………………………………………………….………. 141

List of Figures

Chapter one

Fig (1.1) Geometry of rectangular waveguide……………………………………………..2

Fig (1. 2) The electric and magnetic field distribution on the wall of the waveguide at the TE_{10} mode [3]…………………………………………………………..…...4

Fig (1. 3) Planar transmission lines and propagation E-field plots [19]: (a) Parallel plate,(b) Microstrip, (c) Stripline, (d) Coplanar waveguide, and (e) Slot line [4]...……..…..5

Fig (1. 4) Geometry of SIW. Substrate thickness: b, waveguide physical width: a_{eff} ………6

Fig (1. 5) The amplitude of electric profile of fundamental SIW mode [5]…………………...7

Fig(1. 6) Variable topologies of SIWs [12]…………………………………………………8

Fig (1. 7) Transitions between transmission line and SIW: (a) Microstrip. (b) Coplanar 90^0 bend. (c) Coplanar with current probe.[5]……………….……………..………….12

Fig (1. 8) SIW feeding power divider: (a) T–divider, (b) Y-divider. ……………………..…13

Fig (1. 9) Multistage W-band SIW feeding power divider (corporate feed)[20]..…………13

Fig (1. 10) 16-way series SIW feeding divider (distributed feed) [20]…………….……14

Chapter Two

Fig (2. 1) Structure of dual slot antenna [10]……………...………………………………21

Fig (2. 2) Structure SIW slotted narrow wall fed cavity antenna [11]……………..………..21

Fig (2. 3) Geometry of SIW linear slotted array with tuning vias [12]…………......……..22

Fig (2. 4) Photograph of switched beam antenna and structure of overlay showing capacitive pads, pin diode, inductive chokes, and bias wires [13]……………………………22

Fig (2. 5) Proposed structure for open ring slot antenna [14]………………………………..23

Fig (2. 6) Half and full mode structure [9]………………………………………………...23

Fig (2. 7) SSIW Electric field distribution at $TE_{1/2,0}$ mode [5]……………………………...24

Fig (2. 8) Slotted Substrate Integrated Waveguide Antenna [5]……………………………..26

Fig (2. 9) Slotted SIW structure design……………………………………………………27

Fig (2. 10) Slot width effect on reflection coefficient versus frequency (other parameters are the same in table (2.1)…………………………………………………………29

Fig (2. 11) L_2 changing effect on return loss versus frequency (other parameters are the same in Table (2.1)……………………………………………………………………….29

Fig (2. 12) L_1 parameter change effect on reflection coefficient versus frequency (other Parameters are the same in Table (2.1)……………..……………………………30

Fig (2. 13) Effect width of the SSIW on reflection coefficient (other parameters are the same in Table (2.1)………………………………………………………………….....30

Fig (2. 14) Effect thickness change on return loss, other parameters are the same in Table (2.1)…………………………………………………………………………….....31

Fig (2. 15) Electric field distribution: (a) L_2=13 mm, (b) L_2=12 mm, (c) L_2=11 mm, (d) L_2=10 mm…………………………………………………………………..32

Fig (2. 16) (a) Single slot resonant waveguide (b) Equivalent circuit [13]…………….….33

Fig (2. 17) Impedance versus frequency: (a) Real part (b) Imaginary part……………..…...34

Fig (2. 18) Frequency against Z_A…………………………………………………………..35

Fig (2. 19) Equivalent T-network for slotted substrate integrate waveguide antenna…..….35

Fig (2. 20) Fabrication design of SSIW……………………………………………………...36

Fig (2. 21) Comparison of S_{11} between measurements and simulation……………………..37

Fig (2. 22) Radiation pattern at 2.5 GHz: (a) E-plane, (b) 3D pattern.……………………..…37

Fig (2. 23) Comparison of radiation pattern between simulation and measurement at 2.5 GHz: (a) E-plane, (b) H-plane ……………………….……………………………..37

Fig (2. 24) (a) Electric field distribution at 2.5 GHz. (b) gain comparison against Frequency……………………………………………………….……………..38

Fig (2. 25) Electric field distribution at: (a) 2.92 GHz, (b) 3.4 GHz……………………….....38

Fig (2. 26) Radiation pattern at 2.9 GHz: (a) H-plane, (b) E-plane, (c) 3D pattern.………………………………………………………………….……...…39

Fig (2. 27) Radiation pattern at 3.4 GHz: (a) E-plane, (b) H-plane, (c) 3D pattern.………....39

Fig (2. 28) 1×2 structure design……………………………………………………………...40

Fig (2. 29) Reflection coefficient S_{11} against frequency for 1 × 2 SSIW………...…………41

Fig (2. 30) Electric field distribution at resonant frequency at 2.64 GHz…………………....41

Fig (2. 31) Radiation pattern at 2.64 GHz: (a) E-plane, (b) 3D with directivity, (c) H-plane, (d) 3D with gain……………..……………………………..…………...42

Fig (2. 32) Electric field distribution at 2.76 GHz…………………..………………..…..42
Fig (2. 33) Radiation pattern at 2.76 GHz: (a) E-plane, (b) H-plane, (c) 3D pattern.……..…43
Fig (2. 34) Electric field distribution at 3.03 GHz…………………………………………...43
Fig (2. 35) Radiation pattern at 3.03 GHz: (a) E-plane, (b) H-plane, (c) 3D pattern.….……43
Fig (2. 36) (a) 2 × 2 array SSIW. (b) Microstrip feeding line SSIW………………………...44
Fig (2. 37) Reflection coefficient against frequency…………………………………………45
Fig (2. 38) Electric field distribution at 2.65 GHz…………………………………………...45
Fig (2. 39) Radiation pattern at 2.65 GHz: (a) E-plane, (b) 3D with gain, (c) H-plane, (d) 3D with directivity……………………………………………...……….……...46
Fig (2. 40) E-field distribution at 2.76 GHz……………………………………..………...47
Fig (2. 41) Radiation pattern at 2.76 GHz: (a) E-plane, (b) H-plane, (c) 3D pattern.……….……………………………………………………….…….….…..47
Fig (2. 42) Element spacing effect on array factor [19]……………….…………………..48

Chapter three

Fig (3. 1) Schematic diagram of triangular planer V-inverted antenna.[1]……...…………..53
Fig (3. 2) Dual band Bow-tie slot antenna [2]………...…………………………………...53
Fig (3. 3) L-shaped slot SIW (a) proposed. (b) Structure [3]……….…………………...….54
Fig (3. 4) Leaky-wave antenna (a) Transverse slots on top. (b) Circular slots on bottom [4]…………………………………………………………………………..54
Fig (3. 5) Fabricated structure of self- duplexing antenna [5]……………………………….55
Fig (3. 6) Proposed SIW slot antenna ………………………………………………………..56
Fig (3. 7) Coordinates at the open end of SIW…………………………………………......56
Fig (3. 8) S_{11}versus frequency for the proposed SIW slot antenna (L_2=20 mm)…………....58
Fig (3. 9) Electric field distribution at (a) 3.94 GHz (mode 1). (b) 5.38 GHz (mode 3). (c) 6.4 GHz (mode 4)……………………………………………………………………...58
Fig (3. 10) Radiation pattern at 6.4 GHz: (a) 3D pattern, (b) H-plane, (c) E-plane.…………59
Fig (3. 11) The proposed structure by increasing slot length (L_2=40 mm)…………………60
Fig (3. 12) Return loss against frequency for the proposed structure (after increasing slot length L_2=40 mm)…………………………………………………….……….60

Fig (3. 13) Tri-band SIW structure divided into two half modes of the waveguide: (a) Design, (b) Equivalent network…………………………………………..……………61

Fig (3. 14) Electric field distribution at: (a) 3.57 GHz (Mode 1) (b) 4.38 GHz. (Mode 2) (c) 5.163 GHz (Mode 3). (d) 5.85 GHz. (Mode 4). (e) 6.43 GHz. (Mode 5)…………....62

Fig (3. 15) Normalised phase shift $\emptyset/\pi$ along the structure showing the resonant modes of tri-band antenna using matlab……………………………………………………..63

Fig (3. 16) Radiation plot at 5.163 GHz: (a) 3D pattern, (b) H-field, (c) E-field…………...66

Fig (3. 17) Radiation pattern at 5.85 GHz: (a) 3D pattern, (b) H-plane, (c) E-plane.……..…66

Fig (3. 18) Radiation pattern at 3.57 GHz: (a) 3D pattern, (b) H-plane, (c) E-plane.……......67

Fig (3. 19) Radiation pattern at 4.38 GHz: (a) 3D pattern, (b) H-plane, (c) E-plane………...68

Fig (3. 20) Radiation pattern at 6.43 GHz: (a) 3D pattern, (b) H-plane, (c) E-plane.……......68

Fig (3. 21) Adding slots of length L_2 at the direction of the widest section of SIW……..…69

Fig (3. 22) S_{11}versus frequency (with the addition of slots L_2 perpendicular to the main slot L_1)……………………………………………………………………...70

Fig (3. 23) Electric field distribution at: (a) 3.48 GHz. (b) 4.25 GHz. (c) 5.11 GHz. (d) 6.08 GHz……………………………………………………………………70

Fig (3. 24) Radiation pattern at 5.11 GHz: (a) 3D pattern, (b) H-plane, (c) E-plane.……..…71

Fig (3. 25) Radiation pattern at 3.48 GHz: (a) 3D pattern, (b) H-plane, (c) E-plane.……..…71

Fig (3. 26) Radiation pattern at 4.25 GHz: (a) 3D pattern, (b) H-plane, (c) E-plane.………..72

Fig (3. 27) Radiation pattern at 6.06 GHz: (a) 3D pattern, (b) H-plane, (c) E-plane.…………72

Fig (3. 28) Adding two slots of length L_2 perpendicular to the slot L_1 in opposite direction..73

Fig (3. 29) S_{11} versus frequency showing all the resonant modes when adding two sections of the slot in opposite direction……………………………………………..73

Fig (3. 30) Electric field distribution at: (a) 3.5 GHz. (b) 4.344 GHz. (c) 5.15 GHz. (d) 5.76 GHz (e) 6.1 GHz……………………………………………………………74

Fig (3. 31) Radiation pattern for Mode 3 at 5.15 GHz: (a) E-plane, (b) H-plane, (c) 3D Pattern…………………………………………………………………….75

Fig (3. 32) Radiation pattern for Mode 4 at 5.76 GHz: (a) E-plane, (b) H-plane, (c) 3D pattern ……………………………………..……………………………..75

Fig (3. 33) Radiation pattern for Mode 1 at 3.5 GHz: (a) 3D pattern, (b) H-plane, (c) E-plane……………………………………………………………………………..76
Fig (3. 34) Radiation pattern for Mode 2 at 4.34 GHz: (a) 3D pattern, (b) H-plane, (c) E-plane…………………………………………..……………………...76
Fig (3. 35) Radiation pattern for Mode 5 at 6.1 GHz: (a) 3D pattern, (b) H-plane, (c) E-plane……………………………………………………………………………..76
Fig (3. 36) Configuration of the proposed tri-band SIW with tuning………………………77
Fig (3. 37) S_{11} against frequency by adding two slots L_2 perpendicular to the main slot L_1……………………………………………………………………….....78
Fig (3. 38) Electric field distribution at: (a) 3.5 GHz (Mode 1). (b) 4.27 GHz (Mode2). (c) 5.17 GHz (Mode 3). (d) 5.57 GHz (mode 4). (e) 6.17 GHz (Mode 5)…………..78
Fig (3. 39) L_1 versus reflection coefficient (all other parameters are same) ………………..80
Fig (3. 40) L versus reflection coefficient (all other parameters are same)……………..…..80
Fig (3. 41) L_2 versus reflection coefficient (all other parameters are same)………...………81
Fig (3. 42) W_1 versus reflection coefficient (all other parameters are same)………………..81
Fig (3. 43) W_3 versus reflection coefficient (all other parameters are same)……………....82
Fig (3. 44) Photograph structure of tri-band SIW……………………………………………83
Fig (3. 45) Radiation pattern at 5.16 GHz: (a) H-plane, (b) 3D pattern, (c) H-plane comparison, (d) E-plane comparison. ……………………………………..………84
Fig (3. 46) Radiation pattern at 5.56 GHz: (a) H-plane, (b) 3D pattern, (c) H-plane comparison, (d) E-plane comparison……………………………………..…..85
Fig (3. 47) Comparison of gain between measurement and simulation……………………...85
Fig (3. 48) Radiation pattern at 3.5 GHz: (a) H-plane, (b) 3D pattern, (c) H-plane comparison, (d) E-plane comparison……………………………………………….…………86
Fig (3. 49) Radiation pattern at 4.27 GHz: (a) E-plane, (b) H-plane, (c) 3D pattern…………………………………………………………………………...….87
Fig (3. 50) Radiation pattern at 6.15 GHz: (a) E-plane, (b) H-plane, (c) 3D pattern………………………………………………………………..…………..87
Fig (3. 51) 1×2 SIW array structure…………………………………………………………88
Fig (3. 52) S-parameter for the proposed 2×1 SIW………………………………………..89

Fig (3. 53) Z-component of E-field at: (a) 3.46 GHz. (b) 3.6 GHz (c) 4.22 GHz. (d) 4.6 GHz. (e) 5.16 GHz. (f) 5.56 GHz. (g) 6.08 GHz. (h) 6.24 GHz……………………………..90

Fig (3. 54) Radiation pattern at 5.15 GHz: (a) E-plane, (b) H-plane, (d) 3D pattern………...91

Fig (3. 55) Radiation pattern at 5.5 GHz: (a) E-plane, (b) H-plane, (c) 3D pattern…………91

Fig (3. 56) Radiation pattern at 3.46 GHz: (a) E-plane, (b) H-plane, (c) 3D pattern.……......92

Fig (3. 57) Radiation pattern at 3.6 GHz: (a) E-plane, (b) H-plane, (c) 3D pattern.………...92

Fig (3. 58) 2 × 2 SIW: (a) Simulated design. (b) Fabricated design…………………...…93

Fig (3. 59) Comparison of S_{11} between measurement and simulation for 2 × 2 SIW array…94

Fig (3. 60) Electric field distribution at 2 × 2 array: (a) Mode 1 (2.86 GHz and 3 GHz). (b) Mode 2 (3.77 GHz). (c) Mode 3 (4.31 GHz). (d) Mode 4 (5 GHz). (e) Mode 5 (5.2 GHz)………..…………………………………………………………………95

Fig (3. 61) Radiation pattern at 5 GHz: (a) H-plane, (b) 3D pattern, (c) H-plane comparison, (d) E-plane comparison.…………………………...…………………………………96

Fig (3. 62) Radiation pattern at 5.24 GHz: (a) H-plane, (b) 3D pattern, (c) E-plane comparison, (d) H-plane comparison…...………………………………………..97

Fig (3. 63) Comparison of gain between measurement and simulation against frequency for the 2 × 2 SIW array…..…………………………………………………………..98

Fig (3. 64) Radiation pattern at 2.86 GHz (Mode 1): (a) H-plane. (b) E-plane, (c) 3D pattern………………………………………………………………………………..98

Chapter Four

Fig (4. 1) Structure of Si-Sio_2-graphene……………………………………………………101

Fig (4. 2) Graphene waveguides (a) Si–Sio_2–graphene–dielectric-stripe–metal,…………..102

Fig (4. 3) Tuning SIW dynamically using graphene [11]…………………………………..103

Fig (4. 4) Graphene- based tuneable microstrip structure:(a) single pair graphene pad on microstrip line, (b) Two pair of graphene pads places on microstrip line [12]……104

Fig (4. 5) 3D structure of reconfigurable antenna: (a) cross section view, (b) top view. [13]……………………………………………………………………104

Fig (4. 6) (a) Configuration of the graphene-based HMSIW attenuator. (b) Structure with biased voltage [14]……………………………………………………………105

Fig (4. 7) Surface conductivity against frequency: (a) real part, (b) imaginary part [16]…106

Fig (4. 8) Relationship between chemical potential and electrostatic bias [17]…………….107

Fig (4. 9) Conductivity of graphene $\sigma_{D'} - j\sigma_{D''}$ against frequency: (a) μ_c=0, (b) $\mu_c(0 - 1.5)$……………………………………………………………………….108

Fig (4. 10) Real part of sheet impedance against frequency with variation of μ_c…………..109

Fig (4. 11) Imaginary part of sheet impedance against frequency with variation of μ_c…….109

Fig (4. 12) Structure of slotted SIW attenuator [18]……………………………………..…111

Fig (4. 13) Varying resistance at the slotted SIW (b) structure of SSIW [18]…………..….111

Fig (4. 14) Only graphene placed over SSIW……………………………………………….112

Fig (4. 15) Structure of silicon dioxide graphene tuning SSIW…………………………….112

Fig (4. 16) Silicon dioxide graphene of conductivity 20000 S/m of SSIW………………..113

Fig (4. 17) Silicon dioxide graphene with silicon conductivity of 2 S/m…………………..113

Fig (4. 18) Resistance variation effects on S_{21} by increasing silicon dioxide graphene to 1.5 µm……………………………………………………………………………...114

Fig (4. 19) One port three-term error model for one-port calibration in (a) S-parameter.(b) error term representation……………………………………………………..116

Fig (4. 20) Fictitious two-port error boxes A, B with the three standards (Through-Reflect-Line) [20]……………………………………………………………………..117

Fig (4. 21) Waveguide with aperture………………………………………………………..118

Fig (4. 22) Graphene on open aperture……………………………………………………...119

Fig (4. 23) Graphene on open aperture with variation of sheet resistance of graphene: (a) Return loss, (b) Smith chart…………………………………………….…….119

Fig (4. 24) Quartz placed on the waveguide………………………………………………..120

Fig (4. 25) Quartz only on aperture: (a) Return loss, (b) Smith chart. ………………120

Fig (4. 26) Impedance against frequency (quarts on the waveguide)………………………121

Fig (4. 27) SIW structure with quarts and metal on top…………………………………….121

Fig (4. 28) Return loss versus frequency (quarts sample with metal on top)……………….122

Fig (4. 29) Electric field distribution at 57.7 GHz………………………………………….122

Fig (4. 30) Radiation pattern at 57.7 GHz: (a) E-plane, (b) 3D pattern.………………..…..122

Fig (4. 31) Graphene on top of waveguide………………………………………………….123

Fig (4. 32) Graphene placed on the top of the aperture:(a) Return loss, (b) Smith chart…...123

Fig (4. 33) At 6.35 GHz: (a) Electric field distribution, (b) 3D pattern.…………………....124
Fig (4. 34) Graphene sample on bottom……………………………………………………124
Fig (4. 35) Graphene placed on bottom: (a) Return loss, (b) Smith chart.…………….………125
Fig (4. 36) Graphene bottom metal top…………………………………………………..125
Fig (4. 37) Graphene bottom with metal on top with Sheet resistance variation: (a) Return loss, (b) Smith chart.…………………………………………………………....126
Fig (4. 38) At 62.5 GHz: (a) Electric field distribution, (b) 3D pattern………..…………..126
Fig (4. 39) Graphene on aperture only with metal on top………………………………..127
Fig (4. 40) Graphene on aperture with top metal with graphene sheet resistance variation: (a) Return loss, (b) Smith chart ………………………………………………………127
Fig (4. 41) Measurement setup, showing quartz substrate with graphene layer placed onto an open-ended WR-15 waveguide: (a) side-view, (b) top-view……………………128
Fig (4. 42) Photograph of measurement setup……………………………………………...128
Fig (4. 43) Comparison of quarts between measurements and simulation…………………129
Fig (4. 44) Comparison of graphene at the top in mono, Bi and tri layers between simulation and measurements…………………………………………………………………..130
Fig (4. 45) Comparison of graphene at the bottom of the waveguide between measurements and simulations………………………………………………………………..130
Fig (4. 46) Comparison between simulation and measurements of graphene at the bottom with metal at the top in mono, bi and tri layers…………………………………131
Fig (4. 47) De-embedding circuit…………………………………………………………...132
Fig (4. 48) Measured S-parameters. Dotted lines show repeat measurements……………...133
Fig (4. 49) The de-embedded value of normalized admittance for mono-, bi- and tri-layer graphene samples with graphene in bottom…………………………………...133
Fig (4. 50) The de-embedded value of normalized admittance for mono-, bi- and tri-layer graphene samples with graphene in bottom and metal in top…………………...134

List of Tables

Chapter Two

Table (2. 1) Parameters of the single SIW antenna……………………………………….28

Table (2. 2) Comparison the effect of L_2 on resonant frequency theoretically and simulation (CST) (the other parameters are same in table 2.1)…………..………………….31

Table (2. 3) Parameters dimensions for 1 × 2 SSIW……………………………………...40

Table (2. 4) Parameter dimension for 2 × 1 SSIW array……………………………………..44

Chapter three

Table (3. 1) Parameters for the proposed structure (see Fig (3.36) for definitions of the parameters)…………………………………………………………………...76

Table (3. 2) Parameters of 1 ×2 array of substrate integrated waveguide antenna…………..87

Table (3. 3) Parameters dimensions of 2×2 SIW array…………………………………...…93

Publication:

Y. F. Azeez and P. R. Young, "Slotted substrate integrated waveguide antenna," *12th European Conference on Antennas and Propagation (EuCAP 2018)*, London, 2018, pp. 1-4

Y. F. Azeez, R. J. Collier, N. M. Ridler and P. R. Young, "Establishing a New Form of Primary Impedance Standard at Millimeter-Wave Frequencies," in *IEEE Transactions on Instrumentation and Measurement*, vol. 68, no. 1, pp. 294-296, Jan. 2019.

Y.F. Azeez and P.R. Young “Tri-band substrate integrated waveguide antenna”. submitted in IEEE Antennas and Wireless propagation letters

Chapter One

Introduction

1.1 Introduction

The rapid development of the wireless communication from 1G network which was designed for voice communication only, had reached wireless standard such as IEEE 802.16m and LTE advance requirements towards 5G operating at 25 GHz. Recently, mobile phones, online games and internet are everywhere, resulting in an increased number of users and thereby requires a high data transmission. Millimeter-wave frequency technology from 30 GHz to 300 GHz can provide a high data rate and increased bandwidth.

The wireless communication is divide into three stages: transmission, propagation and reception. The signal passes through the transmitter, which modulates the signal with a high frequency carrier; the signal is then propagated in the form of a wave then transmitted by an antenna. Lastly, it is received and demodulated in the receiver.

1.2 Millimeter-wave communications

The wireless communication system is divided into high frequency (3 MHz to 30 MHz), very high frequency (30 MHz to 300 MHz) and ultra-high frequency (300 MHz to 3 GHz).

Implementing millimeter-wave frequencies from 30 GHz to 300 GHz may be a possible solution for future wireless networks. The future millimeter frequency will provide a higher bit rate, high directional beamforming antennas and will be part of the new 5G network. This frequency range will increase data capacity, expand channel bandwidth and could be used for spatial techniques like massive MIMO (Multiple Input Multiple Output).

The advantages of millimeter-wave communications are:

- A small antenna due to the small guided wavelengths for this frequency range and integrated part packaging.
- Large bandwidth.
- High data rate.

- Narrow beam widths which can be used in radar detection and line-of-site communications. More antennas can be packed at a millimeter wave frequency than a microwave.

The disadvantages are:

- Signals propagation may suffer because of the blockages by obstacles due to the weak diffraction ability [1].
- The compact antenna and smaller wavelength may increase cost of the manufacture.
- Propagation loss.
- At higher carrier frequency, attenuation occurs due to oxygen absorption in the atmosphere at around 60 and 120 GHz.
- Rain and humidity can reduce signal strength and affect the signal performance.

1.3 Waveguides

The usual transmission medium for millimeter wave systems is a waveguide, to guide the electromagnetic waves from one point to another. The main common shapes of waveguides are circular and rectangular. The main qualities of rectangular waveguide are the simplicity, how easy it is to fabricate and how widely it is used in the field of antenna designs. The rectangular waveguide is shown in Fig (1. 1)

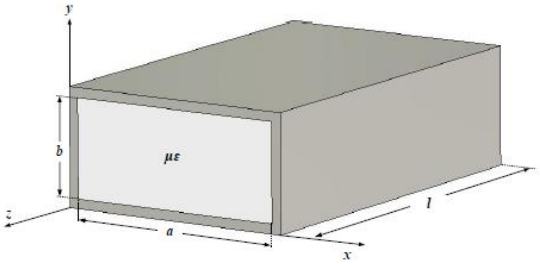

Fig (1. 1) Geometry of rectangular waveguide.

Rectangular waveguides supports both transverse electric (TE) and magnetic (TM) modes [2]. Both the TE and TM modes have a cut off frequency. If the waveguide operates above cutoff frequency, then the electromagnetic wave will propagate. Below cutoff frequency, the propagation of electromagnetic wave through the waveguide is not possible.

The cutoff frequency of both TE and TM modes can be calculated according to the following relationship [2]:

$$f_{cmn} = \frac{1}{2\pi\sqrt{\mu\varepsilon}}\sqrt{\left(\frac{m\pi}{a}\right)^2 + \left(\frac{n\pi}{b}\right)^2} \tag{1.1}$$

Where:

μ and ϵ: the permittivity and permeability of the material inside the waveguide respectively.

a and b: the width and height of the waveguide

m and n: the positive integer number that generate the $\mathrm{TE_{mn}}$ and $\mathrm{TM_{mn}}$ modes.

The guided wavelength is always longer than the free space wavelength and is given by the following formula at the first mode $\mathrm{TE_{10}}$ [2]:

$$\lambda_{g10} = \frac{\lambda_0}{\sqrt{1-\left(\frac{\lambda_0}{2a}\right)^2}} \tag{1.2}$$

The mode which has the lowest cutoff frequency is called the dominant mode [2]. The first dominant mode, $\mathrm{TE_{10}}$, is the transverse electric mode, whilst $\mathrm{TE_{20}}$ is called the second dominant mode. The frequency range between the two dominant modes is called the bandwidth of the waveguide.

The transverse electric field components for a rectangular wave guide $(\mathrm{T_E}, \mathrm{T_M})$ modes can be given by the following equation [2]:

$$\bar{E}_t(x,y,z) = \bar{e}(x,y)(A^+e^{-j\beta_{mn}z} + A^-e^{j\beta_{mn}z}) \tag{1.3}$$

$\bar{e}(x,y)$: repesents the transvere variation of the mode in both x and y direction.

A^+ and A^-: the amplitudes of the waves propagating forward and backward.

β_{mn}: the propagation constant for both $\mathrm{TE}_{\mathrm{mn}}$ and $\mathrm{TM}_{\mathrm{mn}}$ modes and is given by the following formula:

$$\beta_{mn} = \sqrt{k^2 - \left(\frac{m\pi}{a}\right)^2 - \left(\frac{m\pi}{b}\right)^2} \tag{1.4}$$

The main advantage of a rectangular waveguide is that the signal propagation placed inside the waveguide results in reduced loss and leakage, high power capacity and high quality factor. The disadvantage of the rectangular waveguide is that it is bulky, and has higher costs compared to the planar transmission lines and slow processing.

Fig (1. 2) shows how the current lines are distributed on the wall of the rectangular waveguide at the first mode TE_{10}. The current lines do not pass though the centerline on the wall of the waveguide.

Cuts or slots may affect the performance of the waveguide when the slots interrupt the flow of current, waveguide slot antennas will excite the current line and radiates.

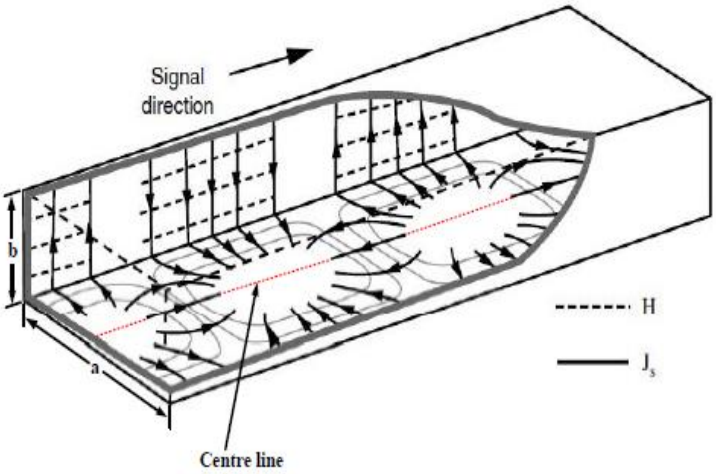

Fig (1. 2) The electric and magnetic field distribution on the wall of the waveguide at the TE_{10} mode [3].

1.4 Planar transmission lines

The planar transmission lines are the most common type of transmission lines, which are shown in Fig (1. 3), due to their characteristics of low-cost manufacturing, being lightweight and having a low profile.

Fig (1. 3a) shows the parallel-plate waveguide (PPWG), microstrip, stipline, slotline and coplanar waveguide. The planar transmission line can be integrated into one single board sharing the same dielectric layer. Planar transmission line can work as power dividers, couplers, antennas and filters as well in integrating active components.

The disadvantages are the conducting metal surface, which are uncoated and placed directly to the substrate in which sometime may be exposed to air. Therefore, the main disadvantages of the planar transmission lines are suffering from serious radiation leak, coupling and interference, and limited power capacity.

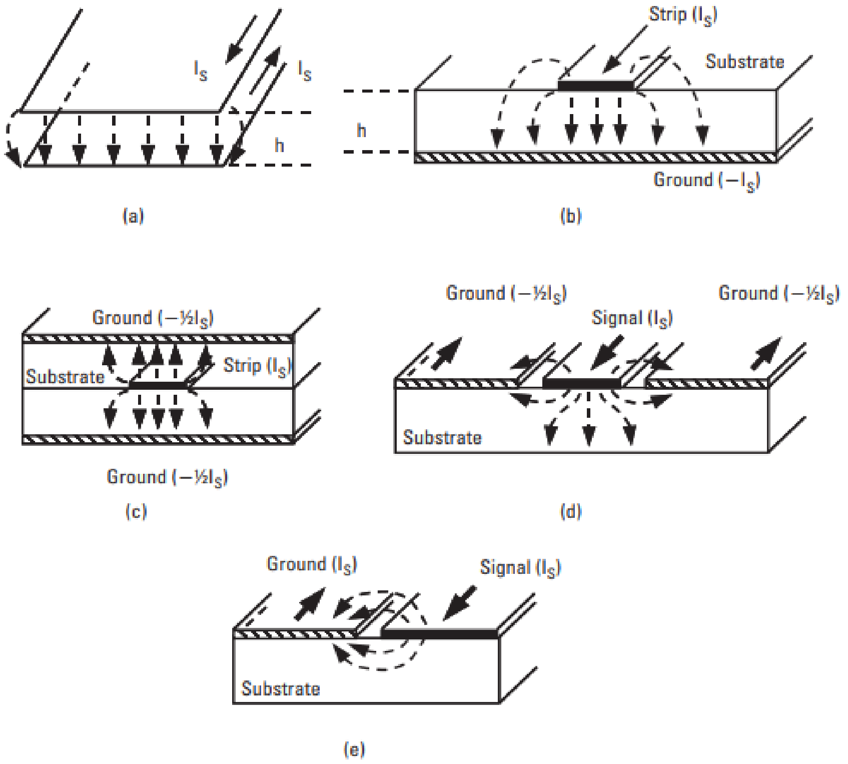

Fig (1. 3) planar transmission lines and propagation E-field plots [19]: (a) parallel plate,(b) Microstrip, (c) stripline, (d) coplanar waveguide, and (e) slot line [4].

1.5 Substrate integrated waveguide

Active components, passive components and transmission components are usually made with different manufacturing methods, which increase losses during the insertion and transmission processes.

Substrate integrated waveguide (SIW) is a form of a waveguide that enables the implementation of a non-planar rectangular waveguide in a planar form and can be used in millimeter wavelengths at high frequencies, as shown in Fig (1. 4).

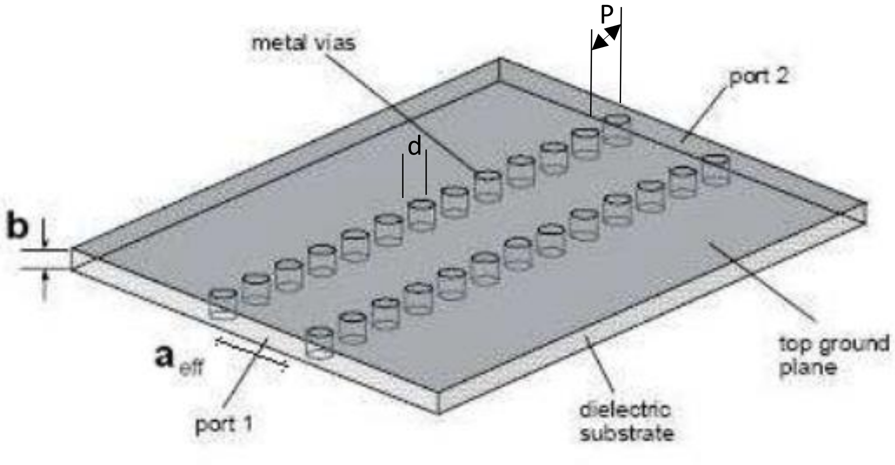

Fig (1. 4) Geometry of SIW. Substrate thickness: b, waveguide physical width a_{eff} .

When compared to the conventional waveguide, the inner-filled dielectric of a SIW is the substrate material; the two metallic broad walls of conventional waveguides are replaced by a printed circuit board (PCB) metallisation. The narrow wall of a waveguide are replaced by two cylinders vias or holes at the bottom and top of the PCB. These holes are electroplated to each other, which have the same diameter and the spacing between holes are equal, to support guided wave propagation with minimum radiation loss and control the leakage of the radiation field out of the waveguide.

The propagation characteristics of SIW are similar to the rectangular waveguides RWGs, provided that the holes or metallic vias spacing are very close and the leakage can be neglected [5].

The propagation modes of a SIW is similar to RWGs namely TE_{n0} with n=1,2,… for example the mode TE_{10} for SIW is similar to a rectangular waveguide with the vertical electric current density on the side walls. Fig (1. 5) shows the amplitude of electric profile of fundamental SIW which is similar to the fundamental of RWG.

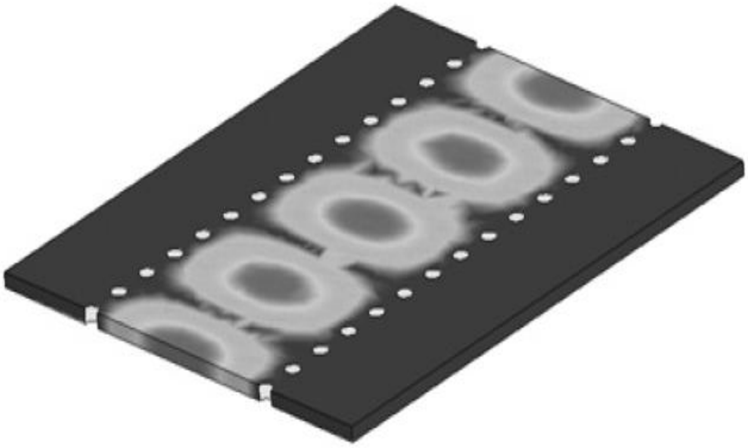

Fig (1. 5) The amplitude of electric profile pf fundamental SIW mode [5].

1.5.1 Size and bandwidth of SIW

Size and bandwidth are an important role for SIW, which is limited in compactness and bandwidth. The width and permittivity ε_r of the substrate of SIW determine cutoff frequency of the fundamental mode.

Many researchers demonstrated many waveguide topologies to improve compactness of SIW structures. Substrate integrated folded waveguides was proposed by [6] which reduces the size by a factor more than two and increases the bandwidth with a cost of slightly high losses. Half mode substrate integrated waveguide was proposed [7], by the approximation of the vertical cut of the waveguide as a virtual magnetic wall which reduced size of the structure to approximately 50%. A combination of both folded and half mode SIW techniques is also possible and proposed by [7] which resulted in further reduction in size but increased in its complexity and called folded half-mode substrate integrated waveguide (FHMSIW).

For further improvement of bandwidth, the substrate integrated slab waveguide (SISW) was proposed by [8], the medium is dielectric and periodically perforated with holes filled with air and placed near the edge of the waveguide as shown, an improvement of bandwidth up to 40% was provided. For further enhancement of bandwidth, a central ridge has been applied to the SIW as proposed by [9]; at the center of the longest side of waveguide a ridge was placed by using a row of thin partial height metal posts. 37% bandwidth enhancement was achieved for frequency range 4.9 to 13.39 GHz.

Slot SIW was also investigated by [10] and [11], which acts as a wave attenuator and leaky antennas.Fig(1. 6) shows all the different topologies of SIW that have been briefly explained.

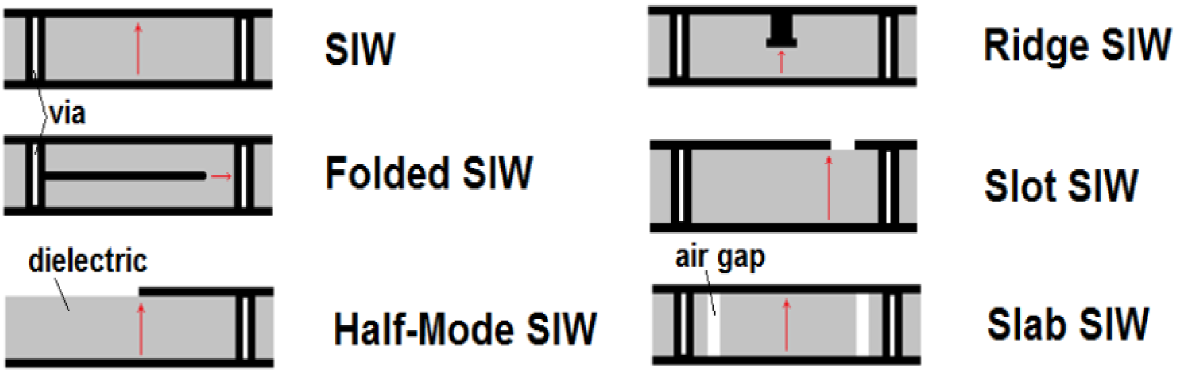

Fig(1. 6) Variable topologies of SIWs [12].

1.5.2 Losses in SIW

Energy that propagates through transmission medium suffers from radiation losses. Several reasons lead to SIW losses, the conductor and dielectric losses, vias and the spacing between the vias add additional losses because of the radiation leak between the vias.

Losses in SIW are related to attenuation constant. The total attenuation constant α_{total} can be found through the equation :

$$\alpha_{total} = \alpha_c + \alpha_d + \alpha_R \tag{1.5}$$

Where α_c: the attenuation constant due to conduction losses.
α_d: the attenuation constant due to dielectric losses.
α_R: the attenuation constant due to radiation losses.

Conduction loss is the power dissipated in the conductor when the wave travels through the waveguide. The attenuation constant can be given on the following equation [13]:

$$\alpha_c = \frac{\sqrt{\pi f \varepsilon_0 \varepsilon_r}}{h\sqrt{\sigma_c}} \frac{1+2(\frac{f_c}{f})^2 h/a_{eff}}{\sqrt{1-(\frac{f_c}{f})^2}} \tag{1.6}$$

Where :
a_{eff}: the effective width of rectangular waveguide.
σ_c: the metal conductivity.
ε_r: the relative permittivity of dielectric filled waveguide.
f_c: the cutoff frequency of SIW.
h: the dielectric thickness.

Therefore, by increasing thickness of the dielectric waveguide, the conduction loss will be reduced.

The attenuation constant due to dielectric loss α_d is associated with loss tangent tan δ of the dielectric and relative permittivity of the dielectric. The equation for the dielectric loss of the fundamental mode of SIW is:

$$\alpha_D = \frac{\pi f \sqrt{\varepsilon_r}}{c\sqrt{1-(f_c/f)^2}}\, Tan\delta \tag{1.7}$$

Where:

c: the speed of light.

The radiation loss that causes the vias and periodic distance between the vias, have a leakage radiation from them. To reduce radiation loss, the spacing between the vias *(P)* must be greater than the diameter of the vias *(d)* [14][15]:

$$P > d$$

In general, the radiation loss has not been considered by many researchers. By avoiding band gap and under the following condition:

$$(P/\lambda_c) < 0.25$$

Where λ_c is the cutoff wavelength.

It is preferred to be the number of the vias less than 20 per cutoff wavelength as in the following condition:

$$(P/\lambda_c) > 0.05$$

1.5.3 Design rule for SIW

To design a substrate integrated waveguide antenna, many parameters should be considered to achieve a successful operation. The choice of dielectric substrate is the material selection, related to relative permittivity (ε_r) and its thickness that are appropriate for fabrication process and frequency range.

The side walls of SIW, the diameter of the vias and the spacing between them should be considered to reduce radiation loss as explained in the previous section.

The effective width of SIW is associated with the selection the cutoff frequency and relative permittivity of substrate according to following equation :

$$a_{eff} = \frac{c}{2f_{c(1,0)}\sqrt{\varepsilon_r}} \tag{1.8}$$

The width of SIW (W) can be determined under the following formula [16]:

$$W = a_{eff} + \frac{d^2}{(0.95 \times P)} \tag{1.9}$$

Where *d:* the diameter of vias

P : the spacing between the vias

This equation does not consider the relation of diameter to width (d/a), which may cause an error.

The two accurate formula were suggested by [17] [18]:

$$W = a_{eff} - 1.08\frac{d^2}{P} + 0.1\frac{d^2}{a} \tag{1.10}$$

$$a = \frac{2W}{\pi} cot^{-1}(\frac{\pi P}{4W} + ln\frac{P}{2d}) \tag{1.11}$$

In general, the SIW is narrower than the conventional rectangular waveguide. The electromagnetic field along SIW remains constant, TM is not possible in SIW as the distance between the vias does not allow the current flow through them.

1.6 Transitions

There are different ways to a transition between planar transmission lines and SIW. The most common type of transmission line is microstrip as shown in Fig (1. 7a). The main features of a microstrip line is the simple structure (light and more compact) and easy fabrication, less expensive, good impedance matching and does not affect the bandwidth of SIW. The microstrip transmission line is used in the slotted SIW chapter two and triple band SIW in chapter three.

Fig (1. 7b) shows the coplanar to SIW transitions, this type is used for thicker substrate that the microstrip is not appropriate for, and to reduce conductor losses. The main problem of this type is the limited bandwidth of SIW. The coplanar transition to SIW uses two slots with 90^0 bend within the SIW; for high permittivity substrates a cavity was added around the bend [5] or a stub may add to improve matching.

Coplanar to SIW for grounded CPW was developed, where the current is used to feed SIW as shown in Fig (1. 7c). The current flowing through the via will generate a magnetic field inside SIW.

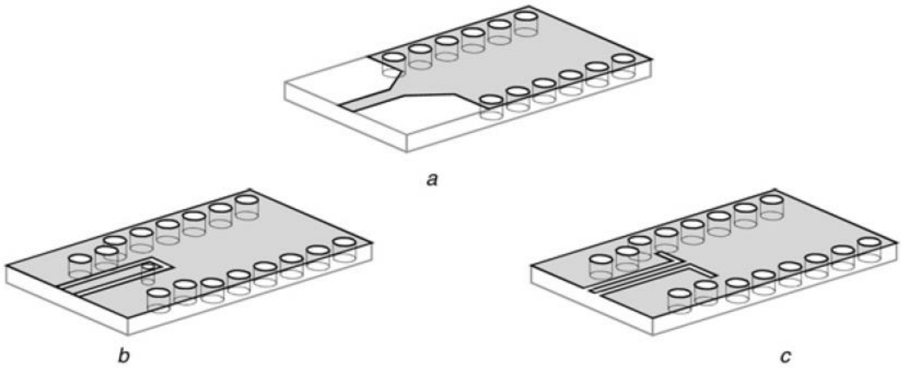

Fig (1. 7) Transitions between transmission line and SIW: (a) Microstrip. (b) Coplanar 90^0 bend. (c) Coplanar with current probe [5].

1.7 Substrate integrated waveguide power dividers

An array system developed to increase gain with minimum loss that included conductor losses and dielectric losses. SIW power divider and some techniques like Dolph-Chebyshev and Taylor distribution can be used to increase gain and reduce side lobe level with acceptable bandwidth.

SIW power dividers are three layers. The top and bottom layer is copper and the middle layer is dielectric. There are different types of power dividers; the first type is called parallel feeding divider that has an equal transmission coefficients and symmetrical configuration. Two configurations of parallel feeding network are the T-divider and Y-divider.

As shown in Fig (1. 8) T- junction is a metal adaptive via which is implemented in the substrate to reduce losses. Two parameters of T-junction may have an effect to achieve better matching between the input port and output port: the offset position and diameter of the metalized adaptive .

Y-divider is the other type of SIW parallel feeding power divider, the width of the input feeding (a_i) and the distance between the two discontinuities (L), affects on achieving better matching power division [19].

Many stages of parallel feeding powers dividers may be grouped to increase gain for the array system, however this will lead to a complex structure, larger array system and may increase side lobe level. Fig (1. 9) is an example of 16-way power divider that is using Y-junction.

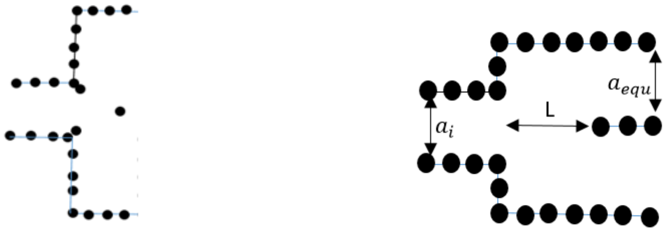

(a) (b)

Fig (1. 8) SIW feeding power divider: (a) T–divider, (b) Y-divider.

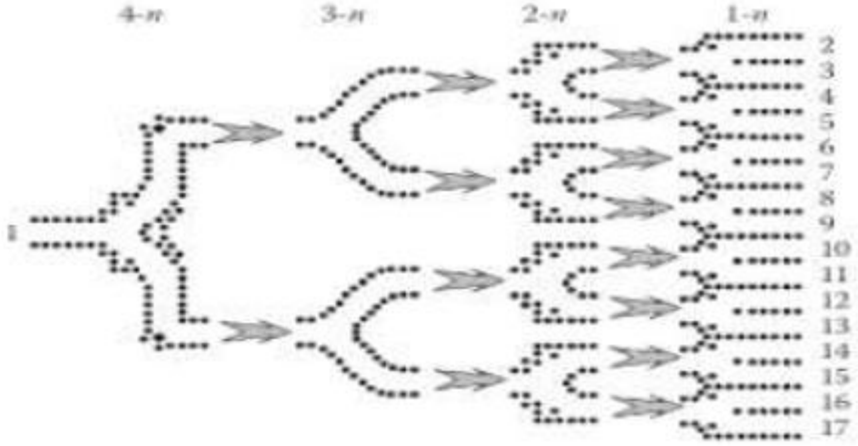

Fig (1. 9) Multistage W-band SIW feeding power divider (corporate feed)[20].

To overcome the complexity of multiple stages of power divider, another technique has been used which is called series feeding power divider as shown in Fig (1. 10). This technique is similar to Dolph-Chebyshev or Taylor distributions, the series array system will reduce the size of an array system and low side lobe level.

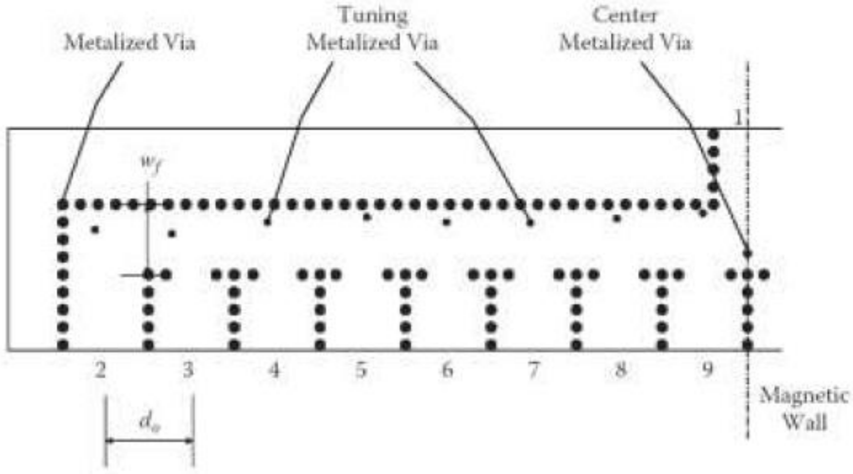

Fig (1. 10) 16-way series SIW feeding divider (distributed feed) [20].

1.8 SIW filters and couplers

Filters is a frequency selective device, many filters have been proposed. A band-pass filter proposed by [21], by using SIW triangular cavities at frequency 2.4 GHz. Ref [6] developed a folded (FSIW) which has an advantage of reducing the area of the waveguide and the filter response is defined purely in terms of a photo-lithographically response on a planar layer.

Half mode substrate integrated waveguide band pass filter is presented by [22], using three poles and five poles. A triple mode filter is based on quarter SIW [23]. Cavity filters with circular and rectangular cavities were presented by [24][25], which give high selectivity. A compact of super-band pass filter is presented by [26], which cover the frequency range 8.5 GHz to 16.5 GHz.

The other passive components beside filters are couplers. A single layer of directional couplers on SIW is presented [27], -3 dB, -6 dB and -10 dB directional couplers designed. A magic-T

[28], circulators [29], and six port circuit were also designed [30] and planar SIW duplexer at 5 GHz and 25 GHz were also presented [31].

1.9 Thesis organization

Chapter Two entails an introduction for a novel slotted substrate integrated waveguide antenna, studying the parameters effects on the cutoff frequency, return loss, the comparison between measurements and simulation and the possibility of designing an array of SSIW to increase gain.

Chapter Three introduces different structures of SIW antennas and studying their radiation mode. A tri band substrate integrated waveguide antenna is demonstrated in single array, explains how each parameter affects radiation modes, makes comparisons between simulation and measurements and designing a two by two array antenna to increase gain.

Chapter Four introduces the use of graphene for waveguide devices. Calculation of graphene conductivity and the relationship between chemical potential or the applied voltage and sheet resistance of graphene are shown. The chapter also shows the possibility for tuning a SIW using silicon dioxide-graphene by changing its sheet resistance. Further, it also demonstrates ways of establishing a new form of impedance standard using graphene with mono, bi- and tri-layer.

Chapter Five, summarizes the work and presents a conclusion for each chapter and future work.

1.10 References

[1] T. S. Rappaport, S. Sun, R. Mayzus, H. Zhao, Y. Azar, K. Wang, G. N. Wong, J. K. Schulz, M. Samimi, and F. Gutierrez., “Millimeter Wave Mobile Communications for 5G Cellular : It Will Work !,” in IEEE Access, vol. 1, IEEE, 2013, pp. 335–349.

[2] D. M. Pozar, Microwave Engineering. 2009.

[3] Sorrentino, R. and G. Bianchi, Microwave and RF engineering. 2010.

[4] Eric Holzman, Essentials of RF and Microwave Grounding. Norwood: MA: Artech House Publishers, 2006.

[5] M. Bozzi, A. Georgiadis, and K. Wu, “Review of substrate-integrated waveguide circuits and antennas,” IET Microwaves, Antennas Propag., vol. 5, no. 8, p. 909, 2011.

[6] N. Grigoropoulos, B. Sanz-izquierdo, P. R. Young, and S. Member, “Substrate Integrated Folded Waveguides (SIFW) and filters,” IEEE Microw. Wirel. Components Lett., vol. 15, no. 12, pp. 829–831, 2005.

[7] G. H. Zhai, W. Hong, K. Wu, J. X. Chen, and J. Wei, H.J. Tang, “Folded half mode substrate integrated waveguide 3 dB coupler,” IEEE Microw. Wirel. Components Lett., vol. 18, no. 8, pp. 512–514, 2008.

[8] C. Bozzi, M. Deslandes, D. Arcioni, P. Perregrini, L. Wu, K. and G, “Efficient analysis and experimental verification of substrate integrated slab waveguides for wideband microwave applications,” Int. J. RF Microw. Comput. Aided Eng., vol. 15, no. 3, pp. 296–306, 2005.

[9] W. Che, C. Li, P. Russer, and Y. L. Chow, “Propagation and Band Broadening Effect of Planar Integrated Ridged Waveguide in Multilayer Dielectric Substrates,” IEEE MTT-S Int. Microw. Symp. Dig. Atlanta, pp. 217–220, 2008.

[10] R. F. Xu, B. S. Izquierdo, P. R. Young, and S. Member, “Switchable Substrate Integrated Waveguide,” IEEE Microw. Wirel. Components Lett., vol. 21, no. 4, pp. 194–196, 2011.

[11] R. F. Xu, A. J. Farrall, and P. R. Young, “Analysis of loaded substrate integrated waveguides and attenuators,” IEEE Microw. Wirel. Components Lett., vol. 24, no. 1, pp. 62–64, 2014.

[12] A. J. Farrall, “Rotated Half-Mode Substrate Integrated Waveguide and other Planar Integrated Structures.,” 2015.

[13] R.E.Collin, Field theory of guided waves. Oxford university press.

[14] R. Garg, I. Bahl, and M. Bozzi, Microstrip Lines and Slotlines, Rtech Hous. (Artech House Microwave Library (Hardcover). Artech House: Artech House Microwave Library (Hardcover). Artech, 2013.

[15] L. Yan, W. Hong, K. Wu, and T. J. Cui, Investigations on the propagation characteristics of the substrate integrated waveguide based on the method of lines. 2005.

[16] Y. Cassivi, L. Perregrini, P. Arcioni, M. Bressan, K. Wu, and G. Conciauro, “Dispersion Characteristics of Substrate Integrated Rectangular Waveguide,” IEEE Microw. Compon. Lett, vol. 12, no. 9, pp. 333–335, 2002.

[17] F. Xu and K. Wu, “Guided-Wave and Leakage Characteristics of Substrate Integrated Waveguide,” IEEE Trans. Microw. Theory Tech, vol. 53, no. 1, pp. 66–73, 2005.

[18] W. Che, K. Deng, D. Wang, and Y. L. Chow, “Analytical equivalence between substrate-integrated waveguide and rectangular waveguide,” IET Microwaves Antennas Propag.

[19] X. Xu, R. G. Bosisio, and K. Wu, “A New Six-Port Junction Based on Substrate Integrated Waveguide Technology,” IEEE Trans. Microw. Theory Tech., vol. 53, no. 7, pp. 2267–2273, 2005.

[20] Y. J. Cheng, Substrate Integrated Antennas and Arrays. CRC Press, 2014.

[21] Y. L. Zhang, W. Hong, K. Wu, J. X. Chen, and Z. C. Hao, “Development of compact bandpass filters with SIW triangular cavities,” in 2005 Asia-Pacific Microwave Conference Proceedings, 2005, vol. 1, p. 4 pp.

[22] Y. Wang, W. Hong, Y. Dong, B. Liu, H. J. Tang, J. Chen, X. Yin, and K. Wu “Half Mode Substrate Integrated Waveguide (HMSIW) Bandpass Filter,” IEEE Microw. Wirel. Components Lett., vol. 17, no. 4, pp. 265–267, 2007.

[23] C. Jin, Z. Shen, and S. Member, “Compact Triple-Mode Filter Based on Quarter-Mode Substrate Integrated Waveguide,” IEEE Trans. Microw. Theory Tech., vol. 62, no. 1, pp. 37–45, 2014.

[24] H. J. Tang, W. Hong, Z. C. Hao, J. X. Chen, and K. Wu, “Optimal design of compact millimetre-wave SIW circular cavity filters,” Electron. Lett., vol. 41, no. 19, pp. 1068–1069, 2005.

[25] X. Chen and K. Wu, “Substrate Integrated Waveguide Cross-Coupled Filter With Negative Coupling Structure,” IEEE Trans. Microw. Theory Tech., vol. 56, no. 1, pp. 142–149, 2008.

[26] Z. Hao, W. Hong, J. X. Chen, X. Chen, and K. Wu, “Compact super-wide bandpass substrate integrated waveguide (SIW) filters,” IEEE Trans. Microw. Theory Tech., vol. 53, no. 9, pp. 2968–2977, 2005.

[27] K. Hao, Z.C. Hong, W. Chen, J.X. Zhou, and H.X. Wu, “Single-layer substrate integrated waveguide directional couplers,” IEE Proc. Microw., Antennas Propag., vol. 153, no. 5, pp. 426–431, 2006.

[28] F. He, K. Wu, X. Chen, L. Han, and W. Hong, “A planar magic-T structure using substrate integrated circuits concept,” in 2010 IEEE MTT-S International Microwave Symposium, 2010, pp. 720–723.

[29] W. D’Orazio and K. Wu, “Substrate-Integrated-Waveguide Circulators Suitable for Millimeter-Wave Integration,” IEEE Trans. Microw. Theory Tech., vol. 54, no. 10, pp. 3675–3680, 2006.

[30] K. Xu, X., Bosisio, R.G., Wu, “A new six-port junction based on substrate integrated waveguide technology,” IEEE Trans. Microw. Theory Tech., vol. 53, no. 7, pp. 2267–2273, 2005.

[31] Z. C. Hao, W. Hong, J. X. Chen, X. P. Chen, and K. Wu, “Planar diplexer for microwave integrated circuits,” IEE Proc. - Microwaves, Antennas Propag., vol. 152, no. 6, pp. 455–459, 2005.

Chapter Two

Slotted Substrate Integrated Waveguide Antenna

2.1 Introduction

At higher microwave and millimeter-wave frequencies such as the proposed 5G, 30 GHz band, microstrip circuits become lossy due to increased conduction, dielectric and radiative losses. Traditionally, at these frequencies, rectangular waveguide has been the preferred type of guiding structure due to its low loss, high quality factor (Q-factor) and high-power handling capabilities. Unfortunately, a conventional waveguide is bulky, non-planar, expensive to produce and has lower power capacity.

Many researchers prefer planar antennas in microwave and millimeter wave applications because of being lower in costs and being easy to fabricate, more compact and light weight. This is desired in commercial applications such as base stations and handset antennas. However, planar antennas may have narrow bandwidth in different applications, unwanted side lobes, lower power capacity and poor cross polarisation. The main types of planar antennas are patch antennas and resonant slot antennas.

Over the last decade, SIW has overcome these problems, allowing more convenient implementation for millimeter-wave frequencies compared with conventional rectangular waveguide [1][2]. SIWs have specific features from a combination of planar and non-planar 3D structure, low cost, high bandwidth and high power capacity that support the low loss TE_{10} mode [3], [4].

Moreover, SIW has the possibility to integrate all active and passive components on the same substrate. Also, one or more chips can be integrated in the same substrate. System on substrate (SOS) is ideal for lower cost, easy integration and fabrication [5].

Unfortunately, the only way to integrate discrete devices with SIW is to use some form of transition to microstrip or CPW transmission line, which have matching losses and this problem has recently been overcome by introducing SSIW with characteristics similar to half mode SIW [6], [7], but with easy integration of components via a longitudinal slot.

This chapter presents a novel SSIW antenna, due to the available fabrication facilities a prototype at 2.5 GHz is demonstrated, although the application of SSIW and SIW is really in the upper microwave and millimeter-wave frequencies. Our design could ofcourse be easily scaled to those frequencies.

This chapter is organized as follows:

A brief of literature review of slotted substrate integrated waveguide (SSIW) is presented in the following section beginning with Elliot procedure. Using CST simulation, the effect of variable parameters on the S-parameter such as return loss is presented. The fabrication process with comparison between simulation and measurements is then given.

This chapter will discuss the enhancing of gain, using 1×2 array of SSIW using CST simulation, showing all the far field and radiation pattern at the resonant frequency. Furthermore, simulating 2×2 array to increase gain at the radiating frequency. Last but not least, some conclusions are drawn and discussed at the end of the chapter.

2.2 Literature review

Elliot [8] devised a procedure for the design of SSIW with longitudinal slots cut out of the broadside of the waveguide. Elliot [9] improved the slotted waveguide by determining how voltage was induced in the slot. He then used a reciprocity theorem to develop an equation that related the slot voltage to the TE modes that pass through the waveguide and mutual coupling of the slots. Later on, he improved the slotted waveguide by studying the high order mode that scattered of the slot.

In ref [10], single and dual resonant integrated waveguide slot antennas were designed at 10 GHz. In this design, the slots are placed on opposite sides of the waveguide, at intervals of half guided wavelength as shown in Fig (2. 1). The dual slot has 3 dBi gain higher than a single slot.

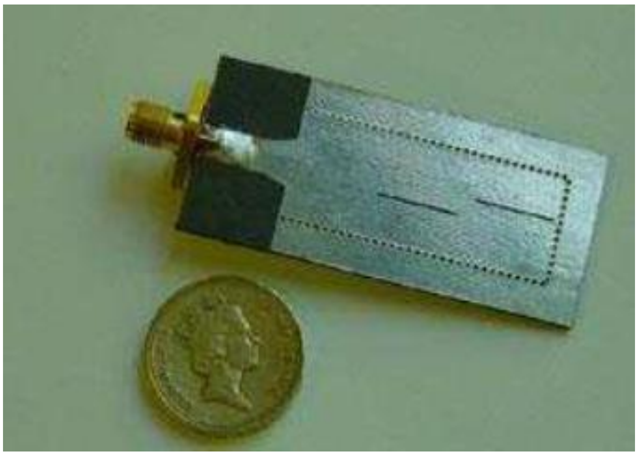

Fig (2. 1) Structure of dual slot antenna [10].

Many techniques have been demonstrated to design a substrate integrated waveguide slot antenna. A slotted narrow wall SIW is presented in [11], the design proposed a feeding SIW and a slotted narrow wall that fed high permittivity dielectric loaded substrate integrate cavity (SIC) in co-planar configuration. This design achieved a bandwidth of 10% and operated at a frequency of 35 GHz and 60 GHz. Fig (2. 2) shows the structure of a SIW slotted narrow wall fed cavity antenna.

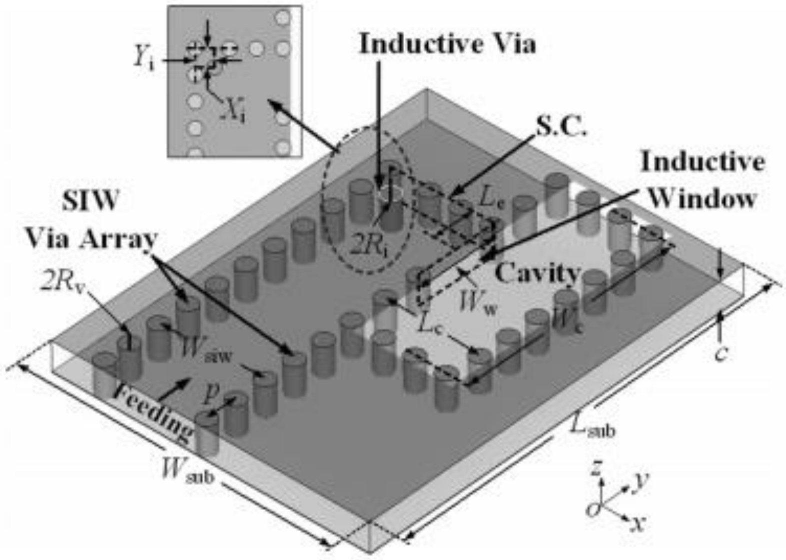

Fig (2. 2) Structure SIW slotted narrow wall fed cavity antenna [11].

A SIW linear array is presented in ref [12]. The single radiator consists of four cross-tilted slots; tuning metallic vias is included to improve reflection of the longest slot. A 16-element antenna designed and fabricated at 17 GHz is shown Fig (2. 3), achieving 26 dBi and 80% radiation efficiency.

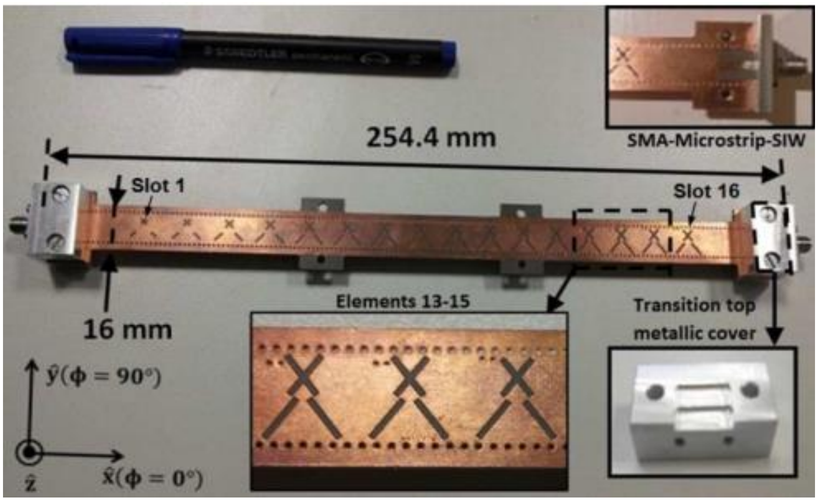

Fig (2. 3) Geometry of SIW linear slotted array with tuning vias [12].

Liang Wu [13], designed SIW switch beam antenna at 2.45 GHz. To achieve a switch beam antenna in 360^0, four PIN diodes have been integrated directly to the structure that can be easily controlled and is a perpendicular reflection plane as shown in Fig (2. 4). When the diodes are in forward biased (on state), this presents a short circuit to the slot. If the diodes are in its reverse biased (off state), this presents an open circuit to the slot and allows the slot to radiate significantly. The measured gain is between 3 dBi and 6 dBi.

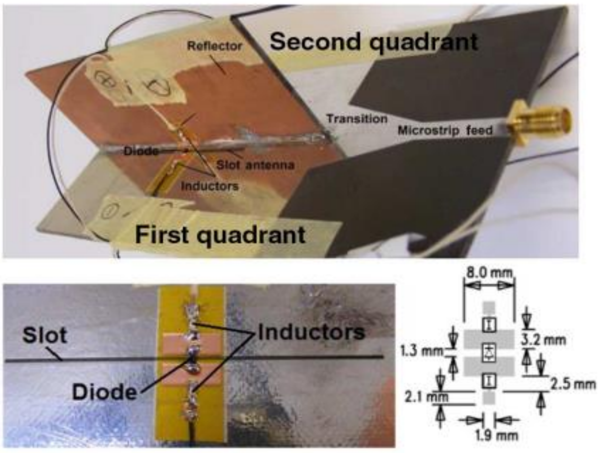

Fig (2. 4) Photograph of switched beam antenna and structure of overlay showing capacitive pads, pin diode, inductive chokes, and bias wires [13].

In ref [14], a compact proximity-fed open-ring slot antenna loaded with a SIW is designed to cover the frequency range 3.8 GHz to 11 GHz (ultra-wide band operation). The stub as shown in Fig (2. 5) is used to improve lower band matching. For extra bandwidth up to 20 GHz, a metallic via-holes through substrate, that connect top and metal plates was aligned.

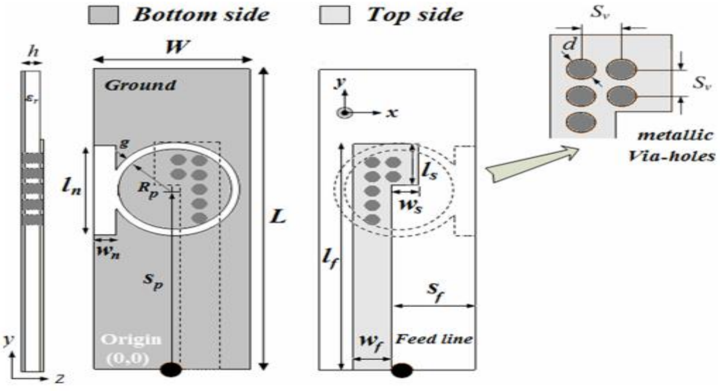

Fig (2. 5) Proposed structure for open ring slot antenna [14].

2.3 SSIW theoretical analysis

The normal SIW that works on the first mode TE_{10} can be split symmetrically along the waveguide and enable the half width of the waveguide to work the same as the full mode. This type of mode is called half mode SIW (HMSIW) $\mathrm{TE}_{1/2,0}$ [15]. The slotted substrate integrated waveguide sometimes referred to as SSIW [13] is similar to the standard SIW, but with an additional slot along the top of the conducting surface.

Fig (2. 6) shows the electric field distribution along the waveguide in half mode and full mode SIW. The SSIW field is shown in Fig (2. 7) and resembles the half mode $\mathrm{TE}_{1/2,0}$ mode.

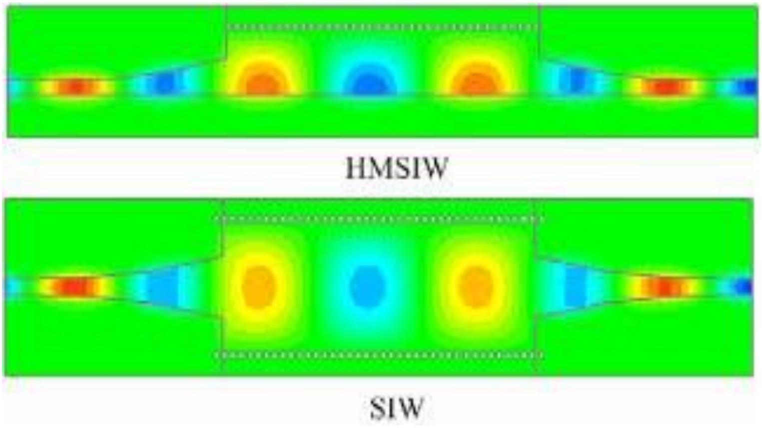

Fig (2. 6) Half and full mode structure [9]

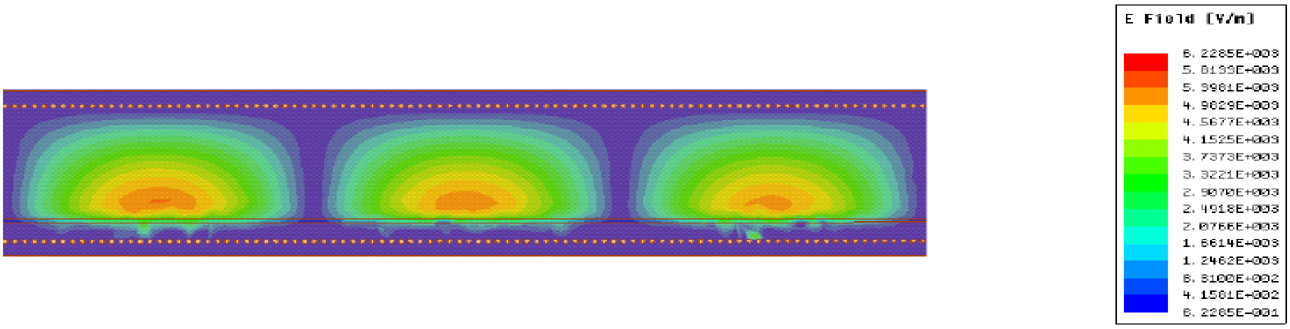

Fig (2. 7) SSIW Electric field distribution at $TE_{1/2,0}$ mode [5]

2.3.1 Theoretical analysis

The main structure of SSIW is shown in Fig (2. 8), shows how discrete components can be easily integrated with the guide according to equation (1.1).

In free space, the electromagnetic waves travel at the speed of light ($c = f\lambda$). However, when EM wave travels in a lossless medium it is affected by the dielectric medium and the wavelength reduces to the following equation:

$$\lambda_m = \frac{v_m}{f} \;\; where \; v_m = \frac{1}{\sqrt{\mu_0 \mu_r \varepsilon_0 \varepsilon_r}} = \frac{c}{\sqrt{\varepsilon_r}}$$

For TEM waves $\lambda_g = \lambda_m = \frac{2\pi}{k}$ where k is the modified wave number.

For TE or TM waves:

$\lambda_g = \frac{2\pi}{\beta}$. The wave number in free space, $\mathrm{k_0}$ can be calculated using the following equation $k_0 = \frac{\omega}{c} = \frac{2\pi f}{c}$ while the wavenumber in medium $k = \frac{\omega}{v_m} = \frac{\omega\sqrt{\varepsilon_r}}{c} = k_0\sqrt{\varepsilon_r}$

For the $\mathrm{TE_{mn}}(\mathrm{TM_{mn}})$ mode, the cutoff wave number is:

$$k_c = \sqrt{\left(\frac{m\pi}{a}\right)^2 + \left(\frac{n\pi}{b}\right)^2} \tag{2.1}$$

And the phase constant:

$$\beta = \sqrt{\varepsilon_r k_0^2 - k_c^2} \tag{2.2}$$

From β, the effective relative permittivity can be defined by:

$$\varepsilon_{reff} = \left(\frac{\beta}{k_0}\right)^2 \quad (2.3)$$

Using λ_c to find cutoff frequency f_c:

$$f_c = \frac{v_m}{2\pi} k_c \quad (2.4)$$

Remembering that $$v_m = \frac{c}{\sqrt{\varepsilon_r}} \quad (2.5)$$

According to equation (1.1), the SSIW supports a quasi $TE_{1/2,0}$ mode similar to a half mode SIW and therefore the formula would be:

$$k_c = \frac{\pi}{2L_3} \quad (2.6)$$

The phase constant is approximately the same as a half mode SIW of width L_3 and given by

$$\beta = \sqrt{\varepsilon_r k_0^2 - \left(\frac{\pi}{2L_3}\right)^2} \quad (2.7)$$

A more accurate determination of β is given in [5]. As long as $\beta > k_0$, then the guide does not radiate. This can be proven by the following equations:

If we assume that:

k_y the wave number in Y direction

β the phase constant in X direction

$$K_y = \sqrt{k_0^2 - \beta^2} \quad (2.8)$$

So k_y is imaginary part if $\beta^2 > k_0^2$:

$$\varepsilon_r k_0^2 - k_c^2 > k_0^2 \quad (2.9)$$

Yield to:

$$(\varepsilon_r - 1)k_0^2 > k_c^2 \quad (2.10)$$

$$k_0 > \frac{k_c}{\sqrt{\varepsilon_r - 1}} \quad (2.11)$$

$$\frac{2\pi f}{c} > \frac{\pi}{2L_3\sqrt{\varepsilon_r - 1}} \quad (2.12)$$

$$f > \frac{c}{4L_3\sqrt{\varepsilon_r - 1}} \tag{2.13}$$

Below f, the waveguide leaks energy and radiates as it propagates along the guide. By reducing the value of L_3 at a certain point along the guide, the above condition can be satisfied resulting in a region where the slot will radiate as demonstrated in Fig (2. 8).

By controlling the step width and length of the reduced width section and by placing an offset open circuit section at the other end of the guide, the waveguide can be matched to the radiating region resulting in a resonant antenna. A microstrip to SSIW transition can then be used to excite the structure [17].

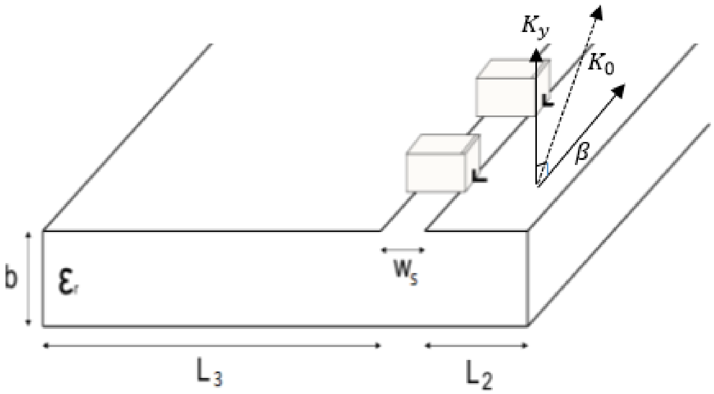

Fig (2. 8) Slotted Substrate Integrated Waveguide Antenna [5]

2.4 SSIW design (simulation and fabrication)

To design the slotted waveguide antenna operating at the cutoff frequency of 2.5 GHz, the structure is shown in Fig (2. 9) was designed under the following equations by determining the cutoff frequency as follows :

The cutoff wave number k_c for the $\text{TE}_{1/2,0}$ type:

$$k_c = \frac{\pi}{2(W_{2-}L_2)} \tag{2. 14}$$

Substituting W_2 = 33 mm to the equation yields : $k_c = 74.79$ m^{-1}

Now the cutoff frequency:

$$f_c = \frac{ck}{2\pi\sqrt{\varepsilon_r}} = 2.5 \text{ GHz}$$

The phase constant $\beta = \sqrt{\varepsilon_r k_0^2 - \left(\frac{\pi}{2W_2}\right)^2}$ which result $\beta = 105.9$ radian/m

The design was based on a RT/ Duroid 5580 substrate with thickness 0.787 mm, relative permittivity of 2.2 and a loss tangent of 0.0015. The top and bottom of the substrate were connected with the vias to form the conductive sidewalls of the SSIW. The slot is a capacitive air gap of width 0.5 mm and the top surface is copper. The S-parameter such as the return loss is affected by the width (*W*) of the SIW which is chosen to be 43 mm. The microstrip feed line was designed to be 4 mm in width and 5 mm in length to match the 50 Ω SMA PCB connector, which is used to provide low loss transition to the waveguide.

The sidewalls of the waveguide are conductive copper wires 0.5 mm in diameter that connects the top and bottom layer by using row of vias. The separation between the vias is 1 mm. This guaranteed low radiation leakage. The SSIW was designed and simulated using a Computer Simulation Technology (CST) Microwave Studio Suite, at resonant frequency 2.5 GHz. All the parameters that are chosen can fit to the fabrication process.

Table (2. 1) shows all the parameters dimension of the structure.

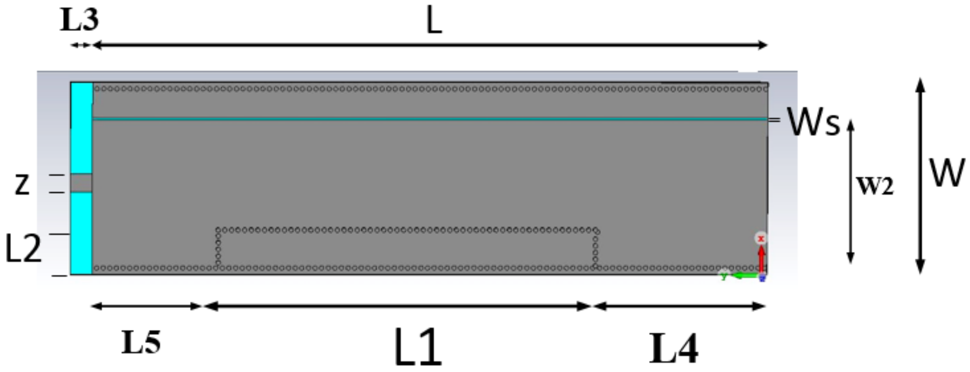

Fig (2. 9) Slotted SIW structure design.

Parameter	**Optimized value (mm)**	**Description**
L	153	Length of the waveguide
W	43	Width of the waveguide
W_2	33	Width from vias to the slot
W_s	0.5	Width of the slot
Z	4	Mirostrip width
L_1	93	
L_2	11	
L_3	5	Length of microstrip
L_4	21	
L_5	39	
B	0.787	Thickness of substrate

Table (2. 1) Parameters of the single SIW antenna.

2.4.1 Study the Parameters effect of SSIW

This section aims to study and discuss the comprehensive parameters of the design.

As shown in Fig (2. 10), by increasing the width of the slot W_s (reducing the capacitance between the offset gap of the slot), the resonant frequency will increase as well as an increasing return loss and bandwidth of the antenna. By decreasing L_2, the resonant frequency decreases and the refection coefficient also decreases. Moreover, by increasing L_1, the cutoff frequency increases. To obtain the best matching at the desired frequency, a variation of L_2 , L_1 is needed to obtain the resonance frequency 2.5 GHz with return loss below 10 dB. This is shown in Fig (2. 11) and Fig (2. 12). As shown in Fig (2. 13), by increasing the total width of the waveguide the frequency decreases. This parameter and a corresponding change in the other parameters can be used to rescale the design to other frequency bands.

Fig (2. 14) shows the effect of thickness of the substrate on the resonant frequency. When the thickness of substrate increases, the resonant frequency will decrease and the bandwidth increases. In this design, the thickness is 0.787 mm because if we increase the thickness of the substrate, the microstip feeding line width will increase more than 4 mm .This is difficult to fabricate in this situation and as a matter of fact, increasing the thickness of the substrate will be costly and bulkier.

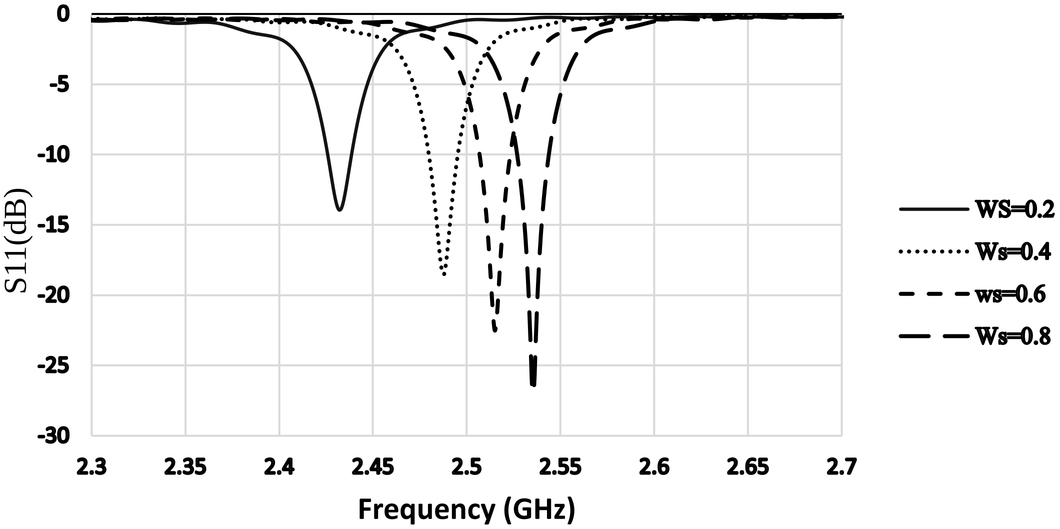

Fig (2. 10) Slot width effect on reflection coefficient versus frequency (other parameters are the same in Table (2.1).

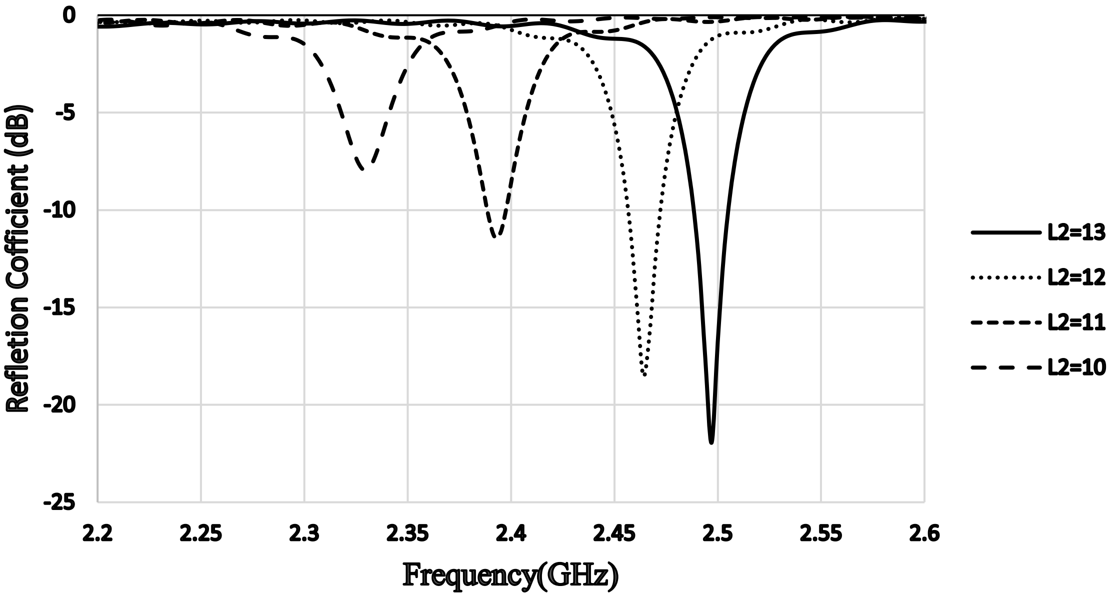

Fig (2. 11) L_2 changing effect on return loss versus frequency (other parameters are the same in Table (2.1).

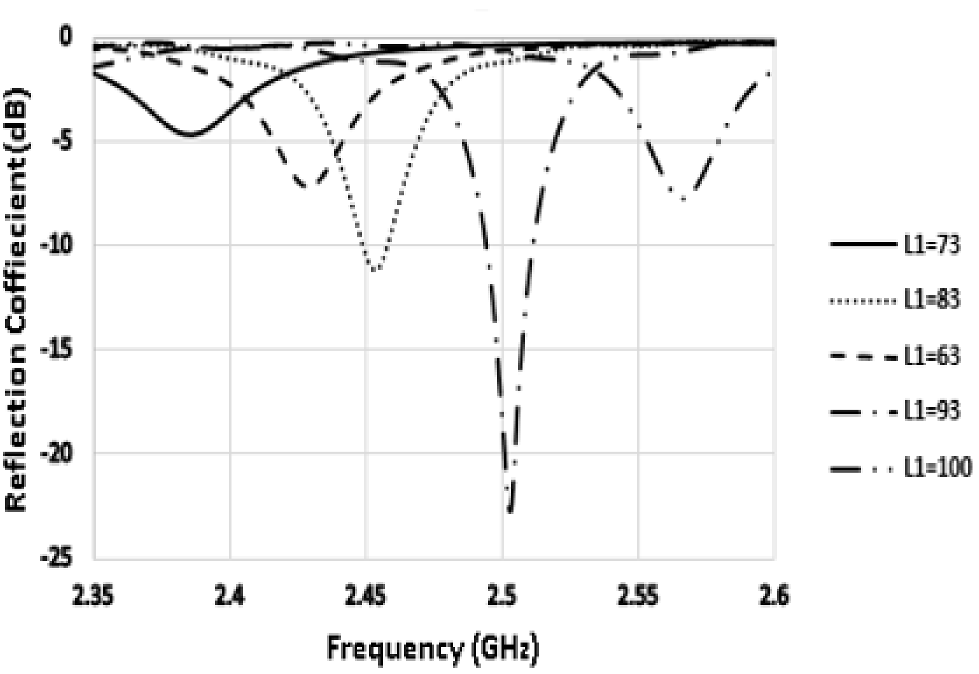

Fig (2. 12) L_1 parameter change effect on reflection coefficient versus frequency (other parameters are the same in table (2.1).

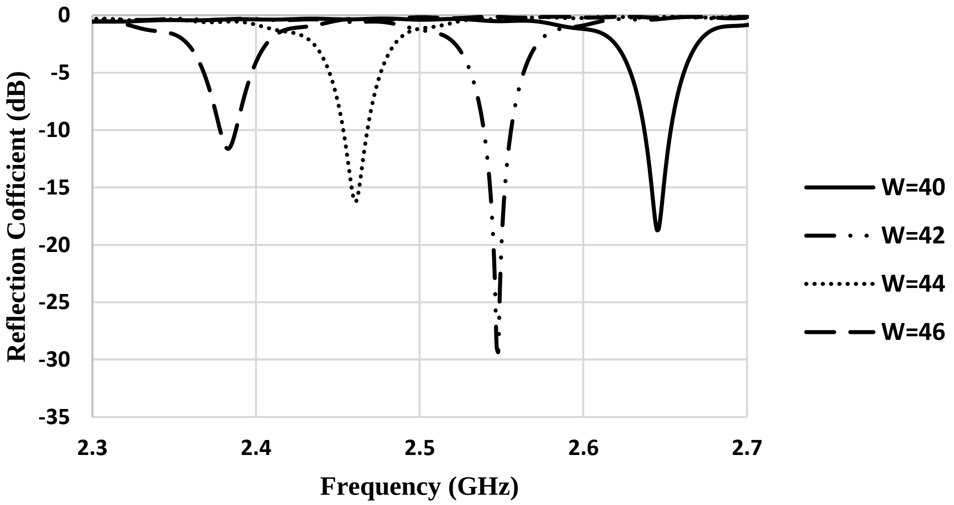

Fig (2. 13) Effect width of the SSIW on reflection coefficient (other parameters are the same in table (2.1).

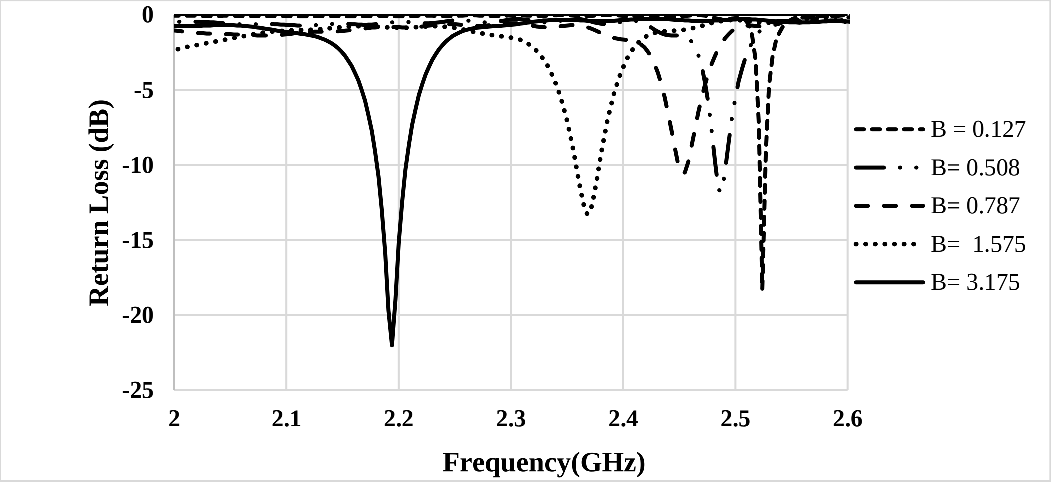

Fig (2. 14) Effect thickness change on return loss, other parameters are the same in table (2.1).

To calculate the effect of L_2 on the resonant frequency theoretically, the approximate equation $f_c = \frac{c}{4(w_2 - L_2)\sqrt{\varepsilon_r}}$ can be used to calculate the cutoff frequency. Table (2.2) shows the comparison of changing L_2 on resonant frequency theoretically and by the simulation shown in Fig (2. 11).

W_2 (Waveguide width from vias to the slot) is 33 mm, which is set the same as the simulation and theoretical calculation. Additionally, c is the speed of light. A very good agreement between the simulation and theoretical calculation can be seen in Table (2.2).

L_2	f_c (simulation GHz)	f_c (theoretical GHz)
13	2.50	2.52
12	2.40	2.40
11	2.35	2.29
10	2.30	2.19

Table (2. 2) comparison the effect of L_2 on resonant frequency theoretically and simulation (CST) (the other parameters are same in table 2.1

Fig (2. 15) shows the electric field distribution along the slot with different length of L_2 in Z plane and for L_2 the change is from 13 to 10 mm. This means that the radiation from the slot will be in the same phase and the wave travels slowly along the slot, resulting the resonant frequency to be nearer to the cutoff frequency.

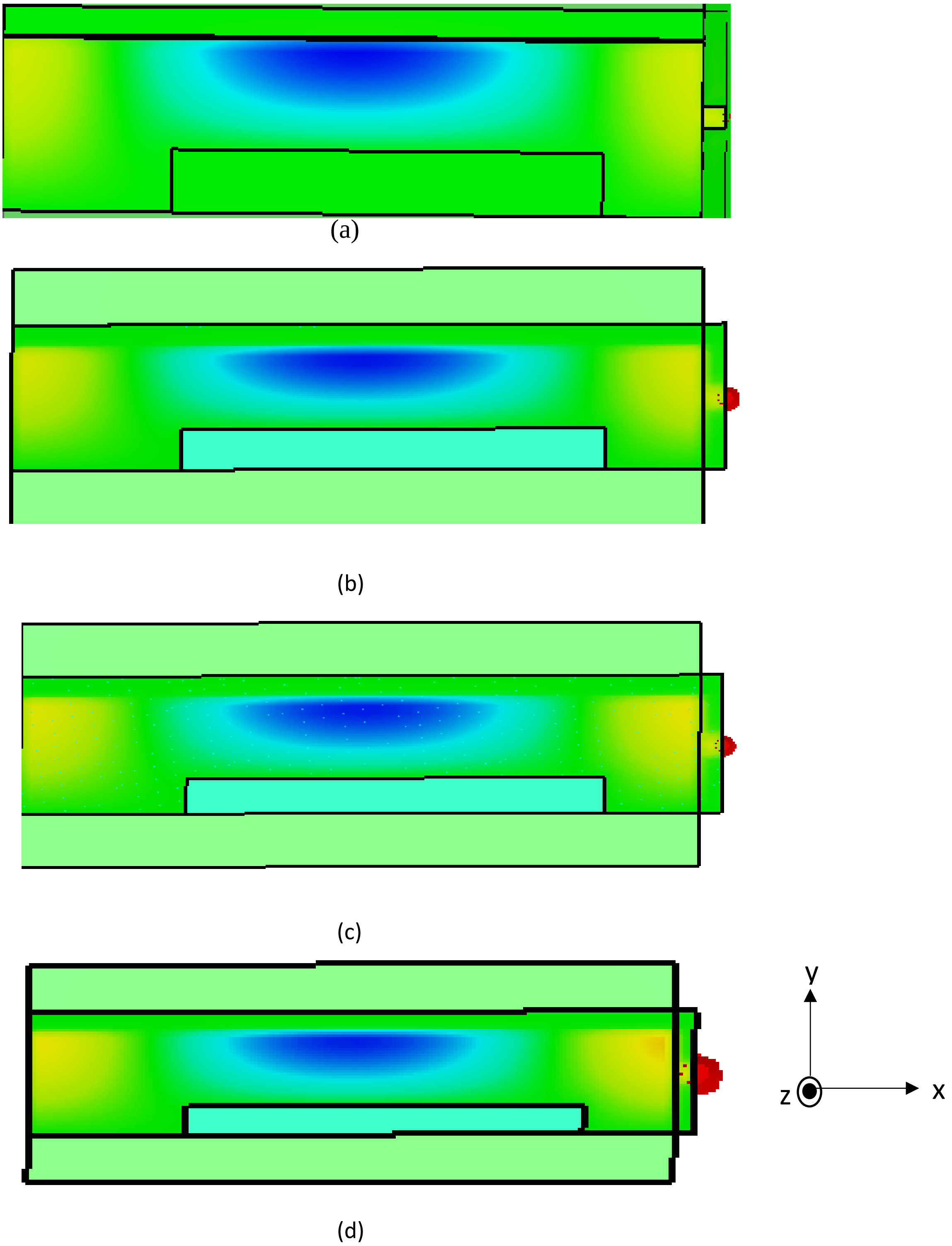

Fig (2. 15) Electric field distribution: (a) $L_2 = 13\ mm, (b)\ L_2 = 12\ mm, (c)\ L_2 = 11\ mm, (d)\ L_2 = 10\ mm.$

The equivalent circuit modelling of single SSIW is shown in Fig (2. 16), the slot placed one quarter wavelength of the waveguide from the short circuit end. The equivalent circuit for the slot is a shunt conductance [13]. The slot is offset by X from the centre of the waveguide and by controlling X the coupling and radiation can be controlled.

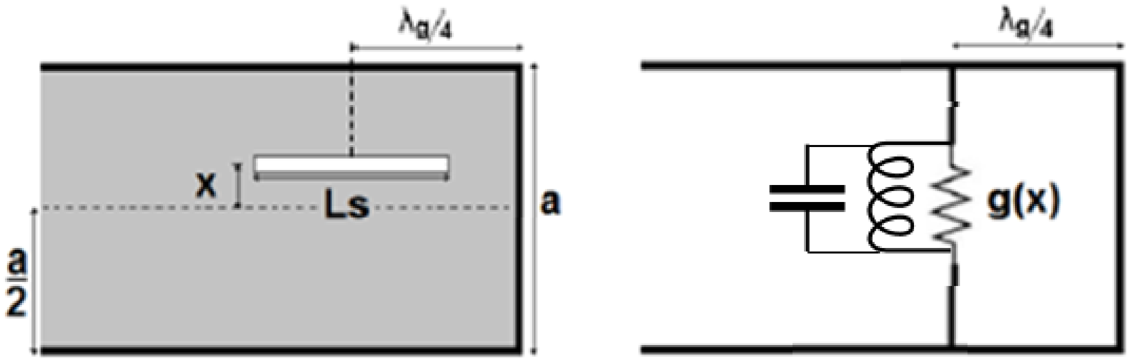

(a) (b)

Fig (2. 16) (a) Single slot resonant waveguide. (b) Equivalent circuit [13].

$$g(x) = g_0 sin^2(k_x x) \tag{2.15}$$

$$\text{Where } g_0 = \frac{4k^2}{G_r} \tag{2.16}$$

At the resonant frequency, the capacitance and inductance cancel each other.

For perfect matching result *g(x)* = 1, k_x is the transverse phase constant of TE_{10} mode, $K_x = \pi/a$, where a is the width of the wave guide , G_r is the radiation conductance of the slot g_0 is the normalized conductance.

The equivalent circuit introduce in the next section has the same concept but with an open-end termination.

2.4.2 Design procedure

The procedure starts by simulating the waveguide antenna as a two port device in CST and determining the network Z parameters. Solid walls are used in the design optimization to reduce the complexity of the simulation. The real part and imaginary part of Z-parameter is shown in Fig (2. 17).

The SSIW antenna can be modelled (are formed T-network) under the following equation:

$$Z = \begin{pmatrix} Z_A + Z_C & Z_C \\ Z_C & Z_B + Z_C \end{pmatrix} \qquad (2.19)$$

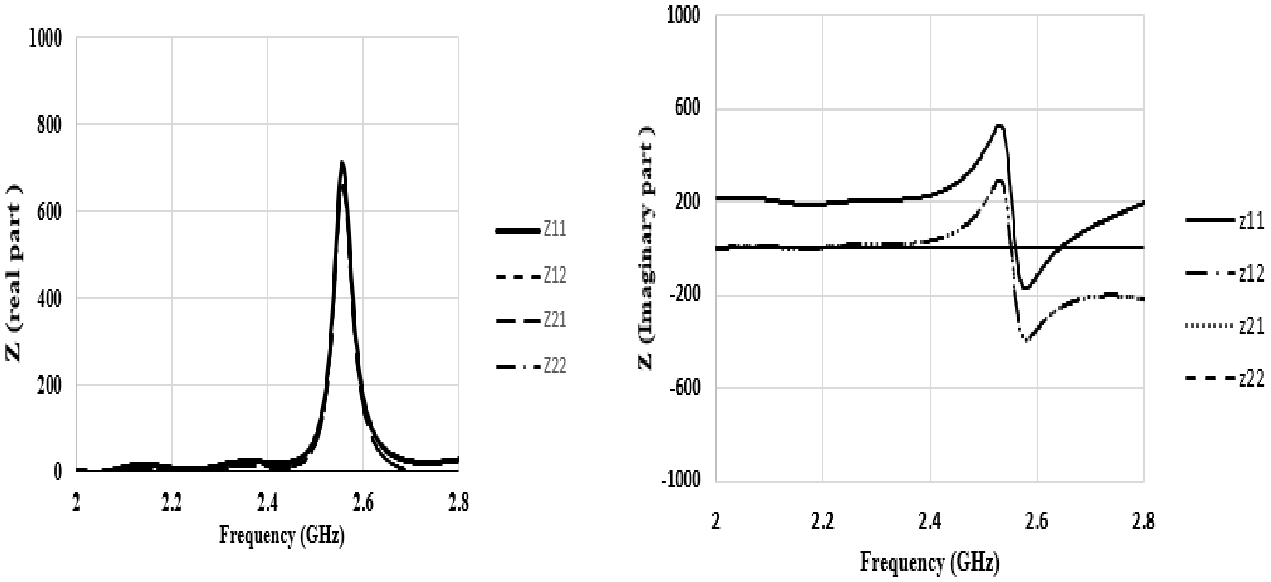

(a) (b)

Fig (2. 17) Impedance versus frequency: (a) Real part, (b) Imaginary part.

According to the Z-parameter as shown in Fig (2. 17), all the Z-parameters in real part are equal at the resonant frequency 2.5 GHz. Therefore only the Z_c term contains a real impedance.

Fig(2. 17b) shows the imaginary part of impedance Z, at 2.5 GHz, Z_{11} , Z_{22} is higher than Z_{12}, Z_{21}.

If we subtract the imaginary part of $Z_{11} - Z_{21}$ as shown in Fig (2. 18), we obtain Z_A.

Fig (2. 19) shows the equivalent T-network for the SSIW antenna, the shunt resistor is equal to the value 618 Ω according to the impedance of the real part of Fig (2. 17a) and it is tuning by a parallel inductor and capacitor which represent an LC parallel network.

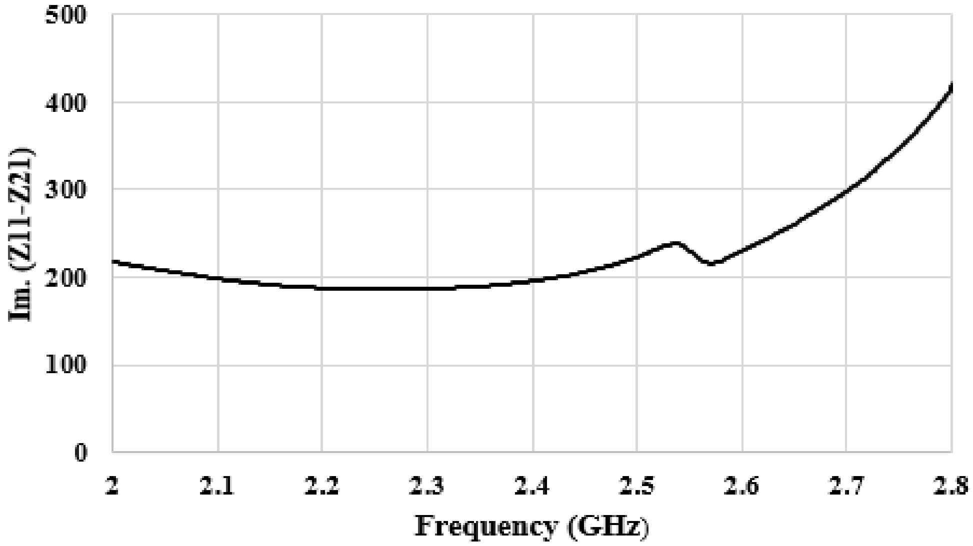

Fig (2. 18) Frequency against Z_A.

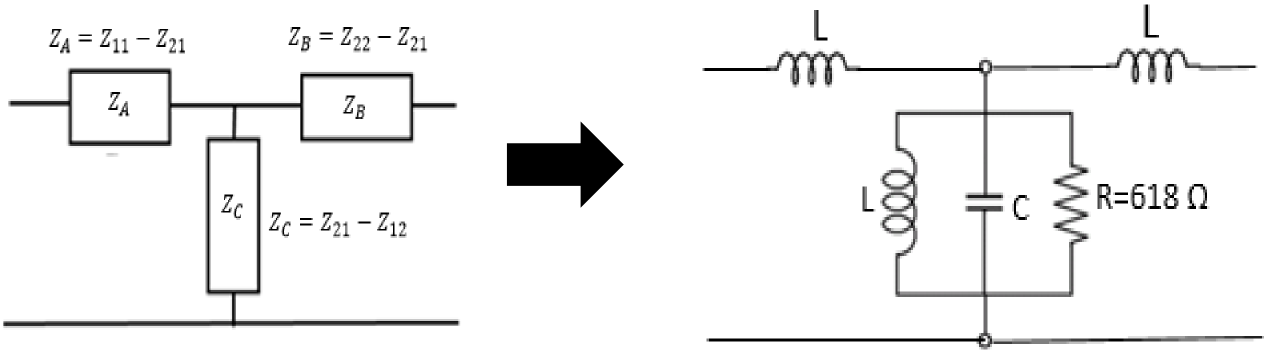

Fig (2. 19) Equivalent T-network for SSIW antenna.

2.4.3 Comparison results between simulation and measurements

The results of the simulation was transferred to fabrication with the same dimensions for the purpose of comparison and analysis as shown in table (2.3). A photograph of the structure is shown in Fig (2. 20).

Note that the antenna has a microstrip to SIW tapered feed that is optimised to connect an SMA connector for measurement.

Fig (2. 20) Fabrication design of SSIW antenna.

S_{11} was measured using a network analyser, which is capable of sweeps from 9 kHz to 13.6 GHz. A PC has connected via GPIB to enable screen shot and record the data of scattering matrix. A calibration has been done before measurements using (open-short-through).

As shown in Fig (2. 21), there is a very good agreement between the measurement and simulation. The antenna has a resonant frequency at 2.5 GHz. In Simulation, the return loss was -23 dB with bandwidth 23 MHz, while in measurements the return loss was -17 dB and bandwidth 27 MHz, which nearly have the same bandwidth and low return loss. A second order mode radiate at 2.9 GHz and a third order mode radiate at 3.4 GHz.

The polar plot and 3D far field radiation pattern at 2.5 GHz is shown in Fig (2. 22), in polar plot the main lobe magnitude is 4.36 dB and has side lobe level of -5.3 dB. The radiation efficiency is -1.0 dB and total efficiency is -1.6 dB. The simulation gain is 4.5 dBi.

The radiation pattern at the resonant frequency 2.5 GHz was measured using an anechoic chamber using two identical antennas with specific distance in the far field. The polar plot shows the comparison of the radiation pattern between simulation in red dash lines and measurement in black solid line. It shows a good agreement as shown in Fig (2. 23) in H-plane and E-plane.

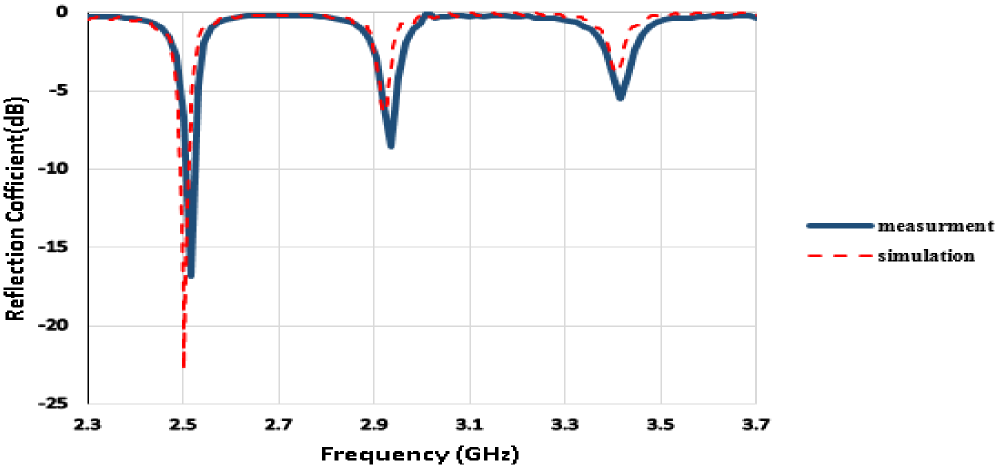

Fig (2. 21) Comparison of S_{11} between measurements and simulation.

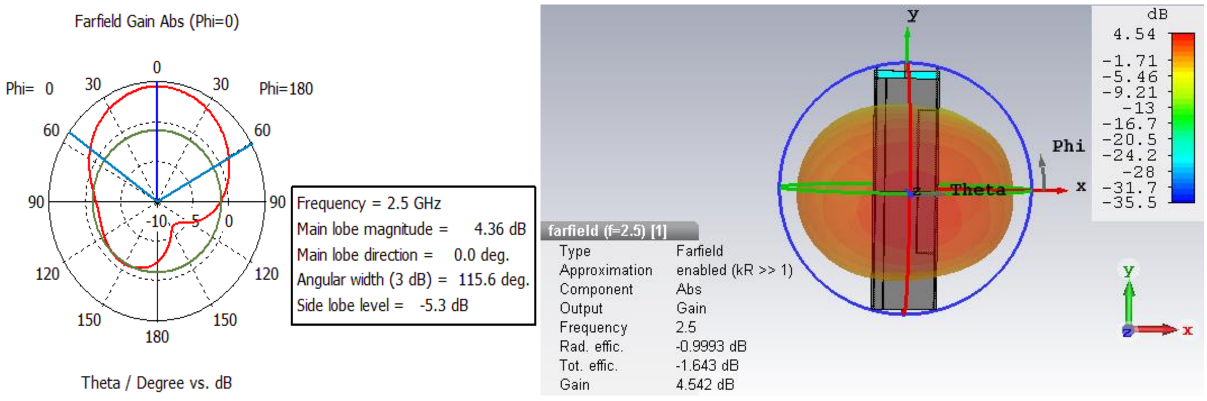

Frequency = 2.5 GHz
Main lobe magnitude = 4.36 dB
Main lobe direction = 0.0 deg.
Angular width (3 dB) = 115.6 deg.
Side lobe level = -5.3 dB

Type	Farfield
Approximation	enabled (kR >> 1)
Component	Abs
Output	Gain
Frequency	2.5
Rad. effic.	-0.9993 dB
Tot. effic.	-1.643 dB
Gain	4.542 dB

(a) (b)

Fig (2. 22) Radiation pattern at 2.5 GHz: (a) E-plane, (b) 3D pattern.

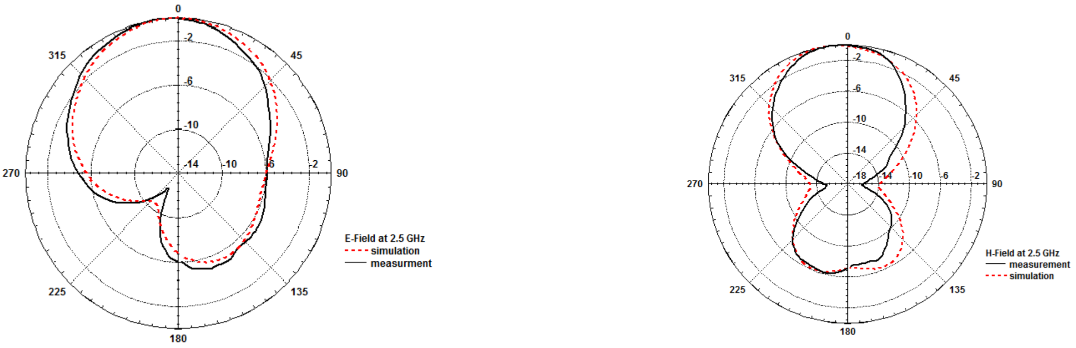

(a) (b)

Fig (2. 23) Comparison of radiation pattern between simulation and measurement at 2.5 GHz: (a) E-plane, (b) H-plane.

Fig (2. 24) shows the simulated electric field distribution at 2.5 GHz inside the antenna, derived from CST, demonstrating half mode variation across the radiating region which shown to be non-uniform and of a cosine shape. Once again, a very good agreement between simulation and measurement of gain is shown in Fig (2. 24 b). The simulation shows that gain at resonant frequency 2.5 GHz is 4.5 dBi while in measurement is 4.7 dBi.

When the waveguide radiates, it has back lobes. To reduce these back lobes, metallic plates should be added at the sides of the waveguide.

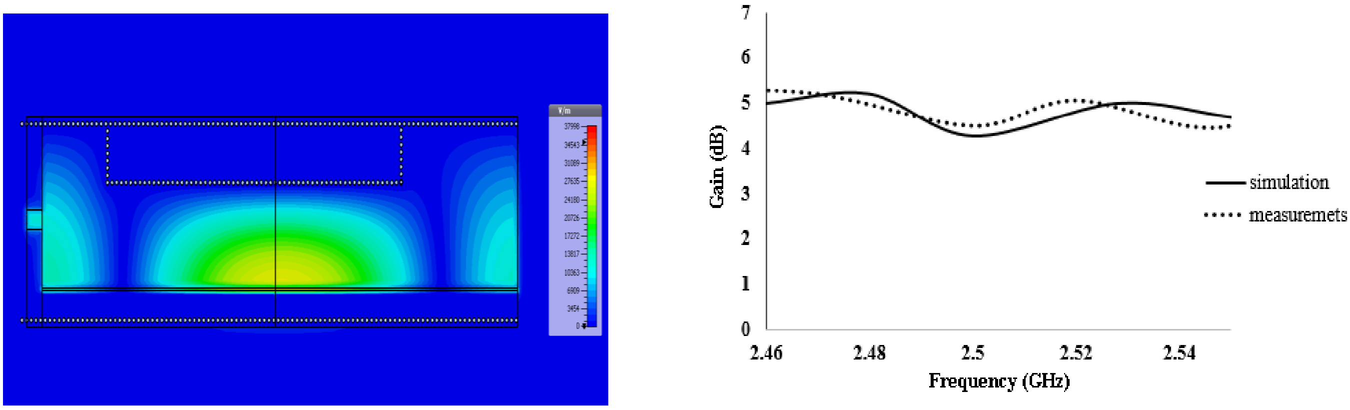

(a)

(b)

Fig (2. 24) (a) Electric field distribution at 2.5 GHz. (b) Gain comparison against frequency.

The following section shows the modes and radiation patterns studied:

Fig (2. 25) shows the electric field distribution at the second and third order mode 2.92 GHz and 3.4 GHz respectively. The polar plot details at 2.9 GHz in H-plane and E-plane, radiates in two directions as shown in Fig (2. 26). The 3D radiation pattern shows how the structure placed vertically, radiates the gain at 2.9 GHz is 5.43 dBi, but the total efficiency is poor (-6.02 dB).

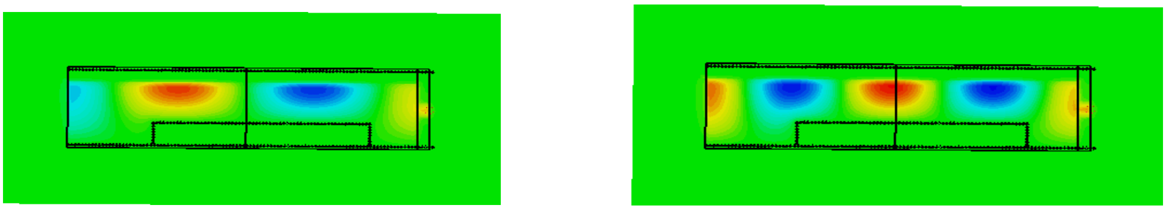

(a)

(b)

Fig (2. 25) Electric field distribution at: (a) 2.92 GHz, (b) 3.4 GHz.

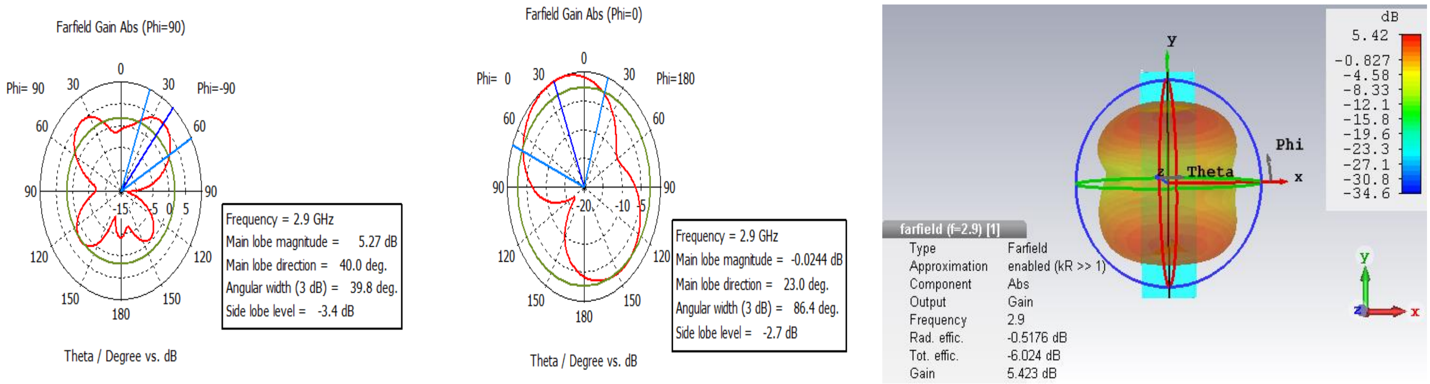

Frequency = 2.9 GHz
Main lobe magnitude = 5.27 dB
Main lobe direction = 40.0 deg.
Angular width (3 dB) = 39.8 deg.
Side lobe level = -3.4 dB

Frequency = 2.9 GHz
Main lobe magnitude = -0.0244 dB
Main lobe direction = 23.0 deg.
Angular width (3 dB) = 86.4 deg.
Side lobe level = -2.7 dB

farfield (f=2.9) [1]

Type	Farfield
Approximation	enabled (kR >> 1)
Component	Abs
Output	Gain
Frequency	2.9
Rad. effic.	-0.5176 dB
Tot. effic.	-6.024 dB
Gain	5.423 dB

(a) (b) (c)

Fig (2. 26) Radiation pattern at 2.9 GHz: (a) H-plane, (b) E-plane, (c) 3D pattern.

The polar plot and 3D radiation pattern for the third order mode at 3.4 GHz are shown in Fig (2. 27). In H-plane the angular width is 34^0 with side lobe level -0.8 dB, the gain is 3.42 dBi with total efficiency -6.17 dB, and radiation efficiency -2.9 dB.

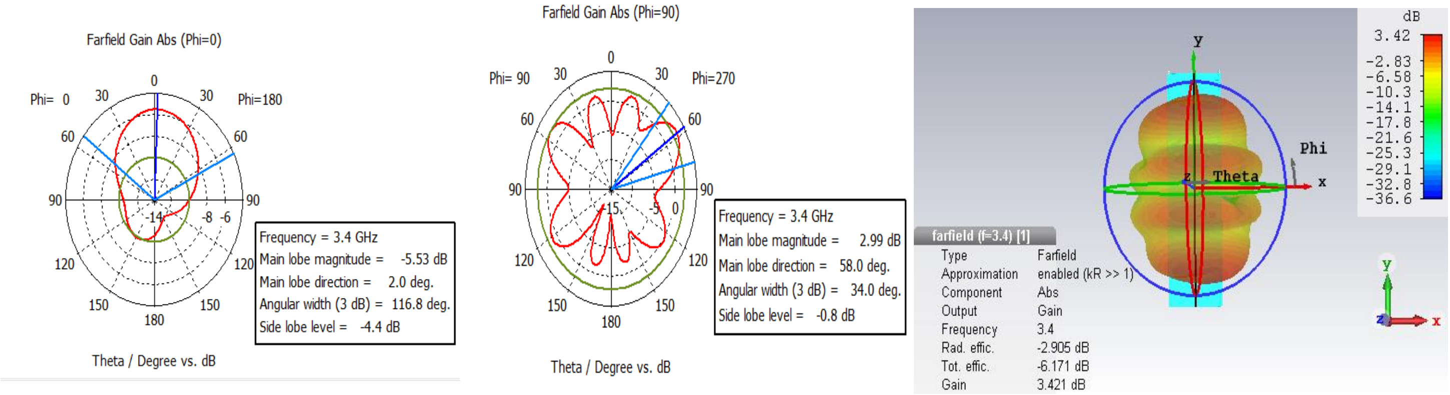

Frequency = 3.4 GHz
Main lobe magnitude = -5.53 dB
Main lobe direction = 2.0 deg.
Angular width (3 dB) = 116.8 deg.
Side lobe level = -4.4 dB

Frequency = 3.4 GHz
Main lobe magnitude = 2.99 dB
Main lobe direction = 58.0 deg.
Angular width (3 dB) = 34.0 deg.
Side lobe level = -0.8 dB

farfield (f=3.4) [1]

Type	Farfield
Approximation	enabled (kR >> 1)
Component	Abs
Output	Gain
Frequency	3.4
Rad. effic.	-2.905 dB
Tot. effic.	-6.171 dB
Gain	3.421 dB

(a) (b) (c)

Fig (2. 27) Radiation pattern at 3.4 GHz: (a) E-plane, (b) H-plane, (c) 3D pattern.

2.5 1 × 2 slotted SIW

The aim for targeting SIW antenna arrays, which usually is a set of identical radiating elements, is to provide higher gain and directivity than single antenna [18]. High radiation efficiency is important for the high performance of the system and lower cost [19].

The design here used a 1×2 slotted waveguide antenna as shown in Fig (2. 28). The length and width of each antenna is the same as the single array, 153 mm and 43 mm respectively. The widest section W_2 is 19.5 mm to get better matching. The microstrip feeding line L_3 is 10 mm and width of Z is 5 mm.

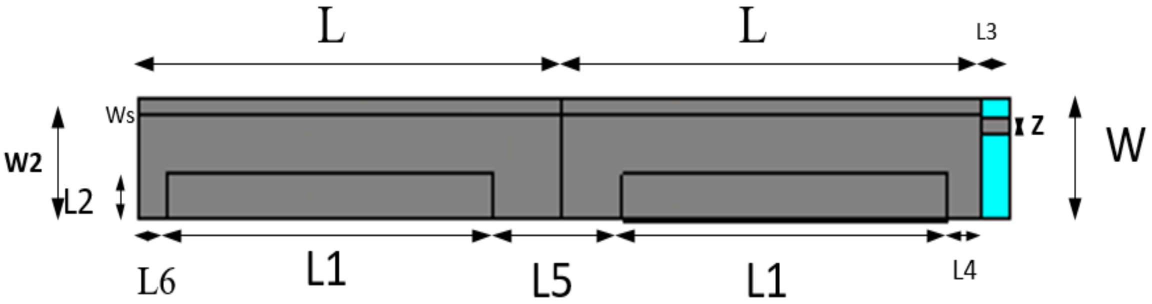

Fig (2. 28) 1×2 structure design.

Parameter	Optimized value (mm)	Description
L	153	Length of the waveguide
W	43	Width of the waveguide
W_2	32	Width from the side to the slot
W_s	0.5	Width of the slot
Z	5	Mirostrip width
L_1	96	
L_2	8	
L_5	73	
L_6	20.5	
L_3	10	

Table (2. 3) Parameters dimensions for 1 × 2 SSIW.

As shown in Fig (2. 29) the antenna resonates at 2.64 GHz, with reasonably good matching below -10 dB. Note that the resonant frequency is slightly shifted compared to the single SSIW antenna because it needs further changes in parameters dimensions to tune at 2.5 GHz. Further optimisation was not studied because it is only for checking the feasibility of an array.

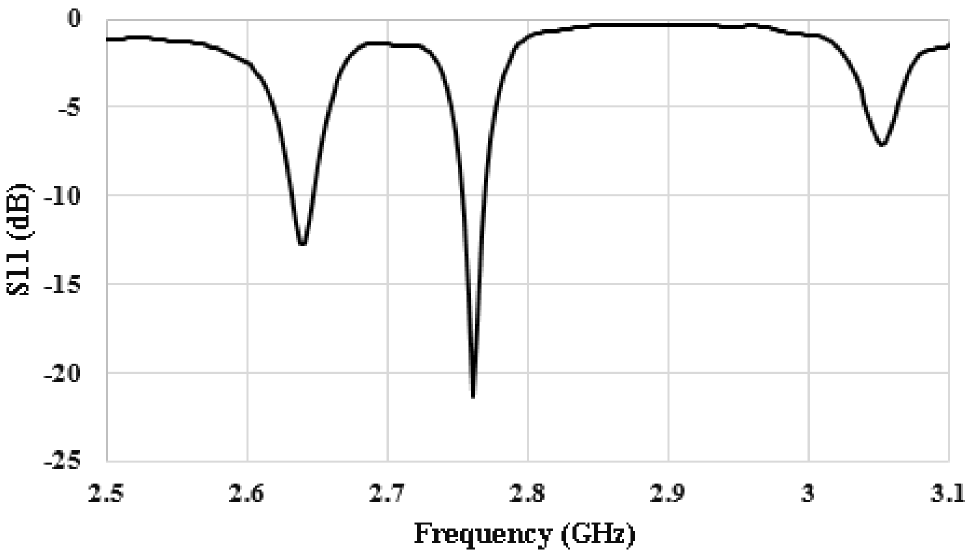

Fig (2. 29) Reflection coefficient S_{11} against frequency for 1 × 2 SSIW

The electric field distribution for 1× 2 array are in the same phase at 2.64 GHz as shown in Fig (2. 30), which looks like cosine shape. The parameters L_1, L_2, L_4, L_5, L_6, w_2 effect on radiation pattern, gain, directivity and matching which is not easy to adjust. The far field radiation pattern in 3D and in polar plot is shown in Fig (2. 31). The gain increased from 4.5 dBi in single element to 9.82 dBi and the directivity increased to 10.2 dB. The radiation efficiency is -0.41 dB and the total efficiency is -0.66 dB. In polar plot in E-plane, the main lobe of the radiation pattern has been offsets 10^0 from the normal direction and the side lobe levels are -10.3 dB . In H-plane, the main lobe magnitude is 9.15 dB and its direction 2^0 from the normal line, the side lobe level is -2.5 dB.

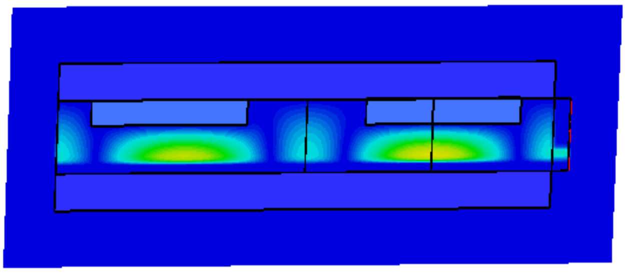

Fig (2. 30) Electric field distribution at resonant frequency at 2.64 GHz.

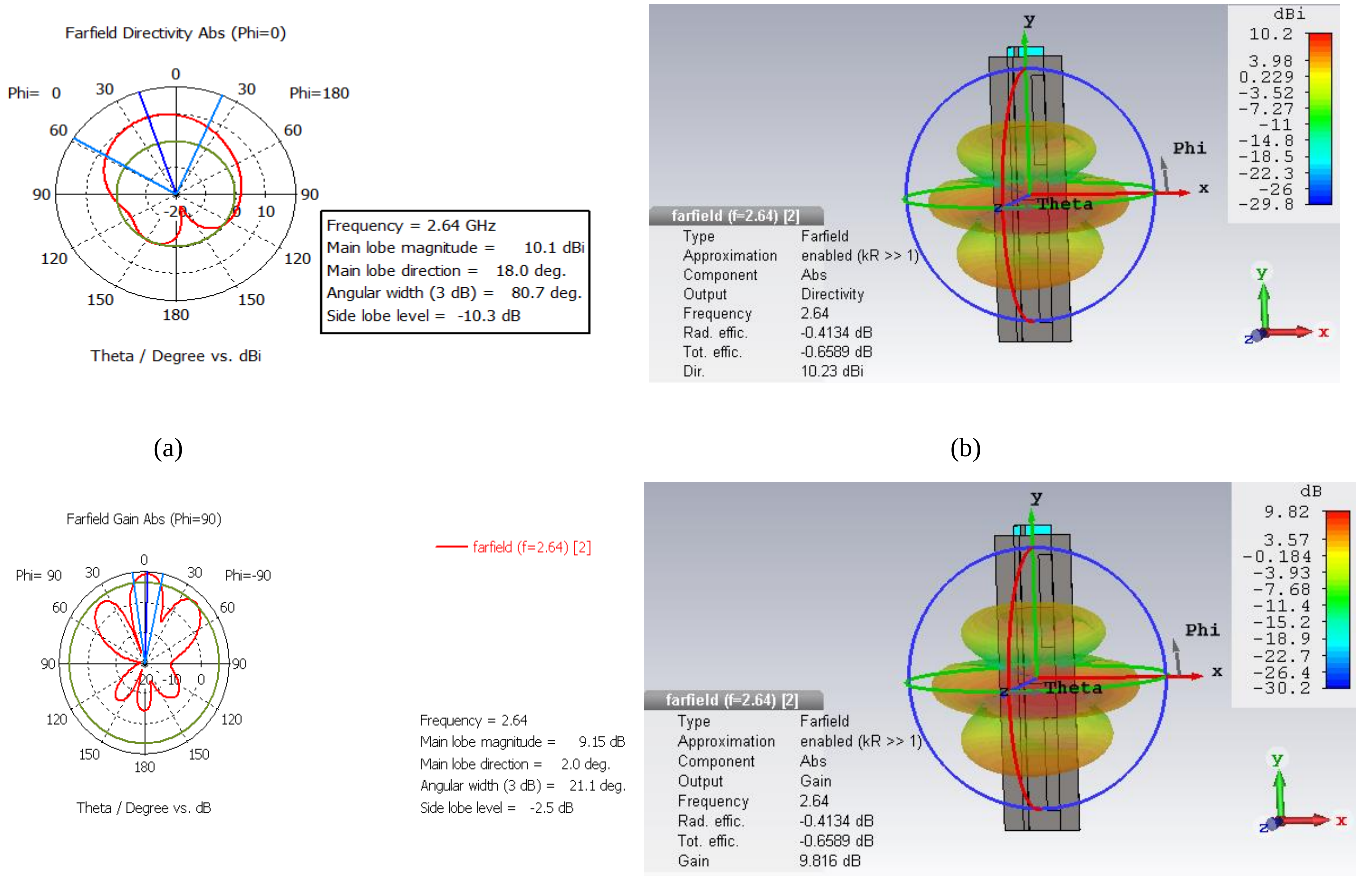

Frequency = 2.64 GHz
Main lobe magnitude = 10.1 dBi
Main lobe direction = 18.0 deg.
Angular width (3 dB) = 80.7 deg.
Side lobe level = -10.3 dB

(a)

Type Farfield
Approximation enabled (kR >> 1)
Component Abs
Output Directivity
Frequency 2.64
Rad. effic. -0.4134 dB
Tot. effic. -0.6589 dB
Dir. 10.23 dBi

(b)

Frequency = 2.64
Main lobe magnitude = 9.15 dB
Main lobe direction = 2.0 deg.
Angular width (3 dB) = 21.1 deg.
Side lobe level = -2.5 dB

(c)

Type Farfield
Approximation enabled (kR >> 1)
Component Abs
Output Gain
Frequency 2.64
Rad. effic. -0.4134 dB
Tot. effic. -0.6589 dB
Gain 9.816 dB

(d)

Fig (2. 31) Radiation pattern at 2.64 GHz: (a) E-plane, (b) 3D with directivity, (c) H-plane, (d) 3D with gain.

Fig (2. 32) and Fig (2. 33) shows the electric field distribution and polar plot radiation pattern at 2.76 GHz. The radiation shows it radiates with odd symmetry at the waveguide, in E-plane polar plot, shows that the main lobe magnitude is -6.3 dB with 38^0 from its main direction, the angular width is 95.7^0. In H-plane, the angular width is 17.9^0 with main lobe magnitude 8.48 dB and direction of 17^0, and the gain is 8.4 dBi.

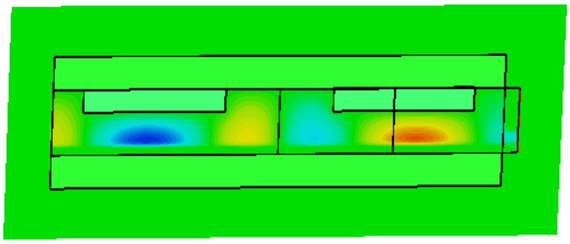

Fig (2. 32) Electric field distribution at 2.76 GHz.

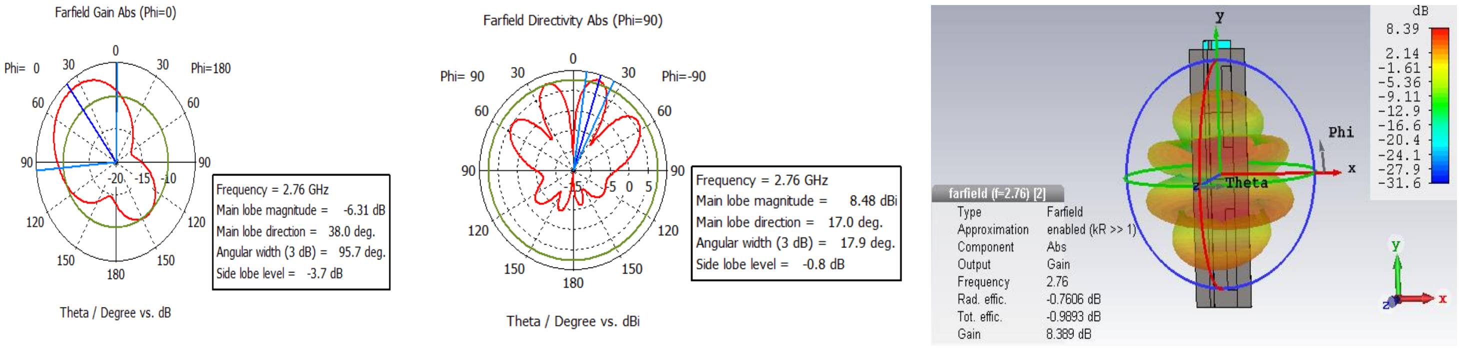

Frequency = 2.76 GHz
Main lobe magnitude = -6.31 dB
Main lobe direction = 38.0 deg.
Angular width (3 dB) = 95.7 deg.
Side lobe level = -3.7 dB

Frequency = 2.76 GHz
Main lobe magnitude = 8.48 dBi
Main lobe direction = 17.0 deg.
Angular width (3 dB) = 17.9 deg.
Side lobe level = -0.8 dB

farfield (f=2.76) [2]
Type Farfield
Approximation enabled (kR >> 1)
Component Abs
Output Gain
Frequency 2.76
Rad. effic. -0.7606 dB
Tot. effic. -0.9893 dB
Gain 8.389 dB

(a) (b) (c)

Fig (2. 33) Radiation pattern at 2.76 GHz: (a) E-plane, (b) H-plane, (c) 3D pattern.

The third radiation mode is 3.03 GHz. The electric field distribution and the far field radiation plot are shown in Fig (2. 34) and Fig (2. 35). In E-plane, the polar plot shows the main lobe magnitude is -12.1 dB with angular beam width is 127^0 while in H-plane, the main lobe magnitude is 6.8 dB with angular width 16^0 and side lobe level -1.3 dB.

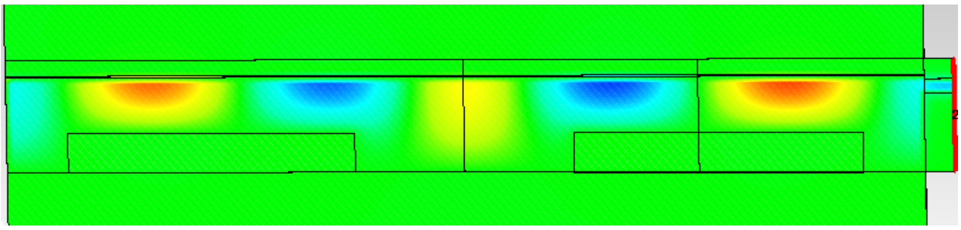

Fig (2. 34) Electric field distribution at 3.03 GHz.

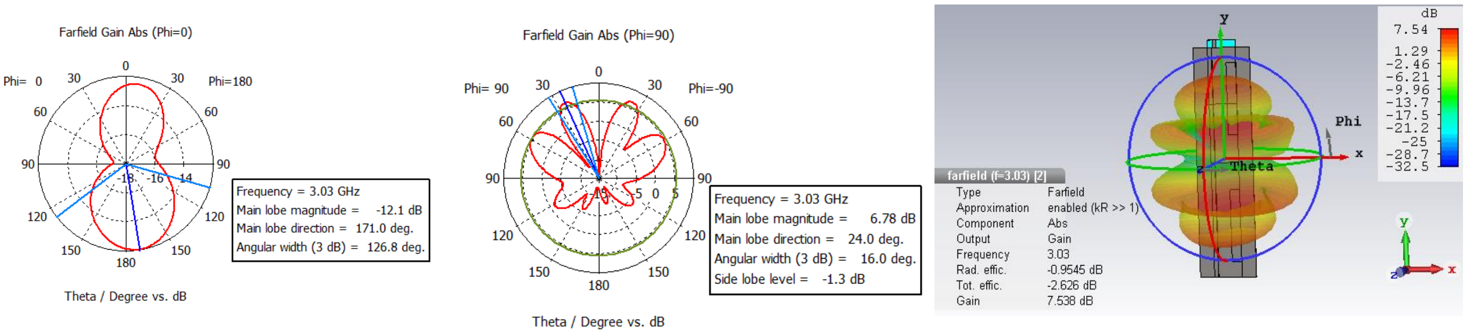

Frequency = 3.03 GHz
Main lobe magnitude = -12.1 dB
Main lobe direction = 171.0 deg.
Angular width (3 dB) = 126.8 deg.

Frequency = 3.03 GHz
Main lobe magnitude = 6.78 dB
Main lobe direction = 24.0 deg.
Angular width (3 dB) = 16.0 deg.
Side lobe level = -1.3 dB

farfield (f=3.03) [2]
Type Farfield
Approximation enabled (kR >> 1)
Component Abs
Output Gain
Frequency 3.03
Rad. effic. -0.9545 dB
Tot. effic. -2.626 dB
Gain 7.538 dB

(a) (b) (c)

Fig (2. 35) Radiation pattern at 3.03 GHz: (a) E-plane, (b) H-plane, (c) 3D pattern.

2.6 2 × 2 SSIW array

For further increase of gain, radiation pattern, directivity and efficiency with low transmission loss. A sub-array 1×2 array grouped with another 1×2 array, to design a 2 × 2 array antenna. The microstrip feeding are proposed using the simulation design CST, all the dimensions are similar to single and 1 × 2 array as shown in Fig (2. 36).

The microstrip feeding line is 1/2 power divider T-shape which symmetric in two subarrays, which is designed to match 50 Ω and low transmission loss, as shown in Fig (2. 36, b). Additionally, the width of the main feeding line is 2 mm in width and 5 mm in length. Table (2.4) shows all the dimensions for the SSIW antenna and the microstrip feeding line.

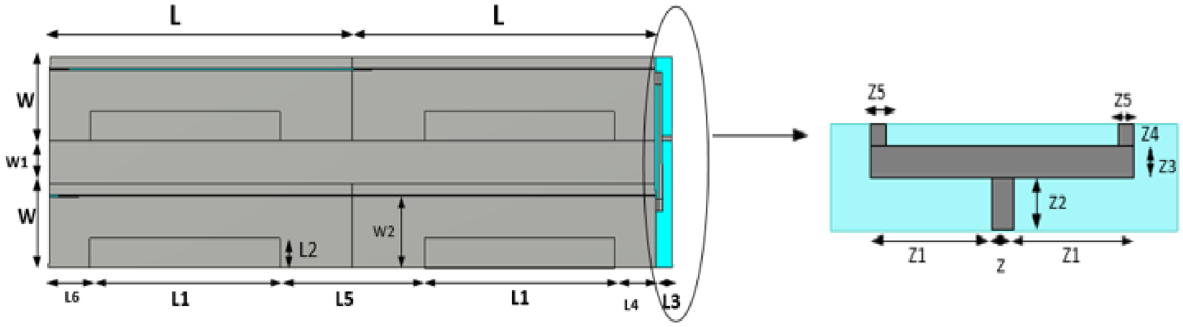

(a) (b)

Fig (2. 36) (a) 2 × 2 array SSIW. (b) Microstrip feeding line SSIW.

Parameter	Optimized value (mm)	Description
L	153	Length of the waveguide
W	39	Width of the waveguide
W_1	21	Width between two array
W_2	31	Width from the side to the slot
L_1	96	
L_2	8	
L_3	10	
L_4	20.5	
L_5	73	
L_6	20.5	
Z	2	
Z_1	30	
Z_2	5	
Z_3	2	
Z_4	1.5	
Z_5	6	

Table (2. 4) Parameter dimension for 2 × 1 SSIW array.

Fig (2. 37) shows the reflection coefficient against frequency. At resonant frequency 2.65 GHz, the reflection coefficient is well matched -14 dB, which works on half mode at 2.65 GHz and the bandwidth is 10 MHz.The electric field distribution at resonance frequency 2.65 GHz, are the same phase for all the antenna elements, the radiation in cosine shape as shown in Fig (2. 38)

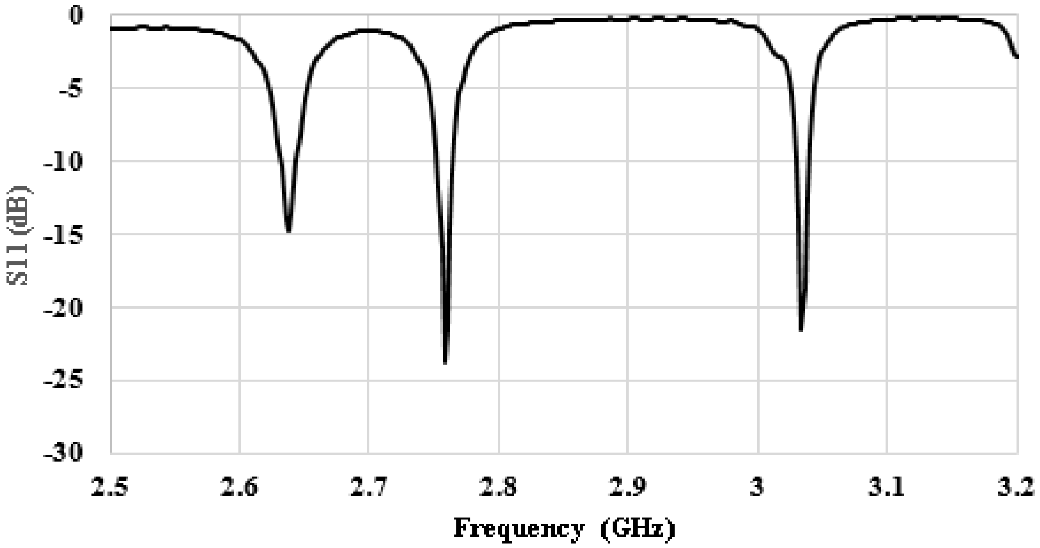

Fig (2. 37) Reflection coefficient against frequency.

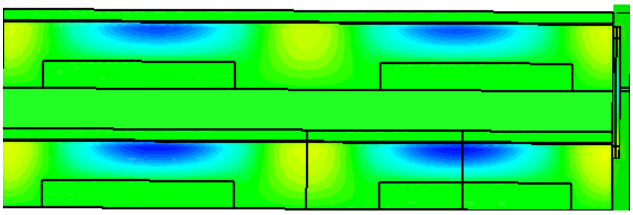

Fig (2. 38) Electric field distribution at 2.65 GHz.

Fig (2. 39) shows the far field radiation pattern in 3D and polar plot in E-plane and H-plane respectively at resonant frequency 2.65 GHz. The gain and directivity has been increased to 11.64 dBi and 11.97 dB respectively. The radiation efficiency is -0.33 dB and the total efficiency is -0.88 dB. In E-plane, the polar plot shows that the main lobe magnitude is 11.5 dB and it offset 6^0 from its main direction, the side lobe level is -21.1 dB. In H-plane the main lobe magnitude is 11.8 dB and it offset 2^0 from its main direction, the angular width is 21^0, but the side lobe level is very high -2.2 dB.

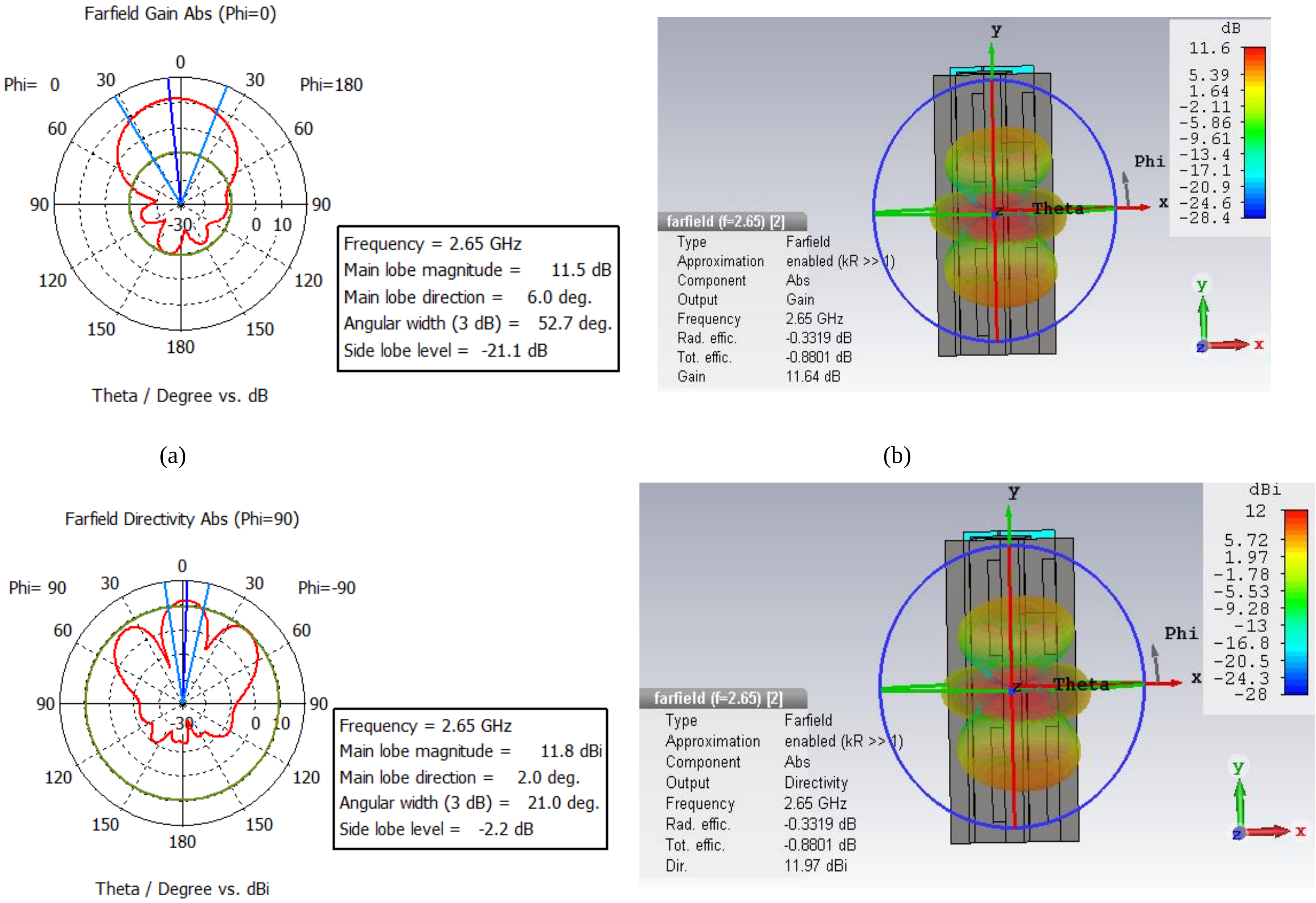

Frequency = 2.65 GHz
Main lobe magnitude = 11.5 dB
Main lobe direction = 6.0 deg.
Angular width (3 dB) = 52.7 deg.
Side lobe level = -21.1 dB

Type	Farfield
Approximation	enabled (kR >> 1)
Component	Abs
Output	Gain
Frequency	2.65 GHz
Rad. effic.	-0.3319 dB
Tot. effic.	-0.8801 dB
Gain	11.64 dB

(a)

(b)

Frequency = 2.65 GHz
Main lobe magnitude = 11.8 dBi
Main lobe direction = 2.0 deg.
Angular width (3 dB) = 21.0 deg.
Side lobe level = -2.2 dB

Type	Farfield
Approximation	enabled (kR >> 1)
Component	Abs
Output	Directivity
Frequency	2.65 GHz
Rad. effic.	-0.3319 dB
Tot. effic.	-0.8801 dB
Dir.	11.97 dBi

(c)

(d)

Fig (2. 39) Radiation pattern at 2.65 GHz: (a) E-plane, (b) 3D with gain, (c) H-plane, (d) 3D with directivity.

At the second order mode the electric field distribution is at 2.76 GHz as shown in Fig (2. 40) and the polar plot shown in Fig (2. 41). In E-plane, the main lobe magnitude is -4.73 dB and it offset 16^0 from its main direction, the side lobe level is -5.3 dB. In H-plane, the main lobe magnitude is 10.6 dB and it offset 16^0, the side lobe level is very poor -0.6 dB. The design 2 × 2 SSIW antenna has not been fabricated because the side lobe level is very poor although the gain is 10.48 dBi.

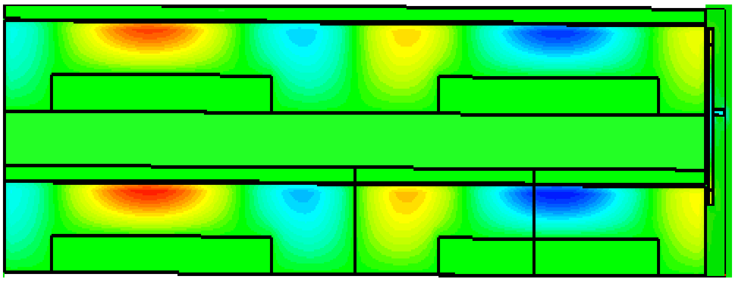

Fig (2. 40) E-field distribution at 2.76 GHz.

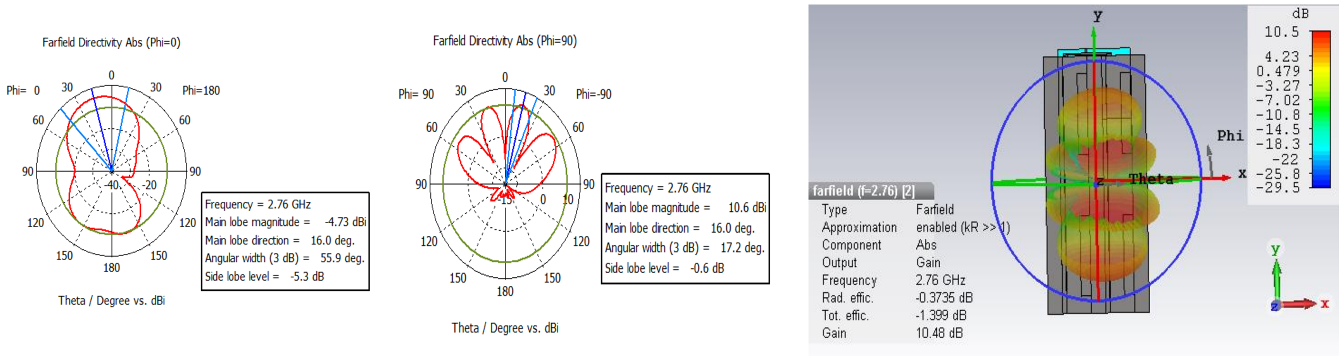

(a) (b) **(c)**

Fig (2. 41) Radiation pattern at 2.76 GHz: (a) E-plane, (b) H-plane, (c) 3D pattern.

Many parameters will affect the resonant frequency, matching, gain, radiation pattern and side lobe level (SLL). SLL is the major problem in arrays of antenna radiation pattern. SLL can be reduced by reducing the number of antenna elements, element spacing and window coefficient which affect array factor (AF) and can be considered as follows [20] :

$$AF = \sum_{i=0}^{N} a_i e^{(kd_i cos\theta + \emptyset_i)} \quad (2.\ 20)$$

Where N is the number of elements, a_i, $\emptyset_i$, k , d_i are the excitation amplitude, the excitation phase, the propagation constant for the i^{th} element and the inter-element spacing.

By increasing the number of elements, the side lobe level will reduce and the half power beam width (HPBW) will also decrease, whilst keeping the distance between the elements constant [19]

The distance between the elements should be close to 0.5 λ [14]. Fig (2. 42) shows a variation of distance changing from $\frac{\lambda}{2}$ up to $\frac{\lambda}{10}$ [15]. If the spacing is larger than $\frac{\lambda}{2}$, the side lobe level is very bad and in this design the spacing is $> \lambda/2$.

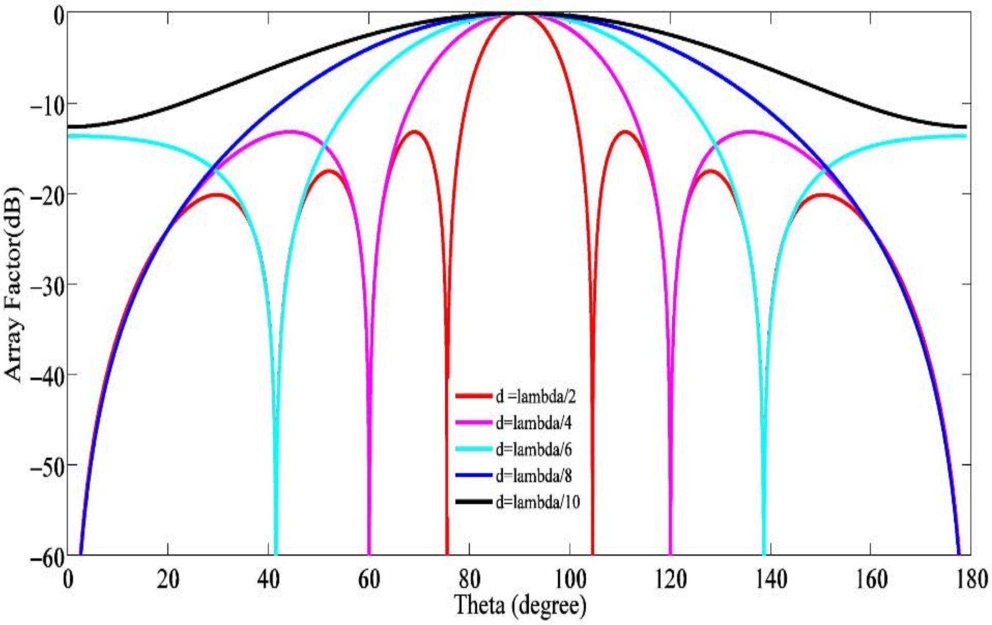

Fig (2. 42) Element spacing effect on array factor [19].

After many trials to enhance the design performance and reduce side lobe level, the design has not been fabricated because of the high side lobe level and low performance by radiating more than one direction.

2.7 Conclusion

A novel SSIW is designed to produce a high gain antenna operating at 2.5 GHz. If scaled to higher frequencies, the antenna may find use at future millimeter-wave frequencies as an antenna for SSIW structures.

Parametric variation of the design has been demonstrated with theoretical analysis for the single SSIW antenna design.

At single SSIW antenna, the measured gain was 4.5 dBi. A very good agreement between measurement and simulation is achieved for reflection coefficient, radiation pattern and gain.

To improve gain at the resonant frequency, a 1 × 2 SSIW array was investigated with challenging many variables to be adjusted. This was to obtain a better matching at the desired frequency. As a result, the gain has been increased to 9.8 dBi with poor side lobe level -2.5 dB. This is because of the bad side lobe level, the 1 × 2 SSIW array is not fabricated.

A 2 × 2 array was simulated for further increase in gain, the gain was 11.64 dBi with side lobe level -2.2 dB. Again, the design has not been fabricated because of the poor side lobe level.

The need for SSIW antenna is to integrate discrete devices along the slot. The narrow bandwidth of the slotted SIW can be useful in sensors.

2.8 References

[1] D. Stephens, P. R. Young, and I. D. Robertson, “Millimeter-wave substrate integrated waveguides and filters in photoimageable thick-film technology,” *IEEE Trans. Microw. Theory Tech.*, vol. 53, no. 12, pp. 3832–3838, Dec. 2005.

[2] D. Deslandes and K. Wu, “Integrated microstrip and rectangular waveguide in planar form,” *IEEE Microw. Wirel. Components Lett.*, vol. 11, no. 2, pp. 68–70, 2001.

[3] T. Li, W. Dou, and H. Meng, “A monopulse slot array antenna based on dual-layer substrate integrated waveguide (SIW),” *APCAP 2016 - 2016 IEEE 5th Asia-Pacific Conf. Antennas Propagation, Conf. Proc.*, pp. 373–374, 2017.

[4] W. Menzel and J. Kassner, “Millimeter-Wave 3D Integration Techniques using LTCC and Related Multilayer Circuits,” in *2000 30th European Microwave Conference*, 2000, pp. 1–4.

[5] R. F. Xu, A. J. Farrall, and P. R. Young, “Analysis of loaded substrate integrated waveguides and attenuators,” *IEEE Microw. Wirel. Components Lett.*, vol. 24, no. 1, pp. 62–64, 2014.

[6] K. Wu, “Towards system-on-substrate approach for future millimeter-wave and photonic wireless applications,” *Asia-Pacific Microw. Conf. Proceedings, APMC*, vol. 3, pp. 1895–1900, 2006.

[7] D. Deslandes and K. Wu, “Accurate Modeling, Wave Mechanisms, and Design Considerations of a Substrate Integrated Waveguide,” *IEEE Trans. Microw. Theory Tech.*, vol. 54, no. 6, pp. 2516–2526, 2006.

[8] R.S. Elliot, *Antenna Theory & Design*. 1976.

[9] R. S. Elliott, “An Improved Design Procedure for Small Arrays of Shunt Slots,” *IEEE Trans. Antennas Propag.*, no. 1, pp. 48–53, 1983.

[10] A. J. Farrall and P. R. Young, “Integrated waveguide slot antennas,” *Electron. Lett.*, vol. 40, no. 16, pp. 10–11, 2004.

[11] Y. Zhang, S. Member, Z. N. Chen, and X. Qing, “Wideband Millimeter-Wave Substrate Integrated Waveguide Slotted Narrow-Wall Fed Cavity Antennas,” *IEEE Trans. Antennas Propag.*, vol. 59, no. 5, pp. 1488–1496, 2011.

[12] P. Sánchez-olivares and J. L. Masa-campos, “Novel Four Cross Slot Radiator With Tuning Vias for Circularly Polarized SIW Linear Array,” *IEEE Trans. Antennas Propag.*, vol. 62, no. 4, pp. 2271–2275, 2014.

[13] L. Wu, A. J. Farrall, and P. R. Young, “Substrate Integrated Waveguide Switched Beam Antenna,” *IEEE Trans. Antennas Propag.*, vol. 63, no. 5, pp. 2301–2305, 2015.

[14] A. A. R. Saad and H. A. Mohamed, “Bandwidth Enlargement of a Low-Profile Open-Ring Slot Antenna Based on SIW Structure,” *IEEE Antennas Wirel. Propag. Lett.*, vol. 16, pp. 2885–2888, 2017.

[15] W. Hong, “Half Mode Substrate Integrated Waveguide- A New Guided Wave Structure for Microwave and Millimeter Wave Application.pdf,” *Proc. Jt. 31st Int. Conf. Infrared Millim. Waves 14th Int. Conf. Terahertz Electron*, vol. 152, p. 4244,

2006.

[16] D. H. Schaubert, “Chapter 6 Review of Microstrip Antenna Array Techniques,” vol. 132, pp. 433–439, 1989.

[17] E. Moldovan, R. G. Bosisio, L. Fellow, and K. Wu, “W -Band Multiport Substrate-Integrated Waveguide Circuits,” vol. 54, no. 2, pp. 625–632, 2006.

[18] C. A. Balanis, “Antenna {T}heory,” p. 959, 1997.

[19] S. Ur Rahman, Q. Cao, M. M. Ahmed, and H. Khalil, “Analysis of linear antenna array for minimum side lobe level, half power beamwidth, and nulls control using PSO,” *J. Microwaves, Optoelectron. Electromagn. Appl.*, vol. 16, no. 2, pp. 577–591, 2017.

[20] K. P. Sankar, T. Sieh Kiong, and J. Koh Siaw Paw, “Optimization of array pattern for efficient control of adaptive nulling and side lobe level,” *4th IEEE Conf. Commun. Networks Satell. COMNESTAT 2015 - Proc.*, pp. 16–21, 2016.

Chapter Three

Tri-band Substrate Integrated Waveguide Antenna

3.1 Introduction

Due to the rapid development of mobile communications, Wi-Fi and Bluetooth with 5G band (3-6 GHz), there is a huge demand to design a multiband and dual-band antennas. For example Wireless local area network (WLAN) operating at frequency range 5.2-5.8 GHz achieves a higher gain and a wider bandwidth.

This chapter will present some antenna designs that were developed to achieve a tri-band antenna. A single slot SIW with open circuit at the end of the waveguide was developed to achieve only one resonant frequency. Then by increasing the length of the slot and adding perpendicular sections to the slot, a tri-band antenna could be achieved.

The modes of each resonant frequency have been analysed. Additionally, parameters effect on resonant modes and matching was also demonstrated. As for the final design, this was fabricated by taking into account the use of simulation and measurement, comparing them side by side. For further enhancing of gain, a 2 × 2 SIW array was developed and fabricated.

3.2 Literature review

This section aims to discuss some relevant research related to our work on tri-band substrate integrated waveguide antenna.

In [1], a triangular planar inverted-F antenna with V-shaped slot is developed to have dual frequency characteristics. Different shorting-wall widths was studied and experimented, to allow dual band frequency operation, achieving impedance bandwidth of more than 30%. Fig (3. 1) shows the schematic structure of the proposed antenna.

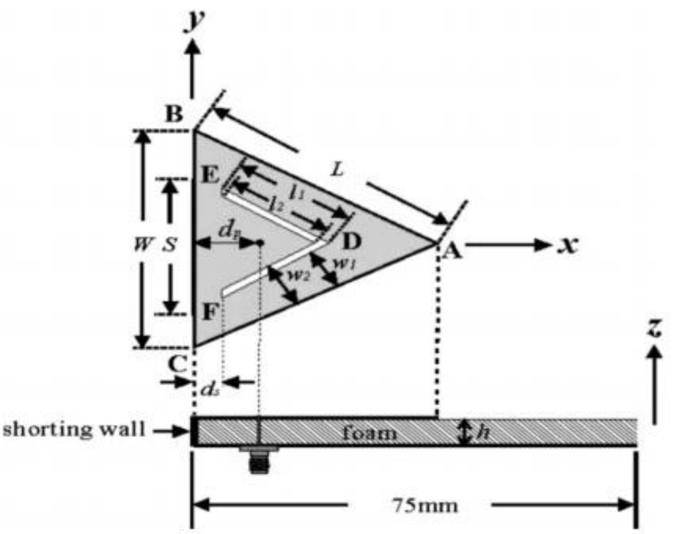

Fig (3. 1) Schematic diagram of triangular planer V-inverted antenna [1].

A dual band substrate integrated waveguide cavity backed planar slot antenna is presented in [2]. The main structure is a number of SIW cavities with various sizes that connect to each other through a window in the sidewall of the cavities. A Bow–tie shaped slots are loaded to give increased bandwidth and placed such that they can be easily tuned to generate hybrid modes. The range of the operating frequency is (8-12 GHz) and the antenna achieved a gain of 5.3 dBi and 4.4 dBi. Fig (3. 2) shows the main structure of the bow tie shaped slot of the cavity backed planar slot antenna.

.

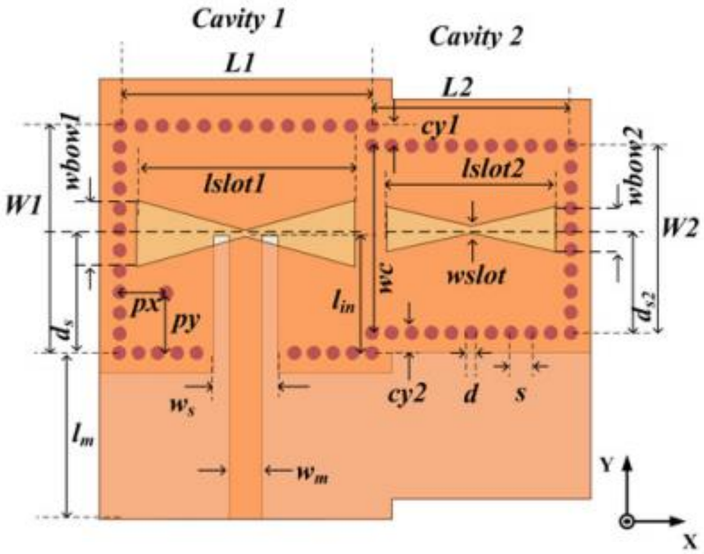

Fig (3. 2) Dual band Bow-tie slot antenna [2].

Another dual band substrate integrated waveguide slot antenna is designed with two slots combined in a L-shape [3]. As shown in Fig (3. 3) the structure uses a slot oriented longitudinal with center frequency 13.28 GHz and transverse slot with 10.25 GHz center frequency. These two slots achieved dual band with frequency range 10.84 GHz to 11 GHz and 12.6 GHz to 12.78 GHz.

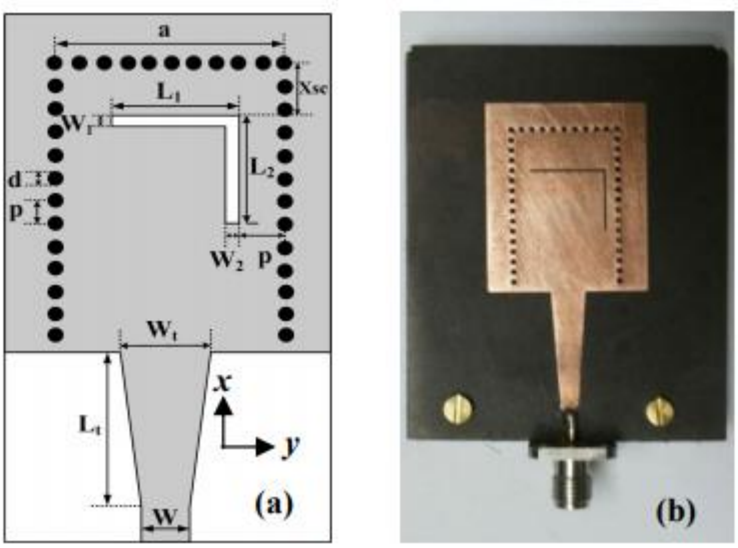

Fig (3. 3) L-shaped slot SIW: (a) proposed, (b) structure [3].

In [4], a dual band, dual polarization leaky-wave antenna was developed which is excited by slotted substrate integrated waveguide. As shown in Fig (3. 4), the top plane of SIW is etched with periodic transverse slots to achieve leaky mode radiation by interrupting current flow. The bottom plane is loaded with circular slots to convert slow mode that excited by slotted SIW to fast-wave mode. This antenna has dual-band 9-10.7 GHz and 13.4-16.2 GHz.

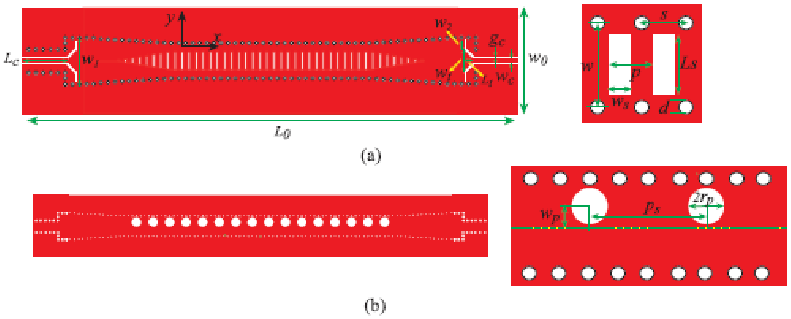

Fig (3. 4) Leaky- wave antenna: (a) Transverse slots on top, (b) circular slots on bottom [4].

A compact self-duplexing antenna using substrate integrated waveguide dual mode is presented in [5]. A square cavity with rectangular ring slot is used for excitation and radiation of dual mode as shown in Fig (3. 5). The dual resonant frequencies are 9.5 and 10.5 GHz, whilst the intermodal coupling enhances the port isolation by achieving greater than 29 dB. Respectively, the measured gain at the two resonant frequencies are 5.75 dBi and 5.95 dBi.

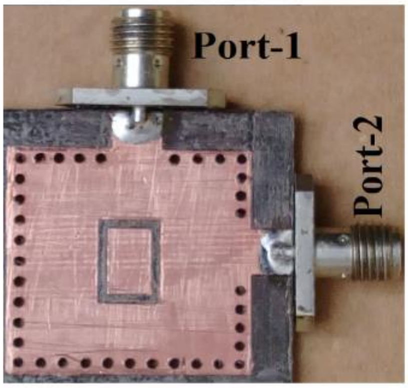

Fig (3. 5) Fabricated structure of self- duplexing antenna [5].

All the previous structures have some disadvantages. For instance, ref [2] has a complex structure (large cross polarization and low gain), whilst in ref [3], the L-shape antenna has a narrow bandwidth. Similarly, ref [4] is also a complex structure (large and dual polarization), whilst ref [5] has low gain. The design proposed here is a simple structure that is used as a tri-band antenna. In addition, the design has the possibility to tuning the resonant frequency by adding sections of the slots to the structure.

3.3 Proposed SIW slot antenna designs

Some SIW antenna designs have been developed and their characteristics studied. For instance, the return loss, radiation pattern and gain were studied until we reached our final proposed design of a tri-band SIW antenna. These will be discussed in the following sections.

3.3.1 SIW single slot antenna design with L_1=20 mm.

This design has been simulated using microwave studio CST. As shown in Fig (3. 6), the waveguide width from vias to vias a = 25 mm, the slot has a length of L_2 = 20 mm, width of 0.5 mm and it is offset by the vias of the waveguide with W_1 = 9 mm . Additionally, the length of the waveguide has been set to L=50 mm and the substrate has a thickness (b) of 0.787 mm, $\varepsilon_r = 2.2$, with the micro strip transmission line matching 50 Ω with L_3 = 9 mm, F =4.5 mm and L_4 = 10 mm.

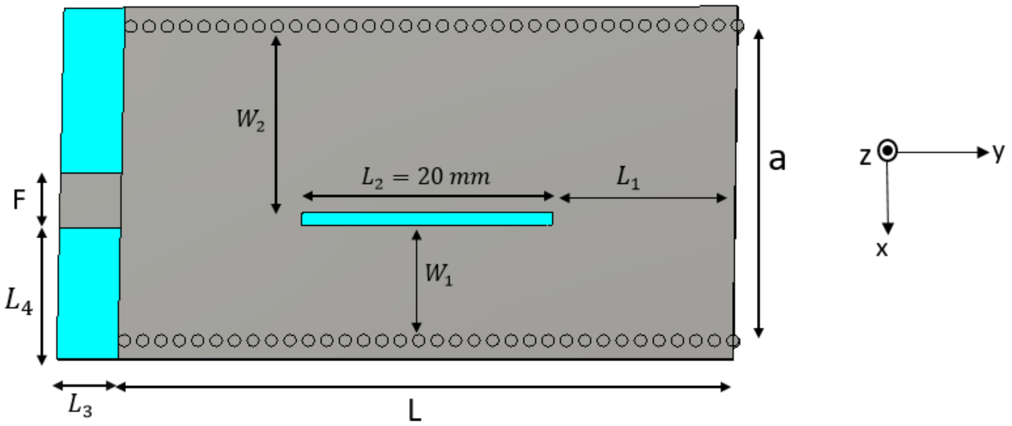

Fig (3. 6) Proposed SIW slot antenna.

This antenna differs from a conventional design by being terminated in an open circuit. This open circuit does not radiate very much due to the SIW implementation.

If we assume the open end of the structure, by a two dimensions of k_y in free space and k_x for the width of the waveguide as shown in Fig (3. 7)

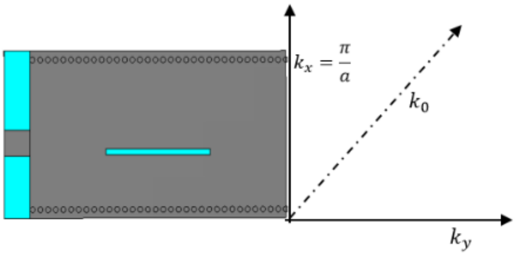

Fig (3. 7) Coordinates at the open end of SIW.

$$k_y = \sqrt{k_0^2 - (\frac{\pi}{a})^2} \tag{3. 1}$$

where

k_0 the cut off wavenumber at the open end of SIW.

k_y the wavenumber radiation in free space.

k_x the wavenumber for the width of SIW.

To radiate at the open end of SIW, this condition must be satisfied

$$k_y > 0$$

When $k_0 > \frac{\pi}{a}$

$$\frac{2\pi f}{c} > \frac{\pi}{a}$$

$$f = \frac{\pi c}{2\pi a}$$

$$f = \frac{c}{2a}$$

When:

The width of SIW is a =25 mm, so that the frequency is 6 GHz.

This means that until the frequency reaches 6 GHz, it will radiate at the open end termination.

As shown in Fig (3. 8), the return loss at the resonant frequency 6.4 GHz is approximately -18 dB. This means that only 1% of the power is reflected back to the power from the antenna. The ripples that are shown for the range 3-3.6 GHz is due to the inaccuracy in the time domain simulation of CST.

The field pattern inside the waveguide, for each mode is shown in Fig (3. 9). At 3.9 GHz (mode 1) the electric field distribution occurs at the widest section of the waveguide W_2. At 5.38 GHz is the second order mode in the wider section (labelled mode 3 for consistency with later sections). However, mode 1 and mode 3 are poor matched.

Mode 4, shown in Fig (3. 9 c), occurs at approximately 6.4 GHz and is the first order resonance of the narrow W_1 section. This occurs someway above the cut-off of the narrower W_1 section. The resonant modes will be described in detail in the following section (sec 3.2.2).

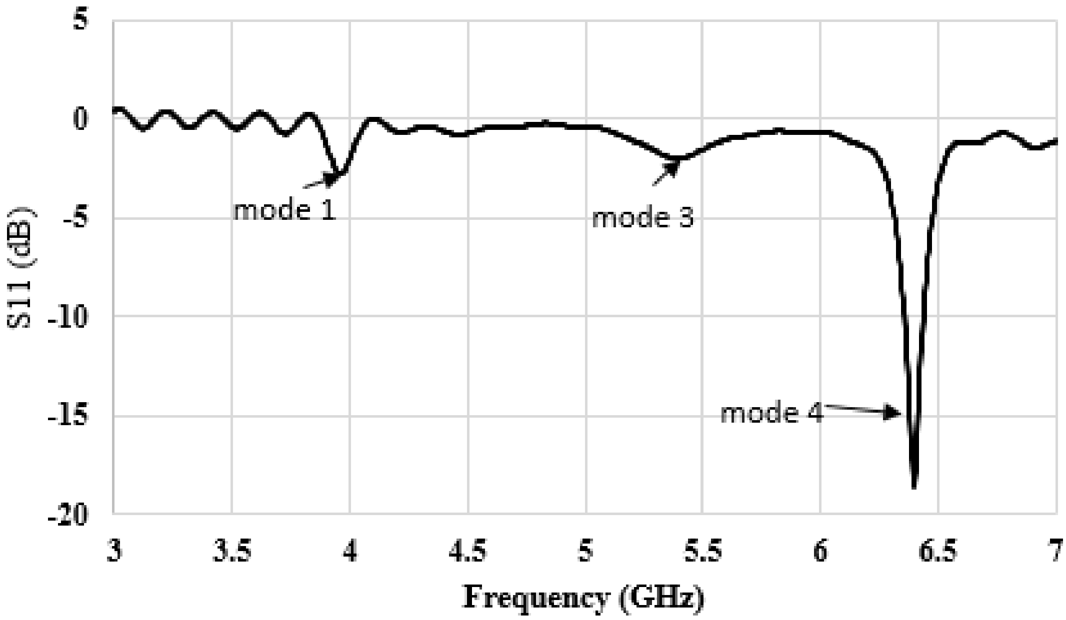

Fig (3. 8) S_{11} versus frequency for the proposed SIW slot antenna ($L_2 = 20\ mm$).

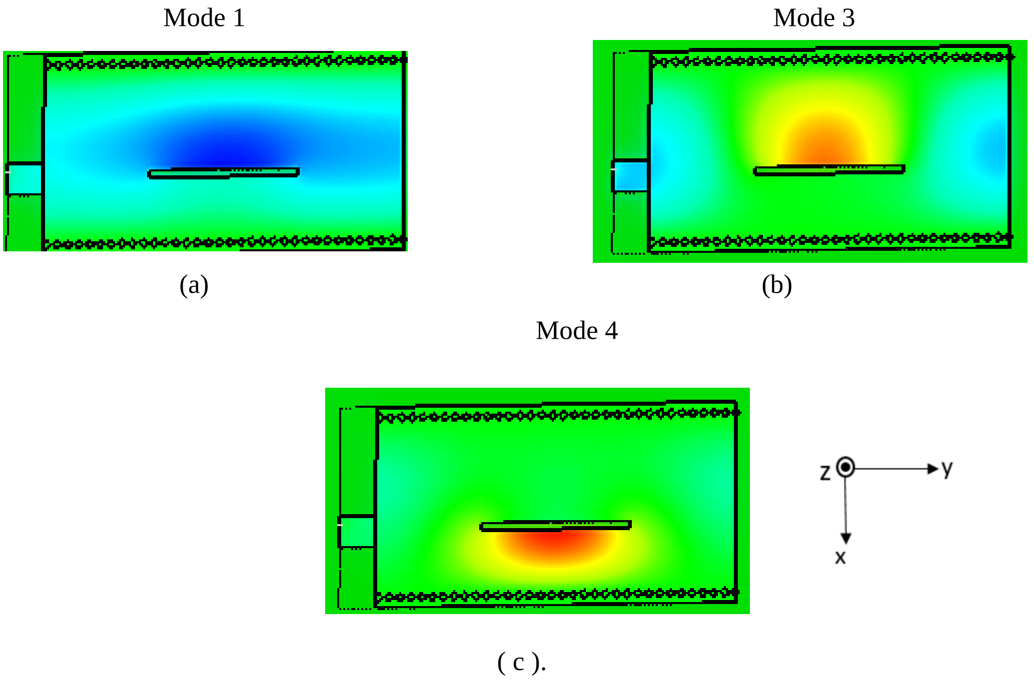

Fig (3. 9) Electric field distribution at: (a) 3.94 GHz (Mode 1). (b) 5.38 GHz (Mode 3). (c) 6.4 GHz (Mode 4).

The far-field radiation pattern at the resonant frequency 6.4 GHz is shown in Fig (3. 10). The radiation efficiency and the total efficiency is -0.5 and -0.9 dB. Thereby, the difference between radiation and total efficiency is 0.4 dB, indicating that the loss is due to impedance mismatch low which has been proven by the corresponding S_{11}. The gain observed to be 5.94 dB in the 3D far field and in the H-plane the main lobe magnitude is 5.57 dB. The reason for this difference of gain is because in 3D the maximum gain is determined with the whole radiation surrounding the antenna, while in polar plot the gain determined at the main lobe direction is offset from zero degree. In H-plane, the angular width is 91.7 degree and the side lobe level is -10.2 dB.

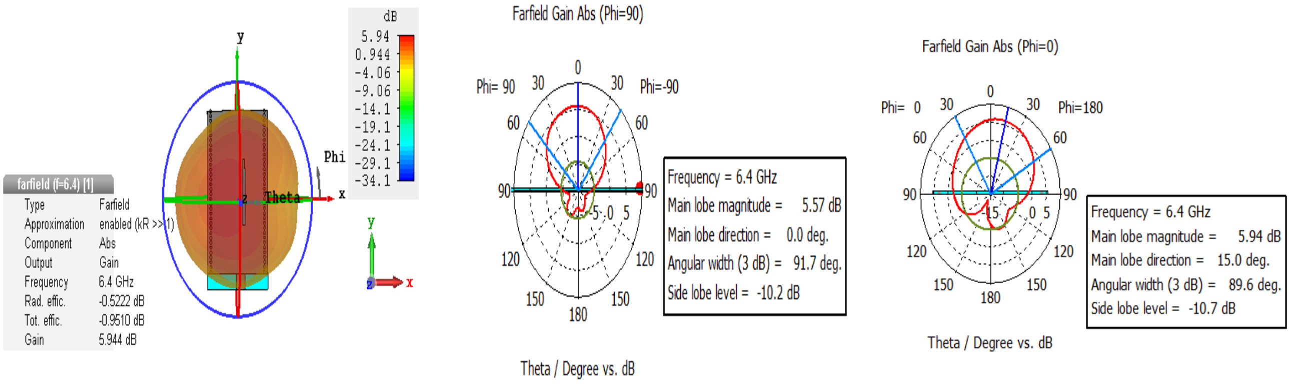
farfield (f=6.4) [1]
Type Farfield
Approximation enabled (kR >> 1)
Component Abs
Output Gain
Frequency 6.4 GHz
Rad. effic. -0.5222 dB
Tot. effic. -0.9510 dB
Gain 5.944 dB

Frequency = 6.4 GHz
Main lobe magnitude = 5.57 dB
Main lobe direction = 0.0 deg.
Angular width (3 dB) = 91.7 deg.
Side lobe level = -10.2 dB

Frequency = 6.4 GHz
Main lobe magnitude = 5.94 dB
Main lobe direction = 15.0 deg.
Angular width (3 dB) = 89.6 deg.
Side lobe level = -10.7 dB

(a) (b) (c)

Fig (3. 10) Radiation pattern at 6.4 GHz: (a) 3D pattern, (b) H-plane, (c) E-plane.

3.3.2 Increasing slot length to improve matching ($L_2 = 40\ mm$)

The length of the slot has been increased to 40 mm to improve matching as shown in Fig (3.11). In comparison with the previous design which held a width waveguide of 25 mm, $W_1 = 9\ mm$, $L_1 = 5\ mm$. The other parameters remain the same. The micro strip transmission line matches 50 Ω with width F = 4.5 mm, $L_4 = 5\ mm$.

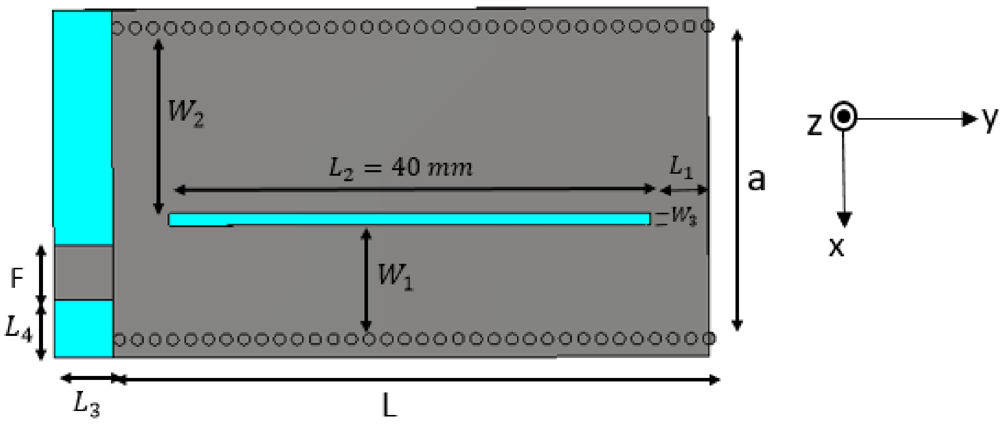

Fig (3. 11) The proposed structure by increasing slot length ($L_2 = 40\ mm$).

The return loss against the frequency shown in Fig (3. 12), there are five resonant modes for the range 3-7 GHz. Mode 1, Mode 3 and mode 4 are well matched and are below 10 dB which result in a tri-band antenna.

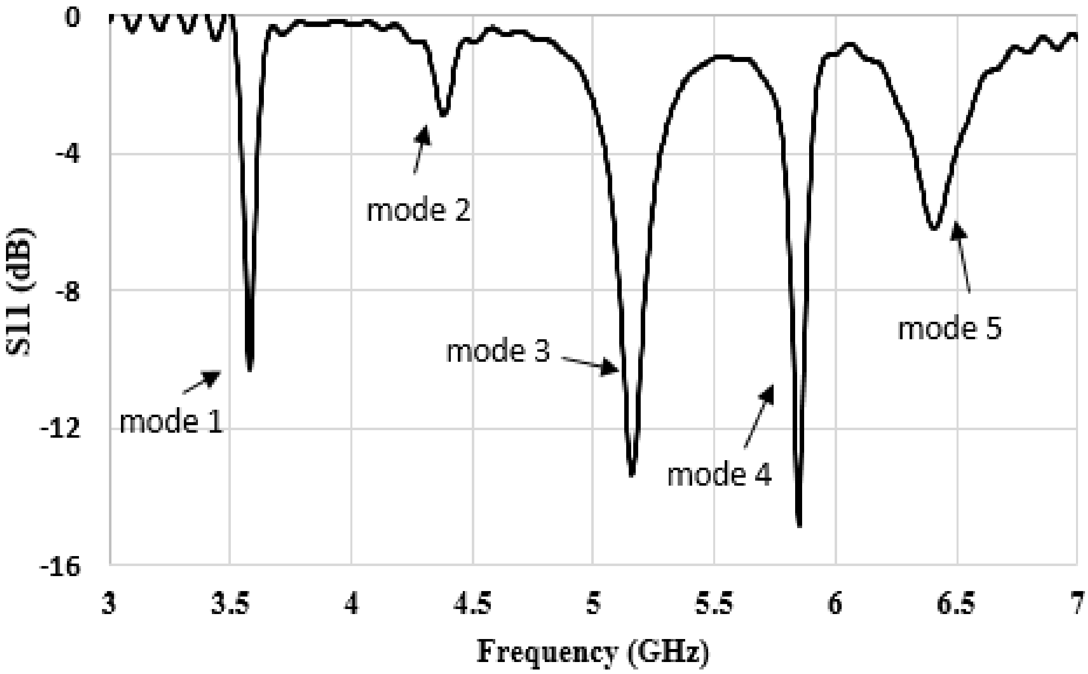

Fig (3. 12) Return loss against frequency for the proposed structure (after increasing slot length $L_2 = 40\ mm$).

To understand the design working in tri band resonant modes better, a diagram of Fig (3. 13) shows that the waveguide can be considered as two regions; one of width W_1 and the other of width W_2. Assuming that the ‘power dividing’ networks do not have any phase shift then the resonant condition will be.

$$\beta(a)L_1 + \beta(W_2)L_2 = n\pi \tag{3. 2}$$

$$\beta(a)L_1 + \beta(W_1)L_2 = n\pi \tag{3. 3}$$

Fig (3. 14) shows all the radiating modes inside the waveguide**.** The nature of the resonant modes can be described qualitatively by considering the slotted region, of length L_2, to be two half mode waveguides[6] that support $TE_{1/2,0}$ type modes.

The slotted region forms a slotted SIW structure that supports hybrid modes [7]. However, since the coupling between the two sections is weak, the modes are well described by the two $TE_{1/2,0}$ modes [8].

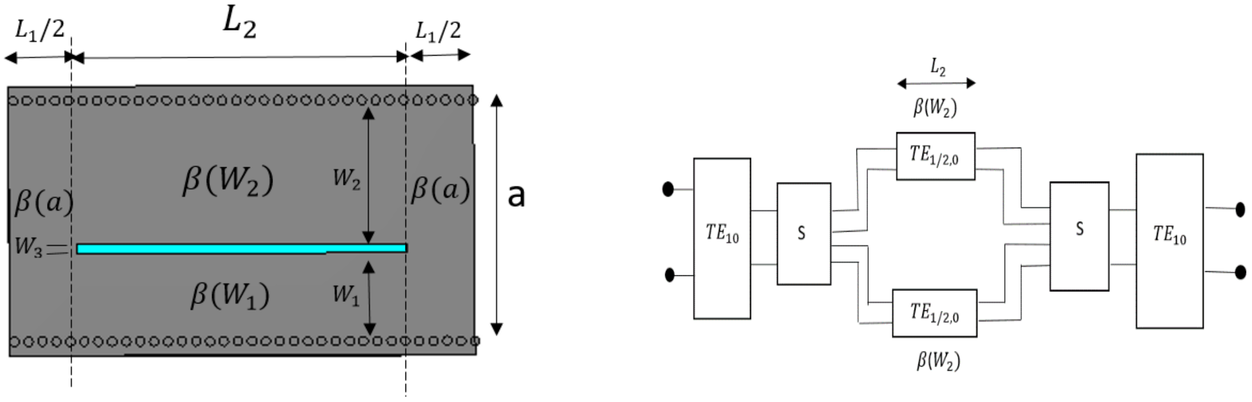

(a) (b)

Fig (3. 13) Tri-band SIW structure divided into two half modes of the waveguide: (a) Design, (b) Equivalent network

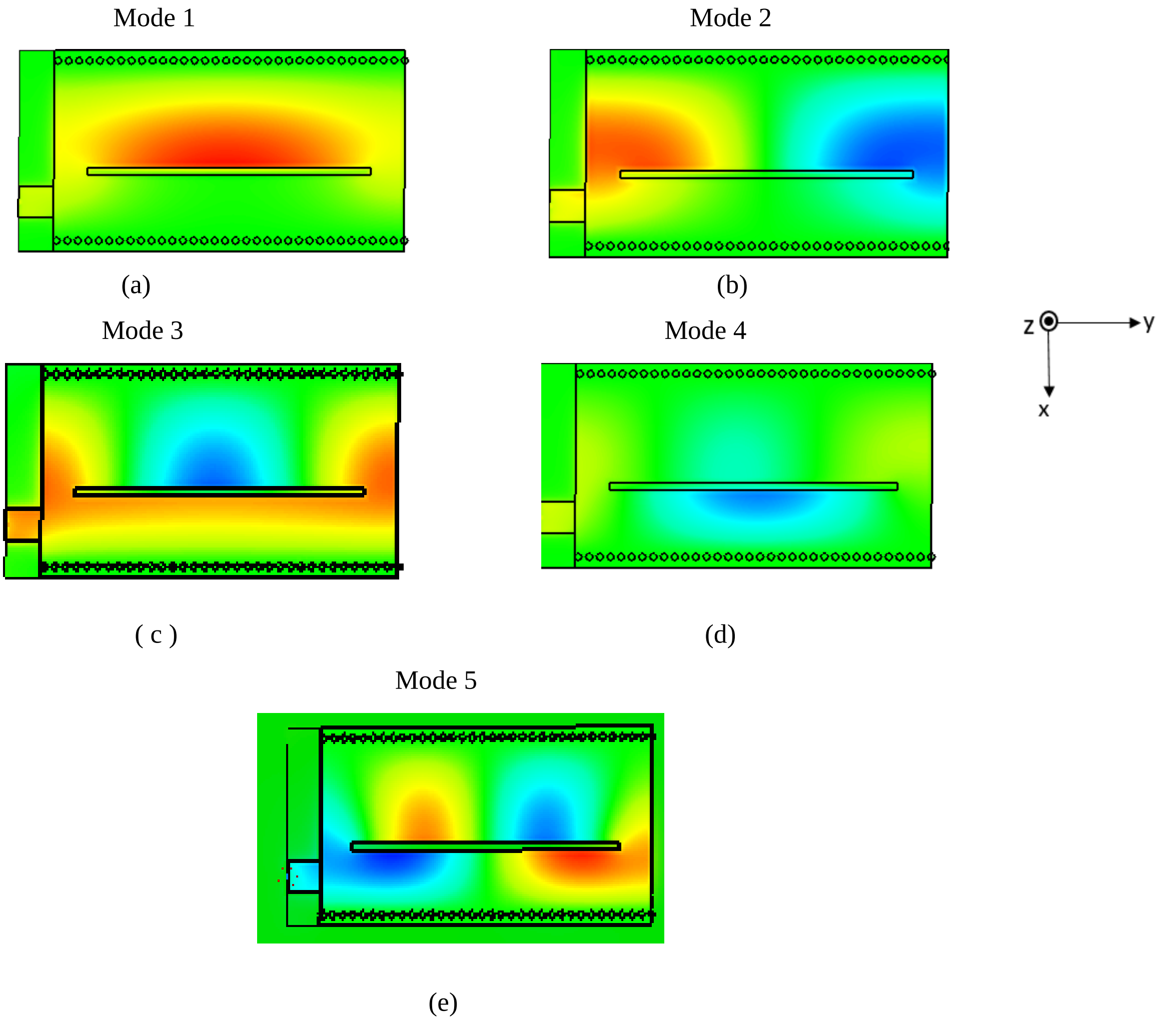
Mode 1

Mode 2

(a)

(b)

Mode 3

Mode 4

(c)

(d)

Mode 5

(e)

Fig (3. 14) Electric field distribution at: (a) 3.57 GHz (Mode 1). (b) 4.38 GHz. (Mode 2). (c) 5.163 GHz (Mode 3). (d) 5.85 GHz. (Mode 4). (e) 6.43 GHz. (Mode 5).

Therefore, the cut-off frequencies of the two sections are given approximately by:

$$f_{W_n} = \frac{c}{4W_n\sqrt{\varepsilon_r}} \tag{3. 4}$$

Where:

n=1 for the narrower section, of width W_1

n=2 for the wider section, of width W_2

c the speed of light in vacuum

ε_r the relative permittivity of the substrate.

Since $W_1 = a\text{-}W_2\text{-}W_3$ the cut-off frequencies are interrelated. The cut-off frequency of the TE_{10} SIW mode is:

$$f_a = \frac{c}{2a\sqrt{\varepsilon_r}} \tag{3. 5}$$

Where:

a the width of the waveguide.

For the dimensions given, f_{w_1} =5.6 GHz, f_{w_2}= 3.3 GHz and f_a = 4.0 GHz.

It is useful to consider the normalised propagation constant in the different regions of the waveguide structure. This can be thought of as a conventional SIW of width (a) and the left and right ends of the structure and a slotted SIW in the middle of the structure formed by the slot

$$\beta(a) = \sqrt{\varepsilon_r k_0^2 - (\frac{\pi}{a})^2} \tag{3. 6}$$

To understand each mode of Tri-band SIW, using Matlab Fig (3. 15), this shows all the modes at the graph with their equations.

Mode 1 as shown in Fig (3. 14) occurs at approximately 3.5 GHz and is similar to the usual slot mode resonance of a SIW waveguide [9]– with fields concentrated in the wider section. However, it differs in this implementation by the fact that the SIW of width *(a)* is below cutoff at 3.5 GHz. Since the feed sections are very short, the mode is still excited from the microstrip feed line by the evanescent waves on the SIW.

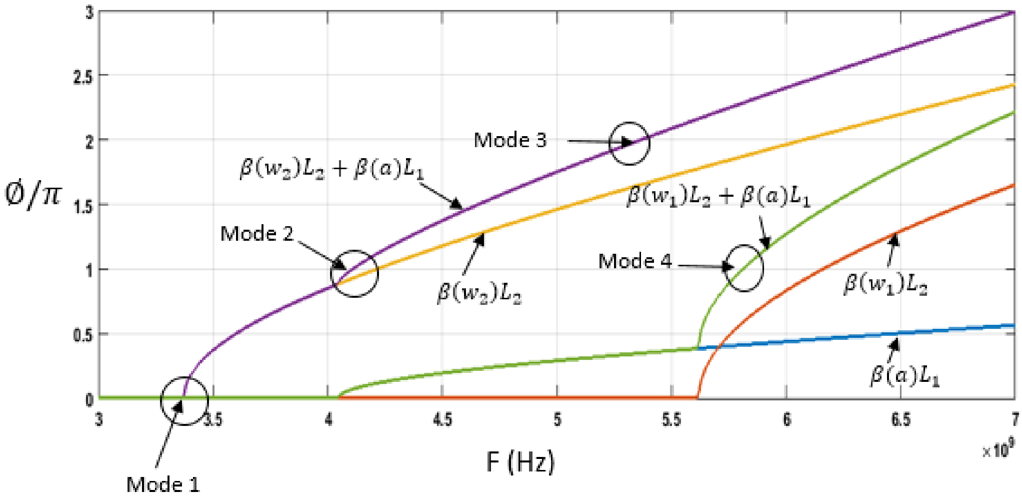

Fig (3. 15) Normalised phase shift $\frac{\emptyset}{\pi}$ along the structure showing the resonant modes of tri-band antenna using matlab.

The field in the slotted section is concentrated in the wider section (W_2) and varies a little along its length. This is because the wider W_2 section has a cut-off frequency of approximately 3.4 GHz for the dimensions of the structure. Therefore, the resonance occurs only slightly above the cut-off of the wider section and as a result, the phase variation along the guide is slow.

We note that there is no field in the narrower slotted section since the mode of this region is well below cut-off. Due to the evanescent nature of the field in the SIW section, this resonance is of the same form as that of a dielectric resonator (standing wave with two evanescent ‘tails’). We note that the mode can only exist if the SIW is below cut-off. The length from the end of the waveguide to the slot is kept short and an open boundary terminates the SIW. Mode 1 shown in Fig (3. 15) occurs around the cutoff or W_2 section.

$$\beta(W_2)L_2 \approx 0 \tag{3. 7}$$

Mode 2 occurs at approximately 4.3 GHz as shown in Fig (3. 14) and corresponds to the first order resonance of the wider section. At this frequency, the SIW is just above cut off (fa = 4 GHz) and therefore there is little phase variation in SIW feed region. Once again, the narrower section is below cutoff frequency and therefore there is no field present in the narrower section. With a short circuit termination at the end of the guide, this mode would be the conventional slot mode of an SIW [10]. However, the open termination ensures odd symmetry for this mode in the longitudinal direction. As a result, the corresponding radiation pattern of this resonance has two lobes and is probably of little practical use, this mode is also poorly matched and is not considered further in this work.

The following equation approximately describes the resonant condition as shown in Fig (3. 15)

$$\beta(a)L_1 + \beta(W_2)L_2 \approx \pi \tag{3. 8}$$

Mode 3 as shown in Fig (3. 14), occurs at approximately 5.2 GHz and is the second order resonance in the wider W_2 section. For careful selection of W_2 (and therefore W_1) this resonant frequency can be set to coincide with the cutoff frequency of the narrower W_1 section creating a zero-order type resonance in the narrower W_1 section. The narrower section is slightly below the cutoff frequency of f_{w_1}= 5.3 GHz. The field in the narrower region is therefore evanescent in nature. However, the resonance occurs only slightly below the cutoff frequency and therefore the attenuation constant is very small and the field remains approximately constant along the length of the slotted region. The evanescent waves in the narrower region are fed from both ends causing a hyperbolic cosine variation along the W_1 region. This can be seen by a small reduction in the field at the centre of the narrower section. This mode only exists for careful selection of W_1 and the length L_1 and L since the second order resonance of the structure must coincide with the cutoff of the narrower section. Furthermore, it requires the SIW to be terminated in an open boundary to ensure the zero-order resonance is fed uniformly from both ends.

The equation that supports Mode 3 and shown in Fig (3. 15):

$$\beta(a)L_1 + \beta(W_2)L_2 \approx 2\pi \tag{3. 9}$$

$$\beta(W_1)L_2 \approx 0 \tag{3. 10}$$

Mode 4, shown in Fig (3. 14 d), occurs at approximately 5.8 GHz and is the first order resonance of the narrow W_1 section. This occurs someway above the cut-off of the narrower W_1 section. The field patterns of both Mode 3 and 4 are relatively similar and result in similar radiation patterns. By careful tuning of the relative frequency of Mode 3 and 4 either dual or broad-band performance can be achieved. In addition, Mode 1 allows the antenna to work as a tri-band antenna.

The equation that support Mode 4

$$\beta(W_1)L_2 + \beta(a)L_1 = \pi \tag{3. 11}$$

Mode 5, as shown in Fig (3. 14 e) has odd symmetry and therefore a dual lobed radiation pattern. It is not considered in our study of tri-band antenna.

We can see from the Fig (3. 14) that single slot SIW radiate in tri-band resonant frequency 5.163 GHz, 5.85 GHz and 3.5 GHz. Fig (3. 16) shows the radiation pattern at 5.163 GHz in

3D. Respectively, the radiation efficiency and total efficiency is -0.3 dB and -0.5 dB. The main lobe magnitude is 6.95 dB and it offsets 1^0 from its main direction . The angular width is $67^0$and have side lobe level of -9.6 dB. The gain at 5.16 GHz is 6.99 dBi

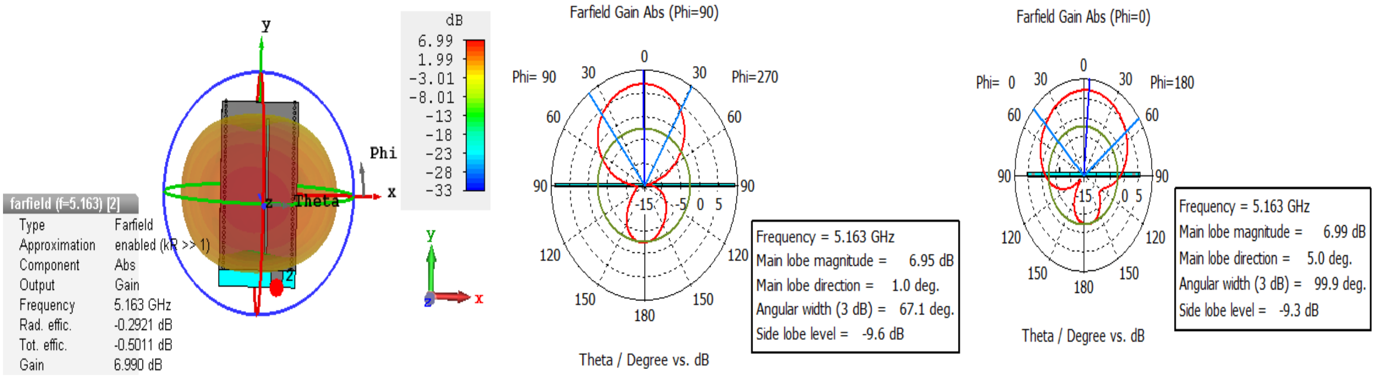

farfield (f=5.163) [2]
Type Farfield
Approximation enabled (kR >> 1)
Component Abs
Output Gain
Frequency 5.163 GHz
Rad. effic. -0.2921 dB
Tot. effic. -0.5011 dB
Gain 6.990 dB

Frequency = 5.163 GHz
Main lobe magnitude = 6.95 dB
Main lobe direction = 1.0 deg.
Angular width (3 dB) = 67.1 deg.
Side lobe level = -9.6 dB

Frequency = 5.163 GHz
Main lobe magnitude = 6.99 dB
Main lobe direction = 5.0 deg.
Angular width (3 dB) = 99.9 deg.
Side lobe level = -9.3 dB

(a) (b) (c)

Fig (3. 16) Radiation plot at 5.163 GHz: (a) 3D pattern, (b) H-field, (c) E-field.

The second resonant frequency is found at 5.85 GHz, as shown in Fig (3. 17) the radiation efficiency and total efficiency is -0.7 dB and -0.9 dB respectively. As shown in polar plot (H-plane), the main lobe magnitude is 5.91 dB, the radiation is offset 12^0 from its main direction due to it being unsymmetrical. The angular width is 76.8^0 and the sidelobe level is -11 dB.

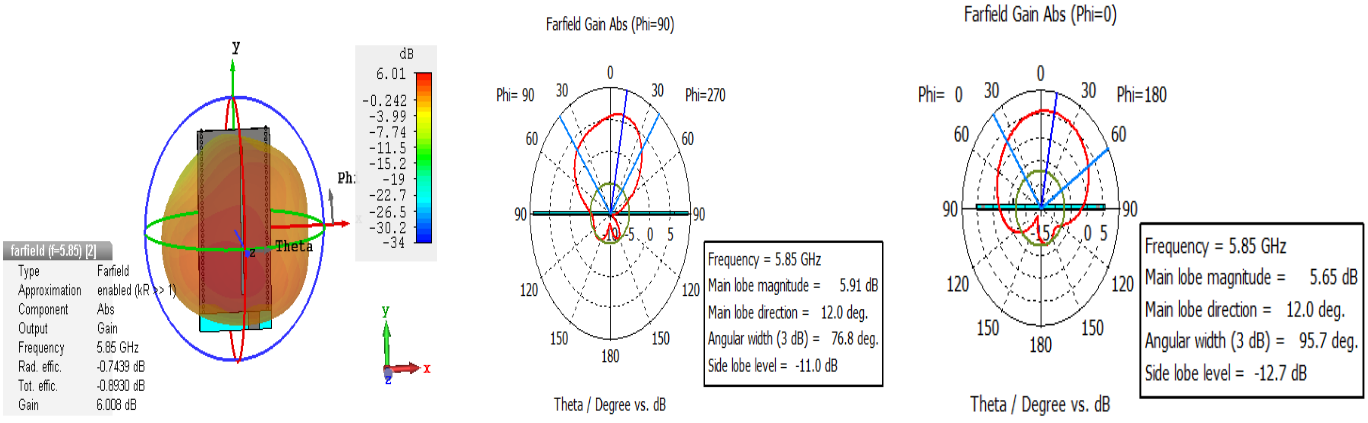

farfield (f=5.85) [2]
Type Farfield
Approximation enabled (kR >> 1)
Component Abs
Output Gain
Frequency 5.85 GHz
Rad. effic. -0.7439 dB
Tot. effic. -0.8930 dB
Gain 6.008 dB

Frequency = 5.85 GHz
Main lobe magnitude = 5.91 dB
Main lobe direction = 12.0 deg.
Angular width (3 dB) = 76.8 deg.
Side lobe level = -11.0 dB

Frequency = 5.85 GHz
Main lobe magnitude = 5.65 dB
Main lobe direction = 12.0 deg.
Angular width (3 dB) = 95.7 deg.
Side lobe level = -12.7 dB

(a) (b) (c)

Fig (3. 17) Radiation pattern at 5.85 GHz: (a) 3D pattern, (b) H-plane, (c) E-plane.

Mode 1 at 3.57 GHz as shown in Fig (3. 18), the radiation efficiency is -2.1 dB and the total efficiency is -2.67 dB, the gain is 3.619 dB. This is lower than Mode 3 and Mode 4 due to the less match in S-parameter. In polar plot, the main lobe magnitude is 3.63 dB and it offsets 3^0 from its main direction and the side lobe level is -6.2 dB.

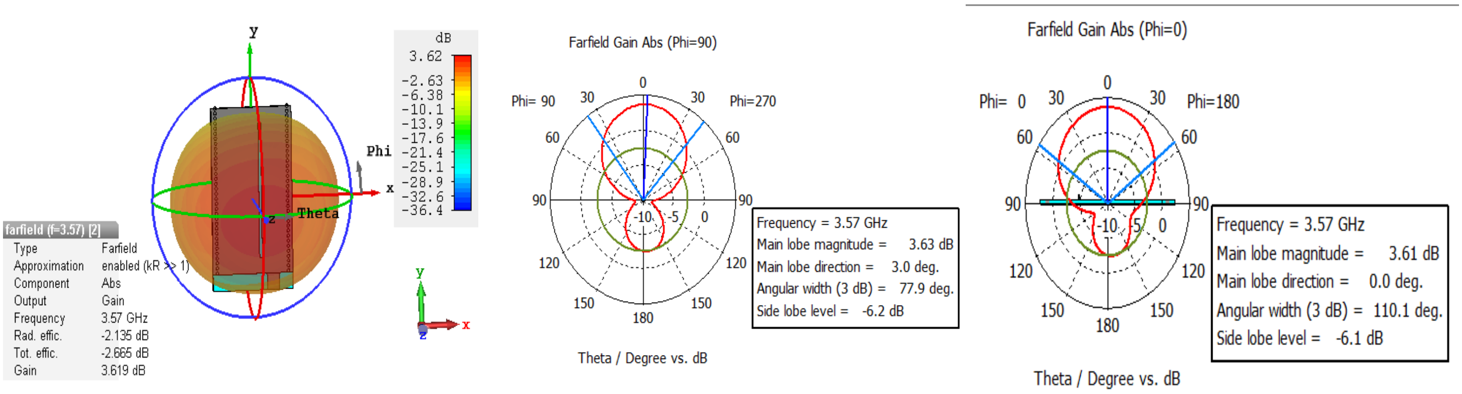

farfield (f=3.57) [2]

Type	Farfield
Approximation	enabled (kR >> 1)
Component	Abs
Output	Gain
Frequency	3.57 GHz
Rad. effic.	-2.135 dB
Tot. effic.	-2.665 dB
Gain	3.619 dB

Frequency = 3.57 GHz
Main lobe magnitude = 3.63 dB
Main lobe direction = 3.0 deg.
Angular width (3 dB) = 77.9 deg.
Side lobe level = -6.2 dB

Frequency = 3.57 GHz
Main lobe magnitude = 3.61 dB
Main lobe direction = 0.0 deg.
Angular width (3 dB) = 110.1 deg.
Side lobe level = -6.1 dB

(a) (b) (c)

Fig (3. 18) Radiation pattern at 3.57 GHz: (a) 3D pattern, (b) H-plane, (c) E-plane.

At 4.38 GHz, the return loss was poor and not in our consideration. However, as shown in Fig (3. 19), the radiation efficiency and total efficiency is -2.8 dB and -5.9 dB respectively. The gain at 4.38 GHz is 3.44 dBi. In polar plot, the main lobe magnitude is 3.42 dB and has a direction of 10^0 from its main lobe. The side lobe level is -2.5 dB with angular width 43^0. This mode has a strange pattern that we are not interested in.

At 6.43 GHz (Mode 5), is also not in our consideration in tri-band antenna, because of its odd symmetry. However, Fig (3. 20) shows that the radiation pattern in H-plane, radiates in two directions. The gain at 6.43 GHz is 6 dB, the radiation efficiency and total efficiency is -0.5 and -1.8 dB respectively.

This antenna with single slot is terminated with an open circuits and can achieve tri-band performance. Unfortunately, there is a limited freedom to tune the resonant frequencies. The next section is to modify the antenna so that it has the ability for tuning the resonant frequency.

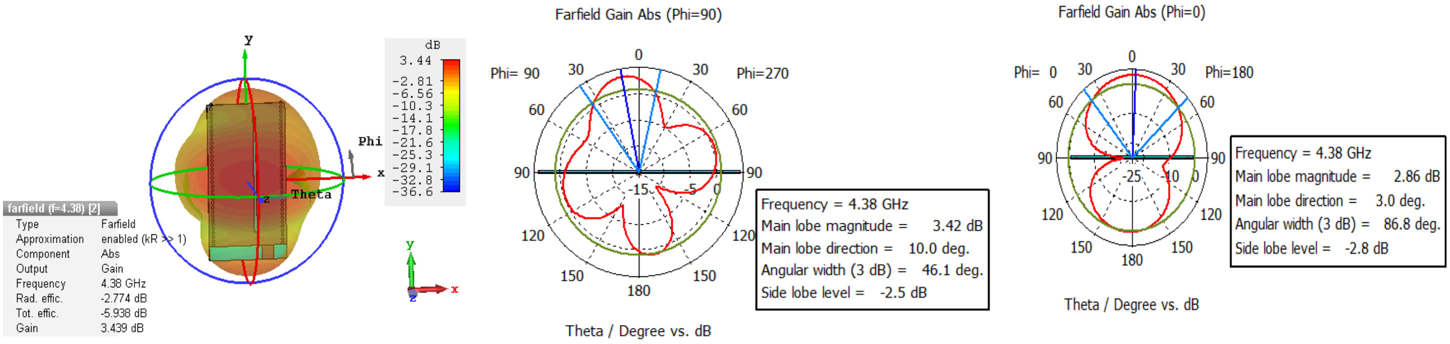

(a) (b) (c)

Fig (3. 19) Radiation pattern at 4.38 GHz: (a) 3D pattern, (b) H-plane, (c) E-plane.

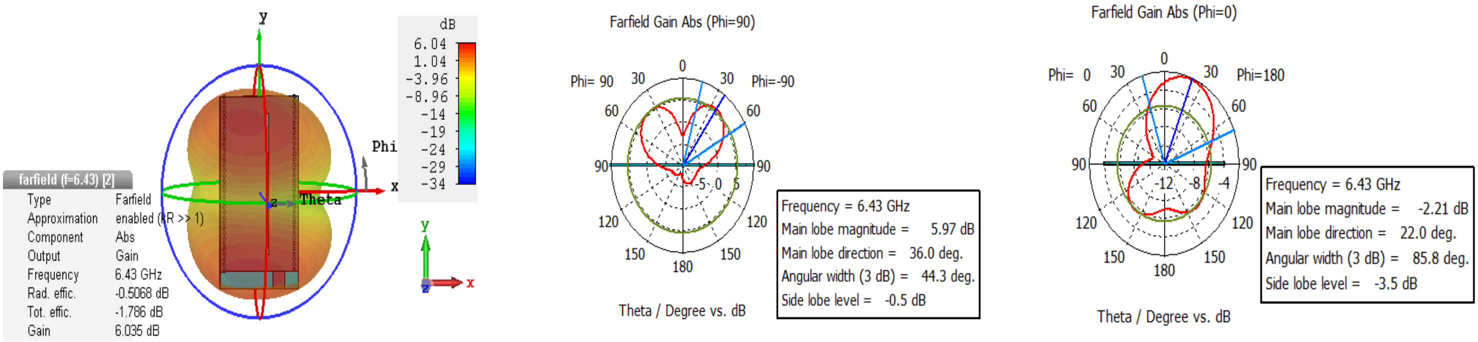

Fig (3. 20) Radiation pattern at 6.43 GHz: (a) 3D pattern, (b) H-plane, (c) E-plane.

3.3.3 Adding sections of the slot to the two ends of the main slot in the direction of the wider section of SIW

Fig (3. 21) shows the structure of the antenna, which resembles a conventional slot antenna of length L_1 but with additional sections of the slot of length L_2 perpendicular at the two ends of the slot. These sections are added to give additional freedom in the tuning of the device.

The proposed structure as shown in Fig (3. 21) is the same as the structure in previous section 3.2.2 with addition of perpendicular slots of length $L_2 = 6\,\text{mm}$ to the two ends of the conventional slot of length $L_1 = 40$ mm. These slots of length L_2 were added to the direction of the widest section W_2. The width of the waveguide a =25 mm from vias to the vias. $W_1 =$ 9 mm. The thickness of substrate is 0.787 mm.

The microstrip transmission line matches 50 Ω with length $L_3 = 5$ mm, $L_4 = 5$ mm and F = 4.5 mm.

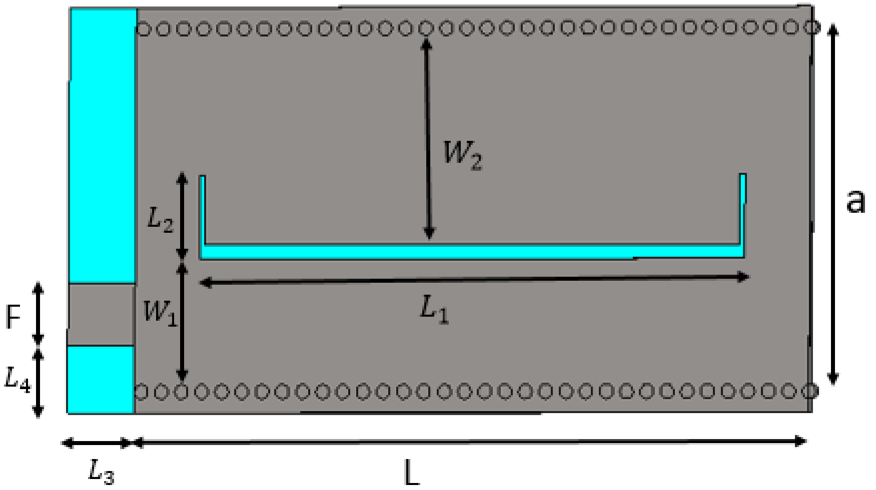

Fig (3. 21) Adding slots of length L_2 at the direction of the widest section of SIW.

As shown in Fig (3. 22), if we compare the modes of this design with the modes of the previous design in section 3.2.2, all the modes does exist, except the mode 4 at frequency of 5.52 GHz which has disappeared from this design. The reason for that, L_2 sections stop the second order resonance in the top section and L_1 not long enough to support second order resonance.

The return loss for the proposed antenna has resonant frequency at 5.11 GHz. The return loss at 5.11 GHz is -26 dB and has bandwidth 79 MHz. The electric field distribution shown in Fig (3. 23), illustrates that the first mode at 3.48 GHz is radiating along the widest section of the waveguide (W-W_1) , at 4.25 GHz is the first order mode of the widest section. At 5.11 GHz is the second order mode of the widest section. Details of each mode has been explained in sec 3.2.2.

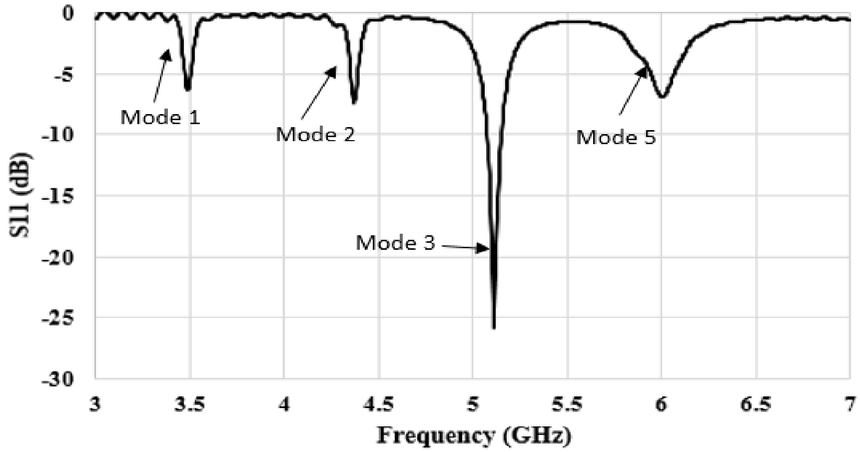

Fig (3. 22) S11 versus frequency (with the addition of slots L_2 perpendicular to the main slot L_1).

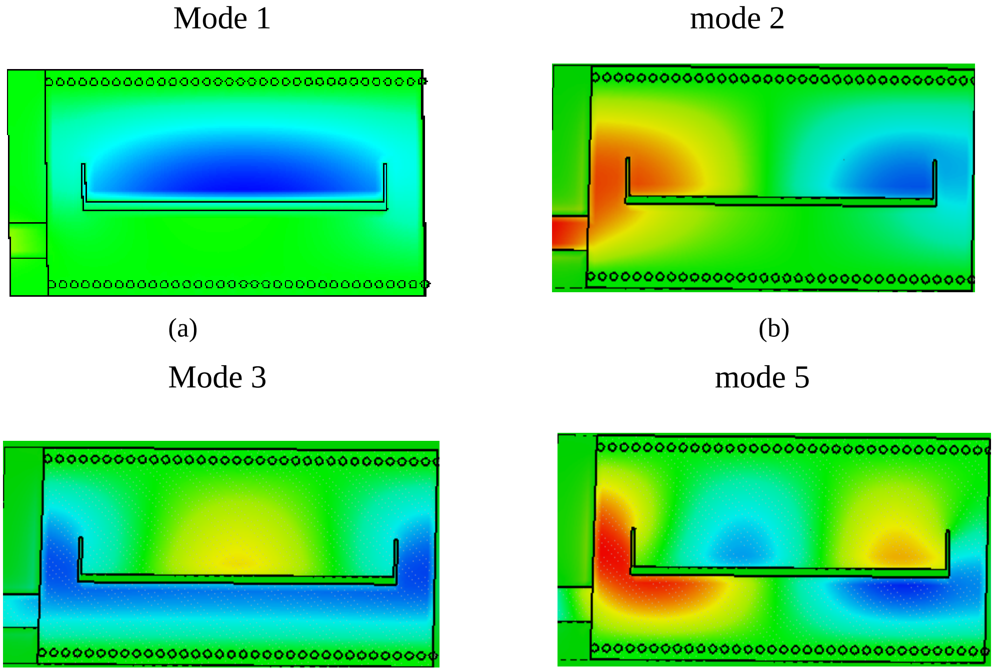

(a) (b)

(c) (d)

Fig (3. 23) Electric field distribution at: (a) 3.48 GHz. (b) 4.25 GHz. (c) 5.11 GHz. (d) 6.08 GHz.

As shown in Fig (3. 24), at 5.1 GHz the radiation efficiency and total efficiency is -0.4 dB and -0.6 dB respectively. The gain is 7 dBi. In H-plane, the main lobe magnitude is 6.98 dB and it offsets 3^0 from its main line, the angular width is 62.5^0 and have side lobe level -9.9 dB. In E-plane, the main lobe magnitude is 6.99 dB and it is away 5^0 from its main direction, the angular width is 100.3^0 and have side lobe level -9.6 dB.

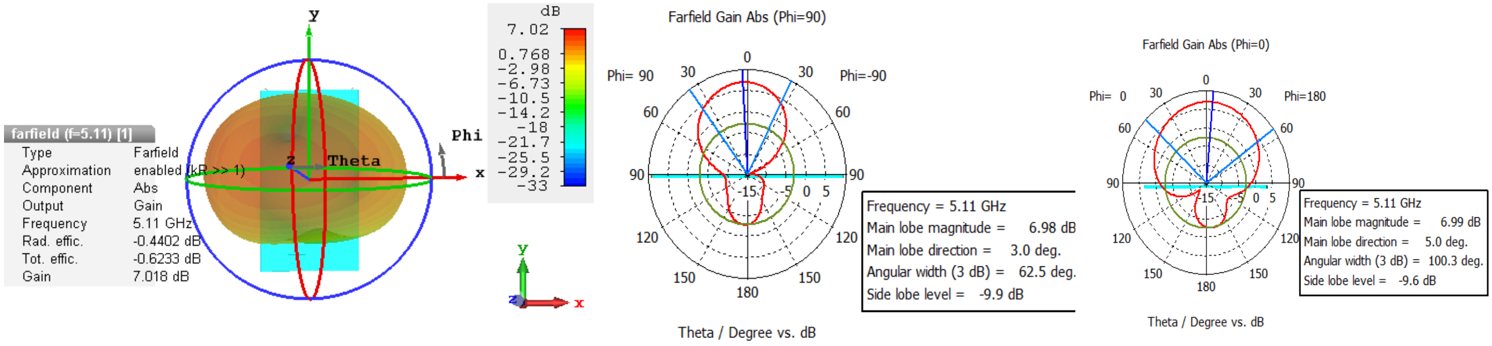
farfield (f=5.11) [1]
Type Farfield
Approximation enabled (kR >> 1)
Component Abs
Output Gain
Frequency 5.11 GHz
Rad. effic. -0.4402 dB
Tot. effic. -0.6233 dB
Gain 7.018 dB

Frequency = 5.11 GHz
Main lobe magnitude = 6.98 dB
Main lobe direction = 3.0 deg.
Angular width (3 dB) = 62.5 deg.
Side lobe level = -9.9 dB

Frequency = 5.11 GHz
Main lobe magnitude = 6.99 dB
Main lobe direction = 5.0 deg.
Angular width (3 dB) = 100.3 deg.
Side lobe level = -9.6 dB

(a) (b) (c)

Fig (3. 24) Radiation pattern at 5.11 GHz: (a) 3D pattern, (b) H-plane, (c) E-plane.

Mode (1) at 3.48 GHz as shown in Fig (3. 25) in polar plot and 3D radiation pattern, the radiation efficiency and total efficiency is -1.7 and -3.7 respectively, The gain is 4.2 dBi and the angular beam width is $74.4^0$and the side lobe level is -5.8 dB

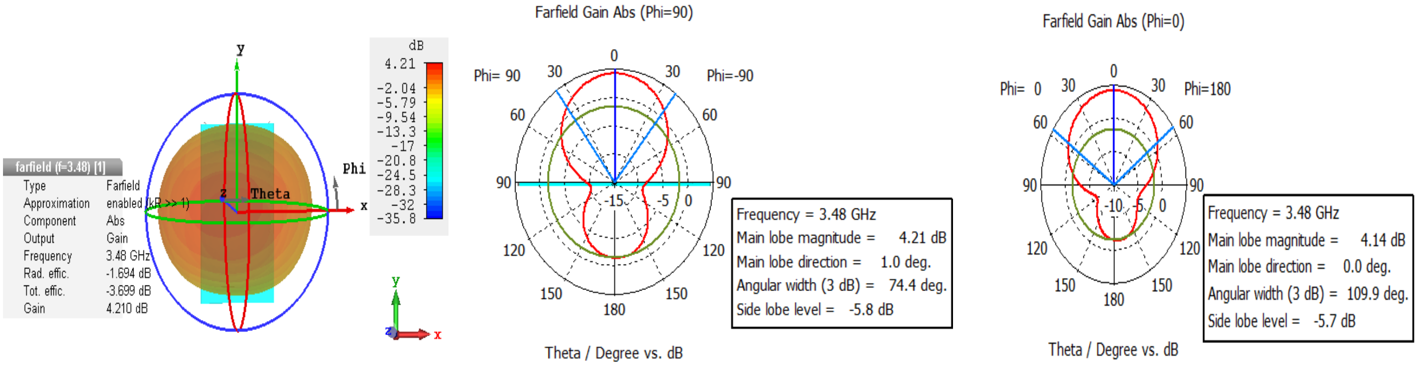
farfield (f=3.48) [1]
Type Farfield
Approximation enabled (kR >> 1)
Component Abs
Output Gain
Frequency 3.48 GHz
Rad. effic. -1.694 dB
Tot. effic. -3.699 dB
Gain 4.210 dB

Frequency = 3.48 GHz
Main lobe magnitude = 4.21 dB
Main lobe direction = 1.0 deg.
Angular width (3 dB) = 74.4 deg.
Side lobe level = -5.8 dB

Frequency = 3.48 GHz
Main lobe magnitude = 4.14 dB
Main lobe direction = 0.0 deg.
Angular width (3 dB) = 109.9 deg.
Side lobe level = -5.7 dB

(a) (b) (c)

Fig (3. 25) Radiation pattern at 3.48 GHz: (a) 3D pattern, (b) H-plane, (c) E-plane.

Fig (3. 26) at 4.25 GHz, shows the radiation pattern in polar plot and 3D. The polar plot shows the radiation is offset 13^0 from its normal main beam. The main lobe magnitude is 2 dB, the angular width is 59.9 degree and has side lobe level -4.3 dB. As shown in 3D plot the radiation efficiency and total efficiency is -4.0 dB and -12 dB. Once again, this is due to the mismatching. The gain at 4.25 GHz is 2.19 dBi.

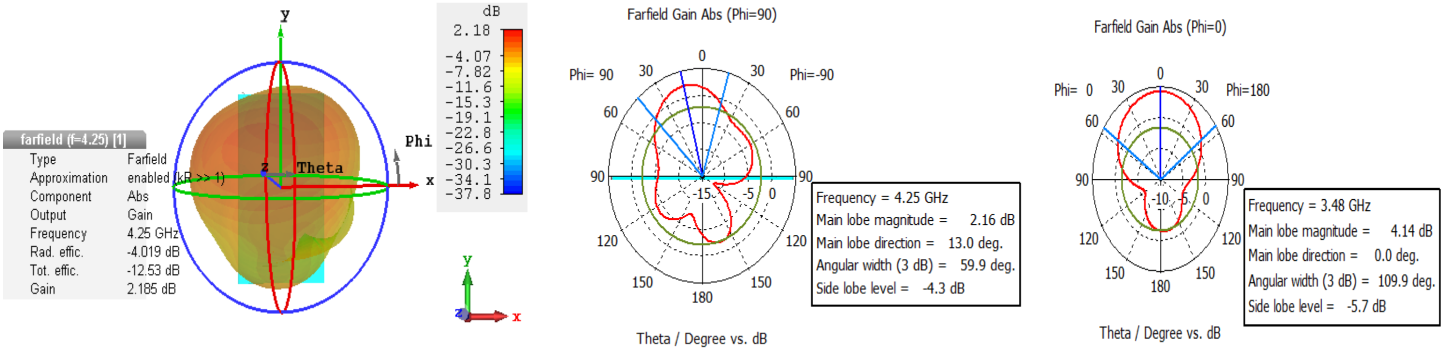

(a) (b) (c)

Fig (3. 26) Radiation pattern at 4.25 GHz: (a) 3D pattern, (b) H-plane, (c) E-plane.

The final resonant frequency radiation pattern at 6.06 GHz as shown in Fig (3. 27). The polar plot shows clearly that the radiation is in two directions . The gain at 6.06 GHz is 5.9 dBi and the radiation and total efficiency is -0.78 dB and -4 dB.

The disadvantage of this design stops resonant at Mode 4. 'Therefore, an alternative design will be developed in the following section.

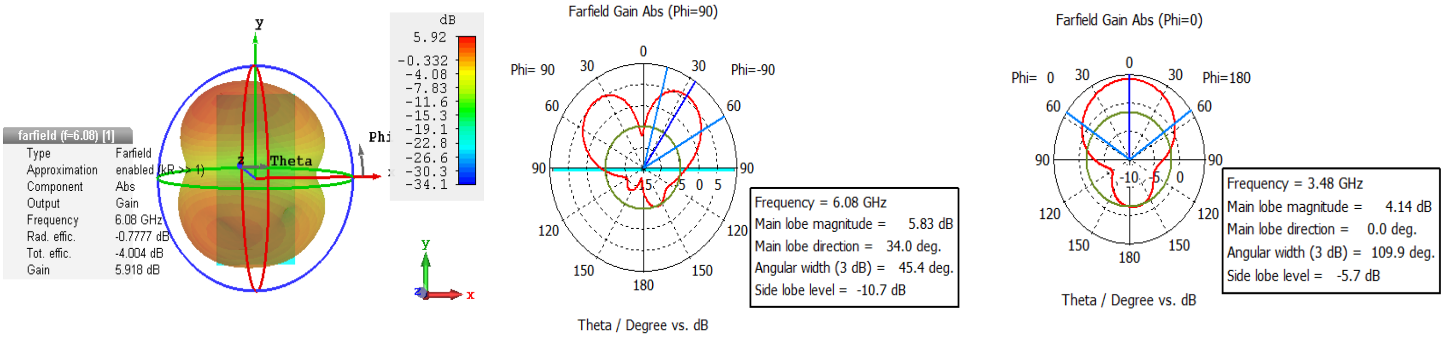

(a) (b) (c)

Fig (3. 27) Radiation pattern at 6.06 GHz: (a) 3D pattern, (b) H-plane, (c) E-plane.

3.3.4 Adding two sections of the slots at the two ends of the main slot in the opposite direction

In order to tune the resonant frequency, two slots with length L_2= 6 mm has been added perpendicular to the main slot of the length L_1. One of the two slots (L_2) at a direction toward the wide section of the waveguide W_2 and the other slot is toward the narrower region W_1. All the other parameters remain the same in Section 3.2.3 except the microstrip feeding has been rescaled $L_4 = 8.5$ mm, $L_5 = 4.5$ mm to obtain a better matching as shown in Fig (3. 28). The resonant modes in Fig (3. 29) shows that at 3.5 GHz it is less matching.

Fig (3. 30) shows the electric field distribution for all the modes. As seen that all the modes remain the same pattern at 3.5 GHz, 4.3 GHz,5.15 GHz and 6.1 GHz. However, it can be distinguished that the mode 5.76 GHz is offset from its main direction. The effect of L_2 on Mode 4 will be explained in Section 3.3 (parameters effect on resonant frequency).

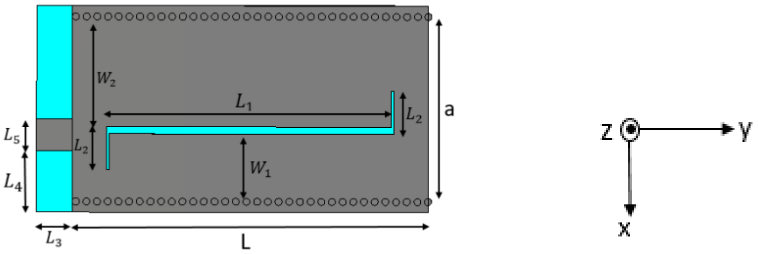

Fig (3. 28) Adding two slots of length L_2 perpendicular to the slot L_1 in the opposite direction.

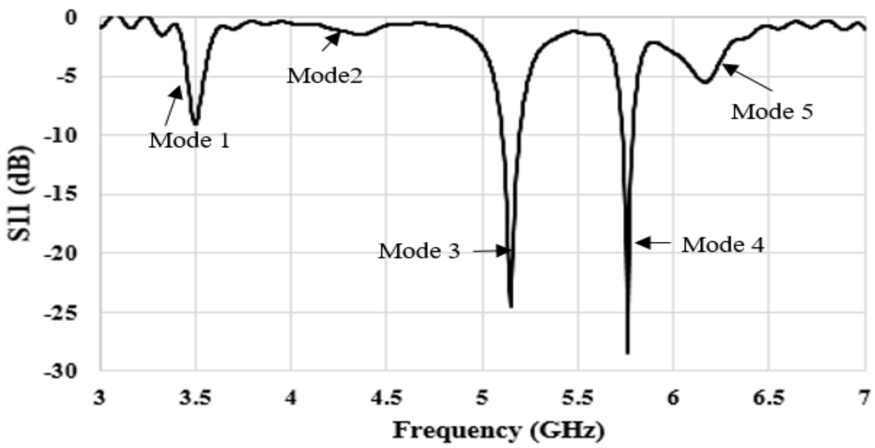

Fig (3. 29) S11 versus frequency showing all the resonant modes when adding two sections of the slot in the opposite direction.

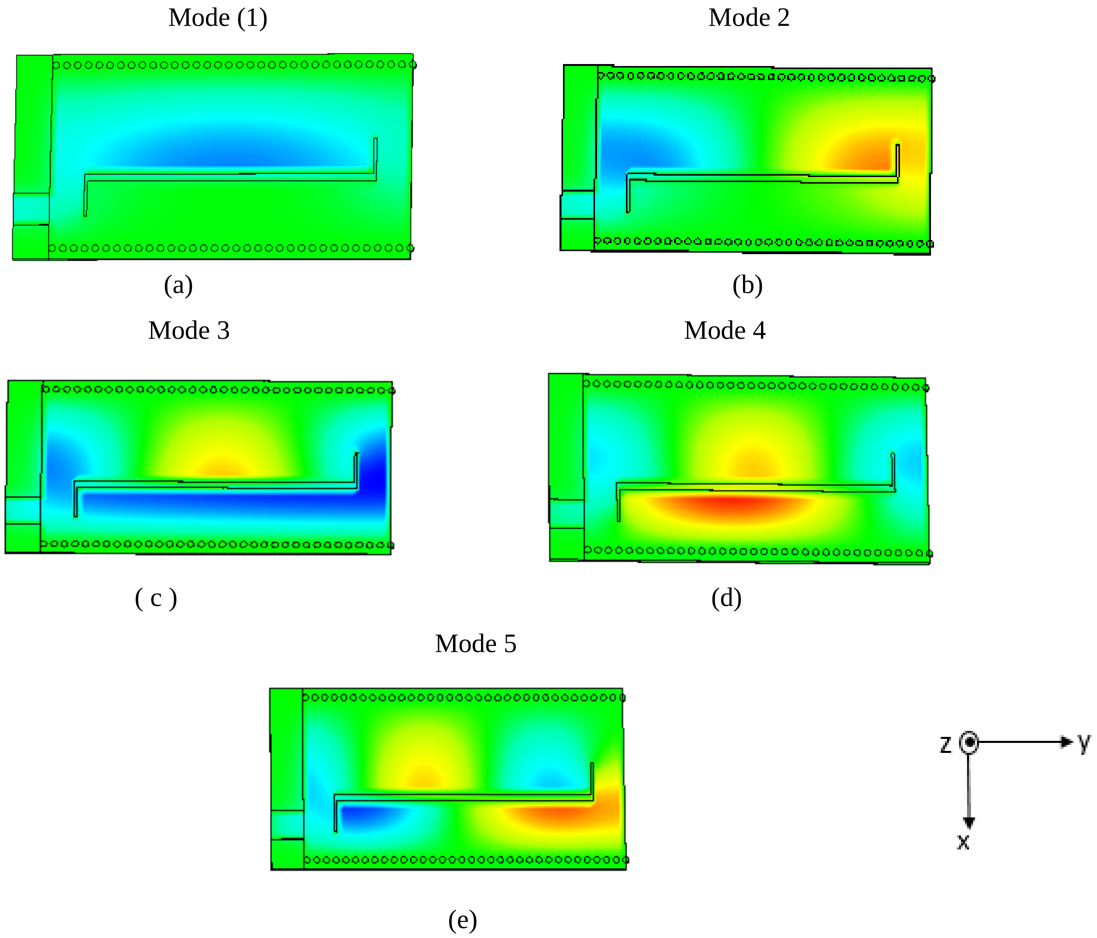
Mode (1)

Mode 2

(a)

(b)

Mode 3

Mode 4

(c)

(d)

Mode 5

(e)

Fig (3. 30) Electric field distribution at: (a) 3.5 GHz. (b) 4.344 GHz. (c) 5.15 GHz. (d) 5.76 GHz. (e) 6.1 GHz.

Mode 3, the radiation efficiency and total efficiency is -0.37 dB and -0.79 dB respectively. The gain at 5.15 GHz is 7 dBi and the H-plane shows that the main lobe magnitude is 6.95 dB with an offset of 2^0 from its main direction. In addition, the angular width is 63^0 with side lobe level -10.2 dB. In E-plane, the main lobe magnitude is 6.98 dB with a direction of 5^0, the angular width is 100^0 and the side lobe level is -9.9 dB.

Mode 4 at 5.76 GHz, as shown in Fig (3. 32), the main radiation is offset $19^0$from its main direction as shown in H-plane plot with 5.7 dB in main lobe magnitude. This is because the side slot of L_2 is toward the narrow region of the waveguide (W_1) and this will cause asymmetry in the field pattern which skews the beam. The angular width is 60.9^0 with side lobe level -8.5 dB. In E-plane, the main lobe magnitude is 4.52 dB with 10^0 offset. The angular width is 95^0 and the side lobe level is -10 dB. The radiation efficiency and total efficiency is -1.29 dB and -1.64 dB.

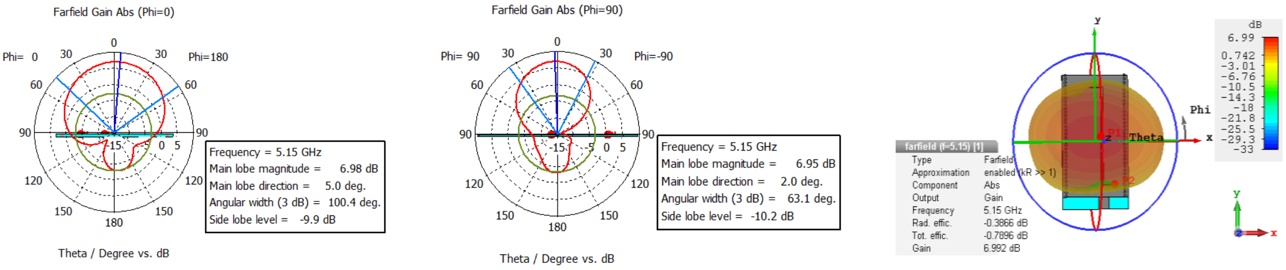

(a) (b) (c)

Fig (3. 31) Radiation pattern for Mode 3 at 5.15 GHz: (a) E-plane, (b) H-plane, (c) 3D pattern.

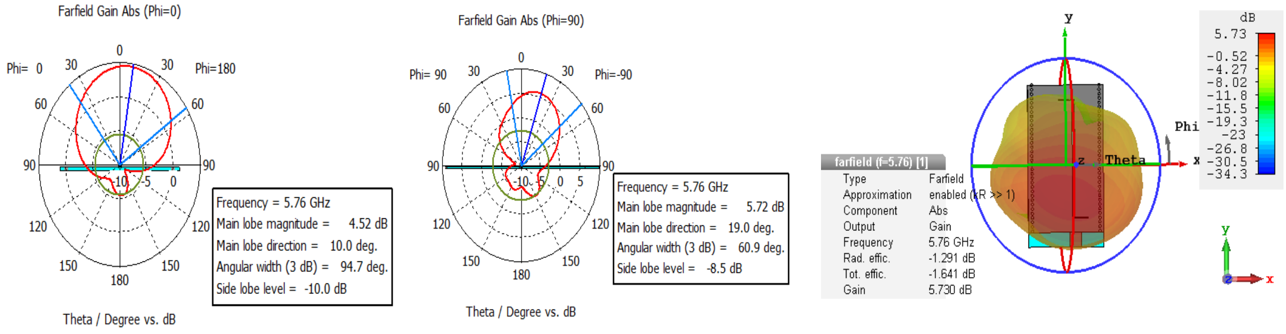

(a) (b) (c)

Fig (3. 32) Radiation pattern for Mode 4 at 5.76 GHz: (a) E-plane, (b) H-plane, (c) 3D pattern.

Mode 1 at 3.5 GHz, the radiation pattern in 3D and polar plot is shown in Fig (3. 33). The gain is 4.28 dB and the radiation efficiency and total efficiency is -1.7 and -1.9 dB respectively. In H-plane the angular width is 72.9^0 with side lobe level is-5.7 dB.

Mode 2 at 4.34 GHz, the radiation pattern in both polar and 3D plot is shown in Fig (3. 34). This mode is not considered in tri-band antenna, the pattern shows that it radiates in different directions and have high side lobe level.

Mode 5 at 6.1 GHz, as shown in Fig (3. 35), indicates that the radiation is in two directions, the side lobe level in both H-plane and E-plane is high.

This asymmetry of this design skews patterns in E-plane. Moreover, the following design is to enhance the pattern and tuning of the device.

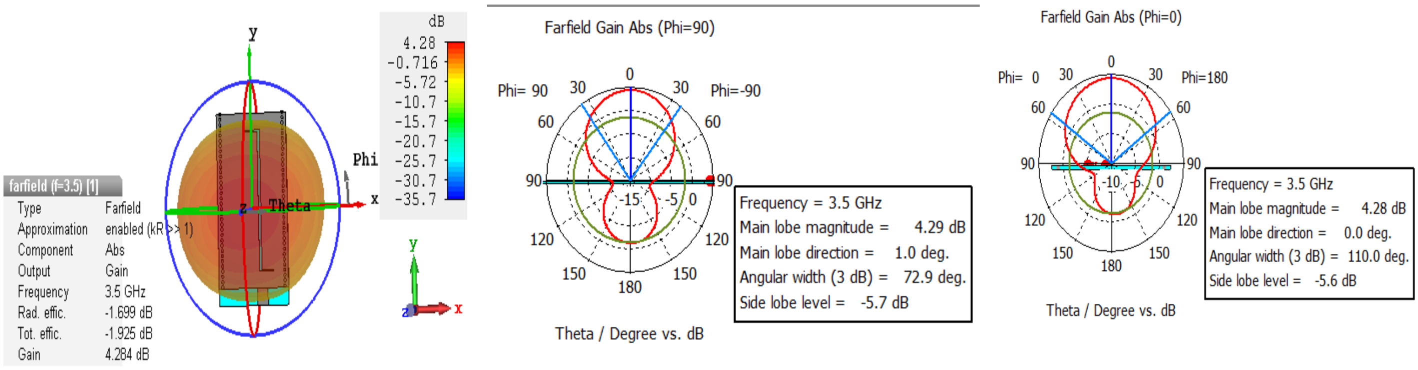

farfield (f=3.5) [1]
Type Farfield
Approximation enabled (kR >> 1)
Component Abs
Output Gain
Frequency 3.5 GHz
Rad. effic. -1.699 dB
Tot. effic. -1.925 dB
Gain 4.284 dB

Frequency = 3.5 GHz
Main lobe magnitude = 4.29 dB
Main lobe direction = 1.0 deg.
Angular width (3 dB) = 72.9 deg.
Side lobe level = -5.7 dB

Frequency = 3.5 GHz
Main lobe magnitude = 4.28 dB
Main lobe direction = 0.0 deg.
Angular width (3 dB) = 110.0 deg.
Side lobe level = -5.6 dB

(a) (b) (c)

Fig (3. 33) Radiation pattern for Mode 1 at 3.5 GHz: (a) 3D pattern, (b) H-plane, (c) E-plane.

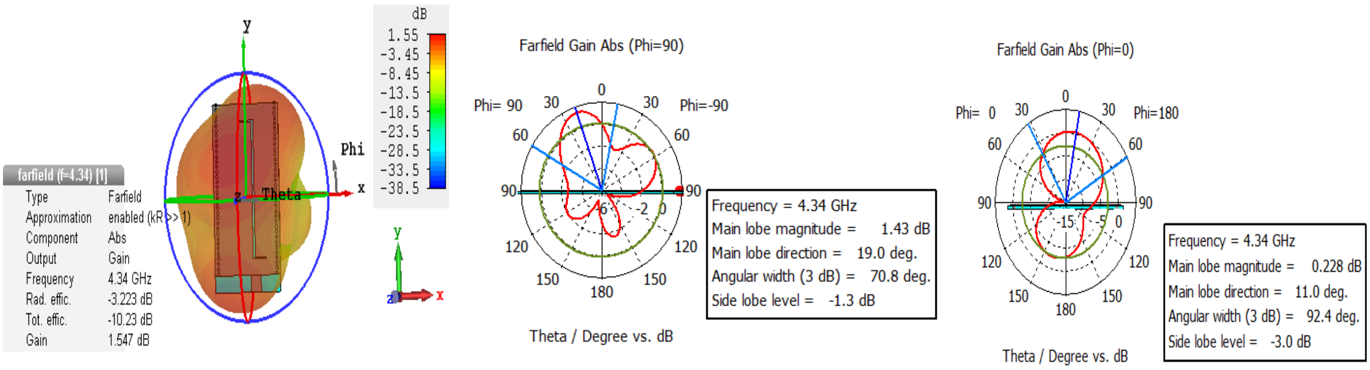

farfield (f=4.34) [1]
Type Farfield
Approximation enabled (kR >> 1)
Component Abs
Output Gain
Frequency 4.34 GHz
Rad. effic. -3.223 dB
Tot. effic. -10.23 dB
Gain 1.547 dB

Frequency = 4.34 GHz
Main lobe magnitude = 1.43 dB
Main lobe direction = 19.0 deg.
Angular width (3 dB) = 70.8 deg.
Side lobe level = -1.3 dB

Frequency = 4.34 GHz
Main lobe magnitude = 0.228 dB
Main lobe direction = 11.0 deg.
Angular width (3 dB) = 92.4 deg.
Side lobe level = -3.0 dB

(a) (b) (c)

Fig (3. 34) Radiation pattern for Mode 2 at 4.34 GHz: (a) 3D pattern, (b) H-plane, (c) E-plane.

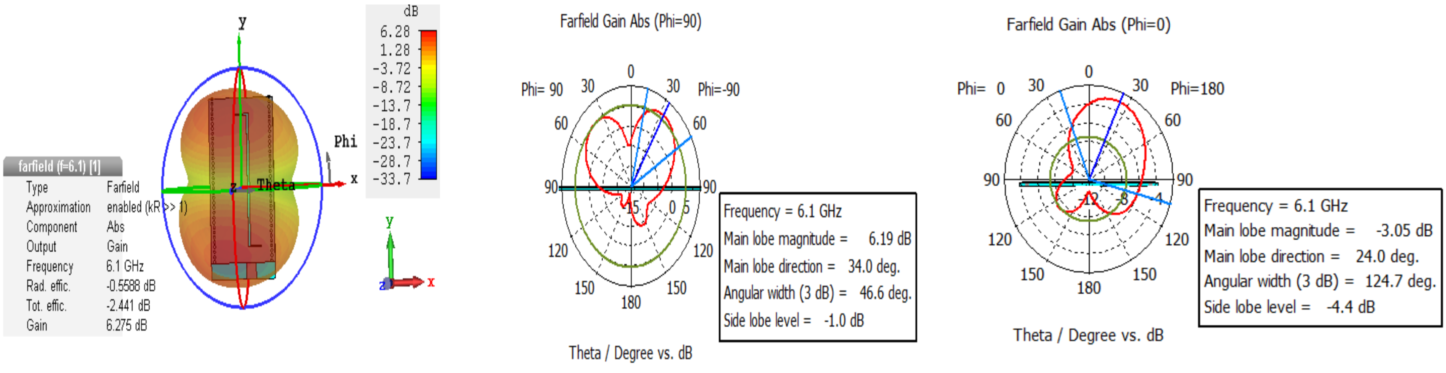

farfield (f=6.1) [1]
Type Farfield
Approximation enabled (kR >> 1)
Component Abs
Output Gain
Frequency 6.1 GHz
Rad. effic. -0.5588 dB
Tot. effic. -2.441 dB
Gain 6.275 dB

Frequency = 6.1 GHz
Main lobe magnitude = 6.19 dB
Main lobe direction = 34.0 deg.
Angular width (3 dB) = 46.6 deg.
Side lobe level = -1.0 dB

Frequency = 6.1 GHz
Main lobe magnitude = -3.05 dB
Main lobe direction = 24.0 deg.
Angular width (3 dB) = 124.7 deg.
Side lobe level = -4.4 dB

(a) (b) (c)

Fig (3. 35) Radiation pattern for Mode 5 at 6.1 GHz: (a) 3D pattern, (b) H-plane, (c) E-plane.

3.4 Final design of tri-band SIW with addition slots for tuning the device

Fig (3. 36) shows the structure of the antenna, which resembles a conventional slot antenna of length L_1 but with additional perpendicular sections of the slot of length L_2 at the two ends of the slot at the direction of the narrow section of the waveguide (W_1). An offset microstrip feed is used to excite the structure with the displacement, L_4, chosen to aid the matching. The dielectric constant has been chosen 2.2.

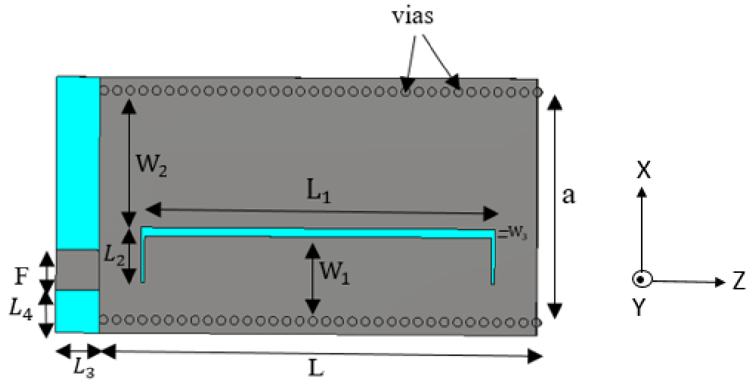

Fig (3. 36) Configuration of the proposed tri-band SIW with tuning.

Parameter	Optimised value (mm)
L	50
L_1	40
L_2	6
L_3	5
L_4	4.85
a	25
W_1	9
W_2	15
W_3	1
F	4.5
b (thickness of substrate)	0.787

Table (3. 1) Parameters for the proposed structure (see Fig (3. 36) for definitions of the parameters)

For the dimensions shown in Table 3.1, the S-parameters of the structure are shown in Fig (3. 37). As it can be seen that there are four resonant modes over the 3.5 to 7.0 GHz range. The corresponding field plots are shown in Fig (3. 39). Each mode has been explained in section 3.2.2

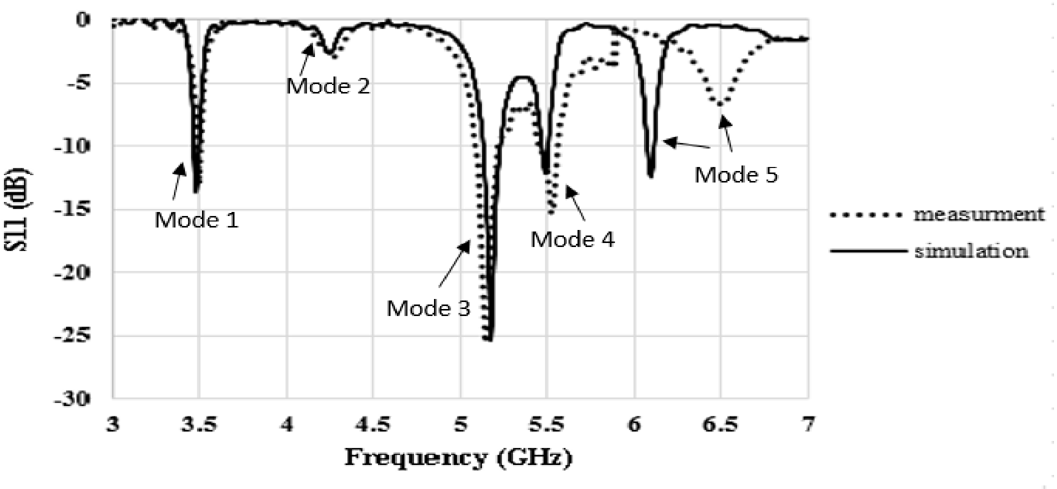

Fig (3. 37) S_{11} against frequency by adding two slots perpendicular to the main slot L_2

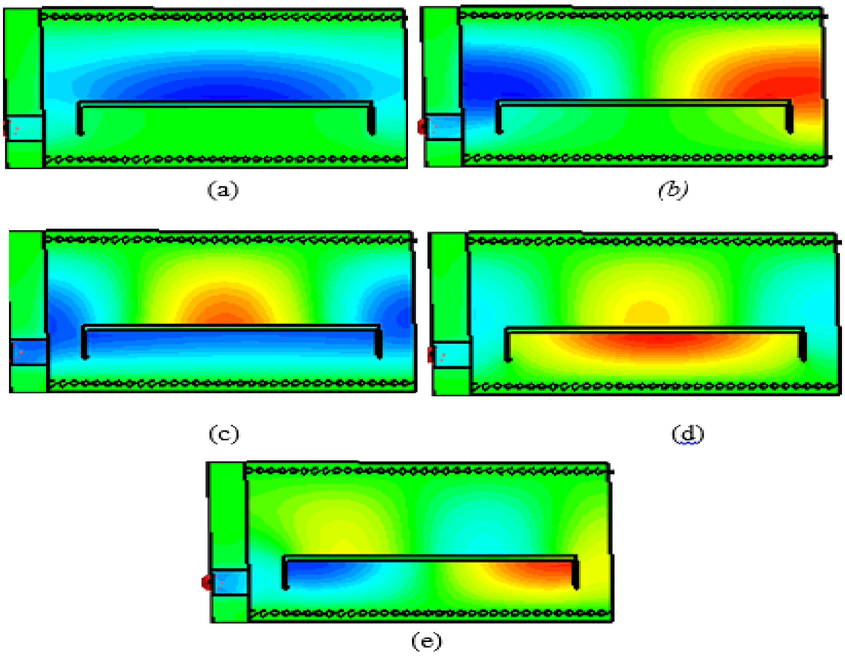

Fig (3. 38) Electric field distribution at: (a) 3.5 GHz (Mode 1). (b) 4.27 GHz (Mode 2). (c) 5.17 GHz (Mode 3). (d) 5.57 GHz (Mode 4). (e) 6.17 GHz (Mode 5).

The effect on various parameters on the performance of the antenna are studied in the next section.

3.5 Parameters effect on resonant frequency

The effect of various parameters on the design has been simulated using the CST simulation to obtain a high performance and to understand how each parameter affects the resonant frequency. All the figures have a frequency range from 3 GHz to 5.8 GHz (Mode 5 is not considered) and show how the S-parameters of the structure vary with the parameters, L_1 (length of the slot), W_1 (width of narrower section) and L_2 (length of perpendicular section of slot). In each of the figures, all other parameters are given by those in Table (3.1). We note that since W_3 is kept constant $W_2 = a$-W_1-W_3.

We see from Fig (3. 39) that the length of the slot L_1 tunes the resonant frequency of all modes with an increase in the length reducing the frequency of resonance of each of the modes. Since L is kept constant, reducing the length L_1 increases the gap between the two ends of the structure and the slot. This has quite a strong effect on the matching of all modes with a reduced S_{11} for decreasing L_1.

Fig (3. 40) shows the effect of the length of the waveguide L to the S-parameter (keeping the slot of the waveguide L_1 constant). By increasing the length of the waveguide L, the resonant frequency decreases and the matching at the resonant frequency decreases.

The effect of L_2 is shown in Fig (3. 41). We see that the L_2 parameter has almost no effect on the Mode 3 and minimal effect on Mode 1. It does however, tune the frequency of Mode 4, an increase in the length L_2 reduces the resonance of Mode 4. This is as expected since the resonant field of Mode 1 and Mode 3 is predominantly set by the W_2 section of the structure, and so the extended perpendicular sections have little effect on the frequency of Mode 1 and 3. In contrast, Mode 4, whose resonance appears predominantly in the W_1 section, is affected by the L_2 sections.

Therefore, W_1 and W_2 affect all of the resonances since they change the cut-off frequency and the longitudinal phase in each of the slotted sections. Due to the dispersion in waveguide, the change in the resonant frequency of Mode 4 is more rapid than that of Mode 3. This is because Mode 3 is set by the second order resonance in the wider W_2 section, which occurs considerably above the cut-off frequency - where dispersion is relatively small. In contrast, Mode 4 is set by the first order resonance in the narrower section, which is only just above the cut-off frequency - where dispersion is large. The increased sensitivity of Mode 4 can be used to tune the frequency difference between Mode 4 to Mode 3. The effect of the narrow section of the waveguide (W_1) on resonant modes is shown in Fig (3. 42).

By increasing the width of the slot W_3, the resonant mode will change because $W_3 = a - W_1 - W_2$ as shown in Fig (3. 43), increasing W_3 results in increasing the resonant frequency.

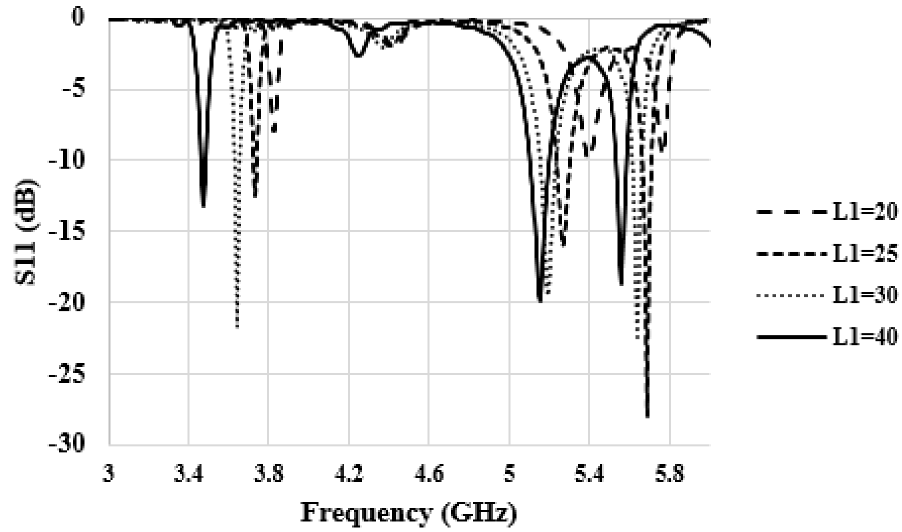

Fig (3. 39) L_1 versus reflection coefficient (all other parameters are the same)

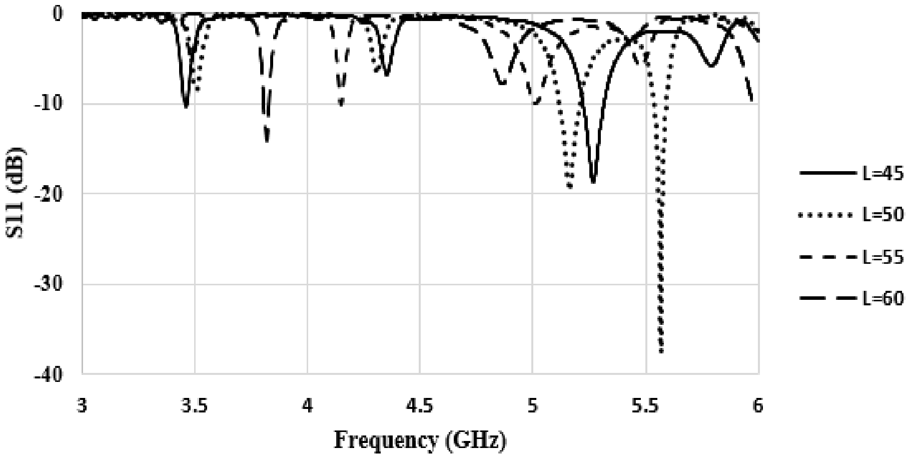

Fig (3. 40) L versus reflection coefficient (all other parameters are the same)

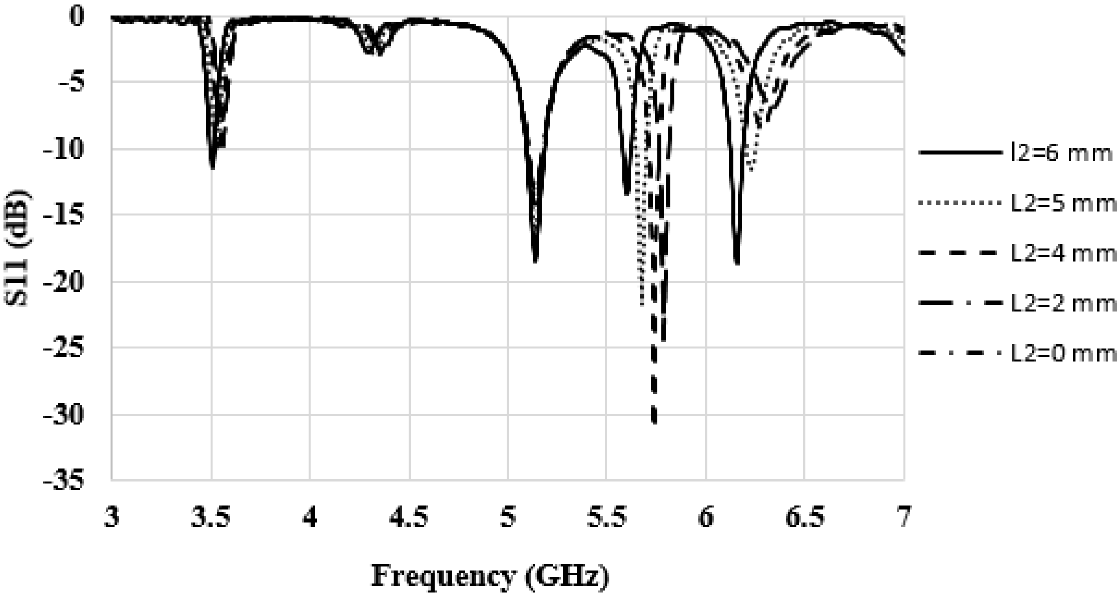

Fig (3. 41) L_2 versus reflection coefficient (all other parameters are the same)

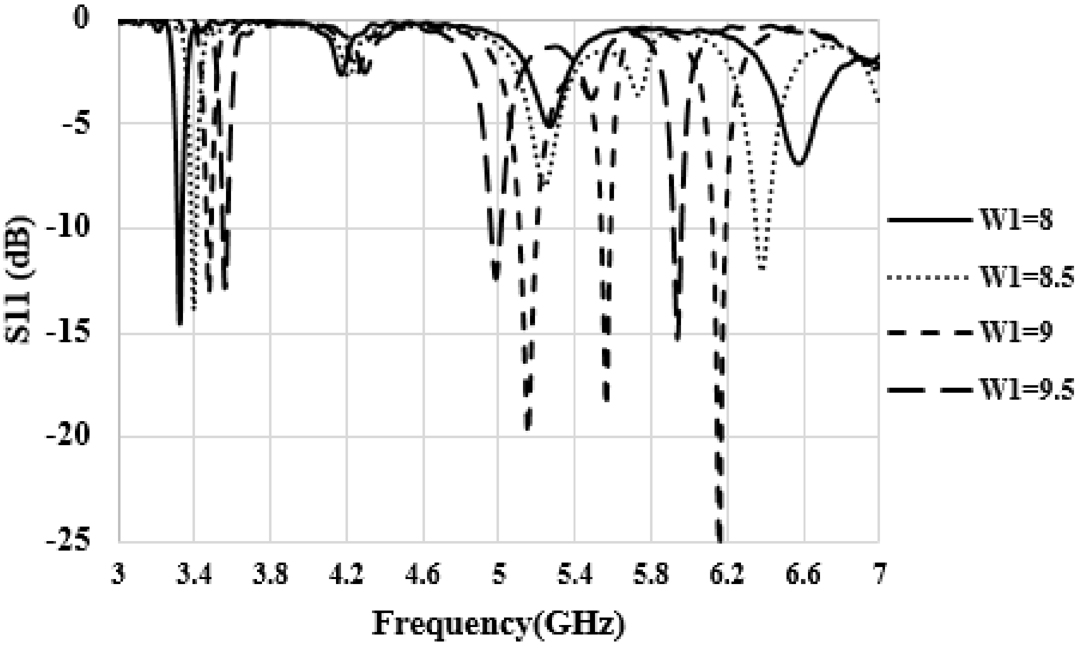

Fig (3. 42) W_1 versus reflection coefficient (all other parameters are the same).

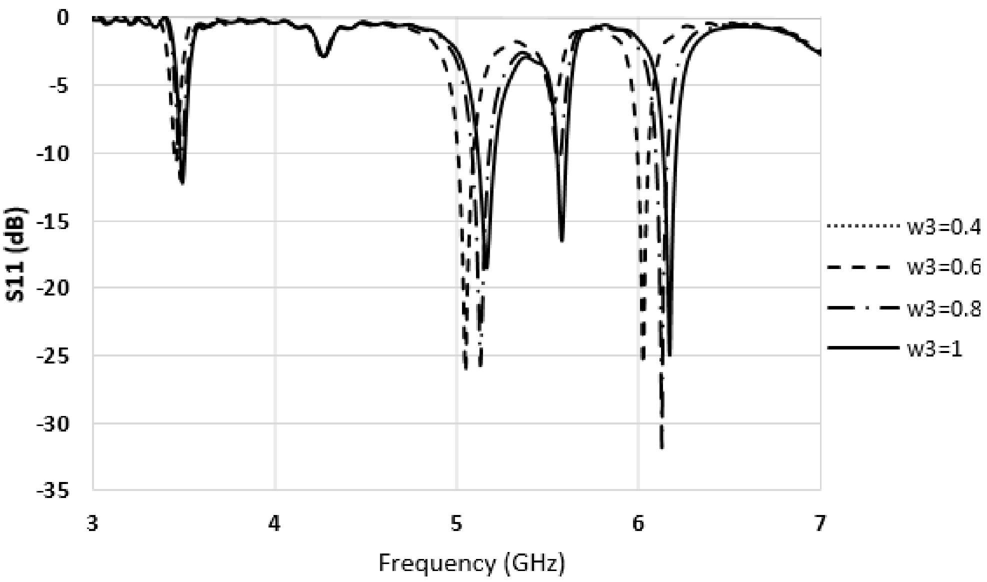

Fig (3. 43) W_3 versus reflection coefficient (all other parameters are the same).

Notice that Mode 2, which resonates at approximately 4.2 GHz is very poorly matched for all values of the parameters: Fig (3. 39) Fig (3. 40), Fig (3. 41) and Fig (3. 42). However, the odd symmetry in the resonance results in a dual beam pattern which may not be useful in practice.

By varying L, L_1 and W_1, the frequency of the resonant modes can be tuned. In the present implementation, Mode 4 and 5 cover the 5.2-5.8 GHz Wi-Fi bands, together with Mode 1 at 3.5 GHz, which may be found useful in future 5G systems. Of course the structure can be scaled to operate at other bands by changing the a dimension of the waveguide and scaling all other parameters accordingly.

3.6 Comparison the results between simulation and measurements

After we studied the effect of each parameter on resonant frequency and matching, the structure was fabricated in RT/ Duroid 5580 with dielectric constant, ε_r= 2.2, loss tangent 0.0015 and a thickness of b = 0.787 mm.

The vias for the sidewalls of the waveguide are 0.5 mm diameter copper wire soldered to the top and bottom metallization; the separation between vias is 1 mm. An SMA connector was used to connect the antenna for measurement.

The dimensions of the other parameters are given in Table (3.2). A photograph of the fabricated structure is shown in Fig (3. 44).

Fig (3. 44) Photograph structure of tri-band SIW

The S-parameters were measured using an Anritsu Vector Network Analyzer (Model ME7808A), calibrated using a coaxial SOLT (Short Open Load and Thru) method. The SMA connector used to connect the device was not de-embedded and therefore forms part of the measurements. It can be seen from Fig (3. 37), that there is a very good agreement for each of the resonant modes over the 3 to 7 GHz range.

The antenna radiation patterns and gain measurements were made using the department's anechoic chamber and are displayed in Fig (3. 45), Fig (3. 46) and Fig (3. 48) respectively. There is a very good agreement between the measured and simulated radiation patterns in both planes for all of the three modes. There is a significant back lobe for all of the modes because of the minimal extent of the conducting top plane of the antenna. This is particularly evident at 3.5 GHz where the physical size of the top metal is small in comparison to the wavelength. The back lobe could be easily reduced extending the top plane beyond the side walls.

As shown in Fig (3. 45), the radiation efficiency and total efficiency at 5.16 GHz is -0.29 dB and -0.36 dB. The 3D radiation pattern simulation shows how the structure is placed vertically to radiate. The main lobe magnitude is 7.0 dB and offset 2^0 from its main direction, whilst the angular width is 66^0 and the side lobe level is -9.6 dB. A good agreement of radiation pattern in polar plot is shown between measurement and simulation.

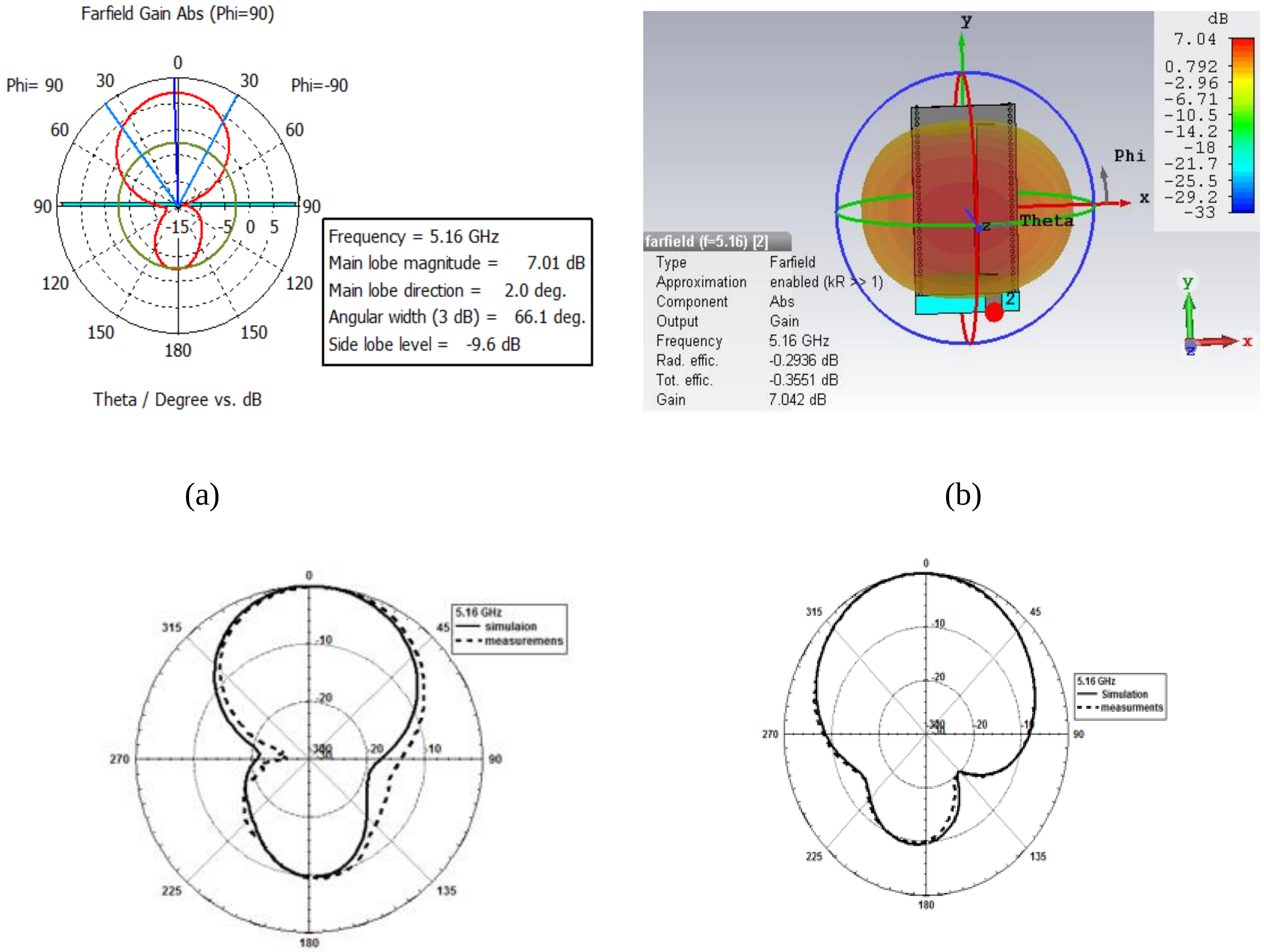

Frequency = 5.16 GHz
Main lobe magnitude = 7.01 dB
Main lobe direction = 2.0 deg.
Angular width (3 dB) = 66.1 deg.
Side lobe level = -9.6 dB

Type Farfield
Approximation enabled (kR >> 1)
Component Abs
Output Gain
Frequency 5.16 GHz
Rad. effic. -0.2936 dB
Tot. effic. -0.3551 dB
Gain 7.042 dB

(a) (b)

(c) (d)

Fig (3. 45) Radiation pattern at 5.16 GHz: (a) H-plane, (b) 3D pattern, (c) H-plane comparison, (d) E-plane comparison.

As shown in Fig (3. 46), the second resonant frequency is at 5.56 GHz and the radiation pattern using CST shows that the radiation efficiency and total efficiency is -0.87 dB and -1 dB respectively. In regards to the structure placed vertically radiating in H-plane, in CST the polar plot shows that the main lobe magnitude is 6.09 dB and it offset 3^0 from its main direction. The angular width is $64^0$and the side lobe level is -9.8 dB. Again, the comparison between simulation and measurement are in good agreement .

Fig (3. 47) shows the gain of the antenna over the 5-5.6 GHz range where Mode 3 and 4 resonate. In this implementation, the resonant frequency of Mode 3 and 4 has been tuned to be very close to each other and therefore the antenna operates as a relatively broadband antenna over this range. This is seen in Fig (3. 47) with a gain in excess of 6 dBi over the 5.1-5.6 GHz range.

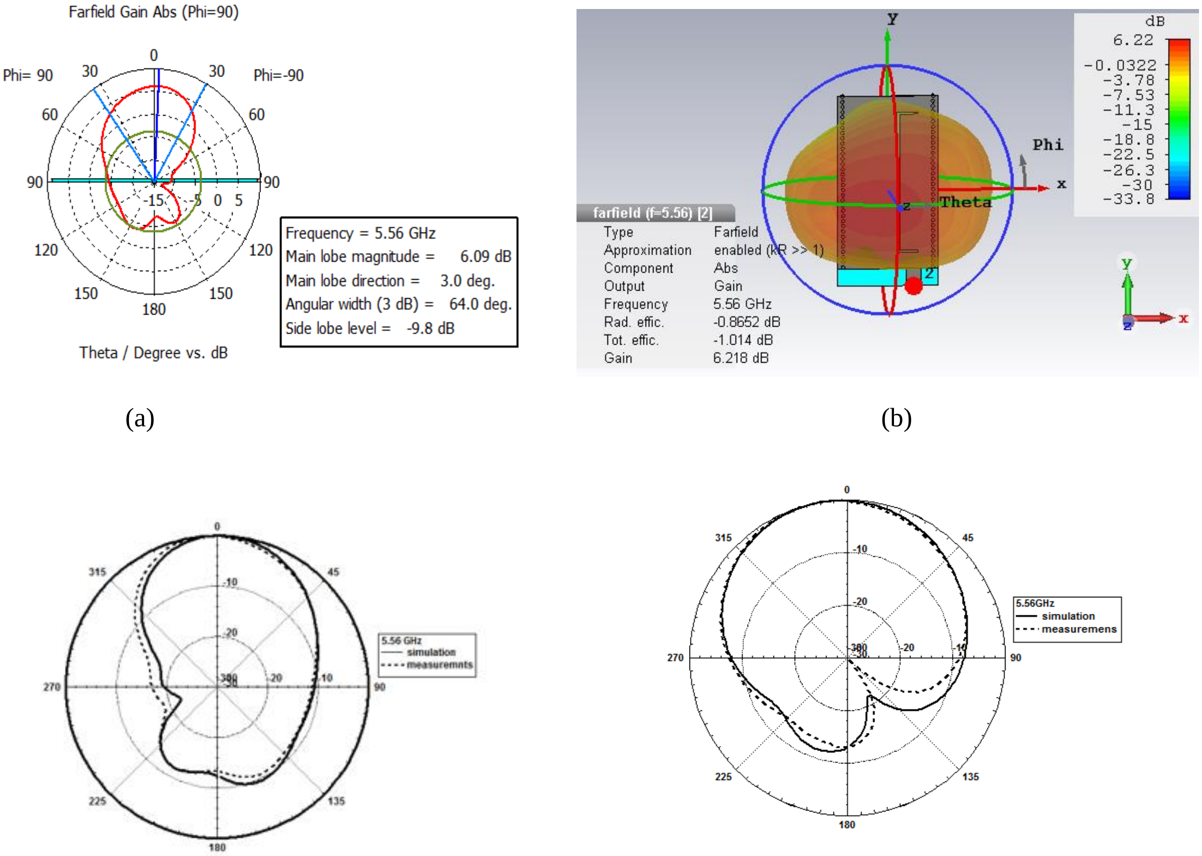

Frequency = 5.56 GHz
Main lobe magnitude = 6.09 dB
Main lobe direction = 3.0 deg.
Angular width (3 dB) = 64.0 deg.
Side lobe level = -9.8 dB

farfield (f=5.56) [2]
Type Farfield
Approximation enabled (kR >> 1)
Component Abs
Output Gain
Frequency 5.56 GHz
Rad. effic. -0.8652 dB
Tot. effic. -1.014 dB
Gain 6.218 dB

(a) (b)

(c) (d)

Fig (3. 46) Radiation pattern at 5.56 GHz: (a) H-plane, (b) 3D pattern, (c) H-plane comparison, (d) E-plane comparison.

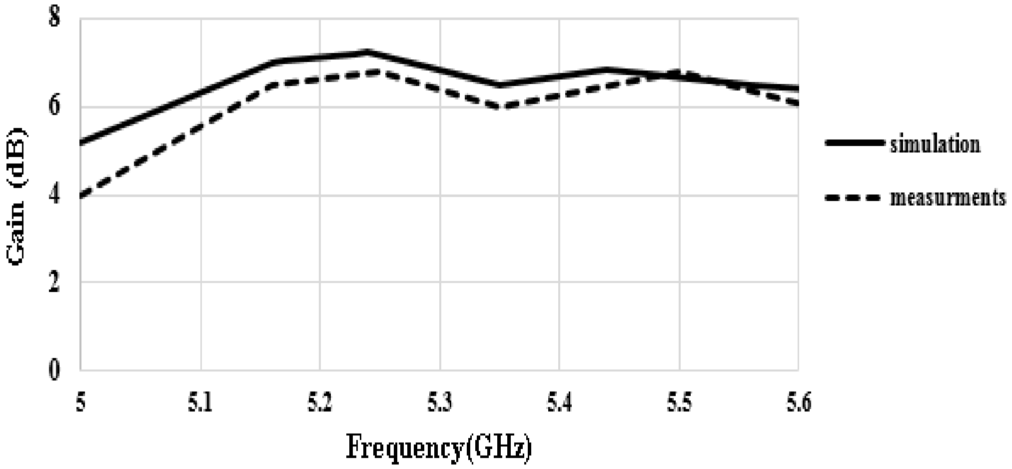

Fig (3. 47) Comparison of gain between measurement and simulation.

Further demonstrating for the other modes will be discussed briefly:

Fig (3. 48) shows the radiation pattern at 3.5 GHz which radiates at the widest section of the waveguide. The radiation efficiency and the total efficiency is -1.87 dB and -2.17 dB respectively. The comparison between the measurement and simulation are well matched. In H-plane, the main lobe magnitude is 4 dB and it offset 2^0 from its main direction, the angular width is 75^0 and the side lobe level is -6 dB. The significant back lobe is at 3.5 GHz where the physical size of the top metal is small in comparison to the wavelength. The back lobe could be easily reduced extending the top plane beyond the side walls. The gain of the resonance at 3.5 GHz was found to be slightly less than the other modes with a value of 4 dBi. This is partly due to the increased back lobe.

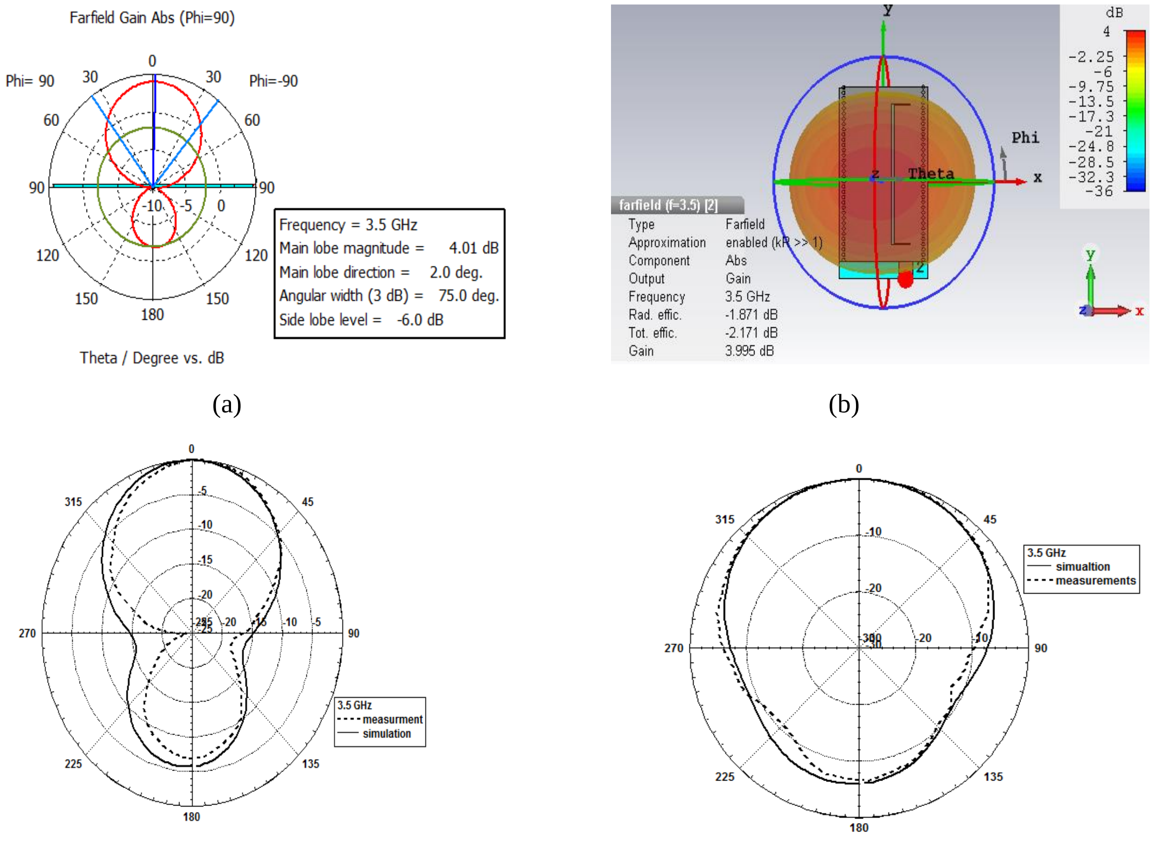

Frequency = 3.5 GHz
Main lobe magnitude = 4.01 dB
Main lobe direction = 2.0 deg.
Angular width (3 dB) = 75.0 deg.
Side lobe level = -6.0 dB

Type Farfield
Approximation enabled (kR >> 1)
Component Abs
Output Gain
Frequency 3.5 GHz
Rad. effic. -1.871 dB
Tot. effic. -2.171 dB
Gain 3.995 dB

(a) (b)

(c) (d)

Fig (3. 48) Radiation pattern at 3.5 GHz: (a) H-plane, (b) 3D pattern, (c) H-plane comparison, (d) E-plane comparison.

The second mode at 4.27 GHz shows the radiation pattern in polar plot and 3D as shown Fig (3. 49). In 3D radiation pattern, radiation efficiency and total efficiency is -2.8 dB and-6.13 dB, thereby indicating it to be poor. The gain is 2.36 dBi, in H-plane the main lobe magnitude is 2.27 dB and it offset 15^0 from its main direction the angular width is 59.7 dB. This mode is not considered in measurement .

Mode 5 at 6.15 GHz, is different in S- parameters shown in Fig (3. 37) between simulation and measurements. However, the radiation pattern in H-plane shown in Fig (3. 50) radiates in two directions. The radiation efficiency and total efficiency is -0.51 and -0.53 dB and the gain is 6 dBi.

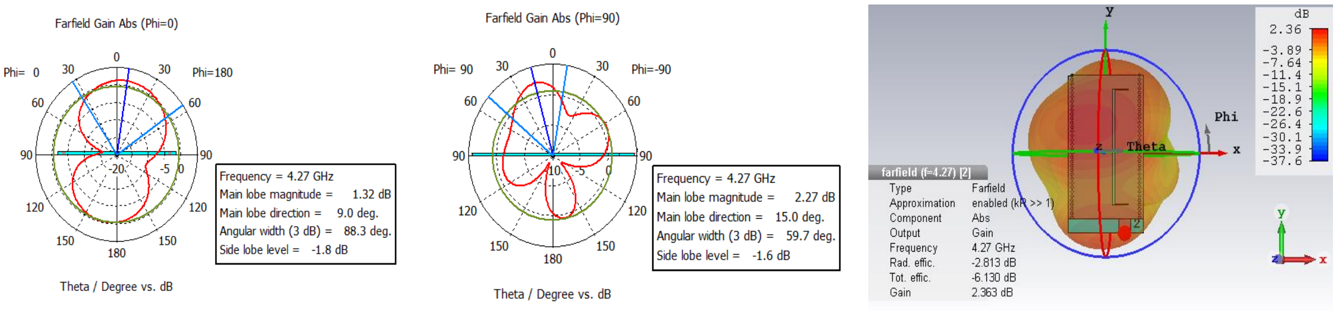

Frequency = 4.27 GHz
Main lobe magnitude = 1.32 dB
Main lobe direction = 9.0 deg.
Angular width (3 dB) = 88.3 deg.
Side lobe level = -1.8 dB

Frequency = 4.27 GHz
Main lobe magnitude = 2.27 dB
Main lobe direction = 15.0 deg.
Angular width (3 dB) = 59.7 deg.
Side lobe level = -1.6 dB

farfield (f=4.27) [2]

Type	Farfield
Approximation	enabled (kR >> 1)
Component	Abs
Output	Gain
Frequency	4.27 GHz
Rad. effic.	-2.813 dB
Tot. effic.	-6.130 dB
Gain	2.363 dB

(a) (b) (c)

Fig (3. 49) Radiation pattern at 4.27 GHz: (a) E-plane, (b) H-plane, (c) 3D pattern.

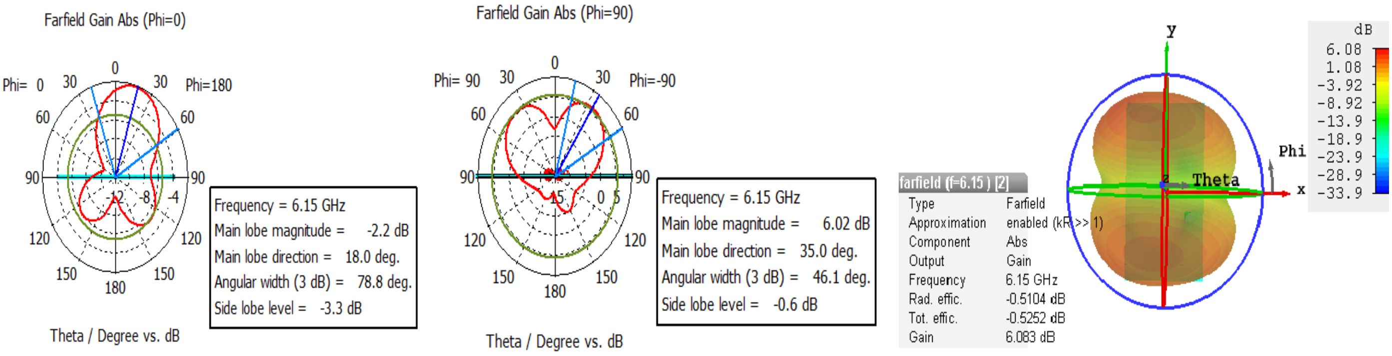

Frequency = 6.15 GHz
Main lobe magnitude = -2.2 dB
Main lobe direction = 18.0 deg.
Angular width (3 dB) = 78.8 deg.
Side lobe level = -3.3 dB

Frequency = 6.15 GHz
Main lobe magnitude = 6.02 dB
Main lobe direction = 35.0 deg.
Angular width (3 dB) = 46.1 deg.
Side lobe level = -0.6 dB

farfield (f=6.15) [2]

Type	Farfield
Approximation	enabled (kR >> 1)
Component	Abs
Output	Gain
Frequency	6.15 GHz
Rad. effic.	-0.5104 dB
Tot. effic.	-0.5252 dB
Gain	6.083 dB

Fig (3. 50) Radiation pattern at 6.15 GHz: (a) E-plane, (b) H-plane, (c) 3D pattern.

3.7 1 × 2 SIW array

Pattern synthesis of an array has to consider different purposes, such as low side lobe level, beam synthesis, high directivity, gain and bandwidth. The purpose of our design is to increase gain, directivity and low side level.

An array antenna is a multiple of radiating elements in space where every single element that radiates individually will be combined with other radiating elements. This is to obtain an overall directional radiation pattern which is higher than the single antenna.

As shown in Fig (3. 51), the array antenna was designed using CST studio. The overall size for the structure is 100×25×0.787 mm^3 with microstrip transmission line 5×25×0.787 mm. The design parameters are shown below in table (3.2). Note that the diameter vias with the space to the sides is 4 mm.

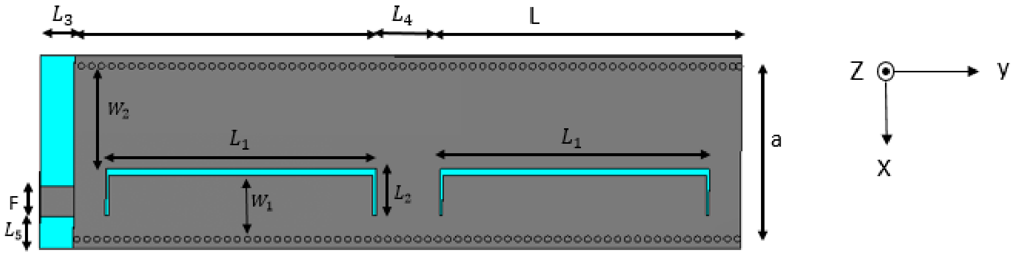

Fig (3. 51) 1 × 2 SIW array structure

Parameter	Optimised value (mm)
L	45.2
L1	40
L2	7
L3	5
L4	9.6
W	25
W1	9
W3	0.5
F	4

Table (3. 2) Parameters of 1 ×2 array of substrate integrated waveguide antenna.

The S-parameters shown in Fig (3. 52), the reflection coefficient at 5.15 GHz is below 10 dB with bandwidth 50 MHz. Nonetheless, the reflection coefficient at 5.5 GHz is -18 dB with bandwidth 42 MHz. The other modes are not matched well. It can be seen that the previous single antenna has only one resonant frequency in each mode. 1 × 2 array, each mode has two resonant frequency, both of an odd and even symmetry pair.

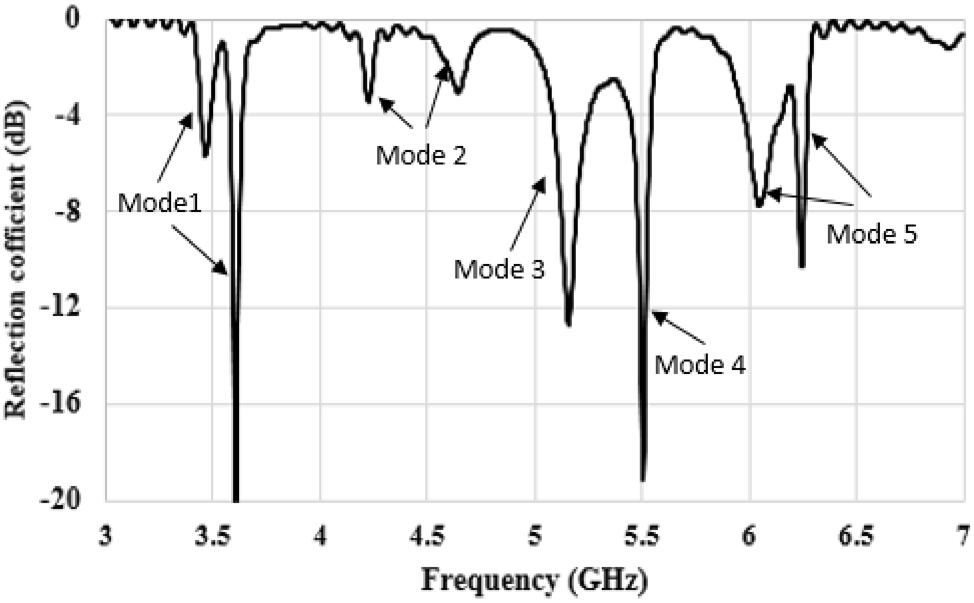

Fig (3. 52) S_{11} for the proposed 1 × 2 SIW

The electric field distribution of each mode will be described as follows:

Mode 1: The electric field distribution at 3.46 GHz and 3.6 GHz is shown in Fig (3. 53 a, b). At 3.46 and 3.6 GHz, the wave radiates at the widest section of the waveguide. The difference of the resonant frequencies due to 3.46 GHz are of even symmetry whilst at 3.6 GHz it is of an odd symmetry in phase variation.

Mode 2: At 4.22 GHz and 4.6 GHz, the electric field distribution is shown in Fig (3. 53 c, d) which are the first order mode of the widest section in the longitudinal direction. A phase variation occurs at both resonant frequency.

The electric field distribution at 5.15 GHz and 5.56 GHz are shown in Fig (3. 53 e, f) which is well matched. They are Mode 3 and Mode 4 respectively.

Fig (3. 53 g, h) shows the field at the first order mode of the narrower section at 6.08 GHz and 6.24 GHz. Nonetheless, due to the mismatching lead, two modes radiating in one single slot more than the other occur.

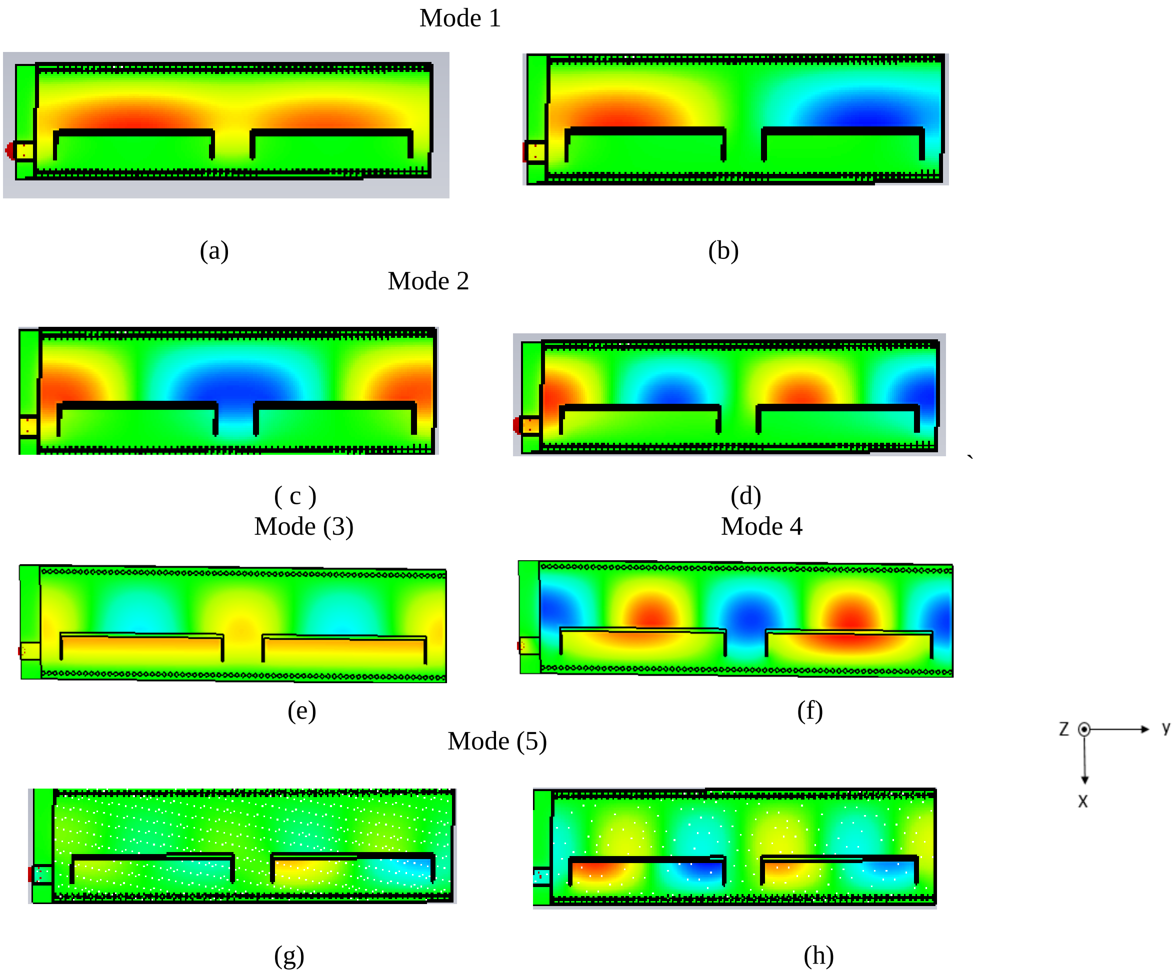
Mode 1

(a) (b)

Mode 2

(c) (d)

Mode (3) Mode 4

(e) (f)

Mode (5)

(g) (h)

Fig (3. 53) Z-component of E-field at: (a) 3.46 GHz. (b) 3.6 GHz. (c) 4.22 GHz. (d) 4.6 GHz. (e) 5.16 GHz. (f) 5.56 GHz. (g) 6.08 GHz. (h) 6.24 GHz.

The far field radiation pattern is shown in Fig (3. 54) at 5.16 GHz. The Electric field in polar plot shows that the main lobe magnitude is 10.3 dB and deviates at 5^0 from its main direction. The 3-dB angular width is 99.6 degree with side lobe level of -9.3 dB as shown Fig (3. 54 a). The H-field polar plot shows that the main lobe magnitude is 10.3 dB and it deviates 1^0 from the normal line, the angular width is 30.6^0 and the side lobe level is -9.6 dB. The 3D plot shows the radiation efficiency is 0.02 dB and total efficiency is -0.24 dB. The gain at 5.15 GHz is increased from 7 dB in single array to 10.33 dB. We can notice that a significant back lobe occurs. Thereby, an extendable metal at both sides of the array might reduce the effect of back lobe on the radiation pattern.

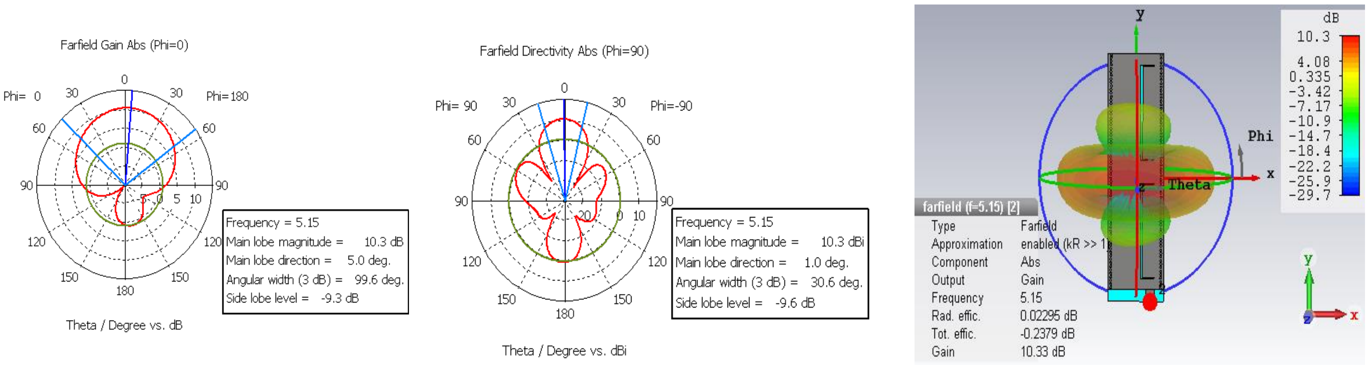

Frequency = 5.15
Main lobe magnitude = 10.3 dB
Main lobe direction = 5.0 deg.
Angular width (3 dB) = 99.6 deg.
Side lobe level = -9.3 dB

Frequency = 5.15
Main lobe magnitude = 10.3 dBi
Main lobe direction = 1.0 deg.
Angular width (3 dB) = 30.6 deg.
Side lobe level = -9.6 dB

farfield (f=5.15) [2]
Type Farfield
Approximation enabled (kR >> 1)
Component Abs
Output Gain
Frequency 5.15
Rad. effic. 0.02295 dB
Tot. effic. -0.2379 dB
Gain 10.33 dB

(a) (b) (c)

Fig (3. 54) Radiation pattern at 5.15 GHz: (a) E-plane, (b) H-plane, (d) 3D pattern.

Moreover, the far field radiation pattern shown in Fig (3. 55) indicates that the electric field in polar plot is at 5.5 GHz. This shows that the main lobe magnitude is 10.1 dB and is deviated at a 8^0 from its main direction. The 3 dB angular width is 97.3^0 with side lobe level is -10.9 dB as shown in Fig (3. 55a). The H-field polar plot shown in Fig (3. 55c), demonstrates that the main lobe magnitude is 10.1 dB and deviated 1^0 from the normal line. It also shows that the angular width is 30.5^0 and the side lobe level is -10.5 dB. The 3D plot as shown in Fig (3. 55b, d) shows that the radiation efficiency is 0.087dB and total efficiency is -0.16 dB. The gain at 5.5 GHz is increased from 6.78 dBi to 10.15 dBi.

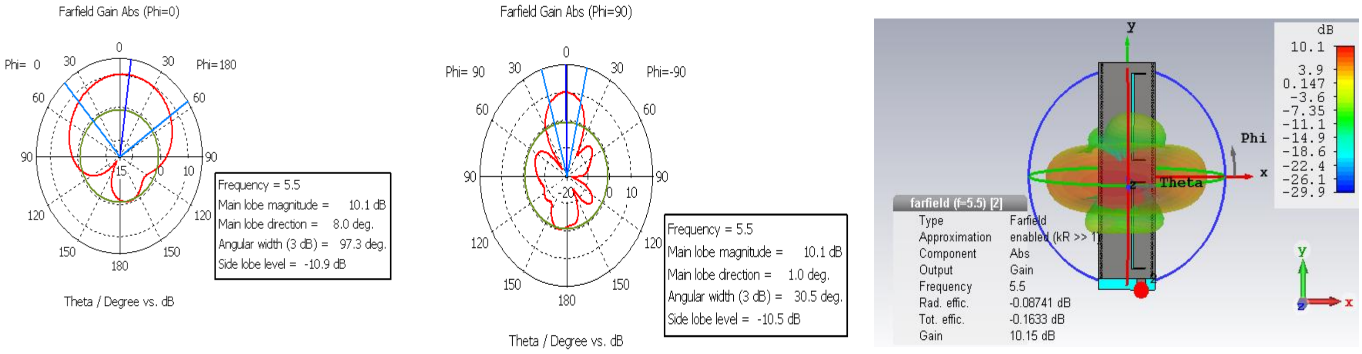

Frequency = 5.5
Main lobe magnitude = 10.1 dB
Main lobe direction = 8.0 deg.
Angular width (3 dB) = 97.3 deg.
Side lobe level = -10.9 dB

Frequency = 5.5
Main lobe magnitude = 10.1 dB
Main lobe direction = 1.0 deg.
Angular width (3 dB) = 30.5 deg.
Side lobe level = -10.5 dB

farfield (f=5.5) [2]
Type Farfield
Approximation enabled (kR >> 1)
Component Abs
Output Gain
Frequency 5.5
Rad. effic. -0.08741 dB
Tot. effic. -0.1633 dB
Gain 10.15 dB

(a) (b) (c)

Fig (3. 55) Radiation pattern at 5.5 GHz: (a) E-plane, (b) H-plane, (c) 3D pattern.

The radiation plot at Mode 1 at 3.46 GHz is shown in Fig (3. 56). The E-field polar plot shows that the main lobe magnitude is 7.6 dB and the angular width is 110^0 and the side lobe level is -5.8 dB. H-plane polar plot shows that the main lobe magnitude is 7.67 dB and has an offset of 3^0 from its main direction, the angular width is 42^0 with side lobe level -5.9 dB. The 3D radiation pattern shows that the radiation efficiency and total efficiency is 0.511 dB and -1.9 dB. The gain at 3.46 GHz is 7.66 dBi.

The odd mode radiation pattern at 3.6 GHz is shown in Fig (3. 57). In H-plane, the radiation shows in two phase with main lobe magnitude being at 6.05 GHz. In E-plane, the main lobe offset from its main beam direction by 17^0. The radiation efficiency and total efficiency is -0.64 and -0.74 dB respectively with gain 6 dBi.

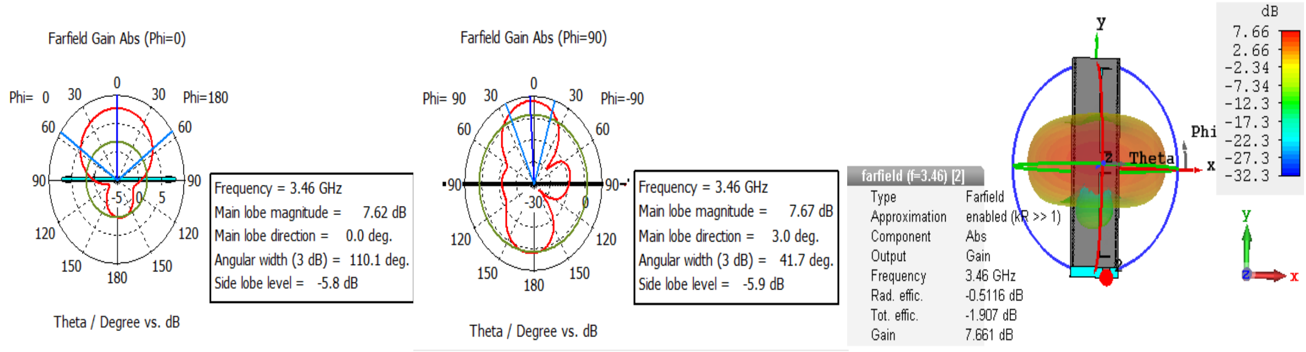

(a) (b) (c)

Fig (3. 56) Radiation pattern at 3.46 GHz: (a) E-plane, (b) H-plane, (c) 3D pattern.

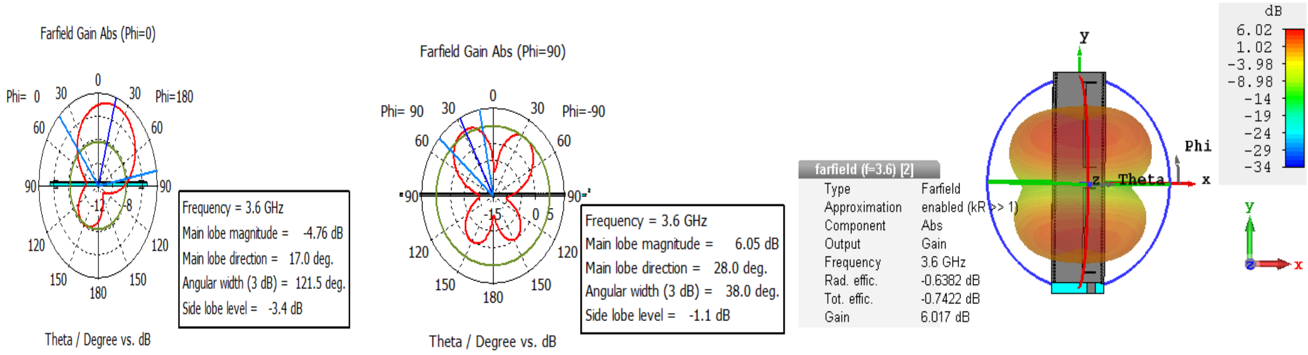

(a) (b) (c)

Fig (3. 57) Radiation pattern at 3.6 GHz: (a) E-plane, (b) H-plane, (c) 3D pattern.

3.8 2 × 2 dual band SIW

To further increase the gain, a 2 × 2 array of substrate integrated waveguide array antenna are demonstrated with a challenge to increase gain without affecting matching, the bandwidth and other performance of antenna.

Fig (3. 58) shows the simulated and fabricated design with the parameters' dimension being in Table (3.3). The 2 × 2 SIW array has been rescaled to obtain a tri-band antenna that radiates at 2.8 GHz, 5 GHz (use for Wi-Fi) and 5.2 GHz (use for WLAN).

The width of the waveguide (a) is set to 29 mm and the widest section of the waveguide (w_2) set to 19 mm. An increased length of the slots L_2 to 8 mm is shown in Fig (3. 58).

The feeding line is a 50 Ω microstrip line to provide transitions between microstrip and SIW. A T-shape 1/2 power divider, which is symmetric and in parallel, feeds at both sides to achieve the required aperture distribution equally. Table (3.3) shows all the parameters dimensions of the structure and feeding line.

The top plane is extended at the two sides of the structure, to reduce back lobes and enhance the main lobe. This structure has an open termination to allow additional modes to exist on the structure that would not exist for a short circuit boundary. Since the implementation is in SIW, there is little radiation from the open boundary termination.

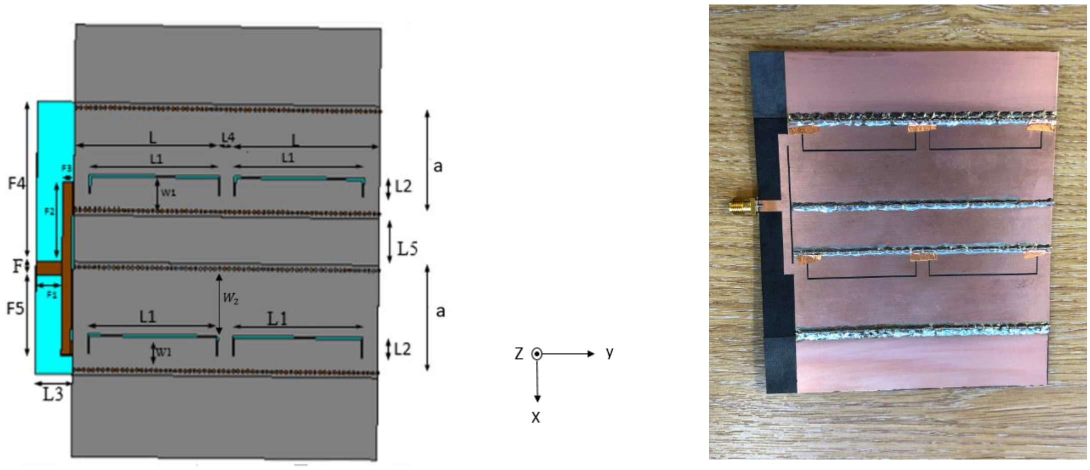

(a) (b)

Fig (3. 58) 2 by 2 SIW: (a) simulated design, (b) Fabricated design.

Parameter	Optimised value (mm)
L	45.2
$L1$	40
$L2$	8
$L3$	16
a	29
W_1	9
W_2	19
$L5$	15
F	4
$F1$	8
$F2$	23
$F3$	15
$F4$	46
$F5$	24

Table (3. 3) Parameters dimensions of 2 × 2 SIW array.

3.9 Comparison between simulation and measurements

After optimising with CST simulation, the design fabricated and we measured the S-parameters using a coaxial SOLT (Short Open Load and Thru) method. A comparison made between simulation and measurements is shown in Fig (3. 59). The S-parameter show a good agreement between measurements and simulation. A small tuning is shown in Mode 1 and Mode 2 in simulation whilst in measurements it disappears. The measurements show that the S-parameter is slightly less than simulation due to measurements and fabrication error.

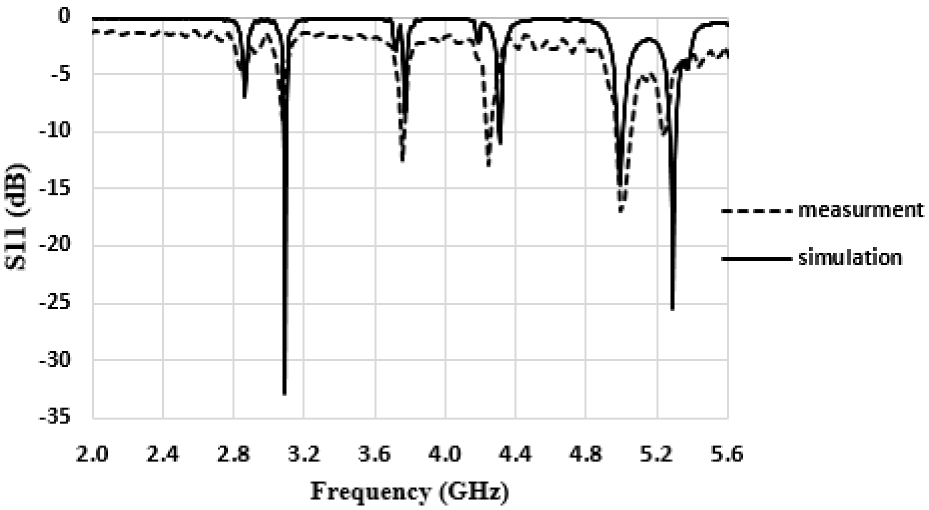

Fig (3. 59) Comparison of S_{11} between measurement and simulation for 2 × 2 SIW array

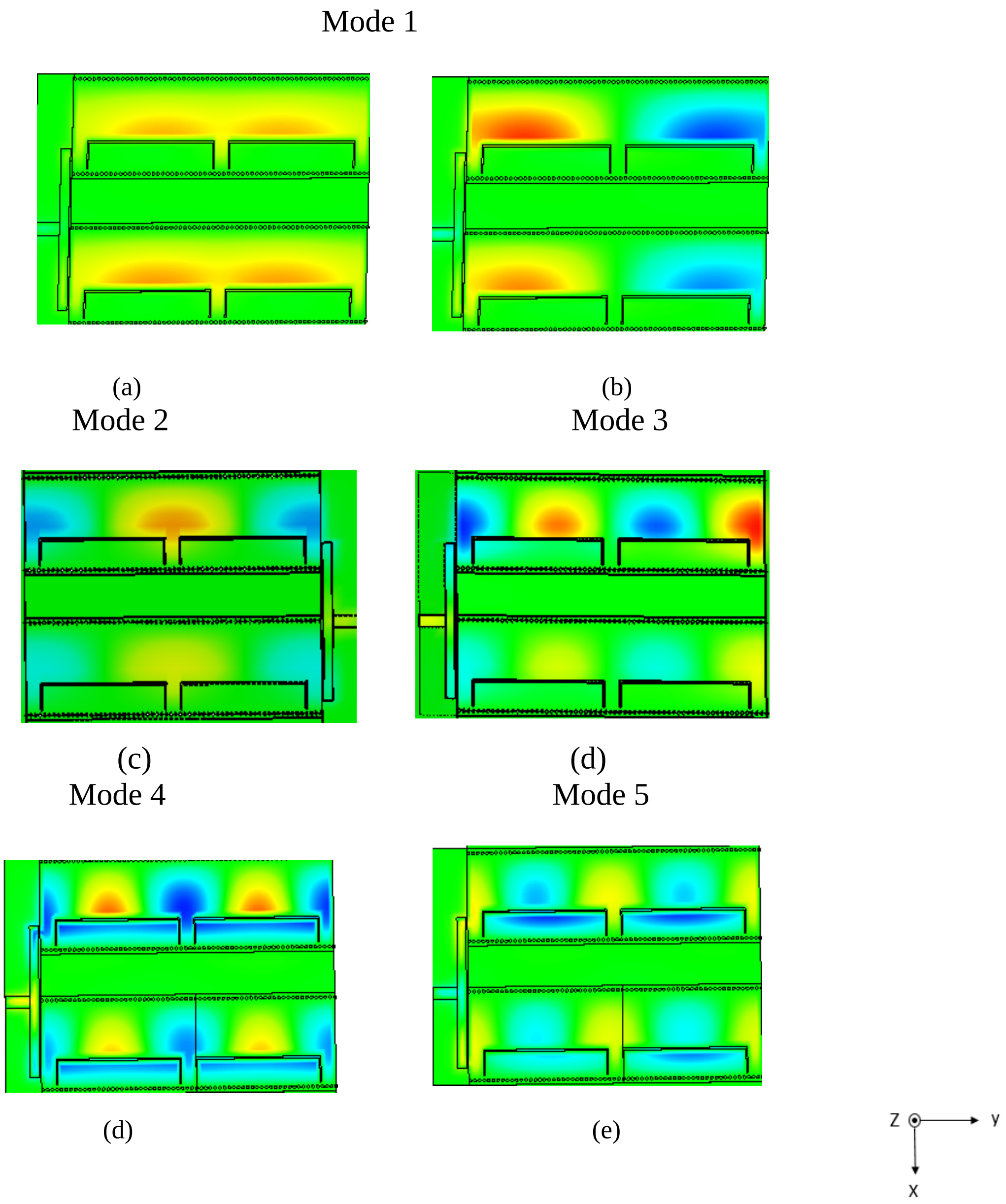

Fig (3. 60) Electric field distribution at 2 × 2 array: (a) Mode 1 (2.86 GHz and 3 GHz). (b) Mode 2 (3.77 GHz). (c) Mode 3 (4.31 GHz). (d) Mode 4 (5 GHz). (e) Mode 5 (5.2 GHz).

The electric field distribution for each mode is shown in Fig (3. 60). Due to the rescaling of the SIW array, the width of the waveguide (a) is set to 29 mm and thereby the modes has been slightly changed.

Mode 1 is resonant at the wide section of the waveguide at 2.86 and 3 GHz but with odd and even symmetry respectively. Mode 2 is the first order mode at the widest section of the waveguide. Mode 3 is the second order mode at the widest section and it resonance at 5 GHz.

Mode 4 is the first order Mode of the narrower section and it is affected by the length L_2, According to Fig (3. 41) in Section 3.3 , by increasing the length L_2, the resonance Mode 4 reduces. In contrast, slot length L_2 may have a slight effect to Mode 1.

Fig (3. 61) at 5 GHz, the comparison has been made between measurements and simulation which are shown to be in good agreement. In H-plane using CST, the main lobe magnitude is 12 dB and it offsets 1^0 from its main direction. The angular width is 37.4 dB and the side lobe level is -7.8 dB. The radiation efficiency at 5 GHz is -0.14 dB while the total efficiency is -0.234 dB and the gain increased to 11.92 dBi.

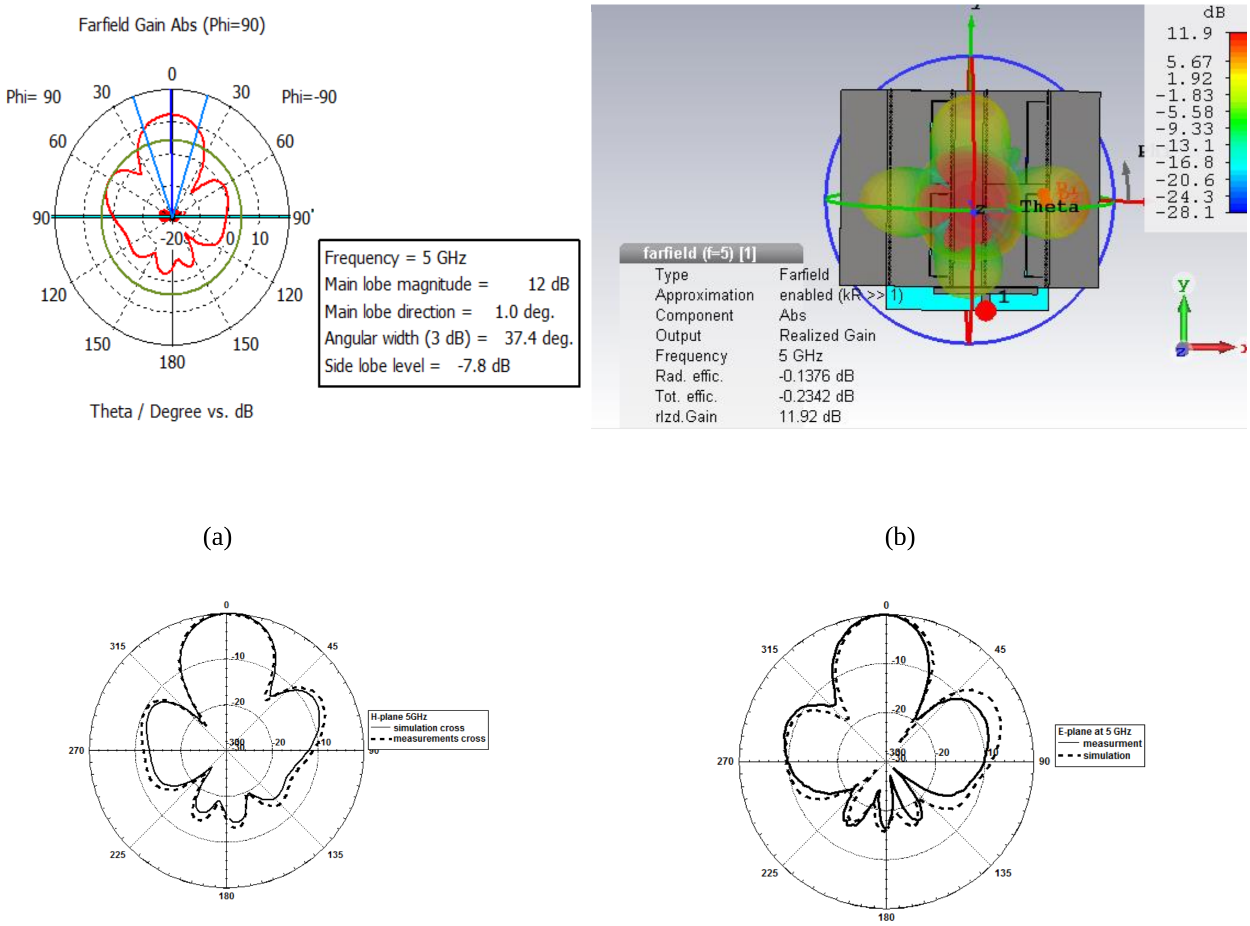

Frequency = 5 GHz
Main lobe magnitude = 12 dB
Main lobe direction = 1.0 deg.
Angular width (3 dB) = 37.4 deg.
Side lobe level = -7.8 dB

farfield (f=5) [1]

Type	Farfield
Approximation	enabled (kR >> 1)
Component	Abs
Output	Realized Gain
Frequency	5 GHz
Rad. effic.	-0.1376 dB
Tot. effic.	-0.2342 dB
rlzd.Gain	11.92 dB

(a)

(b)

(c)

(d)

Fig (3. 61) Radiation pattern at 5 GHz: (a) H-plane, (b) 3D pattern, (c) H-plane comparison, (d) E-plane comparison.

The second resonance frequency of tri-band antenna Mode 4 is at 5.24 GHz. Fig (3. 62) shows a good agreement of radiation pattern between measurements and simulation. In H-plane polar plot using CST, the main lobe magnitude is 11.9 dB having angular width of 35.6^0 and the side lobe level is -12.4 dB.

The radiation measurement is slightly different from the simulation, this difference might be caused by the error of fabrication dimensions.

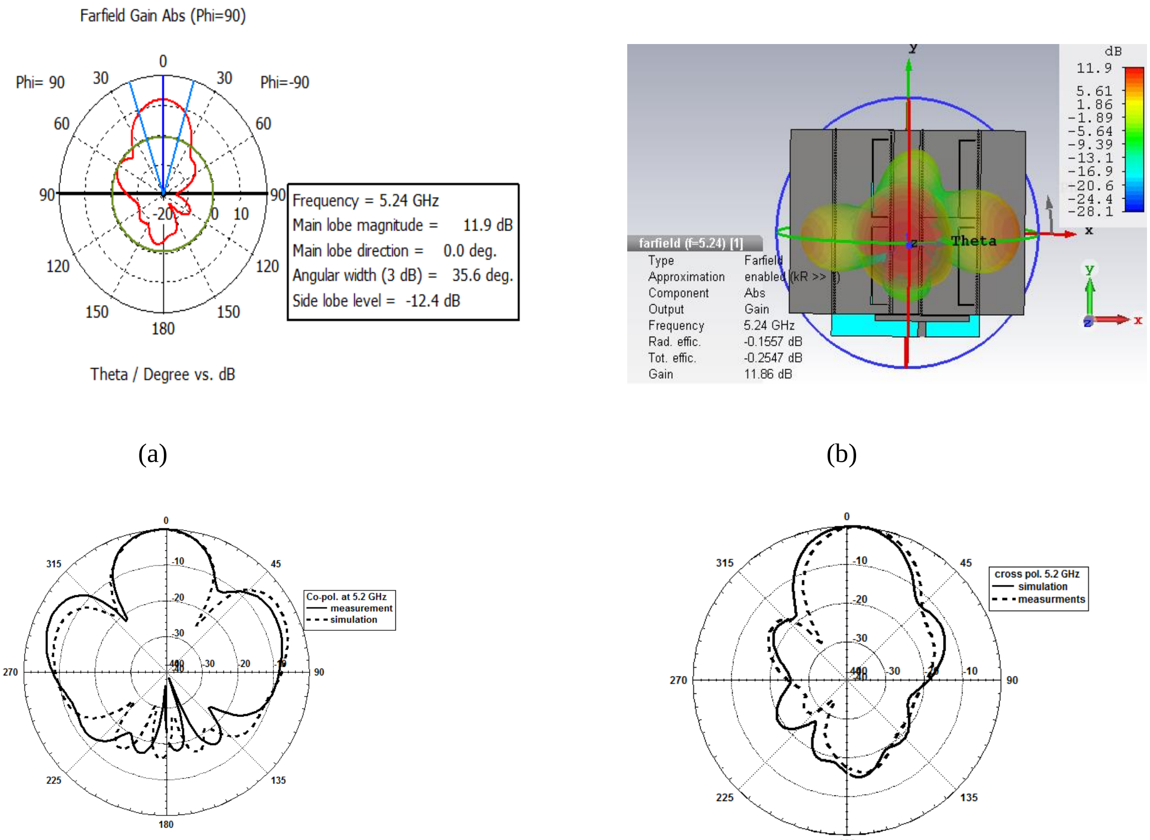

Frequency = 5.24 GHz
Main lobe magnitude = 11.9 dB
Main lobe direction = 0.0 deg.
Angular width (3 dB) = 35.6 deg.
Side lobe level = -12.4 dB

farfield (f=5.24) [1]

Type	Farfield
Approximation	enabled (kR >> 1)
Component	Abs
Output	Gain
Frequency	5.24 GHz
Rad. effic.	-0.1557 dB
Tot. effic.	-0.2547 dB
Gain	11.86 dB

(a) (b)

(c) (d)

Fig (3. 62) Radiation pattern at 5.24 GHz: (a) H-plane, (b) 3D pattern, (c) E-plane comparison, (d) H-plane comparison.

The gain of 2 × 2 array antenna has been measured using standard horn antenna .A comparison of gain between simulation and measurement has been done as shown in Fig (3. 63).

At 5 GHz the gain is 11.9 dBi for both simulation and measurement. At 5.24 GHz the simulation gain is 11.8 dBi while in measurement it is slightly less and equal to 11.2 dBi. We can notice from the graph that the range from 5 GHz to 5.26 GHz is above 10 dB which can be considered as wide band antenna.

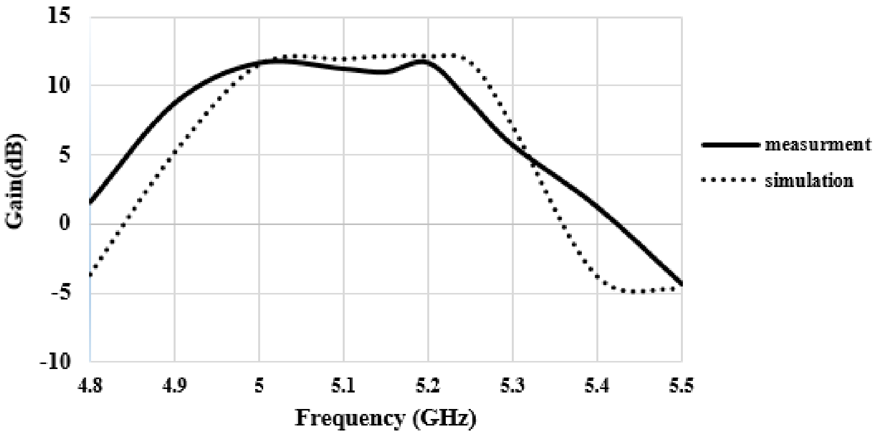

Fig (3. 63) Comparison of gain between measurement and simulation against frequency for the 2 × 2 SIW array.

Mode 1 at 2.86 GHz, the far field radiation pattern is shown in Fig (3. 64), the radiation efficiency and total efficiency is -0.5 and -1.47 dB respectively. The gain has been increased to 9.1 dBi. In H-plane the main lobe magnitude is 8.99 dB and has an angular width of 59^0 with side lobe level of -21.2 dB. In E-plane the angular width is 64^0 and side lobe level of -19.3 dB.

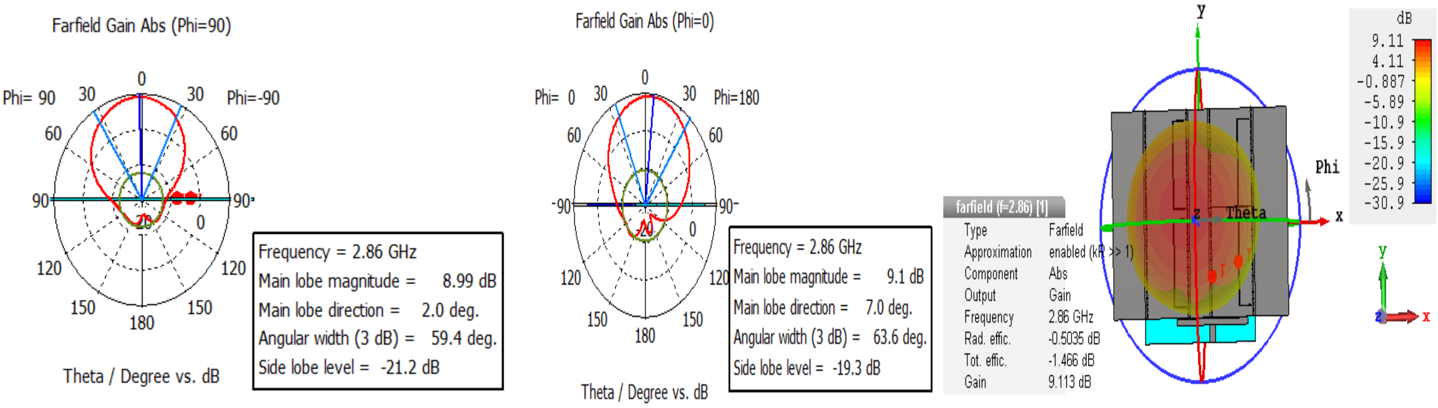

Frequency = 2.86 GHz
Main lobe magnitude = 8.99 dB
Main lobe direction = 2.0 deg.
Angular width (3 dB) = 59.4 deg.
Side lobe level = -21.2 dB

Frequency = 2.86 GHz
Main lobe magnitude = 9.1 dB
Main lobe direction = 7.0 deg.
Angular width (3 dB) = 63.6 deg.
Side lobe level = -19.3 dB

farfield (f=2.86) [1]

Type	Farfield
Approximation	enabled (kR >> 1)
Component	Abs
Output	Gain
Frequency	2.86 GHz
Rad. effic.	-0.5035 dB
Tot. effic.	-1.466 dB
Gain	9.113 dB

Fig (3. 64) Radiation pattern at 2.86 GHz (Mode 1): (a) H-plane. (b) E-plane, (c) 3D pattern.

3.10 Conclusion

A tri-band substrate integrated waveguide antenna has been developed and demonstrated. The antenna has an open end which is different from the conventional waveguide. The antenna radiates at 5.1, 5.8 GHz and 3.5 GHz. The antenna has two sections of the slots L_2 which is perpendicular to the main slot L_1. This addition of the slots give the ability of tuning the antenna.

The gain at 5.1 and 5.8 GHz is above 6 dB which can be considered that the antenna as a broadband antenna and that the 3.5 GHz the gain is 4 dBi. A good agreement of S-parameter and radiation pattern between measurements and simulation.

To increase the gain, a 2 × 2 array antenna was developed and rescaled to radiate at 2.8, 5 and 5.2 GHz. The antenna has an increase in gain to above 11 dBi in the region 5- 5.2 GHz, the gain at 2.8 GHz is 9 dBi. Again, the S-parameter and the radiation pattern shown in good agreement between simulation and measurements.

The tri-band antenna might be useful in 5G applications (3-6 GHz) and can be rescaled to higher frequencies.

3.11 References

[1] J. Row, “Dual-Frequency Triangular Planar Inverted-F Antenna,” EEE Transactions on antennas and Propagation,vol. 53, no. 2, pp. 2004–2006, 2005.

[2] S. Mukherjee and A. Biswas, “Design of dual band and dual-polarised dual band SIW cavity backed bow-tie slot antennas,” IET Microwaves, Antennas & Propagation ,vol. 10, pp. 1002–1009, 2016.

[3] A. Srivastava, R. K. Chaudhary, A. Biswas, and M. J. Akhtar, “Dual-band L-shaped SIW Slot Antenna,” 2013 Int. Conf. Microw. Photonics, vol. 1, pp. 1–3, 2013.

[4] Q. Zhang, S. Member, Q. Zhang, and S. Member, “Dual-Band and Dual-Polarized Leaky-Wave Antenna Based on Slotted SIW,” IEEE Antennas Wirel. Propag. Lett., vol. 18, no. 3, pp. 507–511, 2019.

[5] A. A. Khan, S. Member, M. K. Mandal, and S. Member, “Compact Self-Diplexing Antenna Using Dual-Mode SIW Square Cavity,” IEEE Antennas Wirel. Propag. Lett., vol. 18, no. 2, pp. 343–347, 2019.

[6] W. Hong, “Half Mode Substrate Integrated Waveguide- A New Guided Wave Structure for Microwave and Millimeter Wave Application.pdf,” Proc. Jt. 31st Int. Conf. Infrared Millim. Waves 14th Int. Conf. Terahertz Electron, vol. 152, p. 4244, 2006.

[7] M. Casaletti, G. Valerio, J. Seljan, M. Ettorre, and R. Sauleau, “A full-wave hybrid method for the fast analysis of SIW-based antennas,” 2013 7th Eur. Conf. Antennas Propag., no. Eucap, pp. 3843–3846, 2013.

[8] Q. Lai, S. Member, C. Fumeaux, and S. Member, “Characterization of the Propagation Properties of the Half-Mode Substrate Integrated Waveguide,” IEEE Trans. Microw. Theory Tech., vol. 57, no. 8, pp. 1996–2004, 2009.

[9] L. Yan, W. Hong, G. Hua, J. Chen, K. Wu, and T. J. Cui, “Simulation and Experiment on SIW Slot Array Antennas,” IEEE Microw. Wirel. Compon. Lett., vol. 14, no. 9, pp. 446–448, 2004.

[10] A. J. Farrall and P. R. Young, “Integrated waveguide slot antennas,” Electron. Lett, vol. 40, no. 16, pp. 974–975, 2008.

Chapter Four

Graphene for Waveguide Tuning and Calibration

4.1 Introduction

Graphene is the thinnest and strongest two dimensional material composed of two honeycomb structures, of which carbon was experimentally discovered by Andre Geim in 2004 [1]. Many researches have focused on graphene material. This is due to its characteristics of mechanical, optical, thermal and electrical properties, all of which have supporting large electric current densities of 10^8 A/cm^2.

One of the main features of graphene is the tunable conductivity, which is similar to semiconductors such as silicon. These characteristics of graphene are studied by many researchers in microwave applications and nanotechnology, including waveguides [2] reflect arrays [3], antennas [4], phase shifters [5] and filters [6]. This feature of tunable conductivity suggest to produce high-speed transistors and other switching devices.

A graphene layer must be embedded onto a substrate. This is usually where the graphene is deposited on Si substrate with Sio_2 layer sandwich between graphene and Si as shown in Fig (4. 1). Graphene are affected by the dielectric substrate because of the plasmonic wavelength which depends on the permittivity of the substrate [7]. Thickness and roughness of substrate are also an influence on graphene.

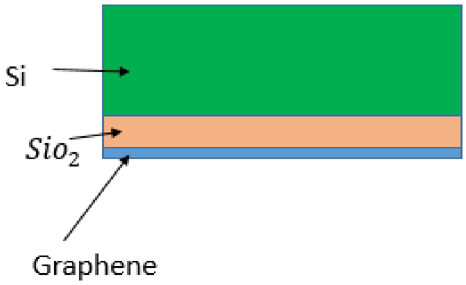

Fig (4. 1) Structure of Si-$Sio_2 - graphene$

This chapter presents the use of graphene in waveguides for tuning, by demonstrating the effect of sheet resistance of graphene, which depends on the chemical potential or the applied voltage.

Furthermore, some initial investigations into using layers of graphene as an impedance standards in waveguides that operating at millimeter-wave frequencies (50 to 75 GHz). At these frequencies, the size of the waveguide is relatively large and therefore it is ideal for testing initial designs of impedance standards. The size-scalability waveguide indicates that any designs found to work at low millimetre-wave frequencies should be able to be scaled. This is to operate at high millimetre-wave frequencies and ultimately at terahertz frequencies.

4.2 Literature review

In 2013 [8][9][10], the first hybrid graphene waveguide published in Fig (4. 2), has two types of multilayer of graphene waveguide which are presented in [8]. The first structure is a layer from Si-Sio_2- graphene-dielectric –strip-metal layers and the second structure is composed of Si-Sio_2-graphene- dielectric –graphene. To provide tuning, a biased voltage was applied to Sio_2 layer and the results shows smaller propagation loss which can be used in switches and polarizers.

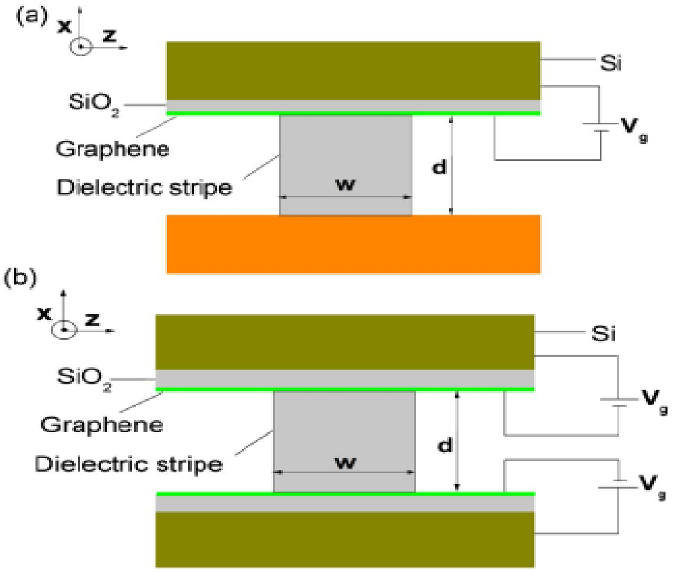

Fig (4. 2) Graphene waveguides: (a) Si–Sio_2–graphene–dielectric-stripe–metal,
(b) Si–Sio_2–graphene–dielectric–graphene–Sio_2–Si [8].

Zhang [11] presents a substrate integrated waveguide antenna which can be tuned dynamically using graphene as shown in Fig (4. 3). Two graphene sandwiches are placed inside the SIW. By applying a biased voltage ranging from 0 to 4 V to the graphene, the attenuation changed from 2 to 15 dB. The operating frequency range was 7 to 14.5 GHz.

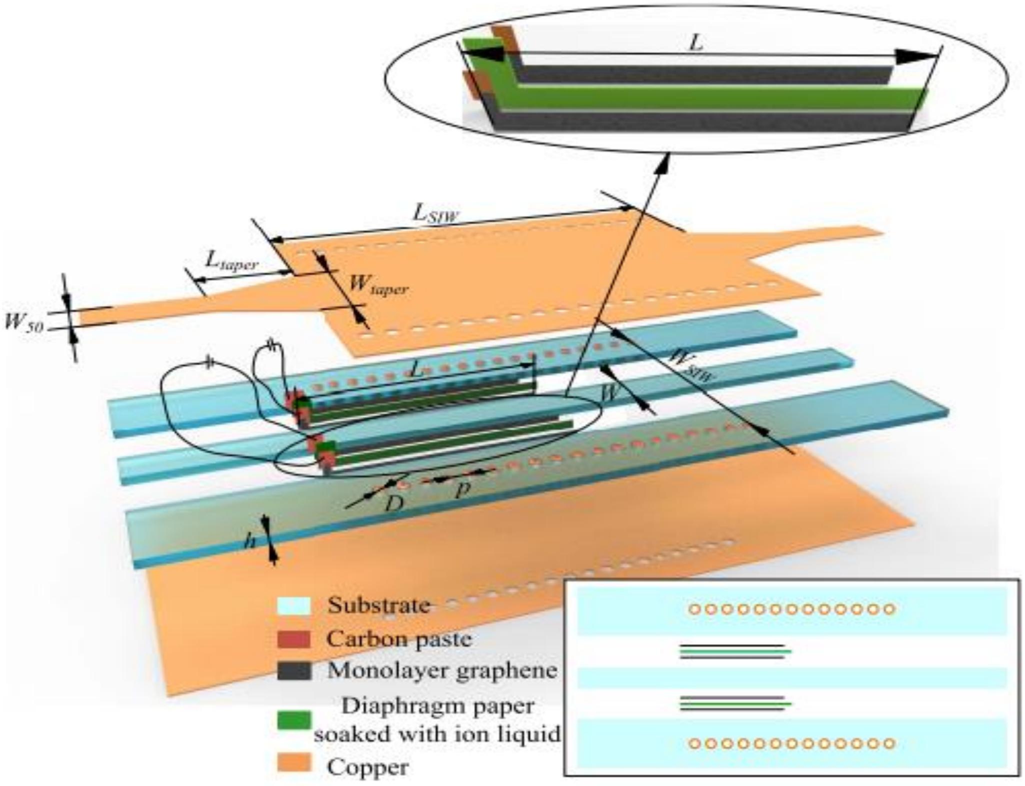

Fig (4. 3) Tuning SIW dynamically using graphene [11].

Ref [12] presents a microstrip attenuator using graphene pads between microstrip line and metal vias, which are positioned at the sides of the microstrip as shown in Fig (4. 4). The applied voltage variations change the insertion loss. The frequency range was 10 GHz and has achieved 25 dB tunability.

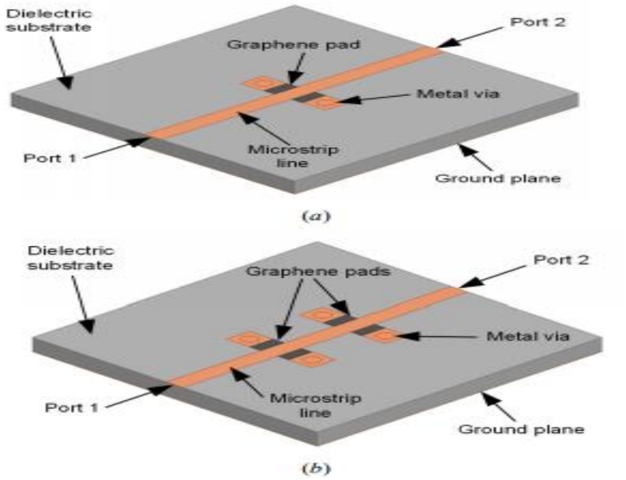

Fig (4. 4) Graphene- based tunable microstrip structure: (a) single pair graphene pad on microstrip line, (b) two pair of graphene pads places on microstrip line [12].

Ref [13], a tunable graphene superstrate has been used at Ka-band, to generate a radiation pattern reconfigurable antenna. The superstrate graphene consists of two symmetrical DC biased graphene-aluminia-silicon structures, separated by a dielectric slab. Fig (4. 5) shows the 3D structure of reconfigurable antenna. By applying the biased voltage variations between the graphene and silicon layer, the resistivity of graphene changes and achieves a tunable radiation gain. Nonetheless, this increased 6.15 dBi to 12 dBi and 3 dB beam width, increased from 22^0 to 40^0.

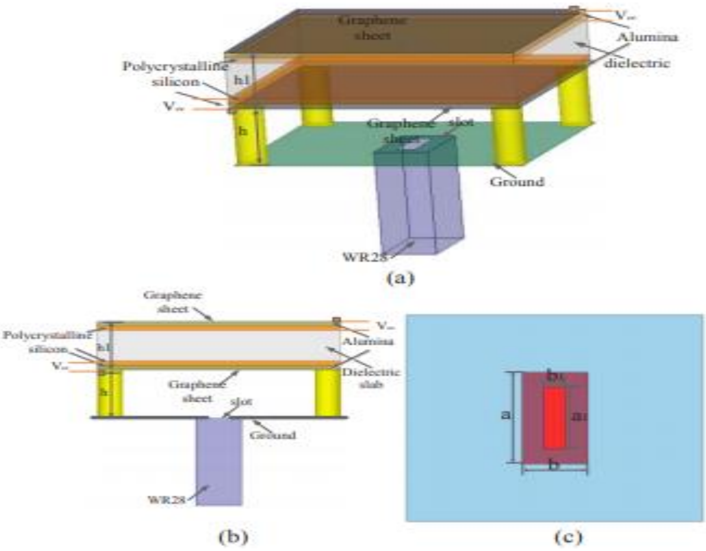

.

Fig (4. 5) 3D structure of reconfigurable antenna: (a) Cross section view, (b) Top view [13].

Ref [14] demonstrates a graphene based attenuator on a HMSIW, to obtain dynamically tunable attenuation. The attenuator is a graphene sandwich structure (GSS) on a half mode of the substrate. The tuning is achieved by applying the bias voltage on GSS (0 V to 4 V), which changes the surface impedance of graphene. Fig (4. 6) shows the structure of the graphene based attenuator on HMSIW and the structure with measurements. The operating frequency range was 7.7 GHz to 19 GHz and the attenuation increased from 3 dBi to 14 dBi.

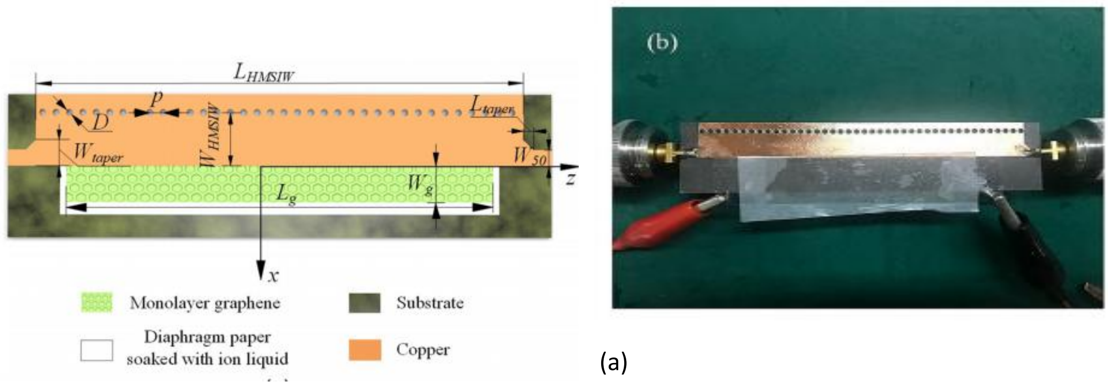

(a)

(b)

Fig (4. 6) (a) Configuration of the graphene-based HMSIW attenuator. (b) Structure with biased voltage [14].

4.3 Electromagnetic model of graphene

The surface conductivity of graphene plays an important role in many applications, as mentioned in the previous section.

The graphene sheets can be used as a conductive sheet for tuning. Starting from Kubo formula below THz frequencies, it simply follows a Drude model [15].

$$\sigma_D \cong -j\frac{q_e^2 K_B T}{\pi\hbar^2(\omega - j2\Gamma)}\left[\frac{\mu_c}{K_B T} + 2ln(1 + e^{-\frac{\mu_c}{K_B T}})\right] \qquad (4.\ 1)$$

The surface conductivity of graphene (σ_D) depends on different parameters as shown in Eq (4.1) :

T : Room temperature = 300 kelvin.

q_e : Electron charge = 1.602 $\times 10^{-19}$ (Coulombs).

K_B : Boltzmann's constant = 1.38$\times 10^{-23}$ (J·K^{-1}).

$\hbar$: Reduced Planck's is 1.054 $\times 10^{-34}$ (J.s).

Scattering rate $\Gamma = 1/2T_s$ with T_s = 0.25 ps.

μ_c : is the chemical potential depending on the applied electrostatic bias $\mathrm{E_{bias}}$

Several studies measure the surface conductivity of graphene as shown in Fig (4. 7) [16].

By inserting the graphene inside the waveguide, the surface conductivity has been measured at frequency range 8-12 GHz and 25 -40 GHz [16], assuming that the chemical potential $\mu_c =$ 0 and the scattering rate $\Gamma = \frac{1}{0.5}$ ps and in room temperature. As shown in Fig (4. 7), below 100 GHz, the real part of surface conductivity remains constant, then starts to decrease after 100 GHz.

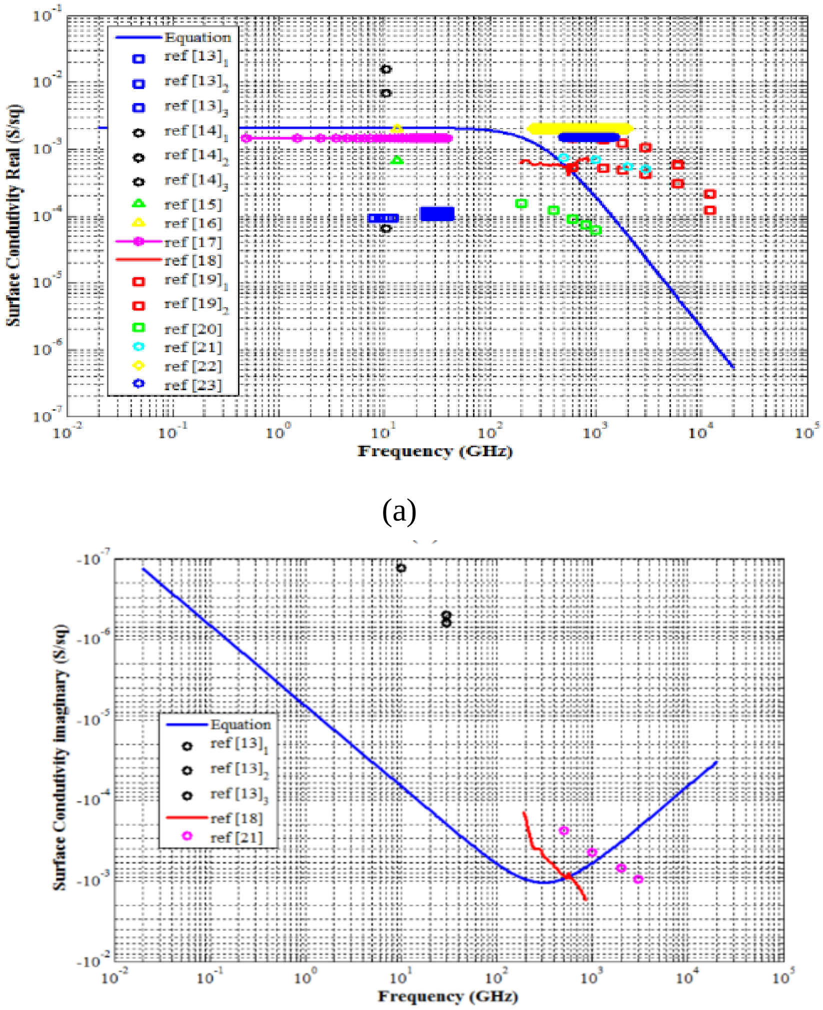

(a)

(b)

Fig (4. 7) Surface conductivity against frequency: (a) real part, (b) imaginary part [16].

Ref [17] shows the relationship between the chemical potential μ_c and electrostatic bias E_{bias} which can be easily tuned from -1 eV to 1 eV as shown in Fig (4. 8).
The relationship between the chemical potential μ_c and the electrostatic bias E_{bias} is given by [17].

$$\frac{\varepsilon_0 \pi \hbar^2 v_f^2}{q_e} E_{bias} = \int_0^\infty \varepsilon\left[n_f(\varepsilon) - n_f(\varepsilon + 2\mu_c)\right] d\epsilon \tag{4. 2}$$

Where n_f is the Fermi-Dirac distribution and given by:

$$n_f(\epsilon) = \frac{1}{1+e^{(\epsilon-\mu_c)/k_B T}} \tag{4. 3}$$

Where

ϵ : is the energy.

v_f : is the Fermi velocity in graphene $\approx 10^6$ m/s.

The electric bias as shown in Fig (4. 8), has a range from (-10 to 10) × 10^{10} Vm^{-1} . This means that for tuning the structure, a high bias voltage or a reduced size of the structure is needed to tune the structure.

:

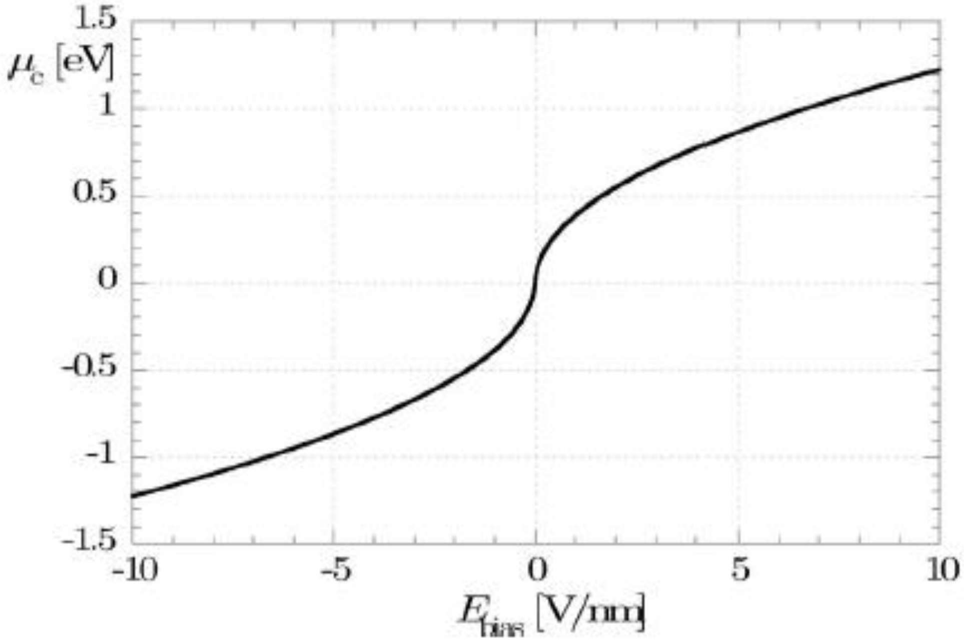

Fig (4. 8) Relationship between chemical potential and electrostatic bias [17].

Therfore, by assuming the electric bias is equal to zero, the chemical potential μ_c is equal zero. Using equation (4.1), the conductivity of graphene $\sigma_0 = \sigma_{D'} - j\sigma_{D''}$ against frequency range from 0 to 1000 GHz is shown in Fig (4. 9a), with the absence of any bias field and assuming $\mu_c = 0$. The minus sign of the imaginary part of $j\sigma_{D''}$ is used to represent both real and imaginary part on the same plot.

A significant change of complex conductivity appear significantly above 10 GHz to THz.

It is evident that the conductivity is frequency-dependent and varies as the change of μ_c. By applying an external field or modifying the type and density of carriers as shown in Fig (4. 9b), a significant change of conductivity increase.

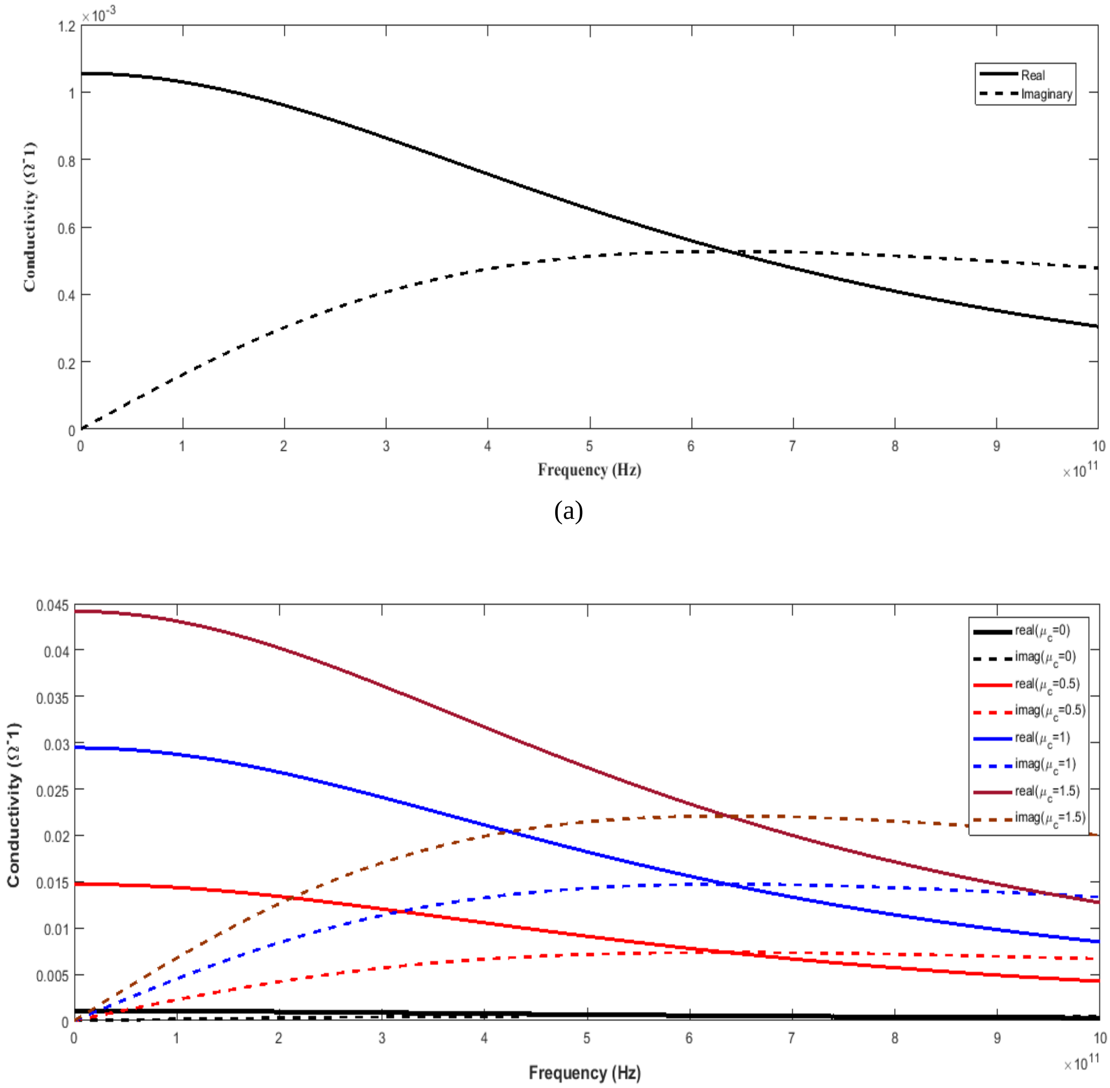

(a)

(b)

Fig (4. 9) Conductivity of graphene $\sigma_0 = \sigma_{D'} - j\sigma_{D''}$ against frequency: (a) $\mu_c = 0$, (b) variation of μ_c (0 to 1.5 eV).

To find sheet impedance of graphene:

$$Z_s = R_s + jX_s \tag{4.4}$$

$$R_s = 1/\sigma_0 \tag{4. 5}$$

As shown in Fig (4. 10) and Fig (4. 11), by increasing μ$_c$ or the applied voltage, the resistance and X_s (inductance) decreases.

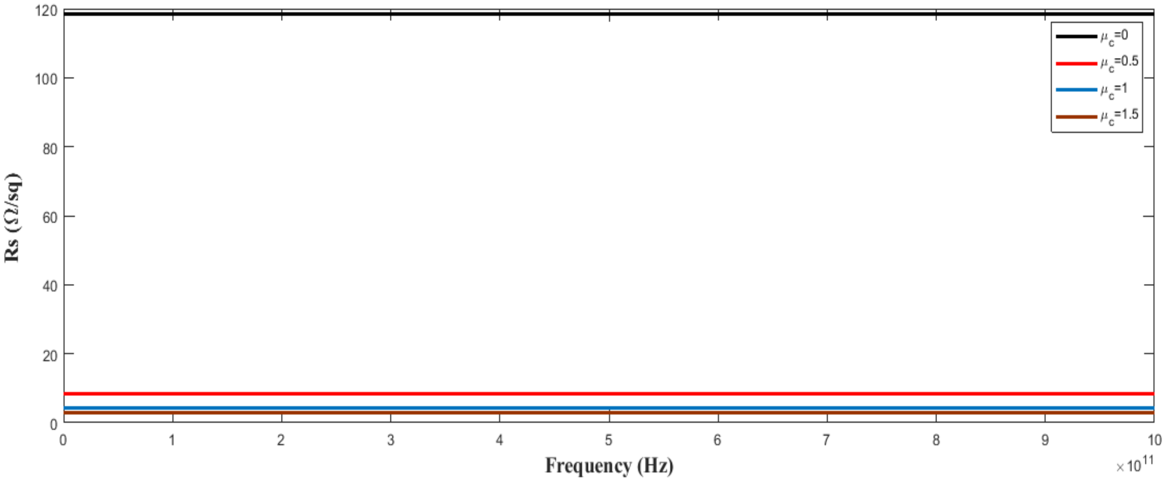

Fig (4. 10) Real part of sheet impedance against frequency with variation of μ_c.

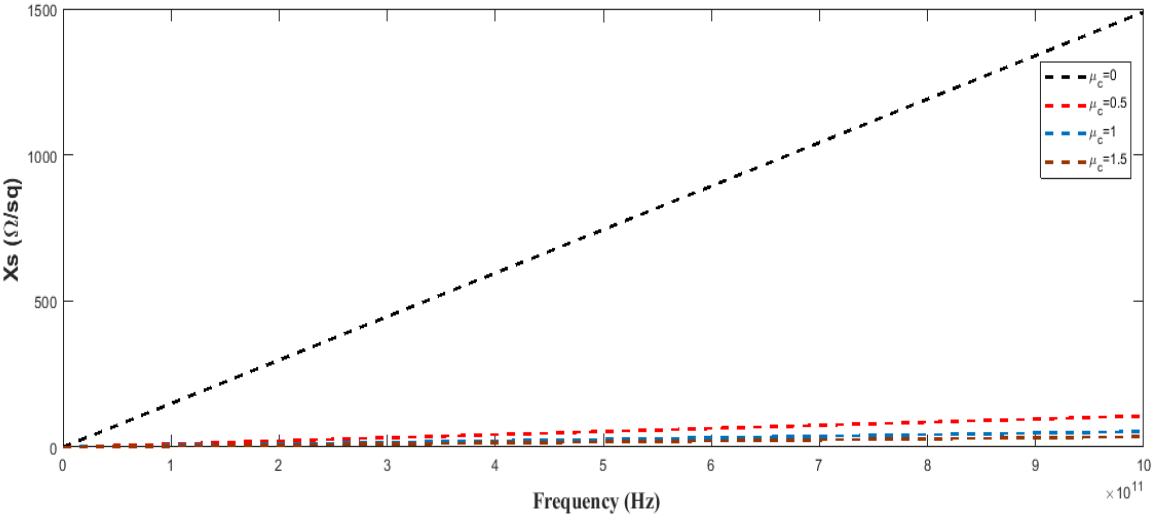

Fig (4. 11) Imaginary part of sheet impedance against frequency with variation of μ_c.

4.4 Tunable substrate integrated waveguide using silicon dioxide graphene

Ref [18] presents a travelling wave attenuator of slotted SIW, operating at a frequency range from 2 GHz to 6 GHz as shown in Fig (4. 12).

By adding the slot along the waveguide, the waveguide is splits into two regions; the section of length L_1 and the section of length L_2.

If the slot fully open, the SSIW works on half mode (TE$_{1/2,0}$) at the section of length L_1. The cut off frequency at the half mode is:

$$f_{c(1/2,0)} = \frac{c}{4L_1\sqrt{\varepsilon_r}} \tag{4.6}$$

If the slot is short, it goes back as full wave standard rectangular SIW, at section of length $a = L_1 + L_2 + W$, the cut off frequency at full wave is:

$$f_{c(1,0)} = \frac{c}{2a\sqrt{\varepsilon_r}} \tag{4.7}$$

The structure of Fig (4. 13), has $L_1 = 15$ mm, $L_2 = 5$ mm, $W = 0.5$mm, $b = 1.575$, relative permittivity $\varepsilon_r = 2.2$ and the length of the waveguide is 135 mm. A silicon PIN diodes placed across the slot of the substrate integrated waveguide to change the resistance from 5000 to 5 Ω by using a biased voltage. The loading resistors are spaced at a 5mm interval.

When the resistance is large (300-5000) Ω, the slot acts as an open circuit and the waveguide works on half mode (TE$_{1/2,0}$), at the cut off frequency $f_c = 3.4$ GHz of width L_1. A variable attenuator is shown in Fig (4. 13).

When the resistance has a small value (5-50) Ω, the slot acts as a short circuit and the waveguide works at full mode (TE$_{1,0}$), at the cut off frequency $f_c = 5.7$ GHz of width $(L_1 + w + L_2)$ a variable attenuator is obtained.

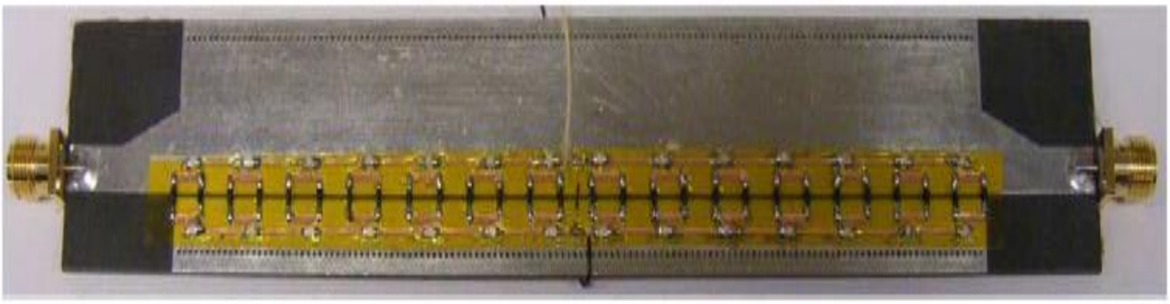

Fig (4. 12) Structure of slotted SIW attenuator [18]

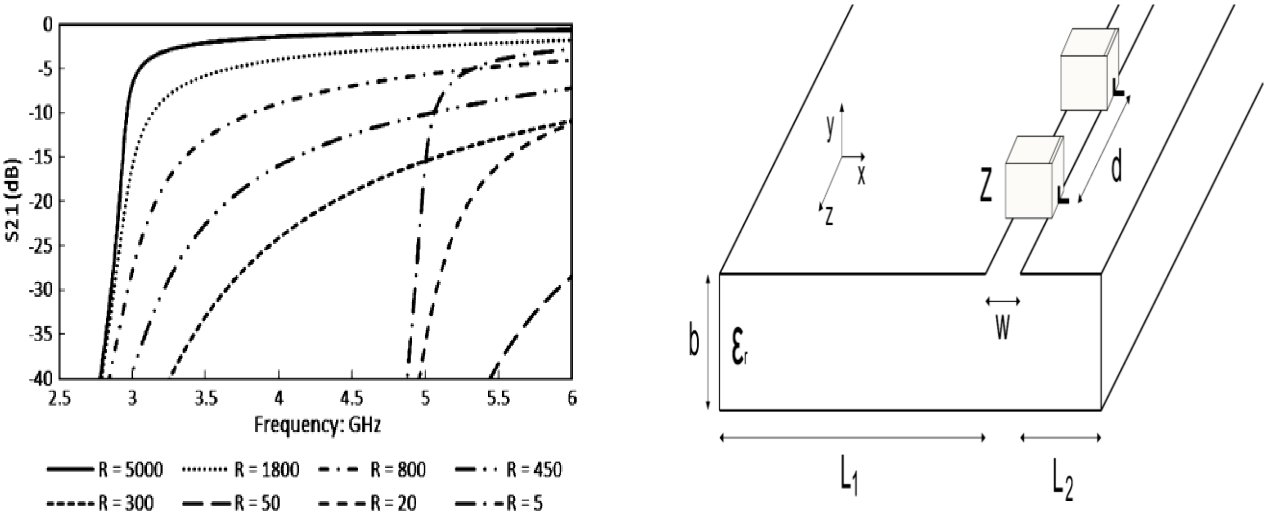

Fig (4. 13) Varying resistance at the slotted SIW.(b) structure of SSIW [18].

Instead of integrate PIN diodes, a layer of graphene was placed on the slot of the SIW. Then by changing the bias to the graphene, a similar effect should be obtained. The graphene layer has a width and length of $8 \times 8\ mm^2$ and has a height of 0.018 mm. The resistance change of graphene proposed from 5 to 1000 Ω (from Fig (4. 10)) a range of μ_c from 0 eV to 1.5 eV, gives a resistance change of 10 to 120 Ω.

As shown in Fig (4. 14), when the sheet resistance of graphene is large (1000 Ω), the waveguide works on half mode ($TE_{1/2,0}$) and when the sheet resistance is small (5 Ω), the waveguide goes into full wave ($TE_{1,0}$) with variable attenuation.

In practice, we cannot place only a graphene layer at the slot of the waveguide because we need an applied voltage to be placed between the silicon and graphene layer.

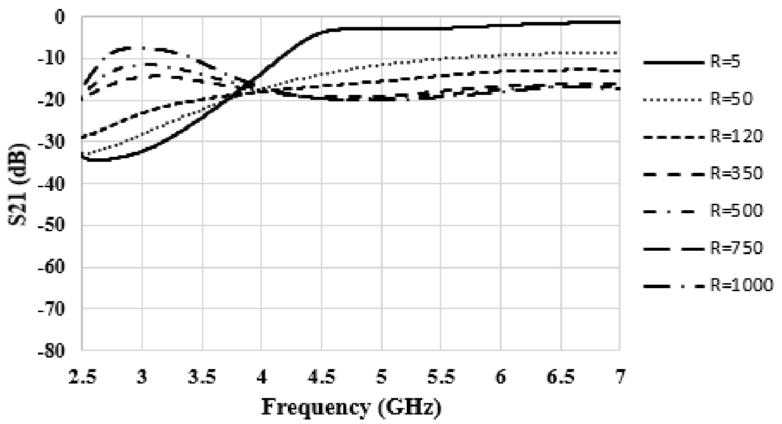

Fig (4. 14) Only graphene placed over SSIW

We consider the more practical structure with graphene on Si with a thin Sio_2 layer between the graphene and the Si. The length and width of silicon dioxide graphene is 8×8 mm^2. The graphene has a height of 0.018 mm with sheet resistance R. Sio_2 has a height and relative permittivity of 300 nm and 3.9 respectively. The silicon layer Si has a height and relative permittivity of 0.525 mm and 11.9 mm respectively and has a high conductivity of 20000 S/m, allowing a bias to be applied to the Si to generate a strong field on the graphene.

Changing the sheet resistance R from 5 to 1000 Ω, at frequency range 2-7 GHz as shown in Fig (4. 16). It is shown that there is no change of the cutoff frequency or insertion loss, the reason for that is the high conductivity of the silicon prevents the structure to tuning. This is because the field penetrates into the lossy silicon which dominates the loss in the waveguide.

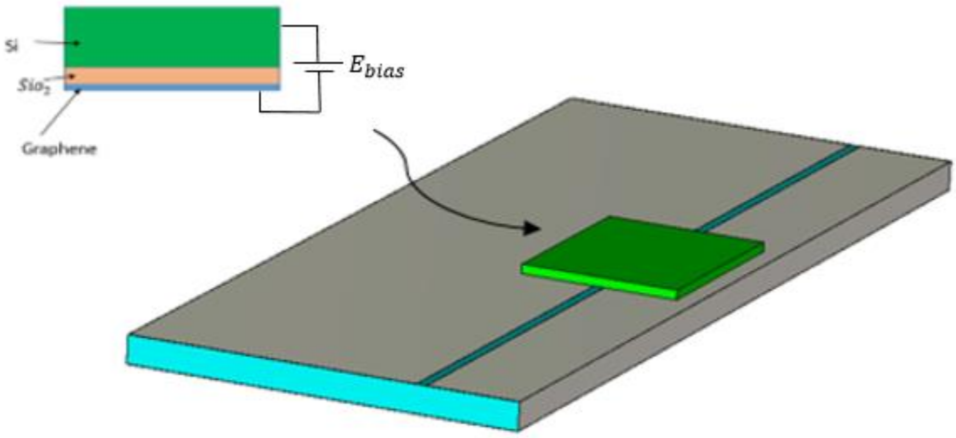

Fig (4. 15) Structure of silicon dioxide graphene tuning SSIW.

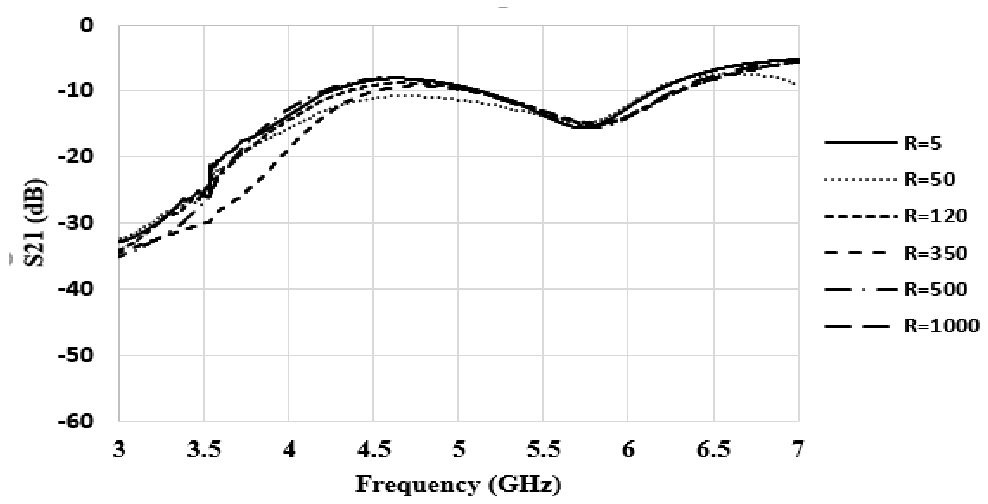

Fig (4. 16) Silicon dioxide graphene of conductivity 20000 S/m of SSIW

By reducing the conductivity of the silicon from 20000 to 2 S/m, we can see that the structure starts to have a tuning effect after the cutoff frequency, using the graphene resistance sheet variation 5 to 350 Ω. Above 350 Ω the return loss remain constant.

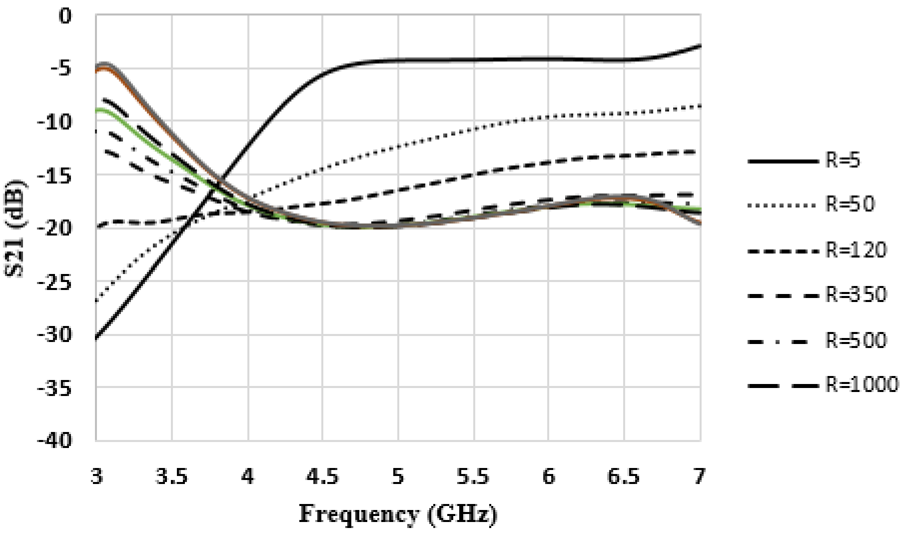

Fig (4. 17) Silicon dioxide graphene with silicon conductivity of 2 S/m

Another solution to tuning the structure is by increasing the width of silicon dioxide sio_2 from 300 nm to 1.5 μm. This is so that the thickness of the layer will reduce the radiation from the slot toward the silicon layer. Fig (4. 18), shows that the structure starts tuning after the cutoff frequency, by increasing the resistance of graphene, the S_{21} will decrease.

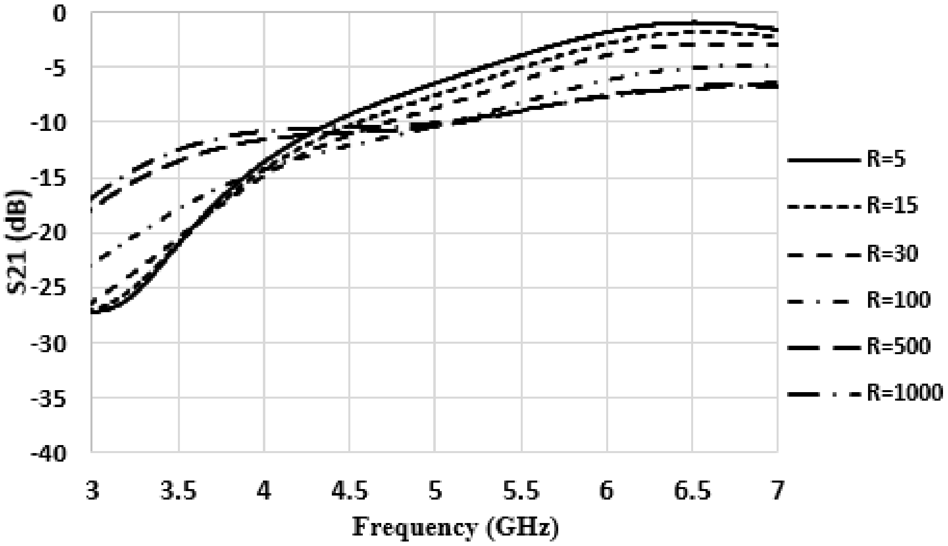

Fig (4. 18) Resistance variation effects on S_{21} by increasing silicon dioxide graphene to 1.5 µm.

The previous suggestions to tuning the structure is made theoretically, some of them are not possible to do measurement, such as placing only the graphene layer over the slot. In practical work, we need a large voltage to apply and some available samples such as the thickness of sio_2 1.5 µm.

4.5 Calibration standards using graphene

Calibration is defined as the “set of operations that establish, under specified conditions, the relationship between values of quantities indicated by a measuring instrument or measuring system, or values represented by a material measure or a reference material, and the corresponding values realized by standards” [17].

Nearly all guided-wave measurements are defined with respect to a nominal characteristic impedance. For example, in coaxial lines, it is common to refer to measurements of scattering parameters (i.e. reflection and transmission coefficients) to a 50 Ω characteristic impedance. It is therefore very important to be able to achieve accurate realizations of characteristic impedance to ensure the reliability of all subsequent, related, measurements.

Calibration is to set a series of measurements at the required frequency of measurement to remove the systematic errors that the instrument may have. These could be the hardware of VNA, the number of ports and measurement receivers and taking into account any accessories that need for measurements such as cables. This process is called “error correction.”

The error model used for one port automated S-parameter error correction is shown in Fig (4. 19). The unknown network that represents the internal configuration of the VNA together with the cables and connectors can be represented by a simple two-port network. That is illustrated in Fig (4. 19a). It is also usual in manufacturers’ datasheets for the coefficients S_{11}, S_{22}, S_{12} to be replaced by ED (directivity), ES (source match) and ER (reflection tracking) [19].

The relationship between the actual S_A of the device under test (DUT) and measured $S_M = A/R$ is:

$$S_{11A} = \frac{S_{11M} - E_D}{E_S(S_{11M} - E_D) + E_R} \tag{4. 8}$$

Calibration requires the determination of ED, ES and ER which is achieved by connecting three (or more) known standards, S11A and solving for the error terms in the set of equations in (4.8). In one-port calibration, usually the known standards are short-circuits, open-circuits and matched loads, sometimes with offset transmission lines.

For the realization of characteristic impedance, at microwave frequencies has been achieved using either precision air-spaced coaxial lines [1, 2], or precision near-matched terminations [3]. During this period, these standards have been successfully used at all microwave frequencies and extended into the millimeter-wave region (to 110 GHz). This was done by using coaxial lines with outer conductor diameters as small as 1 mm [4].

One of the most reliable and accurate calibration techniques is the Thru-reflect-line (TRL) which will be demonstrated in the following section:

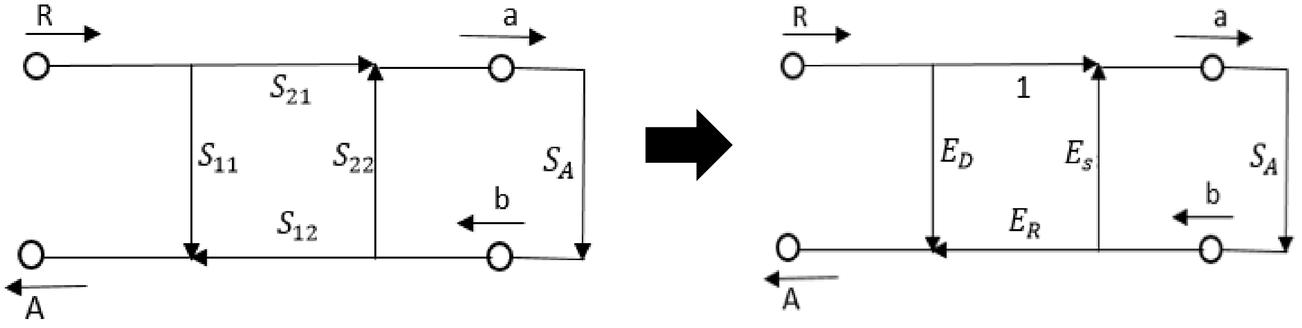

(a) (b)

Fig (4. 19) One port three-term error model for one-port calibration: (a) S-parameter, (b) error term representation.

4.5.1 TRL calibration

The main TRL technique requires a through–line (Through) and a reflecting impedance as standard (Reflect) and a transmission line offset as references (Line).

TRL calibration has an advantage of high accuracy. However TRL calibration has a limitation of lower frequency but this can be solved by using long line standards and some statistical analysis of measurements. To apply the TRL technique, a VNA two port network analyzer has been used.

Briefly, the through step: a zero-length through in which the two test pots are connected together or with short length of transmission line, then the measurement is taken in both directions for S-parameters.

The reflect step: each port is connected with open or short circuit and the S_{11} and S_{22} are measured.

The line step: short length of transmission line different in length from the THRU is inserted between port 1 and port 2 and measures all the S- parameters.
Then, using these measurements to calculate the fictitious two-port error boxes A, B as shown in Fig (4. 20).

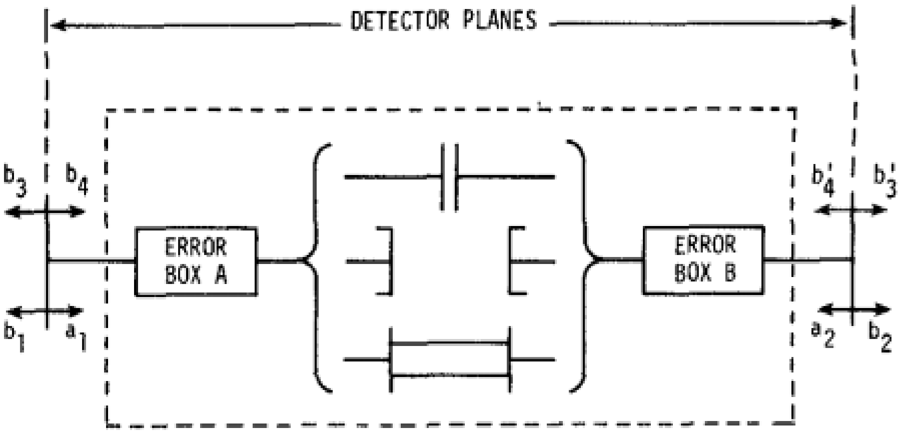

Fig (4. 20) Fictitious two-port error boxes A, B with the three standards (Through-Reflect-Line) [20].

At high frequencies, the error becomes more serious as the high frequency range small cable movements can cause a big phase change as well the amplitude change. So while the TRL technique is the most accurate technique, a small cable movement may limit the accuracy and calibration.

For high millimeter-wave frequencies and above (i.e. above 110 GHz), the preferred transmission medium is a rectangular metallic waveguide, which is nowadays being used for measurements at frequencies to at least 1.1 THz [21]. Although sections of precision air-filled waveguide can be used as impedance standards at these frequencies, the achievable tolerances on the critical dimensions of the waveguide (i.e. the height, width and overall shape of the waveguide) [22] along with the difficulty in accurately aligning the waveguides during connection [23], cause these waveguides to become poorly-defined standards of impedance at these frequencies [24].

This is driving the need for new forms of impedance standard at high millimeter-wave and terahertz frequencies. This is based on using layers of graphene suspended across the waveguide aperture. Sheets of mono-, bi- and tri-layer graphene have been investigated in order to provide different values of impedance for the electromagnetic wave in the waveguide. Since the physical properties of graphene can be linked to fundamental laws of nature (defined by quantum mechanics) [25], the long term goal for this research is to link measurements at millimeter-wave frequencies . Additionally, above these fundamental laws, it is to provide a primary standard of impedance.

The graphene samples (mono-, bi-, tri-) were placed on a quartz substrate, then measured the surface impedance. After de-embedding the effect of quartz on waveguide, it is shown that standards with values of Y_0, $2Y_0$ and $3Y_0$ can be produced by a monolayer ,bilayer, or tri-layer of graphene, respectively, where Y_0 is the characteristic admittance of the waveguide.

.

4.6 Establishing a new form of primary impedance standard

Using CST simulation in the time domain solver, the waveguide has been modeled to work at a frequency range 50-75 GHz, the waveguide as shown in Fig (4. 21), has the dimensions 15 mm × 15 mm with thickness 5 mm in PEC material. The aperture inside the waveguide has the dimensions of 3.8 mm × 1.9 mm with thickness 5 mm. The one port is placed at the aperture to demonstrate the S-parameter.

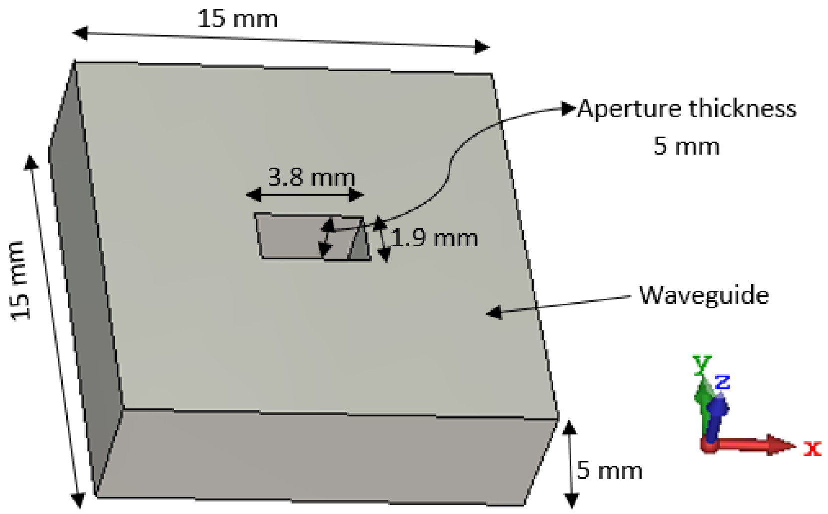

Fig (4. 21) Waveguide with aperture

To demonstrate the better performance of graphene working, quartz has been placed at the open waveguide only and their performance was studied. A graphene with different layers has been placed with quartz and the effects studied as are follows:

4.6.1 Graphene on open aperture

A graphene layer is placed above waveguide, neglecting the quartz substrate as shown in Fig (4. 22). The sheet resistance of graphene (R_s) from 123 to 500 Ω, by increasing the value of R_s, the return loss decreases, and the graphene acts as an inductor on an open aperture as shown in Fig (4. 23).

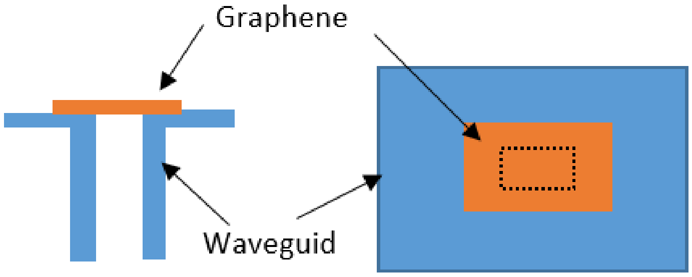

Fig (4. 22) Graphene on open aperture

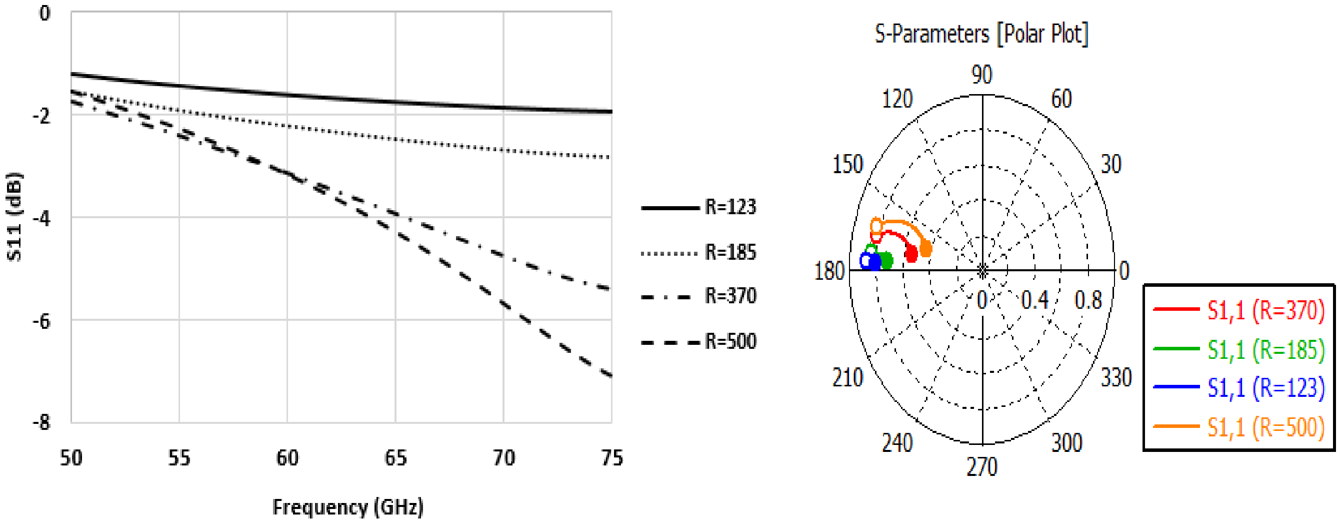

(a) (b)

Fig (4. 23) Graphene on open aperture with variation of sheet resistance of graphene: (a) Return loss, (b) Smith chart.

4.6.2 Quartz sample only on the waveguide

By assuming that only the quartz is placed on the waveguide, the quartz has $\epsilon_r = 3.75$, $tan\delta = 0.0004$ and has been placed on the aperture, with dimensions of 5 mm × 5 mm and has a thickness of 0.5 mm as shown in Fig (4. 24).

The return loss shows how it decreases with frequency from -3.6 dB to approximately -4.3 dB as shown in Fig (4. 25), The Smith chart shows that the quartz works as a capacitance.

The surface impedance shows a reduction in magnitude against frequency from the range 620 to about 450 Ω as shown in Fig (4. 26).

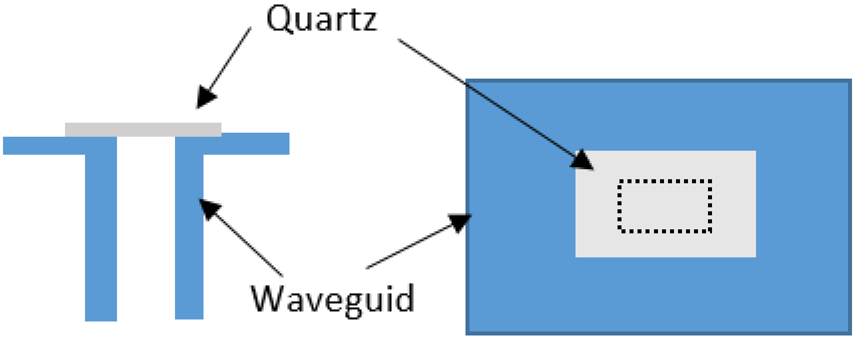

Fig (4. 24) Quartz placed on the waveguide

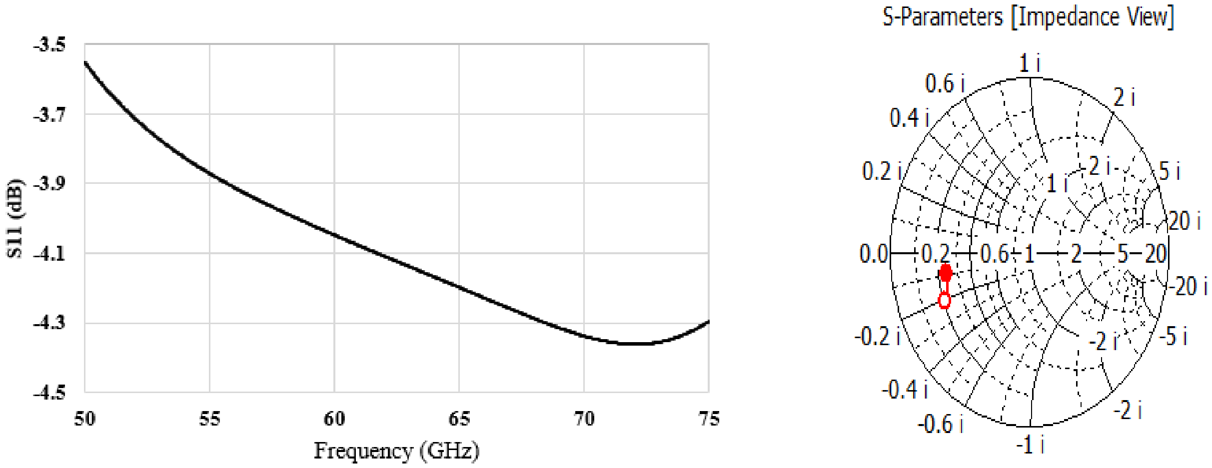

(a) (b)

Fig (4. 25) Quartz only on aperture: (a) Return loss, (b) Smith chart.

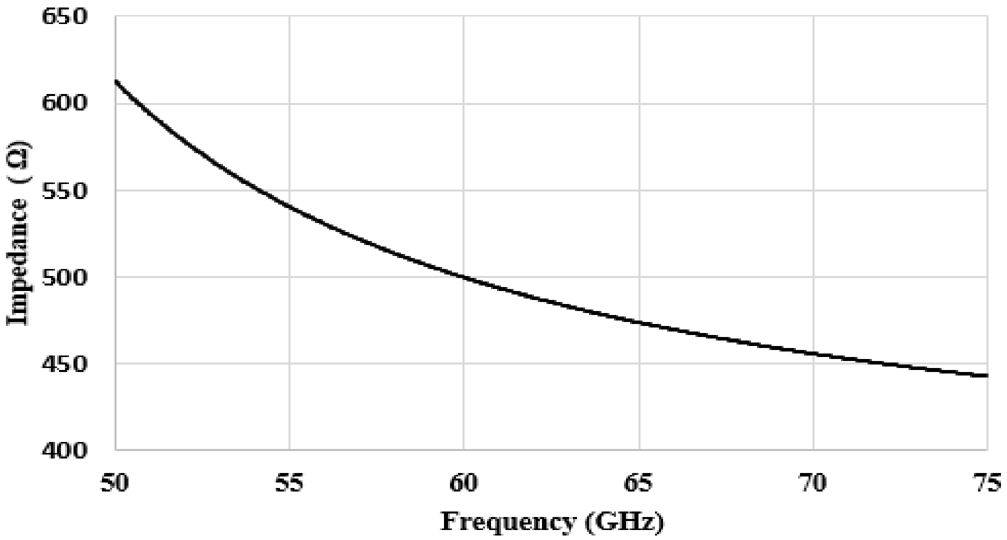

Fig (4. 26) Surface impedance against frequency (quarts on the waveguide).

4.6.3 Quartz sample with metal on top

By adding a metal which has a conductivity of $\sigma = 4.5 \times 10^{7}$ over the quartz as shown in Fig (4. 27), the return loss shows a resonant frequency at 57.7 GHz as shown in

Fig (4. *28*). This happens because of the large leakage from the parallel plate as shown in the electric field distribution of resonant frequency 57.7 GHz.

A resonant frequency appear at 57.7 GHz because the waveguide radiates into the surface as shown in Fig (4. 29). The structure acts as a patch antenna which its pattern is similar to patch antenna as shown in Fig (4. 30). The far field radiation pattern in 3D shows that the total efficiency and radiation efficiency is -0.2784 dB and -0.36 dB respectively. The gain at 57.7 GHz is 7.22 dBi. In polar plot when $\phi = 0$, the main lobe magnitude is 6.29 dB.

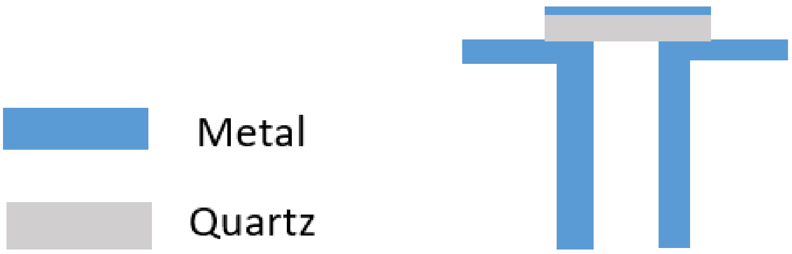

Fig (4. 27) SIW structure with quarts and metal on top

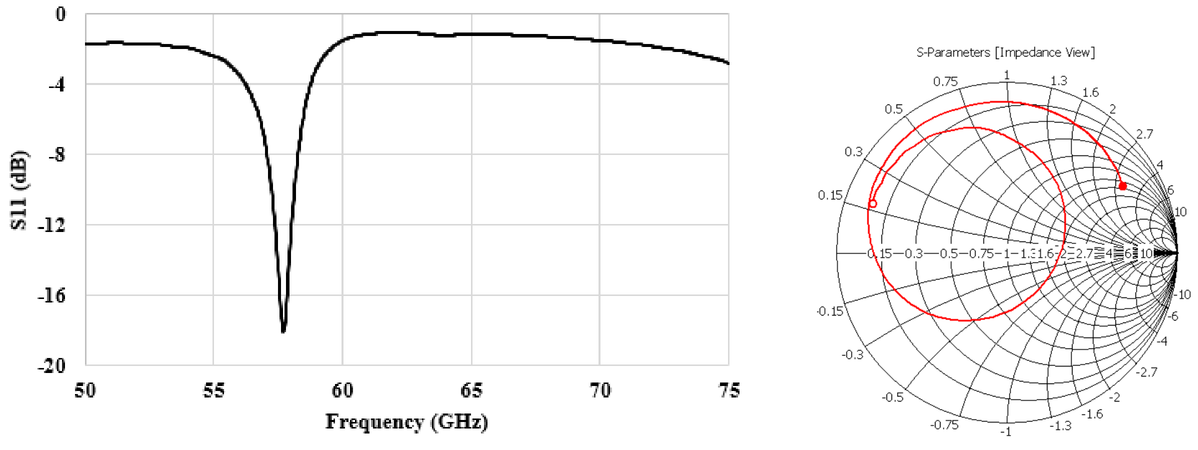

(a) (b)

Fig (4. 28) Quartz sample with metal on top: (a) Return loss, (b) Smith chart.

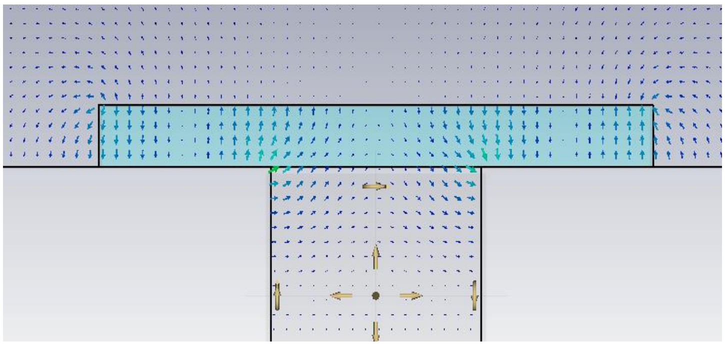

Fig (4. 29) Electric field distribution at 57.7 GHz

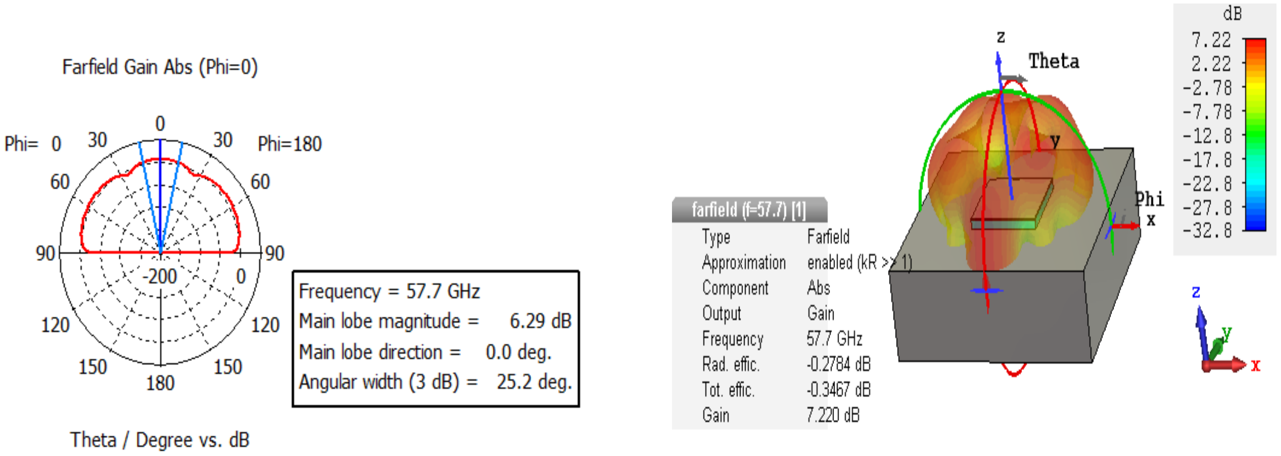

Frequency = 57.7 GHz
Main lobe magnitude = 6.29 dB
Main lobe direction = 0.0 deg.
Angular width (3 dB) = 25.2 deg.

Type	Farfield
Approximation	enabled (kR >> 1)
Component	Abs
Output	Gain
Frequency	57.7 GHz
Rad. effic.	-0.2784 dB
Tot. effic.	-0.3467 dB
Gain	7.220 dB

Fig (4. 30) Radiation pattern at 57.7 GHz: (a) E-plane, (b) 3D pattern.

4.6.4 Graphene sample on top

Graphene layers were added over the quartz on the top of the waveguide, with different sheet resistance of graphene (R_s=123, 185, 370, 500) Ω as shown in Fig (4. 31).

The number of layers for the graphene represents sheet resistance (one layer 350 ,two layers 185, triple layers 123) Ω. As shown in the S-parameter in Fig (4. 32), when the sheet resistance increases the level of S_{11} decreases.

Fig (4. 33) shows the electric field distribution at the open waveguide and the 3D radiation pattern which shows the directivity at frequency -62 GHz is 7 dB, the radiation efficiency and total efficiency is -5.4 dB and -5.9 dB.

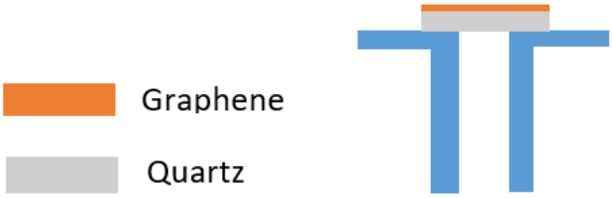

Fig (4. 31) Graphene on top of waveguide.

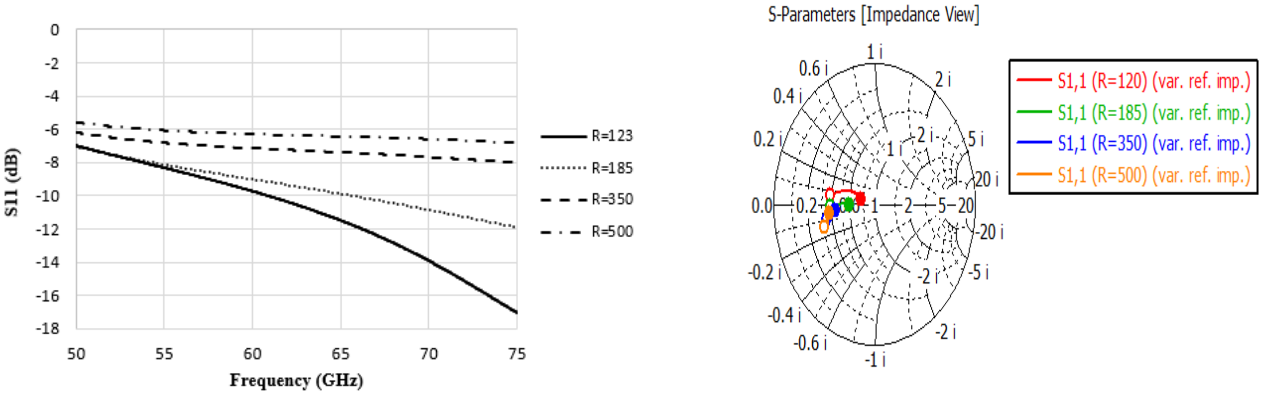

(a)

(b)

Fig (4. 32) graphene placed on the top of the aperture: (a) Return loss, (b) Smith chart.

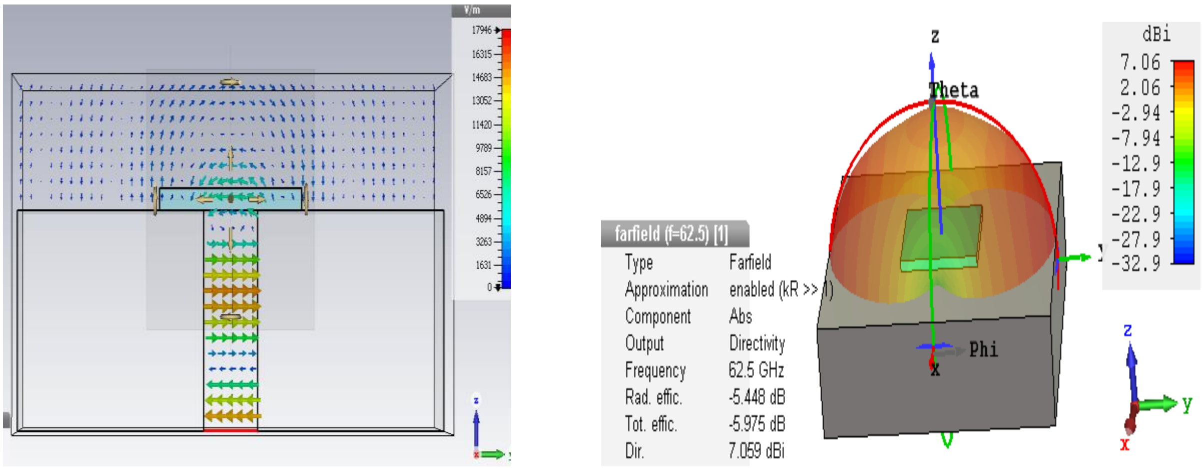

farfield (f=62.5) [1]
Type Farfield
Approximation enabled (kR >> 1)
Component Abs
Output Directivity
Frequency 62.5 GHz
Rad. effic. -5.448 dB
Tot. effic. -5.975 dB
Dir. 7.059 dBi

(a) (b)

Fig (4. 33) At 6.35 GHz: (a) Electric field distribution, (b) 3D pattern.

4.6.5 Graphene sample on bottom

Adding the graphene sample at the bottom of the open waveguide is shown in Fig (4. 34), Fig (4. 35) shows that by increasing the sheet resistance of the graphene the level of S_{11} decreases.

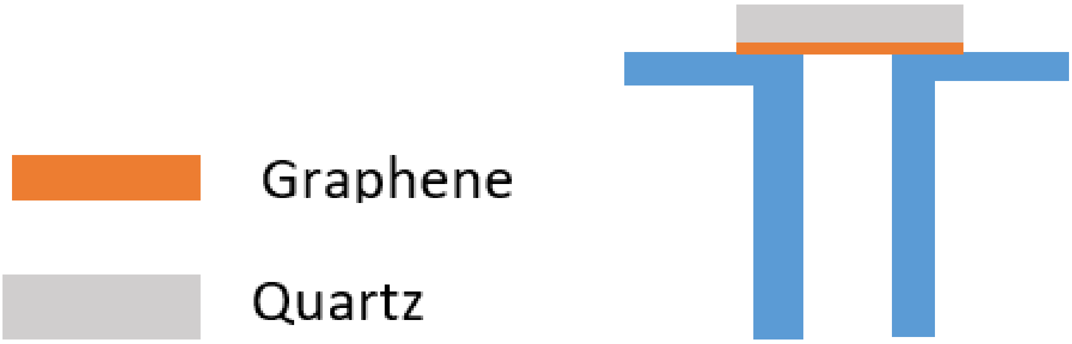

Fig (4. 34) Graphene sample on bottom.

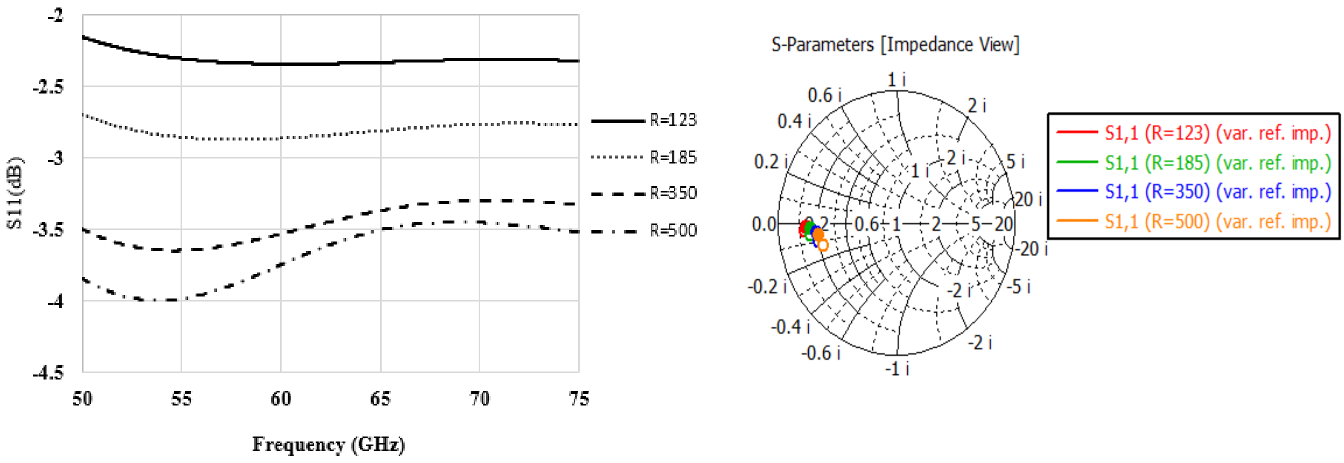

(a) (b)

Fig (4. 35) Graphene placed on bottom: (a) Return loss, (b) Smith chart.

4.6.6 Graphene on bottom metal on top

If we placed the graphene with different sheet resistance at the bottom of the waveguide with metal at the top as shown in Fig (4. 36), by increasing the sheet resistance of graphene the reflection coefficient decreases. Fig (4. 38) shows that the electric field is inside the waveguide.

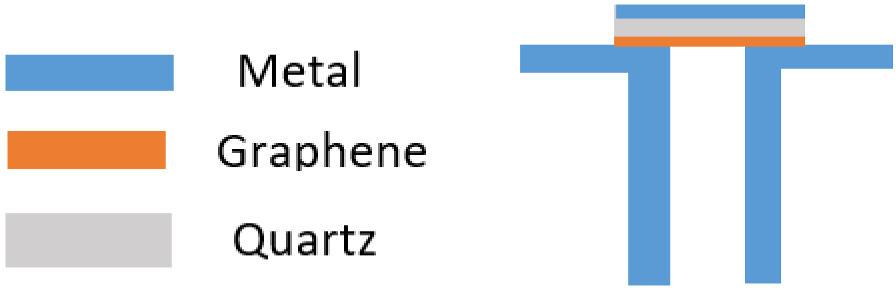

Fig (4. 36) Graphene bottom metal top.

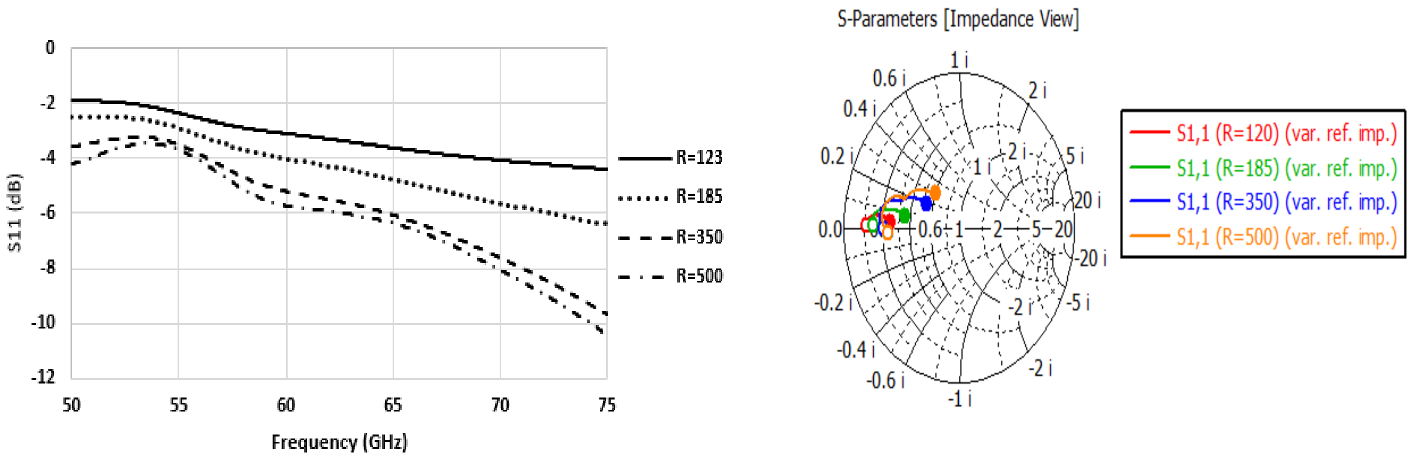

(a) (b)

Fig (4. 37) Graphene bottom with metal on top with Sheet resistance variation: (a) Return loss, (b) Smith chart.

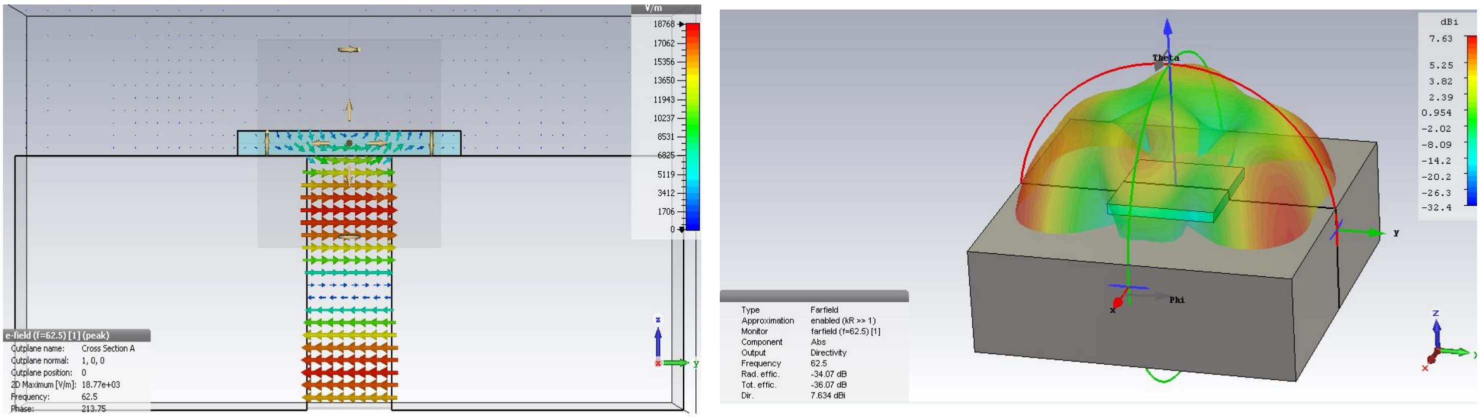

e-field (f=62.5) [1] (peak)
Cutplane name: Cross Section A
Cutplane normal: 1, 0, 0
Cutplane position: 0
2D Maximum [V/m]: 18.77e+03
Frequency: 62.5
Phase: 213.75

Type Farfield
Approximation enabled (kR >> 1)
Monitor farfield (f=62.5) [1]
Component Abs
Output Directivity
Frequency 62.5
Rad. effic. -34.07 dB
Tot. effic. -36.07 dB
Dir. 7.634 dBi

(a) (b)

Fig (4. 38) At 62.5 GHz: (a) Electric field distribution, (b) 3D pattern.

4.6.7 Graphene in waveguide aperture only with metal on top

Adding graphene on the aperture as shown in Fig (4. 39) with metal on top, the reflection coefficient shows that by increasing sheet resistance of graphene, the S11 decreases. A resonant frequency appear when the resistance is (1000-10000) Ω, meaning that the waveguide radiate through the aperture.

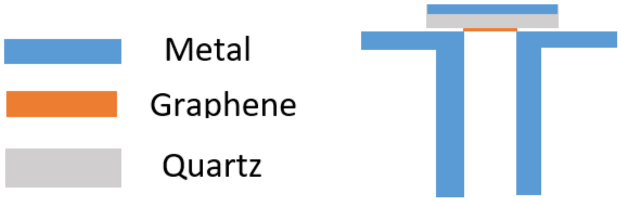

Fig (4. 39) Graphene on aperture only with metal on top

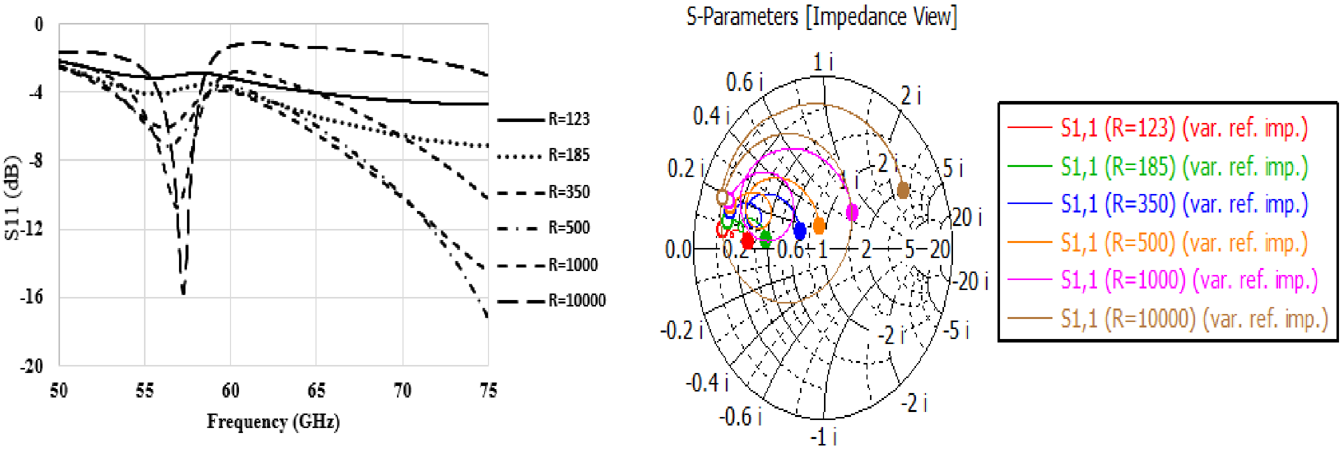

(a) (b)

Fig (4. 40) Graphene on aperture with top metal with graphene sheet resistance variation: (a) Return loss, (b) Smith chart.

4.7 Comparison between simulation and measurements

The graphene mono-, bi- and tri-layer samples were supplied by Graphenea and produced by chemical vapor deposition (CVD), then transferred to quartz substrates by a wet transfer process. Each of the quartz substrates were 500 μm thick and 5 mm by 5 mm wide with a 0.6 nm surface roughness.

To measure the surface impedance of the graphene, the samples were placed directly at the end of an open-ended WR-15 waveguide (which operates from 50 to 75 GHz) with the graphene side touching the waveguide aperture. This setup is shown in Fig (4. 41).

The measurement was done at the National Physical Laboratory (NPL) in London, where it was performed using a Key Sight Technologies PNA-X vector network analyzer (VNA) using VDI waveguide extender heads covering the frequency range 50 to 75 GHz.

The samples were placed on the end of the waveguide aperture and were therefore measured at the reference plane established by the calibration. A photograph of the measurement setup together with a quartz sample is shown in Fig (4. 42).

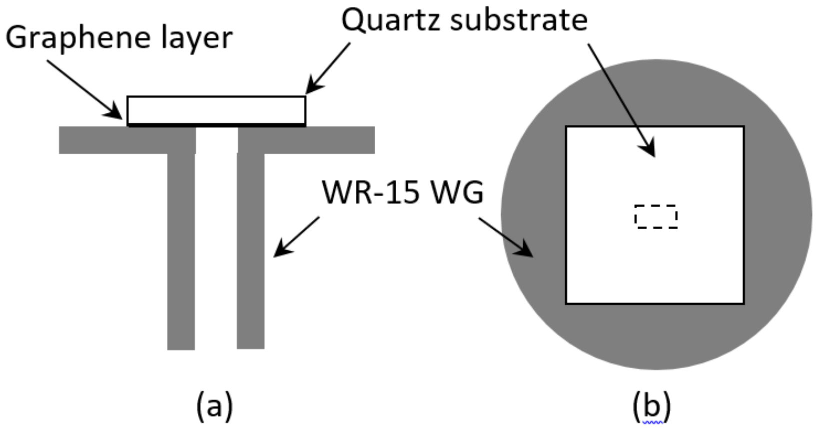

Fig (4. 41) Measurement setup, showing quartz substrate with graphene layer placed onto an open-ended WR-15 waveguide: (a) side-view, (b) top-view.

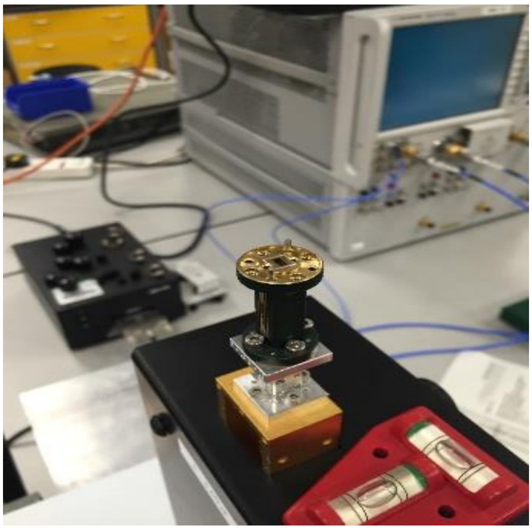

Fig (4. 42) Photograph of measurement setup.

In each case, the samples were measured twice to assess any repeatability issues with the attachment of the samples to the measurement system. A comparison has been made between simulation and measurements for quartz and mono-, bi- and tri- graphene layer.

- **Quartz**

A comparison has been made between simulation and measurements of quartz only and quartz with short end. A good agreement is shown in Fig (4. 43) between simulation and measurements (Quartz with short end). As explained, a resonance happened at 57 GHz because of the large leakage between the two plates of the waveguide, which are different in magnitude between simulation and measurements.

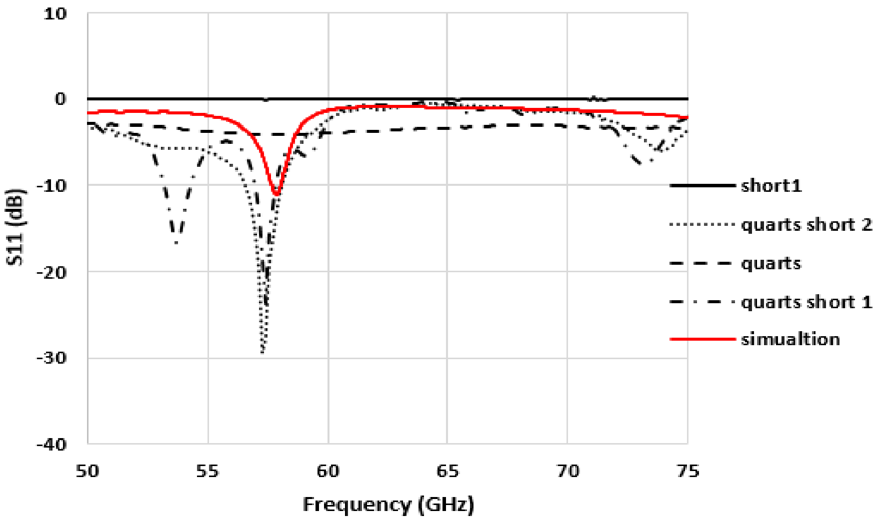

Fig (4. 43) Comparison of quarts between measurements and simulation

- **Graphene top**

Fig (4. 44**)** shows a comparison of graphene placed at the top of the waveguide in mono, bi- and tri-layers . By neglecting the resonant at 57 GHz due to quartz effect, an agreement is achieved between simulation and measurements at the mono and bi- layers. The simulation at tri-layer of graphene has a small shift similar to bi-layer simulation, but slightly different from the measurements of tri-layers.

According to the measurements, the highest reflection coefficient is the mono-layer following by bi and tri-layer respectively.

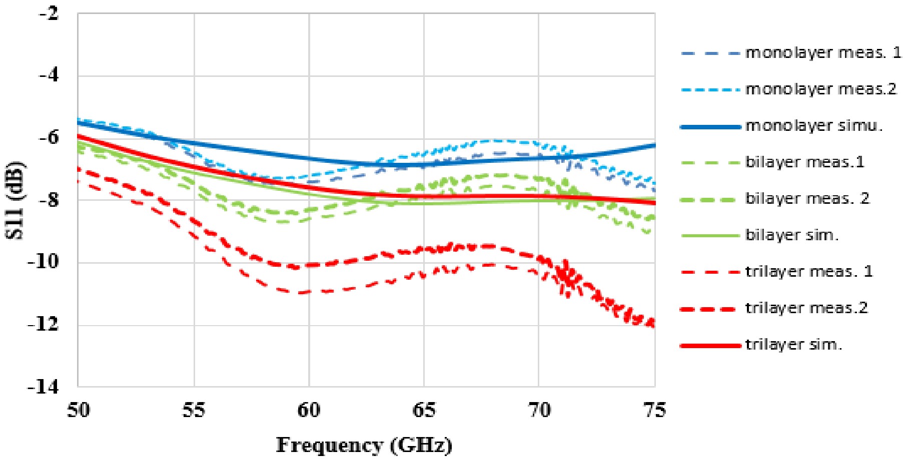

Fig (4. 44) Comparison of graphene at the top in mono, Bi and tri layers between simulation and measurements.

- **Graphene bottom**

A comparison has been made between simulation and measurements at the bottom of the waveguide in different layers. The tri-layer has higher reflection coefficient followed by bi- and Mono-layer in series. The mono-layer measurements is slightly more than simulation.

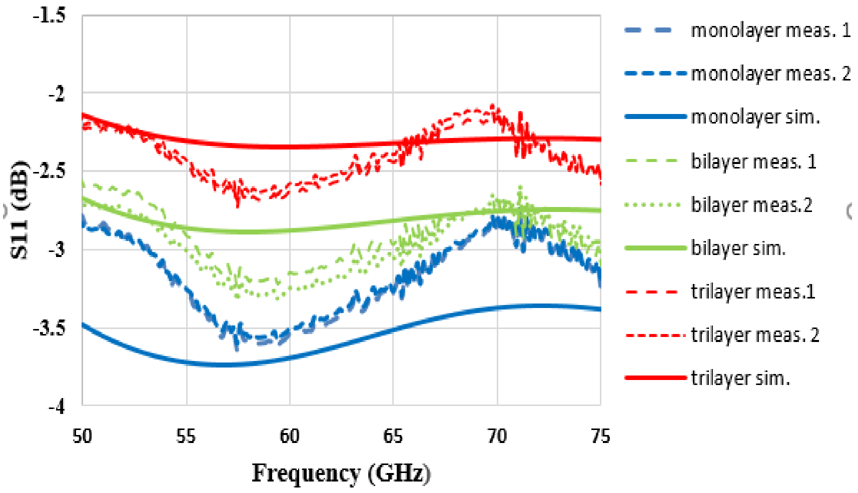

Fig (4. 45) Comparison of graphene at the bottom of the waveguide between measurements and simulations.

- **Graphene bottom metal top**

An agreement shown in Fig (4. 46) between simulation and measurements, the mono-layer measurements is more ripple than other measurements. Again, the reflection coefficients is higher at tri-layer followed by bi-layer and mono-layer.

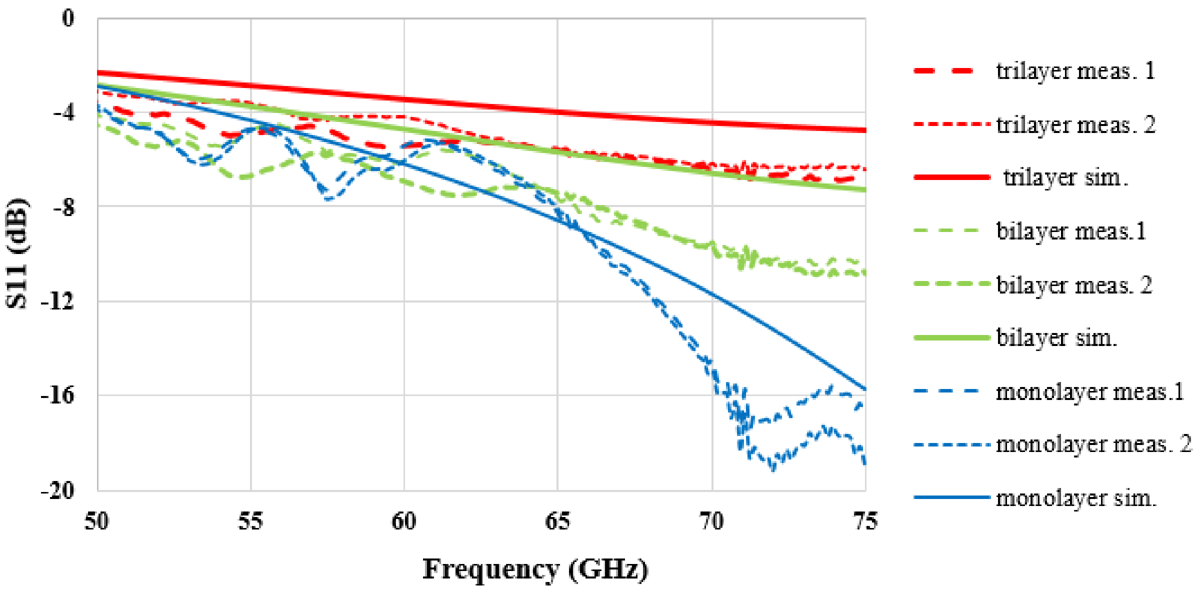

Fig (4. 46) Comparison between simulation and measurements of graphene at the bottom with metal at the top in mono, bi and tri layers.

4.8 De-embedding the effect of quartz from the graphene sample

To de-embed the effect of the quartz sample and determine the admittance of the graphene surface, the following procedure was followed.

First, a quartz sample with no graphene layer was placed at the end of the waveguide and measured, resulting in an S-parameter measurement S_{11q}. Secondly, a quartz sample with a graphene layer was placed on the waveguide resulting in a measured S-parameter S_{11g}. Finally, by assuming that the graphene layer can be modelled as a simple shunt admittance (Y) Fig (4. 47), the value of this admittance is calculated by:

$$\frac{Y}{Y_0} = \frac{Y_{in}}{Y_0} - \frac{Y_q}{Y_0} = \frac{1-S_{11g}}{1+S_{11g}} - \frac{1-S_{11q}}{1+S_{11q}} \tag{4. 9}$$

This is similar to the method applied in [26]. The characteristic admittance of the waveguide, Y_0, is given by [27]:

$$Y_0 = \frac{1}{\eta_0 k_0}\sqrt{k_0^2 - \left(\frac{\pi}{a}\right)^2} \tag{4. 10}$$

Where η_0 and k_0 are the free-space wave impedance and phase constant, respectively, and a is the broad wall dimension of the waveguide; a = 3.75 mm for WR-15.

The above method for determining the admittance was preferred over transmission methods such as in [28][29] because of the relatively large thickness of the quartz substrate.

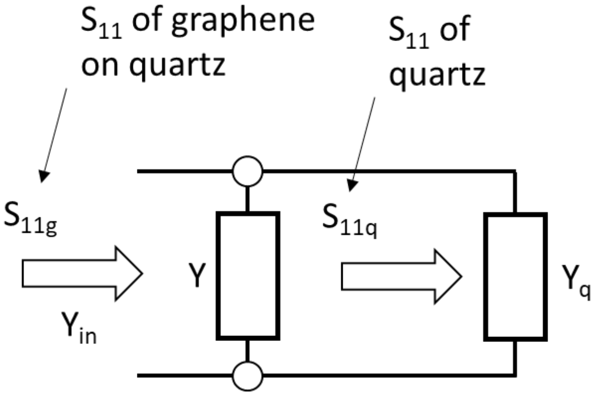

Fig (4. 47). De-embedding circuit.

Fig (4. 49) shows the measurement results after de-embedding using equation (4.8) for the graphene in bottom. It is seen that the mono-, bi- and tri-layers of graphene have a real part of admittance very close to Y_0, $2Y_0$ and $3Y_0$, respectively. Since Y_0 converges to $1/\eta_0$ over the 50-75 GHz waveguide band (equation 4.9), the sheet impedance of the graphene is approximately equal to 377 Ω/sq for a single layer, and 189 Ω/sq and 126 Ω/sq for the bi- and tri-layers, respectively. This suggests that these samples could be used as calibration standards; providing a matched load standard, and reflection standards with linear magnitude of 0.33 and 0.5.

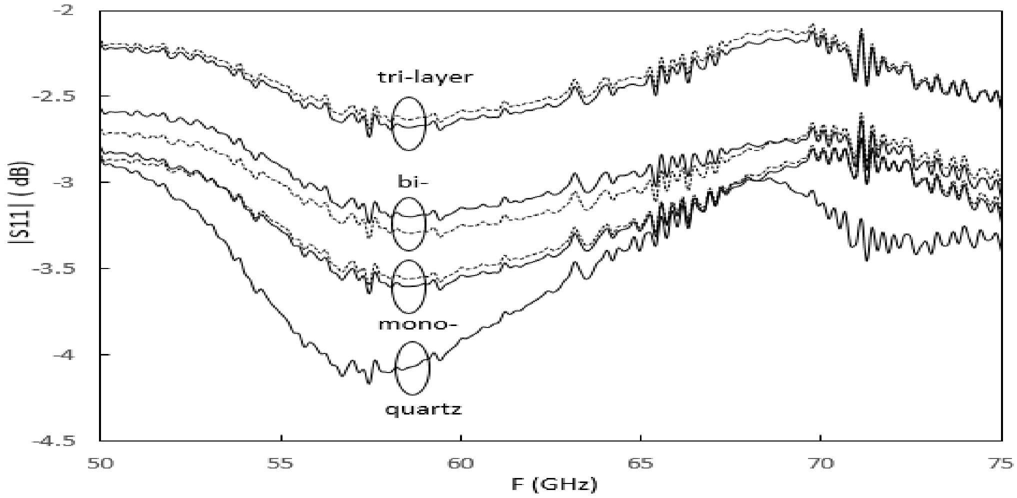

Fig (4. 48) Measured S-parameters. Dotted lines show repeat measurements.

The rapid reduction in the real part of the admittance above 65 GHz is attributed to resonances in the quartz substrate and is not indicative of the graphene. The wavelength in quartz at 75 GHz is approximately 2 mm and therefore there are a number of resonances that can occur in the $0.5 \times 5 \times 5\ \text{mm}^3$ quartz sample over the 50-75 GHz band. Since the de-embedding process required two measurements (one of a quartz substrate and one of a quartz substrate with graphene layer), any small differences in alignment and the geometry of the two substrates would have a much more significant effect on the de-embedded admittance near a resonance. It is believed that this same effect is resulting in the rather inconsistent imaginary component of admittance seen in Fig (4. 49).

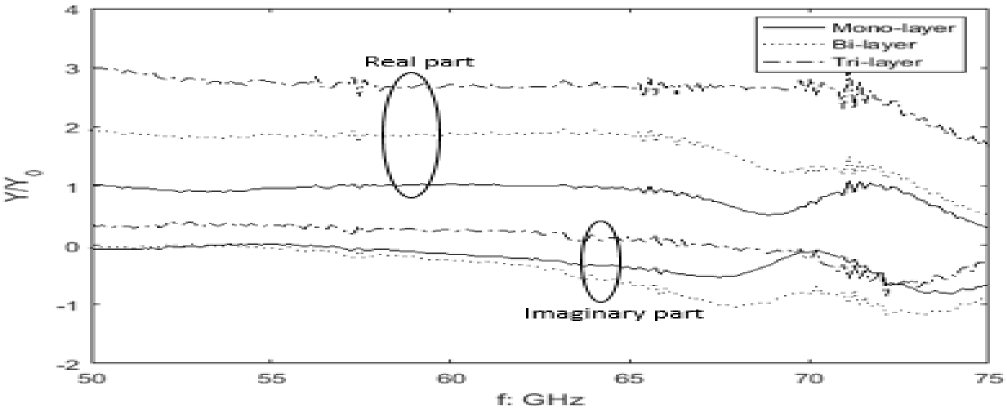

Fig (4. 49) The de-embedded value of normalized admittance for mono-, bi- and tri-layer graphene samples with graphene in bottom.

The real and imaginary part of admittance for graphene in bottom and metal in top shown in Fig (4. 50), a resonance appears at 58 GHz for mono, bi and tri layer. This is because the resonance happened at the quartz with metal as shown in Fig (4. 43). After the de-embedding the resonance appear clearly because a small tuning may cause a large effect as shown below.

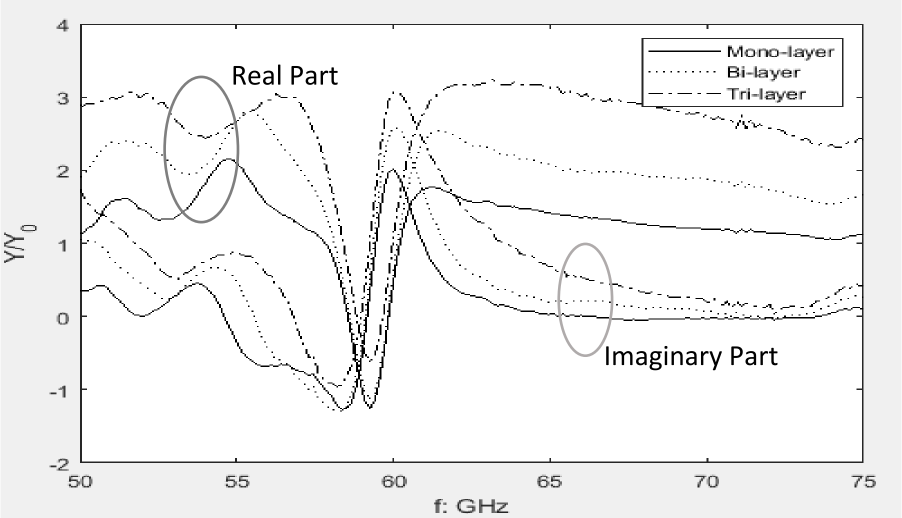

Fig (4. 50) The de-embedded value of normalized admittance for mono-, bi- and tri-layer graphene samples with graphene in bottom and metal in top.

There are likely to be a number of practical difficulties that would need to be overcome to form reliable, repeatable, impedance standards using layers of graphene. As seen in Fig (4. 48), the quartz substrate has a very significant effect on the S-parameters of the structure and consequently the graphene would ideally be suspended at the end of the waveguide without the use of a quartz substrate. In practice, this would be very challenging since a mono-layer of graphene is only one atom thick. However, it would be possible to use a much thinner dielectric supporting layer than the 500 µm quartz used in this investigation. If this layer could be reduced to tens of micrometers, it would have a very small effect on the impedance of the graphene layer.

Another issue that would need to be addressed are the environmental stability of the graphene layer and the effects of repeated use. This could probably be overcome by using a thin dielectric protective layer to ensure the graphene is not exposed to the environment and ‘wear-and-tear’.

4.9 Conclusion

This chapter calculates graphene conductivity and shows how the bias voltage or chemical potential μ_c affects the conductivity of graphene and sheet resistance. This is when the chemical potential is equal to zero, a significant change appear for frequencies above 10 GHz.

Moreover, a silicon dioxide graphene is placed over the slot of the waveguide to attempt tuning frequency of the waveguide by changing the sheet resistance of graphene using CST simulation. We can conclude that due to high conductivity of silicon 20000 S/m the change of sheet resistance does not make any effect of frequency change. When we reduce conductivity of silicon to 2 S/m a significant change of frequency has been shown of the waveguide.

This chapter has shown that it is feasible to realize standards of impedance (or equivalently, admittance) at millimeter-wave frequencies using layers of graphene suspended across waveguide test ports. Such standards could be used to calibrate a waveguide VNA. For example, this chapter has shown that standards with values Y_0, $2Y_0$ and $3Y_0$ can be realized using samples of mono-, bi- and tri-layer graphene, respectively. This is something that would be very difficult to achieve, consistently, using other thin-film conductors. These three standards could be used for three-known-load calibrations employing a 12-term error model [30][31]. This also suggests that further standards could be realised by adding additional layers of graphene so that over-determined calibration schemes could be deployed to further increase the accuracy of a calibrated VNA [32] [33].

By understanding the fundamental physical properties of the graphene, and relating these properties to the observations made by the VNA during calibration, it will be possible to link the calibration of the VNA to quantum realizations of the base units of the International System of Units (SI). This suggests that it may be possible to establish metrological traceability at microwave and millimetre-wave frequencies to quantum phenomena, thus potentially enabling these measurements to be harmonized within the upcoming redefinition of the SI [34] [35].

4.10 References

[1] K.S. Novoselov, A.K. Geim, S.V. Morozov, D. Jiang, Y. Zhang, S.V. Dubonos, I.V. Grigorieva, and A.A. Firsov, "Electric Field Effect in Atomically Thin Carbon Films," *Science,* vol. 306, no. 5696, p. 666 LP-669, Oct. 2004.

[2] J. Christensen, A. Manjavacas, S. Thongrattanasiri, F. H. L. Koppens, and F. J. García de Abajo, "Graphene Plasmon Waveguiding and Hybridization in Individual and Paired Nanoribbons," ACS Nano, vol. 6, no. 1, pp. 431–440, Jan. 2012.

[3] E. Carrasco and J. Perruisseau-Carrier, "Reflectarray Antenna at Terahertz Using Graphene," IEEE Antennas Wirel. Propag. Lett., vol. 12, pp. 253–256, 2013.

[4] M. Tamagnone, J. S. Gómez-Díaz, J. R. Mosig, and J. Perruisseau-Carrier, "Reconfigurable terahertz plasmonic antenna concept using a graphene stack," Appl. Phys. Lett., vol. 101, no. 21, p. 214102, Nov. 2012.

[5] P. Chen, C. Argyropoulos, and A. Alù, "Terahertz Antenna Phase Shifters Using Integrally-Gated Graphene Transmission-Lines," IEEE Trans. Antennas Propag., vol. 61, no. 4, pp. 1528–1537, 2013.

[6] D. Correas-Serrano, J. S. Gomez-Diaz, J. Perruisseau-Carrier, and A. Álvarez-Melcón, "Graphene-Based Plasmonic Tunable Low-Pass Filters in the Terahertz Band," IEEE Trans. Nanotechnol., vol. 13, no. 6, pp. 1145–1153, 2014.

[7] Z. Fei, A. S. Rodin, G. O. Andreev, W. Bao, A. S. McLeod, M. Wagner, L. M. Zhang, Z. Zhao, M. Thiemens, G. Dominguez, M. M. Fogler, A. H. Castro Neto, C. N. Lau, F. Keilmann, and D. N. Basov. "Gate-tuning of graphene plasmons revealed by infrared nano-imaging," Nature, vol. 487, p. 82, Jun. 2012.

[8] He, X. and S. Kim, "Graphene-supported tunable waveguide structure in the terahertz regime," JOSA B, vol. 30(9), pp. 2461–2468, 2013.

[9] Y. Sun, Y. Bian, Z. Zheng, J. Liu, and Z. Gong, "Hybrid Plasmonic Waveguide Incorporating Double Graphene Sheets," 2013 IEEE Photonics Conf., vol. 2, pp. 544–545, 2013.

[10] Y. Sun, Z. Zheng, X. Zhao, Z. Gong, and J. E. D.-K. Liu I., Reitze, D., Alic, N., and Hagan, D., "Low-loss graphene plasmonic waveguide based on a high-index dielectric ridge for tight optical confinement at 30THz," in Frontiers in Optics 2013, 2013.

[11] A. Zhang, W. Lu, Z. Liu, H. Chen, and B. Huang, "Dynamically Tunable Substrate-Integrated- Waveguide Attenuator Using Graphene," IEEE Trans. Microw. Theory Tech., vol. 66, no. 2, pp. 3081–3089, 2018.

[12] M. Yasir, M. Bozzi, L. Perregrini, S. Bistarelli, A. Cataldo, and S. Bellucci, "Tunable and input-matched attenuator based on few-layer graphene," in 2017 47th European Microwave Conference (EuMC), 2017, pp. 192–195.

[13] Z. Zhang and B. Wu, "Radiation Pattern Reconfigurable Antenna Using Double Layer Tunable Graphene Superstrate," 2015 Asia-Pacific Microw. Conf., vol. 3, pp. 1–3, 2015.

[14] A. Zhang, Z. Liu, and W. Lu, “A Tunable Attenuator on Graphene-Based Half-Mode Substrate Integrated Waveguide,” in 2018 IEEE Asia-Pacific Conference on Antennas and Propagation (APCAP), 2018, pp. 4–5.

[15] G. Grüner and M. Dressel, Eds., “Propagation and scattering of electromagnetic waves,” in Electrodynamics of Solids: Optical Properties of Electrons in Matter, Cambridge: Cambridge University Press, 2002, pp. 217–244.

[16] M. Liang, M. Tuo, S. Li, Q. Zhu, and H. Xin, “Graphene conductivity characterization at microwave and THz frequency,” in The 8th European Conference on Antennas and Propagation (EuCAP 2014), 2014, pp. 489–491.

[17] G. Lovat, “Equivalent Circuit for Electromagnetic Interaction and Transmission Through Graphene Sheets,” IEEE Trans. Electromagn. Compat., vol. 54, no. 1, pp. 101–109, 2012.

[18] R. F. Xu, A. J. Farrall, and P. R. Young, “Analysis of Loaded Substrate Integrated Waveguides and Attenuators,” IEEE Microw. Wirel. Components Lett., vol. 24, no. 1, pp. 62–64, 2014.

[19] B. Douglas, K. Rytting, and S. N. Sanders, “A System for Automatic Network Analysis,” no. February 1970, 1998.

[20] G. F. Engen and C. A. Hoer, “’Throgh-Reflect-Line’ : An improved Technique for calibrating the dual six- port automatic network analyser,” 1979.

[21] F. Ghz, N. M. Ridler, and R. G. Clarke, “Establishing Traceability to the International System of Units for Scattering Parameter Measurements,” IEEE Trans. Terahertz Sci. Technol., vol. 6, no. 1, pp. 2–11, 2016.

[22] IEEE Std 1785.1-2012, “IEEE Standard for Rectangular Metallic Waveguides and Their Interfaces for Frequencies of 110 GHz and Above – Part 1: Frequency Bands and Waveguide Dimensions”.

[23] IEEE Std 1785.2-2016, “IEEE Standard for Rectangular Metallic Waveguides and Their Interfaces for Frequencies of 110 GHz and Above – Part 2: Waveguide Interfaces”.

[24] IEEE Std 1785.3-2016, “IEEE Recommended Practice for Rectangular Metallic Waveguides and Their Interfaces for Frequencies of 110 GHz and Above – Part 3: Recommendations for Performance and Uncertainty Specifications”.

[25] R. J. Collier, Transmission lines. Cambridge, UK: Cambridge Univ., 2013.

[26] R. J. Collier and D. G. Hasko, “Measurements of the sheet resistance of resistive films on thin substrates from 120 to 175 GHz using dielectric waveguides” J. Appl. Phys., vol. 91, p. 2547, 2003.

[27] R. J. Collier and D. G. Hasko, “Measurements of the sheet resistance of resistive films on thin substrates from 120 to 175 GHz using dielectric waveguides,” J. Appl. Phys, vol. 91, p. 2547, 2003.

[28] G.F. Engen ; C.A. Hoer, "'Thru-reflect-line'An improved technique for calibrating the dual six-port automatic network analyser," IEEE Trans. Microw. Theory Tech., vol. 27, no. 12, 1979.

[29] J. Fitzpatrick, "Error models for systems measurement," Microw. Journal, vol. 21, no. 5, pp. 63–66, 1979.

[30] J. Fitzpatrick, "Error models for systems measurement," Microw. J., vol. 21, no. 5, pp. 63–66.

[31] D. Rytting, "An analysis of vector measurement accuracy enhancement techniques," RF Microw. Symp. Exhib. Hewlett Packard, 1980.

[32] M. J. Salter, N. M. Ridler, and P. M. Harris, "Over-determined calibration schemes for," 62nd Autom. RF Tech. Gr. conf., pp. 127–142, 2003.

[33] M. J. Salter, N. M. Ridler, and P. M. Harris, "Reduced Uncertainty of Measurement for Vector Network Analysers Employing Regression During Calibration," in 2004 Conference on Precision Electromagnetic Measurements, 2004, pp. 107–108.

[34] T.J.B.M. Janssen, N.E. Fletcher, R. Goebel, J.M. Williams, A. Tzalenchuk, R. Yakimova, S. Kubatkin, S. Lara-Avila, and V.I. Falko, "Graphene, universality of the quantum Hall effect and redefinition of the SI system," New J. Phys. - NEW J PHYS, vol. 13, May 2011.

Chapter Five

Conclusions and Future work

5.1 Conclusion

In this thesis, we can conclude that the work of designing substrate integrated waveguide antennas and the use of graphene for tuning waveguides and calibration as the following:

- Chapter 2 presented a novel Slotted Substrate Integrated Waveguide antenna (SSIW). This design type of waveguide can be integrated with lumped elements or components for tuning along the slot. The antenna design works at a resonant frequency of 2.5 GHz, but has the possibility to be rescaled to millimeter wave frequencies. The design structure supports half mode ($\mathrm{TE}_{1/2,0}$).

  A comparison made between simulation and measurements shows good agreement. The gain of single SSIW antenna was 4.5 dBi. To increase the gain, a 2 × 2 SSIW array antenna was designed achieving 11.64 dBi gain with side lobe level -2.5 dB. Due to the the poor side lobe level, this design was not fabricated.

- A tri-band substrate integrated waveguide antenna was presented in chapter 3. This design differs from the conventional waveguide antenna by being terminated with open end. The open end does not radiate due to the SIW implementation. The structure acts as a two waveguide regions of different widths, which supports half mode $TE_{1/2,0}$ type modes. Five resonant modes are shown for frequency range 3-7 GHz, which has been studied. This design has the freedom to tune the resonant frequencies by varying the parameters of the slot.

  The tri-band resonant frequencies are 3.5 GHz, 5.163 GHz and 5.85 GHz, achieving a gain of 3.6 dBi, 6 dB and 6.99 dBi respectively. A comparison made between simulation and fabrication is shown to be in good agreement.

  To increase gain, a 2 × 2 SIW array antenna was designed and rescaled to operate at 2.8 GHz, 5 GHz (use for Wi-Fi) and 5.2 GHz (use for WLAN), achieving a gain of

9.1, 11.9 GHz and 11.6 dB respectively. Again, a good agreement has been achieved for the S-parameter and radiation pattern. This design is useful in 5 G applications but could be rescaled to higher frequencies.

- Chapter 4 presented the use of graphene for waveguides tuning and calibration; the graphene sheet conductivity has been studied and is related to the applied voltage or chemical potential of graphene. To tune the SIW, an applied voltage to the silicon dioxide/graphene has been applied. Due to the high conductivity of the bulk silicon, the S-parameters did not tune, for frequency range 2-7 GHz.

  Some solutions have been suggested to tuning the waveguide, by reducing the conductivity of silicon from 20000 to 2 S/m, or increasing the thickness of silicon from 3000 nm to 15 μm. By increasing sheet resistance of graphene from 5 to 5000 Ω, the S_{21} can be tuned giving a variable attenuator. These proposed solutions are only using simulation CST studio due to the available graphene samples.
  For high frequencies toward terahertz frequencies, a calibration for measurement using TRL method may cause an error. This may be caused by cable movements due to calibration and will lead to phase and amplitude change. A measurements has been done by placing mono, bi and tri-layers of graphene over the waveguide in different positions, of a frequency range of.. the frequency range 50-75 GHz. After de-embedding the effects quarts on waveguide, we can conclude that the values of Y_0, $2Y_0$ and $3Y_0$ is a new form for impedance standards. A good agreement has been shown between measurements and simulation.

5.2 Future work

- In chapter four, it was concluded that it is difficult to get attenuation at the waveguide because the radiation penetrate through the graphene and sio_2 toward the Si layer, which has high conductivity. The suggested solution was to increase thickness of sio_2 to 1.5 µm to prevent or reduce the radiation toward the Si layer. This is done using CST simulation and needs to be done in practice.

- At high frequencies (50-75 GHz), we measured the effect of graphene in mono-, bi- and tri-layer with quartz substrate in different positions. Thereby, we need to study the conductivity inside the graphene sheet, which is dependent on the chemical potential μ_c and the biased voltage. A more accurate result can be obtained for the calibration of graphene.